

Multifunctional Carbazole-Based Materials as Electrochemical Water Splitting and Photoredox
Catalysis

by

Jinkun Liu

A thesis submitted in partial fulfillment of the requirements for the degree of

Doctor of Philosophy

Department of Chemistry
University of Alberta

© Jinkun Liu, 2023

Abstract

The combustion of fossil fuels releases carbon dioxide and other greenhouse gases into our living atmosphere, which traps heat and causes global warming. Renewable energy, however, can help solve the problem above by producing far fewer greenhouse gases. Renewable energy is a general term for any form of naturally replenishable energy, such as sunlight, wind, waves, or heat of the earth. Converting sunlight or electricity into chemical bond energy has several advantages over traditional energy. One of these benefits is the ability to store clean energy for later use. Another merit is the ability to convert chemicals into more valuable products. This dissertation includes synthesis, characterization, usage, and explanation of catalysts or electrodes for water oxidation, and photoreaction.

The first part of the thesis discusses that the electrolysis of water to form hydrogen and oxygen is a promising method to generate renewable energy. This method requires electrodes that convert water into protons, electrons, and oxygen. We report a multifunctional polymer that conducts electrons, ions, and may coordinate with the metal ions in an oxygen evolution reaction (OER). The electrodes were prepared in two steps from off-the-shelf reagents. They operate with low loadings of abundant catalysts, and are among the most active (100 mA cm^{-2} at 1.43 V vs. RHE (1.41 V , iR corrected), and stable reported to date under harsh conditions ($85 \text{ }^\circ\text{C}$, 6 M KOH , 120 h (0.69 \% loss over the first 14.5 h , then 0.61 \% loss over 105.5 h). Control experiments on glassy carbon electrodes showed that the polycarbazole

system significantly outperformed a Nafion system of the same catalyst loading. This simple strategy can be applied to other types of electrodes.

The next part of the thesis reports the study of the first direct electropolymerization of a dicyanobenzene-carbazole dye functionalized with an imidazole group to prepare redox- and photoactive porous organic polymer (POP) films with a controlled amount by different Cyclic voltammetry (CV) cycles. The POP films were grown on indium-doped tin oxide (ITO) and carbon surfaces using a new monomer, 1-imidazole-2,4,6-tri(carbazol-9-yl)-3,5-dicyanobenzene (3CzImIPN), through a simple one-step process. The structure and activities of the POP films were investigated as photoelectrodes for electrooxidations, as heterogeneous photocatalysts for photosynthetic olefin isomerizations, and their solid-state photoluminescence behavior tunable by lithium-ion concentrations in solution. The results demonstrate that the photoredox-POPs can be used as efficient photocatalysts and have potential applications in sensing.

Preface

Chapter 1 is the introductory section on the background of water oxidation, functions of oxygen evolution electrode binders, and 1,2,3,5-Tetrakis(carbazol-9-yl)-4,6-dicyanobenzene (4CzIPN) and its derivatives.

Chapter 2 has been published as J. Liu, S. H. Bergens, *ACS Appl. Mater. Interfaces* **2023**, *15*, 25624–25632.

I am the first author who contributed to conceptualization, methodology, data acquisition, data analysis, experiments, writing the original draft, reviewing and editing. My supervisor, Prof. Steven H. Bergens, contributed to funding acquisition, project administration, supervision, conceptualization, writing the final draft, reviewing and editing.

Chapter 3 has been accepted as J. Liu, O. M. Perez, D. Lavergne, L. Rasu, E. Murphy, A. G. Rodriguez, and S. H. Bergens, *Polymers*.

I am the first author who contributed to conceptualization, data curation, formal analysis, investigation, methodology, software, visualization, writing the original draft, validation, reviewing and editing. Octavio Martinez Perez and Dominic Lavergne contributed to data curation, validation, formal analysis, writing, reviewing and editing. Dr. Loorthuraja Rasu contributed to conceptualization and methodology. Elizabeth Murphy and Andy Galvez Rodriguez carried out data curation, validation, writing, reviewing and editing. My supervisor, Prof. Steven H. Bergens, provided conceptualization, supervision, methodology, formal analysis, project administration, resources validation, writing, reviewing and editing the final manuscript.

Chapter 4 summarizes the works of this dissertation and illustrates the possible directions of future work.

Acknowledgments

First, I would like to express my deepest gratitude and appreciation to my supervisor, Prof. Steven H. Bergens. Without his guidance, support, and mentorship, it would have been impossible for me to walk through the entire journey of my Ph.D. Constant encouragement and belief in my abilities from Dr. Bergens have shaped me academically and personally, and I am truly indebted to him. My thanks extend to my supervisory committee, Prof. Arthur Mar, and Prof. Jonathan Veinot. I also would like to thank Prof. Jillian Buriak and Prof. Arthur Mar for helping me walk through a very hard time in my Ph.D. study. Furthermore, I extend my heartfelt gratitude to Dr. Anna Jordan for her invaluable assistance in editing, formatting, and treating this thesis with the utmost care and dedication, akin to her own work.

I am grateful to my colleagues, Dr. Shuai Xu, Dr. Prabin Nepal, Eric Beaulieu, Octavio Martinez Perez, Dominic Lavergne, Dr. Loorthuraja Rasu, Elizabeth Murphy, Andy Galvez Rodriguez, Dr. Mona Amiri, Prof. Chao Wang, James W. Pearson, Dr. Riley T. Endean, and Jueun Lee, for their collaboration, insightful discussions, and constant encouragement. Their presence and camaraderie have made the research environment stimulating and enjoyable. Their unwavering support and willingness to help have significantly contributed to the successful completion of this thesis.

My heartfelt appreciation goes to the technicians and the faculty of chemistry and Nanofab, Andrew Yeung, Michael Barteski, Krista Donlevy, Ryan Lewis, Gareth Lambkin, Dr. Ryan McKay, Mark Miskolzie, Dr. Nupur Dabral, Jennifer Jones, Wayne Moffat, Dr. Peng Li, Dr. Shiau-Yin Wu, Dr. Shihong Xu and Dr. Haoyang Yu for their assistance, expertise, and the resources they provided. Their expertise and guidance have been instrumental in conducting experiments, analyzing data, and obtaining meaningful results. I am indebted to them for their valuable contributions to my research.

Last but not least, I would like to extend my sincere thanks to my friends, Guojie Li, Xiaochen Dong, Changhao Fang, Fuwei Wen, Geng Xie, Xiang You, Qichao (Jennifer) Wu, Nicholas Kisson, and my parents Xia Li and Zhongwen Liu

for their love, encouragement, and understanding throughout this arduous journey. Their unwavering support, patience, and belief in me have been my constant source of strength and motivation. Their presence has provided solace during challenging times and has made the joyful moments all the more memorable.

To all those mentioned above and to anyone else who has contributed to my growth and the completion of this thesis, I extend my heartfelt gratitude. Your support and guidance have been invaluable. I am truly grateful for the role each of you has played in my academic and personal development.

Table of Contents

Chapter 1 Introduction	1
1.1 Background	1
1.2 Function of OER Electrode Binders	11
1.3 1,2,3,5-Tetrakis(carbazol-9-yl)-4,6-dicyanobenzene (4CzIPN) and Its Derivatives	14
1.4 References	19
Chapter 2 Electronically Conductive, Multifunctional Polymer Binder for Highly Active, Stable, and Abundant Composite Electrodes for Oxygen Evolution	26
2.1 Introduction	26
2.2 Results and Discussion	27
2.2.1 Substrate Preparation	27
2.2.2 Coordinative Deposition and OER Performance Over PCz/CF	28
2.2.3 Structure of The Ni ₃ Fe ₁ -PCz/CF	33
2.2.4 Ni, Fe on PCz Coated Ni Foam Electrode	35
2.3 Conclusions	38
2.4 Experimental Section	38
2.4.1 Materials and Instrumentation	38
2.4.2 Preparation of Polycarbazole (PCz) on Carbon Fiber Paper (CF) (PCz/CF) or Glassy Carbon (GC)	39
2.4.3 Preparation of Polycarbazole (PCz) on Ni Foam (PCz/Ni _{foam})	40
2.4.4 Loading NiFe or CoFe Metal Ions on PCz/CF or PCz/Ni _{foam} (Ni _x Fe _y -PCz/CF or Ni _x Fe _y -PCz/Ni _{foam})	40
2.4.5 Loading NiFe or CoFe Metal Ions on CF or Ni _{foam} (Ni _x Fe _y /CF or Ni _x Fe _y /Ni _{foam})	41
2.4.6 Loading Ni ₃ Fe ₁ Metal Ions onto The Glassy Carbon Electrodes (GC), CF, or Ni _{foam} Control Electrodes Using Nafion as Binder	41
2.4.7 Electrochemical Measurements	41
2.5 References	42

Chapter 3 A One-Step Electropolymerization of a Dicyanobenzene-Carbazole-Imidazole Dye for Photoelectrodes, Heterogeneous Photocatalysts, and Sensing Applications	47
3.1 Introduction.....	47
3.2 Results and Discussion	49
3.2.1 Preparation of Monomer.....	49
3.2.2 Electropolymerization of 3CzImIPN (1)	50
3.2.3 Properties of The Polymer.....	54
3.2.4 Utilization of Polymer Electrodes as Photoanodes	55
3.2.5 Stilbene Isomerization	57
3.2.6 Photoluminance Li Ion Response.....	59
3.2.7 Understanding The Polymer.....	60
3.3 Conclusions.....	63
3.4 Experimental Section	63
3.4.1 Materials	63
3.4.2 Fabrication of ITO Nanoparticles Coated ITO Glass Electrode (ITO-NP) ...	64
3.4.3 Preparation of Poly 3CzImIPN (1) on ITO-NP, ITO Glass (ITO), or Carbon Fiber Paper (CP)	64
3.4.4 Stilbene Isomerization	65
3.4.5 Photoluminescence Response to Lithium Ions	65
3.4.6 Characterization	65
3.5 References.....	66
Chapter 4 Conclusions and Outlook	72
Bibliography	76
Appendix A Supporting information for Chapter 2	93
Appendix B Supporting information for Chapter 3	121

List of Tables (Chapters)

Table 1.1. Some of the Recent Most Efficient Catalysts for Electrochemical OER under Alkaline Conditions.5

Table 1.2. A Brief Summary of Photoredox Reactions for 4CzIPN and Its Derivatives.16

Table 3.1. Photosynthetic Isomerization of trans- to cis-Stilbene by different ITO-NP Electrodes.....59

List of Tables (Appendixes)

Table S2.1. ICP-OES Results of Different Ratios of Ni, Fe and Ni, Co Electrodes. The Mole Ratios and Double Layer Capacitance (C_{dl}) Numbers are Calculated and Shown in the Table.100

Table S2.2. Table for Comparisons of the Output Results for Electrochemical Water Oxidation.....100

List of Figures (Chapters)

- Figure 1.1** Illustration of (a) proton exchange membrane (PEM) water electrolysis, (b) alkaline water electrolysis, and half-cell reactions on cathode and anode3
- Figure 1.2.** Diagram of OER (a) AEM and (b) LOM mechanism under alkaline conditions8
- Figure 1.3.** Illustration for (a) electrodeposition of NiFe with Bi on Au and H-type cell for OER. (b) The current density of NiFe-Bi catalysts at 300 mA cm^{-2} in 0.25 M KBi-containing KOH (9.5 M) solution with $0.5 \text{ mM Fe}^{\text{II}}$ ions. (c) UV/Vis absorption spectra detecting with different time for Fe^{VI} ; insert is the color change of electrolyte in the anode. (d) Absorbance at 505 nm changes with time. (e) illustration of the reaction mechanism10
- Figure 1.4.** Chemical structure of Nafion (a) and PTFE (b)12
- Figure 1.5.** Illustration for Synthesis of PANI-PA-Metal (Hgel-M_x) Hydrogels for Electrocatalysis of OER13
- Figure 1.6.** (a) structure of 4CzIPN, (b) structure of 3CzImIPN, (c) tradition fluorescence, (d) intersystem crossing (ISC) and reverse intersystem crossing (RISC) participate fluorescence, (e) mechanism of photodynamic therapy (PDT)14
- Figure 1.7.** mechanism of carbazole electro-polymerization17
- Figure 1.8.** (a) C-C coupling mechanism of carbazolyl groups (1) under different oxidation conditions to form dimer (2) or polymer (3). (b) Radical initiated topological polymerizations of monomer containing two carbazolyl moieties (4) under different oxidation conditions to form linear polymer (5) or polymer network (6)18
- Figure. 2.1.** PCz characterization and structure. (a) CV of the isolated, washed PCz/CF electrode (MeCN, 0.1 M LiClO_4). (b) FTIR of PCz/CF and $\text{Ni}_3\text{Fe}_1\text{-PCz/CF}$. (c) The structure of doped polycarbazole illustrating the potential roles of the functional groups during the OER28
- Figure. 2.2.** Performance of electrodes on PCz/CF. (a) OER LSV with different ratios of NiFe, CoFe, and control electrodes (CF, PCz/CF, and Co_3Fe_1 , Ni_3Fe_1 without PCz) in 1 M KOH at 1 mV s^{-1} . (b) Tafel slope, (c) double layer capacitance, and (d) mass activity (left) and TOF (right) at 1.454 V vs. RHE curves for Ni_1Fe_1 , Ni_3Fe_1 , $\text{Ni}_9\text{Fe}_1\text{-PCz/CF}$ 30
- Figure. 2.3.** Stability of $\text{Ni}_3\text{Fe}_1\text{-PCz/GC}$ and $\text{Ni}_3\text{Fe}_1\text{-Nafion/GC}$ electrodes. (a) The galvanostatic OER over $\text{Ni}_3\text{Fe}_1\text{-PCz/GC}$ and $\text{Ni}_3\text{Fe}_1\text{-Nafion/GC}$ for 24 h at 10 mA

cm⁻². (b) LSVs over Ni₃Fe₁-PCz/GC and Ni₃Fe₁-Nafion/GC before and after 24 h stability tests. (c) Nyquist plots (at 0.5 V vs. SCE) for Ni₃Fe₁-PCz/GC and Ni₃Fe₁-Nafion/GC before and after the 24 h stability tests. (d) Tafel slope of Ni₃Fe₁-PCz/GC and Ni₃Fe₁-Nafion/GC before stability tests33

Figure. 2.4. Morphology of Ni₃Fe₁-PCz/CF electrode. (a) SEM surface morphology of the Ni₃Fe₁-PCz/CF and EDX elemental mapping of (b) Ni, (c) Fe, (d) Cl, and (e) O34

Figure. 2.5. Morphology of Ni₃Fe₁-PCz/Ni_{foam} electrode. (a) SEM surface morphology of the Ni₃Fe₁-PCz/Ni_{foam} and EDX elemental mapping of (b) Ni, (c) Fe, (d) C, and (e) N36

Figure. 2.6. OER performance of Ni₃Fe₁-PCz/Ni_{foam} electrode. (a) LSV curves of Ni_{foam}, PCz/Ni_{foam}, Ni₃Fe₁/Ni_{foam}, Ni₃Fe₁-Nafion/Ni_{foam} and Ni₃Fe₁-PCz/Ni_{foam} in 1 M KOH at 1 mV s⁻¹. (b) Galvanostatic tests of Ni₃Fe₁-Nafion/Ni_{foam} and Ni₃Fe₁-PCz/Ni_{foam} at 100 mA cm⁻² over 24 h. (c) Galvanostatic tests of Ni₃Fe₁-PCz/Ni_{foam} at 100 mA cm⁻² over 120 h in 6 M KOH and at 85 °C versus RHE, without (black line) and with (red line) *iR* correction.....37

Figure. 3.1. (a) The X-ray structure of **1**, (b) absorbance UV-Vis spectrum of **1** (0.1 mM) in dichloromethane (DCM), and (c) the excitation and emission curve **1** (of 0.1 mM) in DCM50

Figure. 3.2. (a) CV curves of 10-**1**-ITO-NP in 0.1 M TBAPF₆ and 1mM of **1**. Sweep rate 100 mV s⁻¹, 10 sweeps, sweep range from -0.55 to 1.45 vs Fc/Fc⁺; (b) CV (sweep rate 10 mV s⁻¹; 5, 10, 45 sweeps; sweep range from -0.41 to -1.91 vs Fc/Fc⁺) curves of 5, 10, 45-**1**-ITO-NP compare with ITO-P in 0.1 M TBAPF₆ acetonitrile solution without monomer; (c) FT-IR of 45-**1**-ITO and 45-**1**-CP; (d) Tilted SEM of 45-**1**-ITO and corresponding (e) C and (f) Sn EDX mapping on ITO glass.....51

Figure 3.3. (a) XPS survey scans of 45-**1**-ITO and 45-**1**-CP and corresponding (b) C 1s and (c) N 1s of 45-**1**-ITO. (d) Reflectance UV-Vis of 5, 10, 45-**1**-ITO-NP by deduction of the ITO-NP substrates. (e) Optical band gap of 5, 10, 45-**1**-ITO-NP, and (f) LUMO and HOMO estimations.....55

Figure. 3.4. (a, c) IPCE tests of 5, 10, 45-**1**-ITO-NP in 0.1 M NaClO₄ dissolved in triple distilled water containing 0.02 M hydroquinone (pH = 7.0) (neutral condition) or 0.5 M Et₃N (pH = 12.6) (basic condition) at 0.25 V vs. SCE. (b) Stability test of 10-**1**-ITO-NP in the neutral conditions under simulated AM 1.5G sunlight with UV-light filter57

Figure. 3.5. (a) Reflectance UV-Vis spectra and (b) emission light excited at 420 nm of 45-**1**-CP. (c) The prototype example of Li-ion detection of 45-**1**-CP60

Figure. 3.6. TD-DFT-calculated (a) HOMO and (b) LUMO wave functions of the geometry optimized structures; (c) calculated UV-Vis spectra; (d) a Jablonski diagram for **1**; (e) photoluminescence intensity with applied potential.....61

List of Figures (Appendixes)

Figure S2.1. Growth of polycarbazole on carbon fiber paper (CF). (a) 45 cycles CV of CF electrode (area ~ 1 cm x 1 cm) in MeCN (0.1 M LiClO₄ and 0.005 M carbazole). (b) Corresponding of determining $E_{1/2}$ FC/FC⁺ reference in the same solution. The oxidation peak is at 0.423 V, and the reduction peak is at 0.0674 V vs. Ag/Ag⁺, $E_{1/2} = 0.245$ V.....82

Figure S2.3. Estimation of polymer amount on PCz/CF electrode. (b) I-t curve and (a) corresponding LSV curve; Scan rate 100 mV s⁻¹83

Figure S2.4. Estimation of Ni amount on Ni₃Fe₁-PCz/CF electrode. (b) I-t curve and (a) corresponding LSV curve; Scan rate 1 mV s⁻¹83

Figure S2.5. Comparison of literature with relatively low catalyst mass loading vs. OER overpotential. The mass loading of Ni₃Fe₁-PCz/Ni_{foam} is estimated from the Fe amount in ICP-OES supposing the ratio of Ni to Fe is 3 :1.....84

Figure S2.6. Determine double layer capacitance (C_{dl}) of Ni_xFe_y-PCz/CF electrodes. (a) CV scanning of Ni₁Fe₁-PCz/CF, (b) Ni₃Fe₁-PCz/CF, and (c) Ni₉Fe₁-PCz/CF for ECSA estimation. (d) The corresponding C_{dl} numbers are shown in the graph.....85

Figure S2.7. Determine double layer capacitance (C_{dl}) of Co_xFe_y-PCz/CF electrodes. (a) CV scanning of Co₁Fe₁-PCz/CF, (b) Co₃Fe₁-PCz/CF, and (c) Co₉Fe₁-PCz/CF for ECSA estimation. (d) The corresponding C_{dl} numbers are shown in the graph.....86

Figure S2.8. Stability of Ni₃Fe₁-PCz/GC and 5Ni₃Fe₁-Nafion/GC electrodes. (a) The galvanostatic OER over Ni₃Fe₁-PCz/GC and 5Ni₃Fe₁-Nafion/GC for 24 h at 10 mA cm⁻². (b) LSVs over Ni₃Fe₁-PCz/GC and 5Ni₃Fe₁-Nafion/GC before and after 24 h stability tests. (c) Nyquist plots (at 0.5 V vs. SCE) for Ni₃Fe₁-PCz/GC and 5Ni₃Fe₁-Nafion/GC before and after the 24 h stability tests. (d) Tafel slope of Ni₃Fe₁-PCz/GC and 5Ni₃Fe₁-Nafion/GC before stability tests87

Figure S2.9. Performance of Ni₃Fe₁-PCz/CF and Ni₃Fe₁-Nafion/CF electrodes. (a) The galvanostatic OER over Ni₃Fe₁-PCz/CF and Ni₃Fe₁-Nafion/CF for 20 h at 10 mA cm⁻². (b) LSVs over Ni₃Fe₁-PCz/CF and Ni₃Fe₁-Nafion/CF before and after 20 h stability tests. (c) Nyquist plots (at 0.5 V vs. SCE) for Ni₃Fe₁-PCz/CF and Ni₃Fe₁-Nafion/CF before and after the 20 h stability tests. (d) Tafel slope of Ni₃Fe₁-PCz/CF and Ni₃Fe₁-Nafion/CF before stability tests.....88

Figure S2.10. XPS of the electrodes on CF. (a)The Ni 2p and (b) Fe 2p regions in the high-resolution XPS spectra of Ni₃Fe₁-PCz/CF before (black line), and after the long-term galvanostatic OER (pink line) (conditions: Time, 20 h; current, 10 mA/cm²; solution, 1 M KOH). (c) and (d) are the Co 2p and Fe 2p regions in the high-resolution XPS spectra of Co₃Fe₁-PCz/CF89

Figure S2.11. Picture of glass electrodes. Picture of polycarbazole grown on ITO glass (PCz/ITO); after soaking PCz/ITO in methanol for 24 h and dry (PCz (methanol)/ITO glass); after soaking PCz/ITO in methanol with Ni²⁺ ions for 24 h (Ni-PCz (methanol)/ITO glass) and after soaking PCz/ITO in methanol with Fe²⁺ ions for 24 h (Fe-PCz (methanol)/ITO glass) and dry89

Figure S2.12. UV-Vis of different polycarbazole electrodes on ITO glass. (a) The UV-Vis graph subtracts undoped PCz/ITO glass as blank: Polycabazole on ITO glass without soaking in methanol (doped PCz/ITO glass); Polycabazole on ITO glass after soaking with Ni ions (undoped Ni-PCz/ITO glass); Polycabazole on ITO glass after soaking with Fe ions (undoped Fe-PCz/ITO glass) and Polycabazole on ITO glass after soaking in methanol without metal ions (undoped PCz/ITO glass). (b) The original UV-Vis graph without subtraction. The peak around 700 nm in undoped Ni-PCz/ITO glass represents the presence of Ni ions. The peak around 400 nm in both undoped Ni or Fe-PCz/ITO glass represents the presence of Ni and Fe ions. However, the Fe-PCz/ITO glass peak starts earlier and is stronger90

Figure S2.13. Comparison of CVs with or without carbazole on Ni foam. (a) 45 cycles CV of electropolymerization carbazole on Ni foam with 0.0050 M carbazoles and (b) without carbazole in 0.10 M LiClO₄ MeCN solution.....90

Figure S2.14. Comparison of Ni_{foam} and PCz/Ni_{foam} electrodes. (a) 10 cycles CV of Ni_{foam} and (b) PCz/ Ni_{foam} electrode (area ~1 cm x 1 cm) in DCM with 0.1 M TBAPF₆). (c) Corresponding of determining $E_{1/2}$ of FC/FC⁺ reference in the same solution. The oxidation peak is at 0.555 V, and the reduction peak is at -0.149 V vs. Ag/Ag⁺. Therefore, $E_{1/2} = 0.203$ V91

Figure S2.15. Picture of Ni foam (Ni_{foam}) electrodes. Picture of Ni_{foam}, polycarbazole grew on Ni_{foam} (PCz/Ni_{foam}), and NiFe metal ions coordinate on the polycarbazole (Ni₃Fe₁-PCz/Ni_{foam}).....91

Figure S2.16. Morphology of Ni_{foam} electrodes. SEM surface morphology of the (a) Ni_{foam}, (b) PCz/ Ni_{foam}, and (c) Ni₃Fe₁-PCz/Ni_{foam}.....91

Figure S2.17. Comparison FTIR of Ni_{foam} electrodes. (a) FTIR spectra of the PCz/Ni_{foam} and (b) Ni₃Fe₁-PCz/Ni_{foam} electrodes92

Figure S2.18. Comparison XPS of Ni_{foam} electrodes. XPS of (a) C 1s, (b) N 1s, and (c) O 1s in PCz/Ni_{foam}; XPS of (d) C 1s, (e) N 1s, and (f) O 1s in Ni₃Fe₁-PCz/Ni_{foam}....92

Figure S2.19. Ni, Fe XPS in Ni₃Fe₁-PCz/Ni_{foam}. (a) The Ni 2p and (b) Fe 2p regions in the high-resolution XPS spectra of Ni₃Fe₁-PCz/Ni_{foam}.....93

Figure S2.20. Estimation of Ni amount on Ni₃Fe₁-PCz/Ni_{foam} electrode. (b) *I-t* curve and (a) corresponding LSV curve ; Scan rate 1 mV s⁻¹.....93

Figure S2.21. Galvanostatic stability test of Ni₃Fe₁-PCz/Ni_{foam} at 10 mA cm⁻² over 22 h. The performance of Ni₃Fe₁-PCz/Ni_{foam} at 10 mA cm⁻² was read after the stability test94

Figure S2.22. Tafel slope of Ni₃Fe₁-PCz/Ni_{foam} electrode. Conditions: in 1 M KOH and scan rate of 1 mV s⁻¹94

Figure S2.23. Stability test of Ni₃Fe₁-PCz/Ni_{foam}. (a) The LSV curves of Ni₃Fe₁-PCz/Ni_{foam} electrode before and after 24 h stability test 1 M KOH, scan rate 5 mV s⁻¹. (b) Nyquist plots of the Ni₃Fe₁-PCz/Ni_{foam} electrode before and after the 24 h stability test at 0.5 V vs. SCE. The curves are not in perfect shapes and may originate from O₂ bubble interference at this relatively high voltage95

Figure S2.24. Stability test of Ni₃Fe₁-PCz/Ni_{foam} electrode under harsh conditions. Nyquist plot of the Ni₃Fe₁-PCz/Ni_{foam} electrode after 120 h stability test in 6 M KOH and 85 °C at 0.5 V vs. Hg/HgO reference electrode. The conversion from Hg/HgO to RHE is described in the supplementary text95

Figure S2.25. XPS of CF substrate electrodes. XPS of (a) C 1s, (b) N 1s, and (c) O 1s in Ni₃Fe₁-PCz/CF; XPS of (d) C 1s, (e) N 1s, and (f) O 1s in Co₃Fe₁-PCz/CF96

Figure S2.26. Illustration of atoms observed by XPS. (a) sp² C bonded to -C and -N, (b) N⁺ in doped polycarbazole, (c) N coordinated to the metal96

Figure S2.27. XPS survey spectra. From top to bottom: Co₃Fe₁-PCz/CF; Ni₃Fe₁-PCz/CF; Ni₃Fe₁-PCz/Ni_{foam}; PCz/Ni_{foam}97

Figure S2.28. Chemical stability test of PCz. (a, b) PCz/CF in 6 M KOH and 1 M KOH over 240 h. (c, d) PCz/Ni_{foam} in 1 M KOH and 6 M KOH over 240 h. (e, f) 1 M KOH and 6 M KOH without any electrode97

Figure S2.29. Electrodes before and after CV tests. (a, b) After soaking the PCz/CF electrodes in 6 M KOH or 1 M KOH for 240 h, then washing with triple-distilled water before CV tests. (c, d) After soaking the PCz/CF electrodes in 6 M KOH or 1 M KOH for 240 h, then washing with triple-distilled water before CV tests. (e – h) a, b, c, and d electrodes after CV tests98

Figure S2.30. CVs before and after soaking in KOH. (a, b) CVs of PCz/CF electrodes before and after 1 M KOH soaking over 240 h. (c, d) CVs of PCz/CF electrodes before and after 6 M KOH soaking over 240 h99

Figure S2.31. Performance of electrodes on PCz/CF substrates. (a) Tafel slope, (b) double layer capacitance, and (c) mass activity (left) and TOF (right) at 1.50 V vs. RHE curves for Co₁F₁, Co₃F₁, and Co₉F₁-PCz/CF99

Figure S3.1.(a) CV curves of 5-1-ITO-NP in 0.1 M TBAPF₆ and 1mM **1** in DCM. (b) CV curves of 45-1-ITO-NP in 0.1 M TBAPF₆ and 1mM **1**. Sweep rate 100 mV s⁻¹, 5 or 45 sweeps, sweep range from -0.55 to 1.45 vs Fc/Fc⁺. (c) Determination of E_{1/2} for Fc/Fc⁺ reference in the same solution.....107

Figure S3.2. (a) Negative region CV curves for isolated 5-, 10-, and 45-1-ITO-NP compared to an ITO-NP blank showing the 1 e⁻ redox wave for the dicyanobenzene groups in the polymers (0.1 M TBAPF₆ in MeCN, sweep rate 10 mV s⁻¹ from -0.41 to -1.91 vs Fc/Fc⁺); (b) Determination of E_{1/2} for Fc/Fc⁺ reference in the same solution.....107

Figure S3.3. (a) CV curves for electropolymerization of **1** to prepare 45-1-ITO and (b) 45-1-CP in 0.1 M TBAPF₆ and 1mM **1** in DCM (45 sweeps, sweep rate 100 mV s⁻¹ from -0.55 to 2.45 vs Fc/Fc⁺)108

Figure S3.4. Enlarged FT-IR region with putative assignments of the weak stretching peaks for the dicyano groups on the central aromatic ring in 45-1-ITO and 45-1-CP108

Figure S3.5. The deconvoluted XPS of elements (a) C 1s, (b) N 1s, and (c) O 1s on 45-1-CP108

Figure S3.6. CVs (sweep rate 10 mV s⁻¹ from -0.30 to -1.86 vs Fc/Fc⁺) of the 5, 10, or 45-1-ITO-NP electrodes immersed in CH₂Cl₂ with 0.1 M TABPF₆. The onset potentials were determined, as shown in the figure.....109

Figure S3.7. IPCE measurements with the ITO-NP control, and (a) 10-1-ITO-NP electrodes under neutral and (b) 45-1-ITO-NP electrodes under alkaline conditions. 0.02 M hydroquinone (pH = 7.0) (neutral condition) or 0.5 M Et₃N (pH = 12.6) (basic condition) in triple distilled water at 0.25 V vs. SCE. Each spike in current corresponds to a decrease in wavelength by 10 nm, starting at 700 nm, then down to 400 nm. The light was held at each wavelength for ~8 sec109

Figure S3.8. (a) The steady-state potentiostatic photoelectrooxidation of hydroquinone over 10-1-ITO-NP under neutral conditions, and of triethyl amine over 45-1-ITO-NP under basic conditions. 0.02 M hydroquinone (pH = 7.0) (neutral condition) or 0.5 M Et₃N (pH = 12.6) (basic condition) in triple distilled water at 0.25 V vs. SCE.....110

Figure S3.9. Estimation of electrochemically accessible surface coverage of poly **1** from the charge under the one-electron redox wave for the dicyanobenzene moieties in the polymer. 5-1-ITO-NP: 1.50 x 10⁻⁸ mol; 10-1-ITO-NP: 2.94 x 10⁻⁸ mol; 45-1-ITO-NP: 4.74 x 10⁻⁸ mol.....110

Figure S3.10. ¹H NMR of 3CzImIPN (**1**). The δ region from 10 to 1 ppm showing the ¹H NMR. The spectrum is acquired in CD₃CN with 500 MHz Varian Inova112

Figure S3.11. Zoom in ^1H NMR of 3CzImIPN (1). The δ region from 9 to 6 ppm showing the ^1H NMR. The spectrum is acquired in CD_3CN with 500 MHz Varian Inova	113
Figure S3.12. ^{13}C NMR of 3CzImIPN (1), from 0 to 190 ppm. The spectrum is acquired in acetone by Varian VNMRS 500 MHz NMR spectrometer	114
Figure S3.13. Zoom in ^{13}C NMR of 3CzImIPN (1), from 100 to 160 ppm. The spectrum is acquired in acetone by Varian VNMRS 500 MHz NMR spectrometer.....	114
Figure S3.14. ^1H NMR of stilbene isomerization by ITO-NP for 16 h; the δ region from 10 to 0 ppm.....	115
Figure S3.15. ^1H NMR of stilbene isomerization by ITO-NP for 48 h; the δ region from 10 to 0 ppm.....	116
Figure S3.16. Zoom in ^1H NMR of stilbene isomerization by new ITO-NP for 48 h; the δ region from 6 to 8 ppm.....	116
Figure S3.17. ^1H NMR of stilbene isomerization by 5-1-ITO-NP for 16 h; the δ region from 10 to 0 ppm	117
Figure S3.18. ^1H NMR of stilbene isomerization by 5-1-ITO-NP for 48 h; the δ region from 10 to 0 ppm	118
Figure S3.19. Zoom in ^1H NMR of stilbene isomerization by 5-1-ITO-NP for 48 h; the δ region from 6 to 8 ppm.....	119
Figure S3.20. ^1H NMR of stilbene isomerization by 10-1-ITO-NP for 16 h; the δ region from 10 to 0 ppm	120
Figure S3.21. ^1H NMR of stilbene isomerization by 10-1-ITO-NP for 48 h; the δ region from 10 to 0 ppm	121
Figure S3.22. Zoom in ^1H NMR of stilbene isomerization by 10-1-ITO-NP for 48 h; the δ region from 6 to 8 ppm.....	122
Figure S3.23. ^1H NMR of stilbene isomerization by 45-1-ITO-NP for 16 h; the δ region from 10 to 0 ppm	123
Figure S3.24. ^1H NMR of stilbene isomerization by 45-1-ITO-NP for 48 h; the δ region from 10 to 0 ppm	124
Figure S3.25. Zoom in ^1H NMR of stilbene isomerization by 45-1-ITO-NP for 48 h; the δ region from 6 to 8 ppm.....	125

- Figure S3.26.** ^1H NMR of stilbene isomerization by the second run of 5-1-ITO-NP for 16 h; the δ region from 10 to 0 ppm.....126
- Figure S3.27.** ^1H NMR of stilbene isomerization by the second run of 5-1-ITO-NP for 48 h; the δ region from 10 to 0 ppm.....127
- Figure S3.28.** Zoom in ^1H NMR of stilbene isomerization by the second run of 5-1-ITO-NP for 48 h; the δ region from 6 to 8 ppm.....128
- Figure S3.29.** ^1H NMR of stilbene isomerization by new 5-1-ITO-NP for 88 h; the δ region from 10 to 0 ppm129
- Figure S3.30.** Zoom in ^1H NMR of stilbene isomerization by 5-1-ITO-NP for 88 h; the δ region from 6 to 8 ppm.....129

List of Schemes (Chapters)

Scheme 3.1. Synthesis of the monomer 3CzImIPN (1).....	49
Scheme 3.2. Proposed structure of the polymer in both the neutral and oxidized (doped) forms. This redox behavior is typical of polycarbazoles.....	53
Scheme 3.3. Stilbene isomerization.....	57

List of Abbreviations

3CzImIPN	1-imidazole-2,4,6-tri(carbazol-9-yl)-3,5-dicyanobenzene
4CzIPN	1,2,3,5-Tetrakis(carbazol-9-yl)-4,6-dicyanobenzene
AEM	adsorbate evolution mechanism
AEM	anion exchange membrane
AM 1.5G	air mass 1.5 global
CDCB	carbazoyl dicyanobenzene
C_{dl}	double-layer capacitance
CF	carbon fiber paper
CP	carbon fiber paper
CV	cyclic voltammetry
Cz	carbazolyl
DCM	dichloromethane
ECSA	electrochemical active surface area
EDX	energy-dispersive X-ray spectroscopy
EIS	electrochemical impedance spectroscopy
Fc	ferrocene
FE-SEM	Field Emission Scanning Electron Microscope
FTIR	Fourier transform infrared spectrum
GC	glassy carbon
GDE	gas diffusion electrode
HER	hydrogen evolution reaction
HOMO	highest occupied molecular orbital
HPC	hydroxypropyl cellulose

HQ	hydroquinone
IC	internal conversion
ICP-OES	inductively coupled plasma-optical emission spectroscopy
IPCE	incident photon-to-current efficiency
ISC	intersystem crossing
ITO	indium-doped tin oxide
LDH	layered double hydroxide
LOM	lattice oxygen mechanism
LSV	linear sweep voltammetry
LUMO	lowest unoccupied molecular orbital
NiFe-Bi	Borate intercalated NiFeOOH
NiFe-LDH	nickel-iron layered double hydroxide
OER	oxygen evolution reaction
O _L	lattice oxygen
OLED	organic light-emitting diode
PA	phytic acid
PANI	polyaniline
PANI-PA	polyaniline-phytic acid
PBI	polybenzimidazole
PCz	polycarbazole
PDT	photodynamic therapy
PEM	Polymer Electrolyte Membrane
PEM	proton exchange membrane
POP	porous organic polymer
PS	photosensitizer

PTFE	polytetrafluoroethylene
RHE	reversible hydrogen electrode
RISC	reverse intersystem crossing
SCE	saturated calomel electrode
SEM	Scanning electron microscope
SOMO	singly occupied molecular orbital
TADF	thermally activated delayed fluorescence
TBAPF ₆	tetrabutylammonium hexafluorophosphate
TD-DFT	Time-Dependant Density Functional Theory
TDW	triple distilled water
TEA	triethylamine
TFE	sulfonated tetrafluoroethylene
TOF	turnover frequency
UKS	unrestricted Kohn-Sham
UV/Vis	ultraviolet visible
VO	oxygen vacancy
XPS	X-ray photoelectron spectroscopy
η	overpotential

CHAPTER 1

Introduction

1.1 Background

Our world is facing an unprecedented energy demand due to the increasing global population, industrialization, and economic development. Fossil fuels, such as coal, oil, and natural gas, have been the primary energy sources for decades; however, their environmental impact, including the emission of greenhouse gases and the depletion of non-renewable resources, has become a major concern.¹ Moreover, the energy sector is responsible for emitting approximately three-quarters of anthropogenic global greenhouse gases, which has a critical impact on climate change. Given the severity of the current global crisis, it is urgent for researchers to seek renewable, sustainable, and environmentally friendly energy sources to reduce greenhouse gas emissions and mitigate climate change.² Global efforts are needed to seek viable and sustainable sources of clean energy to achieve carbon neutrality by 2050 or by 2060 at the latest.^{3,4} The current greenhouse gas levels in the atmosphere are at record highs. The World Energy Outlook 2021 reports⁵ that we collectively emit around 50 billion tons of CO₂ each year, which is more than 40% higher than emissions in 1990. Carbon dioxide (CO₂) is one of the most dominant human-induced contributors to greenhouse gas, followed by methane and nitrous oxide. The projected temperature changes depend on the scenarios and assumptions used by different models, but they all show a clear trend of increasing warming unless drastic actions are taken.

The projected temperature changes depend on the scenarios and assumptions used by different models, but they all show a clear trend of increasing warming unless drastic actions are taken. The World Energy Outlook 2021⁵ estimates that in the Net Zero Scenario, where CO₂ emissions are net zero in 2050 globally and there are rapid reductions in all non-CO₂ emissions, the rise in temperature will reach a maximum level of just over 1.5 °C around 2050. However, in the Stated Policies Scenario,

where emissions follow current policies and plans, the rise in temperature would exceed 1.5 °C around 2030 and reach around 2.6 °C by 2100.

A shift from fossil fuels to renewable energy for most applications is essential to achieve decarbonization. Such a shift will require a fundamental transformation of energy transportation, production, and consumption. Hydrogen, with its high mass-energy density (142 kJ g⁻¹, compared to fossil fuels at 10–50 kJ g⁻¹) and zero carbon emissions from its combustion or electrochemical oxidation, makes it a highly attractive option. There are challenges with the wide-scale adoption of hydrogen that largely arise from transportation and storage. Hydrogen can be stored as gas, liquid, or solid form. Gas storage includes compressing hydrogen into tanks or cylinders at high pressures, which is the most common method for small-scale applications. Liquid storage involves cooling to ~ -253 °C, which is being investigated for compact and dense storage for industrial large-scale utilization. Solid-state storage of hydrogen requires binding hydrogen into other materials, such as metals or organic compounds in the solid state.^{6–10} Green hydrogen is produced via renewable energy sources, such as wind, solar, hydro, and thermochemical process.^{11,12} As such, green hydrogen generation holds great promise for enabling a global transition to sustainable energy storage.¹³ Electrolysis driven by electricity is recognized as one of the most common methods for the generation of hydrogen.^{14,15} Moreover, electrolyzers can be powered by renewable electricity sources, like solar, wind, or hydroelectric power, which allow for the production of green hydrogen with near-zero carbon emissions.^{16,17} Furthermore, electrolyzers can be scaled up or down, making them suitable for both centralized and decentralized hydrogen production.¹⁸ Similar to fuel cells, the electrolyzers consist of an anode (oxidation reaction took place) and a cathode (reduction reaction took place) separated by an electrolyte. Electrolyzers can be classified as follows:^{19,20} Polymer Electrolyte Membrane (PEM), also known as Proton Exchange Membrane, is utilized in electrolyzers typically composed of a solid polymer structure and an acid water solution that facilitates proton transport. As shown in Figure 1.1a, in the PEM electrolyzers, water is oxidized to form oxygen and protons at the anode ($2\text{H}_2\text{O}(\text{l}) \rightarrow \text{O}_2(\text{g}) + 4\text{H}^+ + 4\text{e}^-$). Electrons

flow from the anode to the cathode by an external circuit. The protons can move across the PEM from the anode to the cathode. At the cathode, protons are combined with electrons to generate hydrogen ($4\text{H}^+ + 4\text{e}^- \rightarrow 2\text{H}_2(\text{g})$). The membrane of PEM usually is made of a polymer such as Nafion or Aquivion, which has sulfonic acid groups. The catalysts of PEM are typically platinum-based alloys for the hydrogen evolution reaction (HER) and iridium-based alloys for the oxygen evolution reaction (OER). The catalysts are deposited on porous substrates, such as carbon paper or cloth to form gas diffusion electrodes (GDEs) that are attached to the membrane. One of the most recent examples is Elogen, a French company selected by ENERTRAG, which will install its 10 MW PEM electrolyzer on a site near Magdeburg, Germany in 2024 to produce green hydrogen.

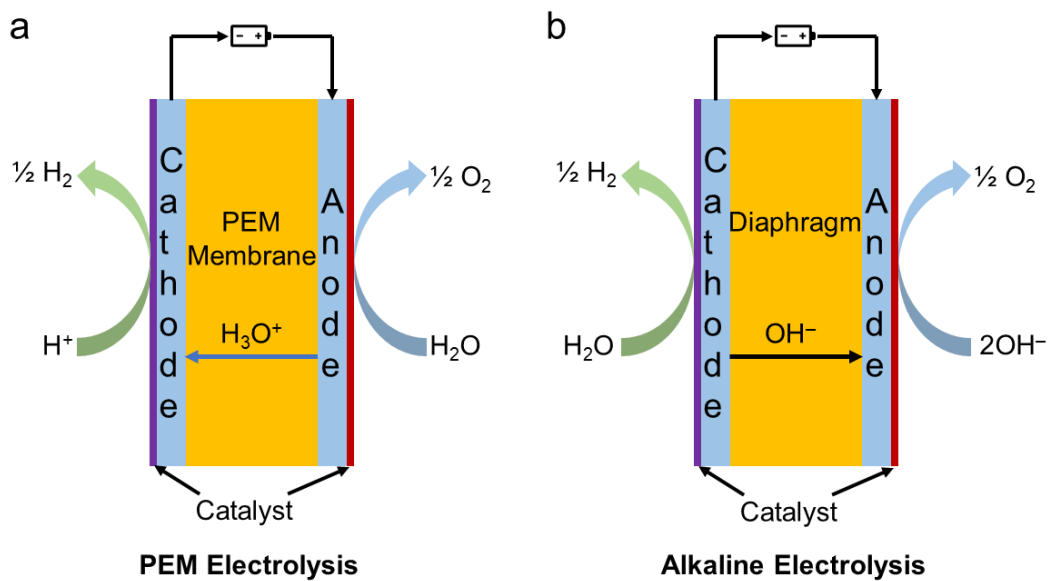


Figure 1.1 Illustration of (a) proton exchange membrane (PEM) water electrolysis, (b) alkaline water electrolysis, and half-cell reactions on cathode and anode

As illustrated in Figure 1.1b, alkaline systems are another common type of water electrolyzer. In contrast with PEM systems, the electrolyte in alkaline electrolyzers is typically potassium hydroxide (KOH) or sodium hydroxide (NaOH) dissolved in water. They typically operate between 30–90°C with 20–30 wt% KOH/NaOH in aqueous solution.²¹ Alkaline electrolyzers often are used in industries

for large-scale hydrogen production due to their reliability and relatively low cost. These electrolyzers operate as follows: OH^- is oxidized to oxygen and water at the anode, with the electrons being transported to the cathode by an external circuit ($4\text{OH}^- \rightarrow \text{O}_2(\text{g}) + \text{H}_2\text{O}(\text{l}) + 4\text{e}^-$). At the cathode, water is reduced to hydrogen and OH^- . The OH^- is transported through the electrolyte ($4\text{H}_2\text{O}(\text{l}) + 4\text{e}^- \rightarrow 4\text{OH}^-(\text{l}) + 2\text{H}_2(\text{g})$). PEM systems generally require noble metal catalysts at the anode and cathode, for example, $\text{RuO}_2/\text{IrO}_2$ as anode and Pt as cathode, resulting in high costs, toxicity, and environmental impact. The membrane of alkaline electrolyzers usually is made of a ceramic material, such as zirconia, or a polymer such as polybenzimidazole (PBI) that has quaternary ammonium groups attached to it. The catalysts of alkaline electrolyzers are typically nickel-based alloys for both HER and OER. The catalysts are deposited on metal meshes or foams to form electrodes that are separated by the separator. The utilization of earth-abundant catalysts brings the possibility of replacing noble metals like Ir and Ru, but abundant catalysts are generally unstable in acidic conditions. Alkaline electrolyzers, on the other hand, operated with abundant catalysts. For example, HydrogenPro is a Norwegian company that plans to debut its 3rd generation of high-pressure alkaline systems for green hydrogen in July 2023. Moreover, the company claimed that as the #1 provider of large-scale green hydrogen technology and systems, they are planning to establish 500 MW of manufacturing capacity in Texas, US by the end of 2024; this will increase the manufacturing capacity to 500 MW in China by 2023 and scale up assembly and manufacturing in Europe.

Generally, water electrolysis can be divided into two half-cell reactions: hydrogen evolution reaction (HER) and oxygen evolution reaction (OER). The main challenges in (commercial) water electrolyzers are to develop efficient and stable electrocatalysts for OER²² and low-cost and stable catalysts for HER.²³ Compared with the two-electron process of HER, the OER reaction is a four-electron process, which requires a higher overpotential to drive the reaction and suffers from slower reaction kinetics.^{24,25} An enormous amount of research has been directed to finding highly effective and stable earth-abundant catalysts to be used in alkaline

electrolyzers, as demonstrated in these recent review articles.^{13,26–28} Table 1.1 summarizes some of the most efficient catalysts reported for the alkaline OER.

Table 1.1. Some of the Recent Most Efficient Catalysts for Electrochemical OER under Alkaline Conditions.

Electrocatalyst	Electrolyte	η (mV) at j (10 mA cm _{geo} ⁻²) vs. RHE	Operation temperature	Tafel slope (mV dec ⁻¹)	Ref
MoC-FeNi@NLC	1.0 M KOH	198	room temperature	69	29
Fe-24h/NF	1.0 M KOH	215	room temperature	47.3	30
Ni _{0.75} V _{0.25} LDH	1.0 M KOH	200	room temperature	48.3	31
NiSe@CoFe LDH/NF	1.0 M KOH	203	room temperature	90.3	32
NiFeW ₃ -LDHs	1.0 M KOH	211	room temperature	36.44	33
Sulfur-doped NiCo-(oxy)hydroxysulfides (NCOSH)	0.1 M KOH	243	room temperature	63	34
(Fe,Co)OOH/MI	1.0 M KOH	230	room temperature	73	35
S-FeOOH/IF	1.0 M KOH	244	room temperature	59	36
NiFeV nanofibers on carbon cloth	1.0 M KOH	181	room temperature	47	37
MoNiFe-27% (oxy)hydroxide	1.0 M KOH	242	room temperature	23	38

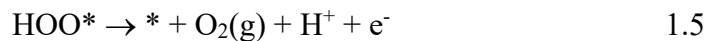
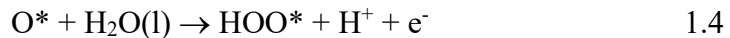
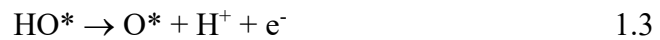
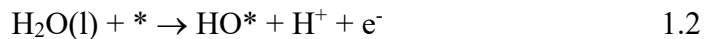
One of the common benchmarks for evaluating the HER or OER performance of an electrode is overpotential (η) at a current density (j) = 10 mA cm_{geo}⁻² (cm_{geo}⁻² is the geometric area of the electrode). 10 mA cm_{geo}⁻² is chosen because it corresponds to a 10% solar-to-fuel conversion efficiency under standard AM 1.5 G light (for the air mass 1.5 (AM 1.5), it is where the sun is about 41° above the horizon and the cell is tilted by 37° from the horizon. A spectrum that includes the blue sky and the surrounding ground is called a global spectrum (G)) by a solar-powered electrolyzer, which is considered sufficient to satisfy the predicted global energy requirements by 2050.³⁹ However, as discussed by Wei and Xu,⁴⁰ there are other factors, such as

catalysts loading, substrate types (results in various catalyst surfaces), and others that result in the current density arising from factors besides intrinsic catalytic activity. In general, the Tafel slope is defined as a linear region in logarithm plot of the current density j versus overpotential η . The Tafel slope provides information on the rate-determining step for the OER.⁴¹ In simple terms, a high Tafel slope means the electrode is inefficient, and results in energy being wasted.

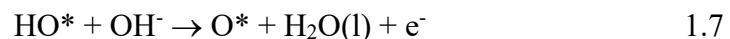
The oxygen evolution reaction (OER) is a complex four-electron transfer process, and it is believed to be the rate-limiting process in electrochemical water splitting. More specifically, the slow step often involves the high energy barrier associated with forming the O–O bond.^{42,43} The energy required to overcome this kinetic barrier drives the actual potential for the OER above the standard reduction potential of 1.23 V. The standard reduction potential for OER is the tendency of oxygen to gain electrons and be reduced to water at standard conditions (298 K, 1 atm, and 1 M solutions). It is measured relative to the reference hydrogen electrode (RHE), which is assigned a potential of zero volts. The standard reduction potential for OER is expressed as the following half-reaction (Eq 1.1):⁴⁴



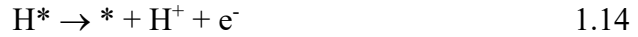
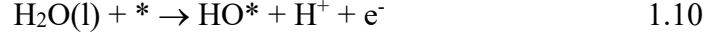
The mechanism of OER is not yet fully understood. However, a widely accepted process in acidic media involves reaction intermediates and active sites (*). It is the adsorbate evolution mechanism (AEM), as described below:⁴⁵



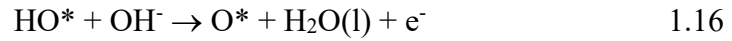
Under alkaline conditions, it can be written as follows:⁴⁶



Different from AEM, the lattice oxygen mechanism (LOM) involves lattice oxygen (O_L) and oxygen vacancy (V_O) of catalysts incorporated in the OER reaction, which can be conducted as follows:⁴⁷



In basic conditions, LOM can be interpreted as follows:⁴⁸



It is important to note that highly concentrated acidic conditions are more corrosive than basic conditions, although increasing the temperatures of electrolyzers can improve the efficiency of water splitting by boosting reaction kinetics and thermodynamic processes. Doing so increases the severity of the conditions at the anode that then must operate at high temperatures in an extremely acidic environment, with large, oxidative overpotentials over long periods of time (thousands of hours). Alkaline environments are used more commonly in industry and most research efforts in this area are directed towards finding a stable, active anode that operates in base. The general, bulk mechanism for the AEM is illustrated in Figure 1.2a. OH^- is adsorbed first on a surface active site(s), forming surface OH^* species after loss of an electron (Eq. 1.6). The active OH^* intermediate is deprotonated by OH^- , leading to the formation of an intermediate O^* species, along with loss of another electron (Eq. 1.7). Then, the intermediate O^* species is attacked by OH^- in the electrolyte, producing an intermediate with an oxygen-oxygen bond, $*OOH$, along with further

loss of an electron (Eq. 1.8). Finally, the $^*\text{OOH}$ species is deprotonated by OH^- to form the product oxygen and water, losing one electron, and regenerating the active site on the surface (Eq. 1.9). This is a broad representation of the mechanism; the details of the steps for an OER electrode will depend upon the specific catalyst, support, and electrolyte. As shown in Figure 1.2b, the alkaline LOM operates by the same first two steps as the AEM.

The formed O^* couples with lattice oxygen (O_L) to liberate oxygen and generate an oxygen vacancy (V_O). The lattice oxygen is proposed to be generated as follows: OH^- binds to a vacant site, resulting in the formation of OH^* through loss of an electron. Then, deprotonation of OH^* by OH^- and loss of an electron forms the lattice oxygen. It should be noted that the LOM mechanism contains single-metal sites or double-metal sites.^{49,50,51}

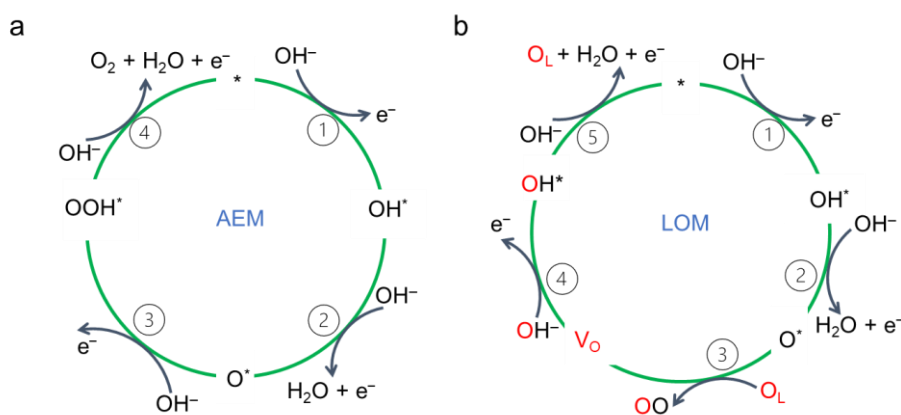


Figure 1.2. Diagram of OER (a) AEM and (b) LOM mechanism under alkaline conditions

The most widely used nonprecious metal catalysts for OER under alkaline conditions are based upon Ni and Fe. The incorporation of Fe into Ni-based catalysts provides a superior OER activity to either Fe or Ni on their own. The exact mechanism for NiFe-based OER catalysts still needs to be determined, and many reports continue to appear in the literature. For some of the recent reviews, please see these references.⁵²⁻⁵⁴ The following is a representative study. For NiFe oxyhydroxides,

leaching of Fe is highly likely even at a low current density of 10 mA cm^{-2} , which will be more obvious at a higher current density (200 mA cm^{-2}).^{55,56} This phenomenon may provide researchers a chance to study the reaction intermediate of Fe species in solution. In a recent study reported by Li et al., the authors claim that Fe is the active site for NiFe-based OER catalysts.⁵⁶ NiFeOOH has intercalated with borate (NiFe-B_i) on Au foil by electrodeposition as the working electrode. The interaction happens in the layer structure of NiFeOOH as borate compensates for the extra charge brought by Fe³⁺ compared to Ni²⁺. This anion compensation happens spontaneously like layered double hydroxide (LDH), where Ni and Fe are in the main plain and anions are intercalated in the middle of each plain.

Then, the NiFe-B_i electrode is tested in a three-electrode-based H-type electrochemical cell, where the anode and cathode are separated by an Axion Exchange Membrane (AEM). Fe^{II} ions were added into the anode half-cell to compensate for the loss of Fe active center during the OER process. To monitor the highly oxidized Fe^{VI} active center in the electrolyte, the authors used a large application current (300 mA cm^{-2}) and a long operation time (350 h, Figure 1.3b). During the OER experiment, the color of the electrolyte changed from transparent to light purple after the first 50 h and further transformed to deep purple after about 300 h. Figure 1.3c shows the changing color of the anolyte along with new peaks (505 and 780 nm) observed by in-situ ultraviolet-visible (UV/Vis) spectroelectrochemistry. These peaks arise from the highly oxidized Fe^{VI} complex [Fe^{VI}O₄²⁻] formed during the OER process. As illustrated in Figure 1.3d, the time when the color change in the solution can be observed (50 h) is consistent with the start of the formation of the Fe^{VI} active species. Based on a self-healing Fe^{II} OER process that the authors discovered before,⁵⁷ the mechanism can be described briefly: The catalyst is composed of nickel-iron layered double hydroxides (NiFe-LDH), with cobalt (Co) as a promoter for in situ redeposition of iron (Fe) catalytic centers and Bi (B₄O₅(OH)₄²⁻) as intercalated ions. The Bi can increase interlayer distance, therefore, facilitating mass transport, improving the self-healing process, and stabilizing the catalysts. During OER, some Fe atoms in NiFe-LDH are oxidized and dissolved into

the electrolyte, causing vacancies. The vacancies are re-deposited by the dissolved Fe ions onto the catalyst surface, with the help of the Co-promoter. The function of Co is to act as a sacrificial agent and reduce the highly oxidized Fe ions to Fe(OH)₂. Lastly, the re-deposited Fe(OH)₂ incorporates into the LDH structure and restores the original composition and morphology of the catalyst. The authors proposed the following reaction mechanism for the OER (Figure 1.3).

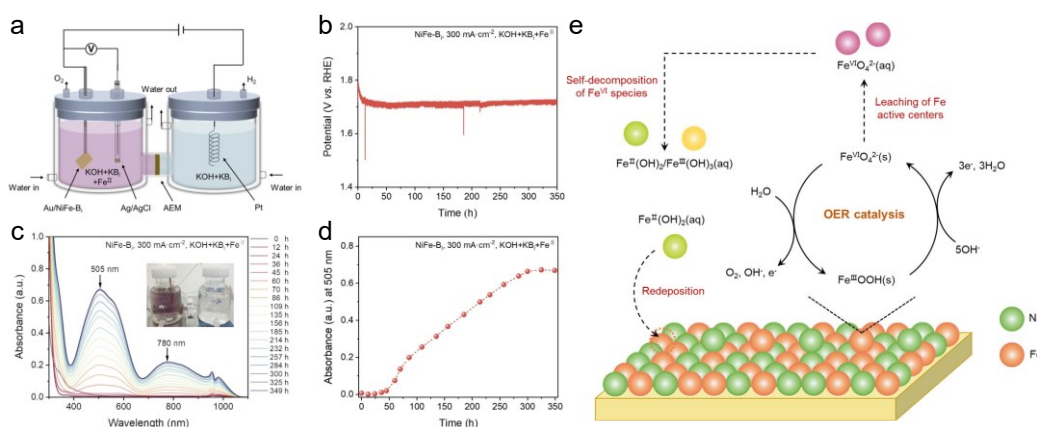
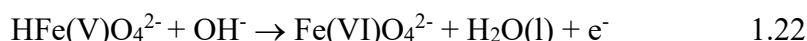


Figure 1.3. Illustration for (a) electrodeposition of NiFe with Bi on Au and H-type cell for OER. (b) The current density of NiFe-Bi catalysts at 300 mA cm⁻² in 0.25 M KBi-containing KOH (9.5 M) solution with 0.5 mM Fe^{II} ions. (c) UV/Vis absorption spectra detecting with different time for Fe^{VI}; insert is the color change of electrolyte in the anode. (d) Absorbance at 505 nm changes with time. (e) illustration of the reaction mechanism. Reproduced with permission from ref. 56. Copyright 2023, John Wiley and Sons

In this paper, the authors propose that Fe is the active center. However, the function of Ni is neglected. If Fe is the active center, future work should focus on how Ni cooperates in the OER reaction. It should be pointed out that most studies conclude that Ni and Fe participate, synergistically enhancing the OER performance.^{48,58} As the prior example was meant to illustrate, there are diverging conclusions about the detailed mechanism of the OER or Ni-Fe systems in the current literature. More studies are needed to explain the relationships between Ni

and Fe, including their respective functions in different concentrations of alkaline and in different NiFe-based materials.

1.2 Function of OER Electrode Binders

Electrode reactions during electrochemical energy conversion are complicated because they involve electron transfers as well as interactions between catalysts, electrolytes, gases, reactants, intermediates, and products.⁵⁹ Electrodes often are prepared by drop-casting, a process that includes mixing catalysts, binders, and conductive compounds to make an ink that is drop casted onto the conductive substrate.⁶⁰ The functions of an ideal binder for the OER include the following:^{18,61}

1. Provide excellent electroconductivity to facilitate electron transfer from a catalyst to the binder and to the substrate.⁶²
2. Chemical and electronic stability. The most common reaction condition for the OER carried out in academic labs include acidic or alkaline electrolytes, room or slightly elevated temperatures, and potentials ranging from 1.2 to 1.6 V vs RHE. Commercial systems, however, typically operate in corrosive, 6 M KOH solutions at 70 °C or 85 °C at high voltages (1.8–2.2 V) to obtain high current densities.^{63,64}
3. The binder should have the ability to adhere to the electrocatalysts and the electrode substrate.
4. The binder should be porous and enhance the transport of ions (OH^- , K^+ , or Na^+), H_2O , and O_2 . Poor mass transport and high electronic resistances will degrade the performance of electrodes significantly. Other processes, such as exfoliation of electrode structures caused by hindered gas flow may shorten the lifetime of the electrode.
5. The binder ideally will act as a cocatalyst for OER.⁶⁵ A binder that participates in the OER with active sites of catalyst will improve the performance of the electrode. For example, a binder may enhance the local concentration of OH^- .

The most common binder used in OER electrodes is Nafion. Nafion is a sulfonated tetrafluoroethylene (TFE)-based fluoropolymer-copolymer, which consists of a hydrophobic backbone TFE and hydrophilic sulfonic acid groups on side chains,

shown in Figure 1.4. The hydrophilic groups assist the transport of water and protons, while the hydrophobic backbone improves stability and assists transport of gases.⁶⁶ Mass transport limitations, limited cocatalytic activity, stability issues in alkaline conditions, and high electronic resistance limit the suitability of Nafion as a binder for the alkaline OER.⁶⁷ Another commonly used binder is polytetrafluoroethylene (PTFE), known for its chemical stability and hydrophobicity.⁶⁸ Like Nafion, PTFE is optimally not suited for OER under alkaline conditions.⁶⁹ There are other disadvantages attending the utilization of TFE-based binders, including high cost, low ionic conductivity, and environmental impact; polyfluorinated organic molecules potentially are forever chemicals.⁷⁰

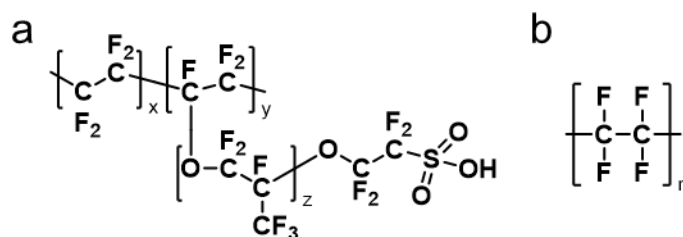


Figure 1.4. Chemical structure of Nafion (a) and PTFE (b)

Multifunction binders are, in principle, more able to fulfill the requirements for an OER binder than are Nafion or PTFE. For example, Asefa et al. recently reported transition metal-functionalized polyaniline–phytic acid (PANI–PA) hydrogels as OER catalysts.⁷¹ Figure 1.5 summarizes their structures. According to the authors, the functions performed by the hydrogels are as follows:

1. Electronic conductivity: the conductivity of the polyaniline (PANI) and phytic acid (PA) hydrogel backbone was an appreciable 0.11 S cm^{-1} . Utilization of a binder that is electronically conductive at OER potentials will reduce resistance losses, especially for thick electrodes that require high catalyst loadings for practical OER geometric current densities.
2. Metal coordination: coordinative bonds between the binder/electrode and the transition metal centers that catalyze OER will result in stronger interactions between the binder and catalyst than noncovalent or ionic interactions. In this study, the

authors tested many transition metal precursors and found that the hydrogels had a strong affinity towards Fe, presumably arising from covalent bonding between the PA groups in the hydrogel and Fe. Further, hydrogels containing both Fe and Co were the most effective OER electrodes the authors studied.

3. High surface area: hydrogels typically have large specific surface areas (m^2/g), leading to more active sites per cm^2 geometric electrode surface area.

4. Versatility: the reported hydrogels can be processed easily by ink-jet printing or spray-coating, techniques that are commonly utilized to prepare OER electrodes.

5. Stability: the structure of the reported hydrogels was stable over the studied time and conditions. Structural stability is a critical requirement of long-term OER electrodes.

The authors did not demonstrate a cocatalytic role played by the binder, and the reported binders are cost-prohibitive. Nevertheless, this study illustrates that utilization of multifunctional binders is beneficial towards the OER reaction, provided the costs, effort, and environmental impacts associated with synthesis and utilization of their molecular complexity can be made applicable to large-scale incorporation.

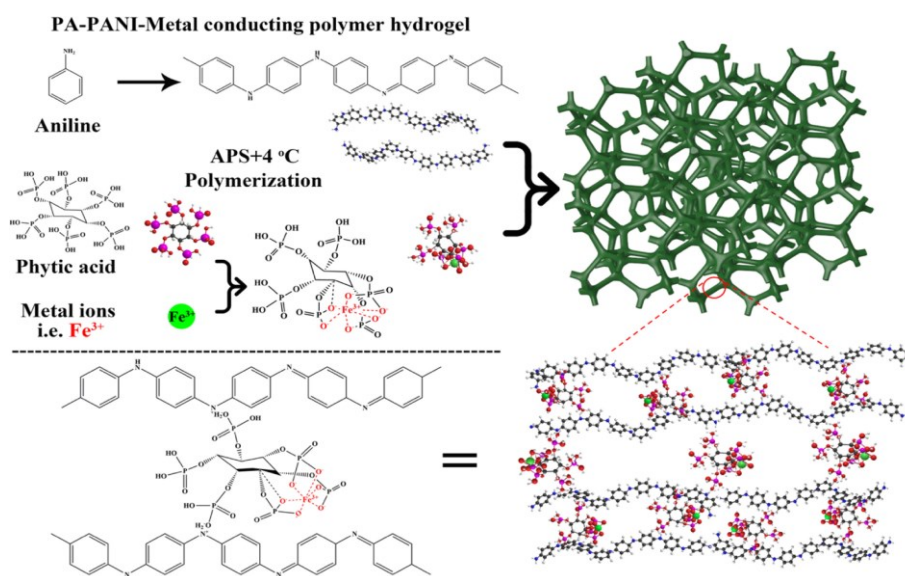


Figure 1.5. Illustration for Synthesis of PANI-PA-Metal (Hgel- M_x) Hydrogels for Electrocatalysis of OER. Reproduced with permission from ref. 71. Copyright 2022, American Chemical Society

Chapter 2 of this dissertation describes the simple, two-step preparation of a multifunctional binder/catalyst electrode for the OER utilizing off the shelf chemicals and procedures. The resulting abundant (low cost) electrodes are among the most active and stable under harsh conditions reported to date.

1.3 1,2,3,5-Tetrakis(carbazol-9-yl)-4,6-dicyanobenzene (4CzIPN) and Its Derivatives

First reported by Adachi et al. in 2012,⁷² the carbazoyl dicyanobenzenes (CDCBs) family of chromophores are comprised of carbazoyl- (Cz) or related groups bonded to dicyanobenzene cores. Tetrakis(carbazol-9-yl)-4,6-dicyanobenzene (4CzIPN), shown in Figure 1.6a, is the parent molecule of this versatile class of organic chromophores/photocatalysts. Figure 1.6b is the derivative 3CzImIPN.

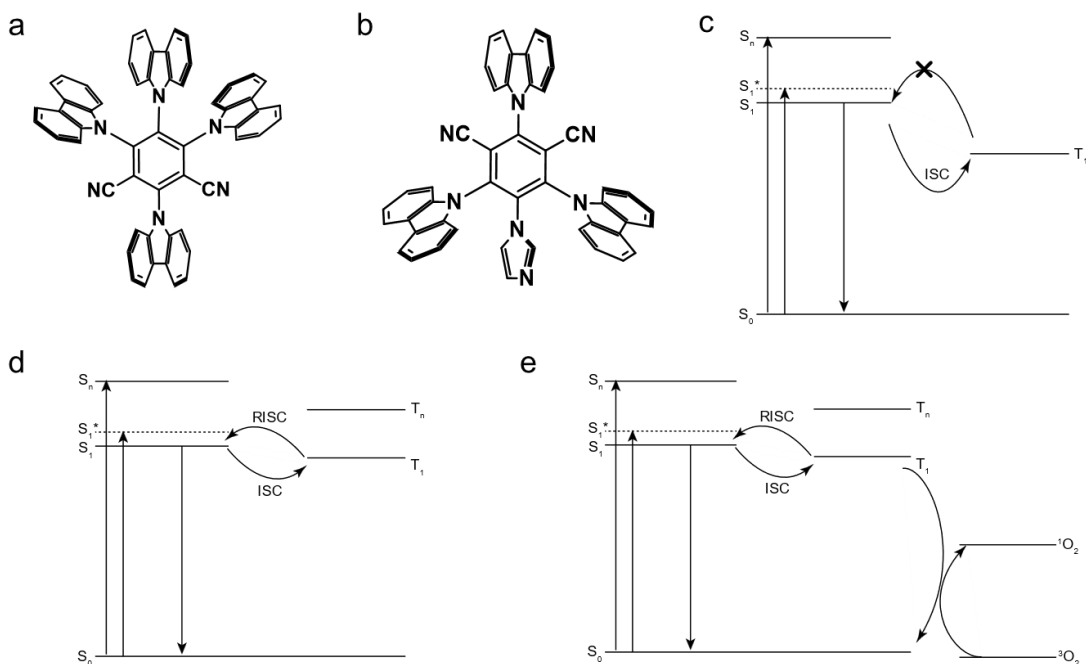


Figure 1.6. (a) Structure of 4CzIPN, (b) structure of 3CzImIPN, (c) tradition fluorescence, (d) intersystem crossing (ISC) and reverse intersystem crossing (RISC) participate fluorescence, (e) mechanism of photodynamic therapy (PDT)

When 4CzIPN is excited by light, an electron in S_0 (the HOMO is centered largely on the carbazole rings) will transfer to the higher energy S_1 (or other unoccupied molecular orbitals). The LUMO is centered largely on the

dicyanobenzene ring, and these are primarily displacement, push-pull excitations. Unlike many organic chromophores, intersystem crossing (ISC) from S_1 to T_1 is relatively facile with this class of molecules, in part because the S_1 and T_1 states are relatively close in energy.⁷³ It is the properties and lifetime of the T_1 state of these molecules that make them effective photocatalysts, potentially display components, and of use in photodynamic cancer therapy treatments. For example, 4CzIPN undergoes thermally activated delayed fluorescence (TADF). TADF is a process where a triplet excited state can be converted to a singlet state by thermal energy, as shown in Figure 1.6b. Typically, the triplet T_1 state undergoes non-radiative emission and cannot transfer back to the singlet S_1 state due to the conservation of angular momentum. However, if the energy gap between triplet and singlet can be minimized by design ($\lesssim 100 \text{ meV}^{72}$), reverse intersystem crossing (RISC) may occur, which will lead to the triplet-to-singlet back electron transfer.⁷⁴ As shown in Figure 1.6c, once the electrons are back in the S_1 state, relaxation of the electrons to S_0 is rapid by fluorescence. Because of the time latency of RISC (about $1 \mu\text{s}$ for 4CzIPN⁷⁵), the fluorescent light from the thermal conversion from T_1 to S_1 , followed by relaxation to S_0 state, occurs after the prompt fluorescence from S_1 to S_0 , hence the name called thermally activated delayed fluorescence.⁷⁶ Utilizing TADF, almost all the excited electrons undergo fluorescence, which results in nearly 100% for internal quantum efficiency. TADF is a strategy being employed actively to circumvent the 3:1 triplet to singlet populations of excited states generated by redox processes in OLED displays, thereby increasing the efficiencies of next-generation organic light-emitting diode (OLED).

Another valuable function of TADF materials is photodynamic therapy (PDT). PDT has been approved for clinical application since 1993, emerging as one of the most promising methods for cancer therapeutics.^{77,78} As demonstrated in Figure 1.6d, in PDT, an energy transfer from excited TADF photosensitizers (PSs) to surrounding O_2 leads to a transformation of ground-state triplet O_2 to active singlet O_2 , which can damage tumor cells.⁷⁹ During this process, effective electron transfer from S_1 to T_1 by intersystem crossing (ISC) is crucial, which is essential for singlet O_2 generation.⁷³

However, the traditional method introduces heavy metals into the PSs, which arouses concerns of toxicity and unexpected degradation in the human body.⁸⁰ Compared to traditional PSs, TADF, as one of pure organic PSs, attracts the attention of people due to its fascinating high-performance photosensitizing abilities.⁸¹ However, most of the TADF materials, including 4CzIPN, are hydrophobic, which lifts a new challenge for the biological aqua environment. One method to solve this problem is to deposit 4CzIPN or other TADF molecules on nanoparticles.⁸²

The T_1 excited state of the parent molecule, 4CzIPN*, and its derivatives contain singly occupied molecular orbitals (SOMOs) centered on the carbazole rings (the lowest energy SOMO) and on the dicyanobenzene moiety (the highest energy SOMO). The redox potentials of these orbitals, as well as of its many derivatives, allow 4CzIPN* to be an effective photoredox catalyst for a variety of organic reactions. During these processes, 4CzIPN* can either accept an electron into the lowest energy SOMO or donate an electron from the highest energy SOMO. The utilization of 4CzIPN and related molecules as photoredox catalysts for organic reactions was reported first in 2016.^{83,84} Table 1.2 briefly summarizes some representative photoredox reactions catalyzed by 4CzIPN and its derivatives. Several review articles have been published on this topic.^{84,85}

Table 1.2. A Brief Summary of Photoredox Reactions for 4CzIPN and Its Derivatives.

Type of photoredox	Category	Reactions	Ref.
4CzIPN with metal as photoredox systems	Radical generation and metal catalyst regeneration	decarboxylative arylation	83
		photooxidation of benzyl bis(catecholato)silicates	86
	Photocatalytic metal catalyst regeneration	hydrocarboxylation of styrenes with CO ₂	87
Metal-free system	Reactions involving C and C double bond	Olefin isomerization	88
		1,2-amidoalkynylation of unactivated alkenes	89
	Reactions involving C and N double bond	decarboxylative benzylation of imines	90
Other reactions	phosphorus-radical-initiated cascade cyclization reaction	Phosphorylated N-Heteroaromatics	91
	Xylose conversion	photocatalytic lactic acid production	92

It is well known that carbazole groups can be electropolymerized.^{93,94} As shown in Figure 1.7, the mechanism of carbazole electropolymerization can be described as follows:^{95,96} carbazole monomers are oxidized at an electrode surface to form carbazole radical cations under a low potential. However, these carbazole radical cations are extremely unstable and more favorable to bond with each other at the 3-position of carbazole forming 3,3'-dicarbazyl dimers. When increasing the applied potential at an electrode surface, the dimers may undergo further oxidation to form quinoid-like dication, which can bind with other carbazoles to form poly(3,6-carbazole)s and are deposited on the surface of an electrode. The carbazole chain increases under these oxidations and coupling steps until electropolymerization stopped.

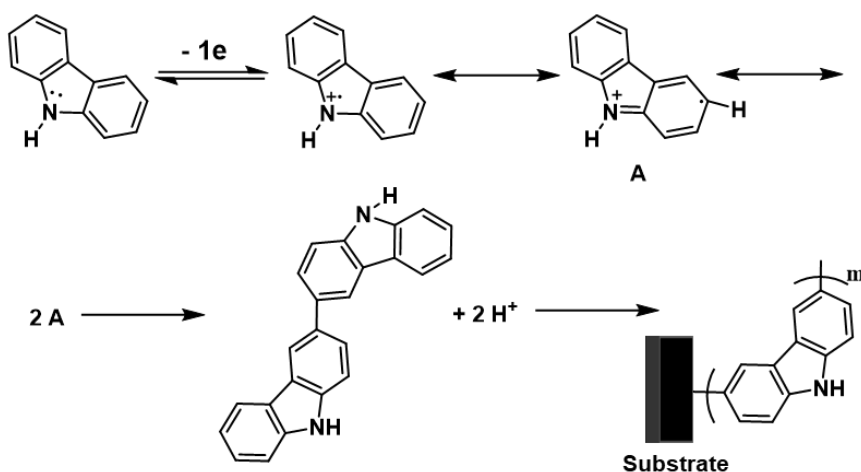


Figure 1.7. Mechanism of carbazole electro-polymerization

Li et al. first introduced the control of one or both of the C(3)-C(3') and C(6)-C(6') coupling reactions of carbazoyl, by both electrochemical and chemical methods.⁹⁷ As presented in Figure 1.8, with 9-hexyl-3-carbazole (**1**) as the monomer, under weakly oxidizing conditions (FeCl_3 or a potential of 1.0 V vs. Ag/Ag^+), the 9,9'-dihexyl-3,3'-dicarbazoyls (**2**) are the sole products. However, when under strongly oxidizing conditions ($(\text{NH}_4)_2\text{S}_2\text{O}_8$) or at a high oxidative potential of >1.2 V vs. Ag/Ag^+ , multiple oligomers and polymers (**3**) form. Thus,

α,ω -bis(N-carbazolyl)hexane (**4**) can either form as a C(3)-C(3') coupling linear polymer (**5**) under weakly oxidizing conditions or both a C(3)-C(3') and C(6)-C(6') coupling as cross-linked polymer (**6**) under strongly oxidizing conditions. It should be noted that the crucial parameter in electropolymerization is the applied potential at the working electrode. High potential or low potential will result in different coupling approaches.

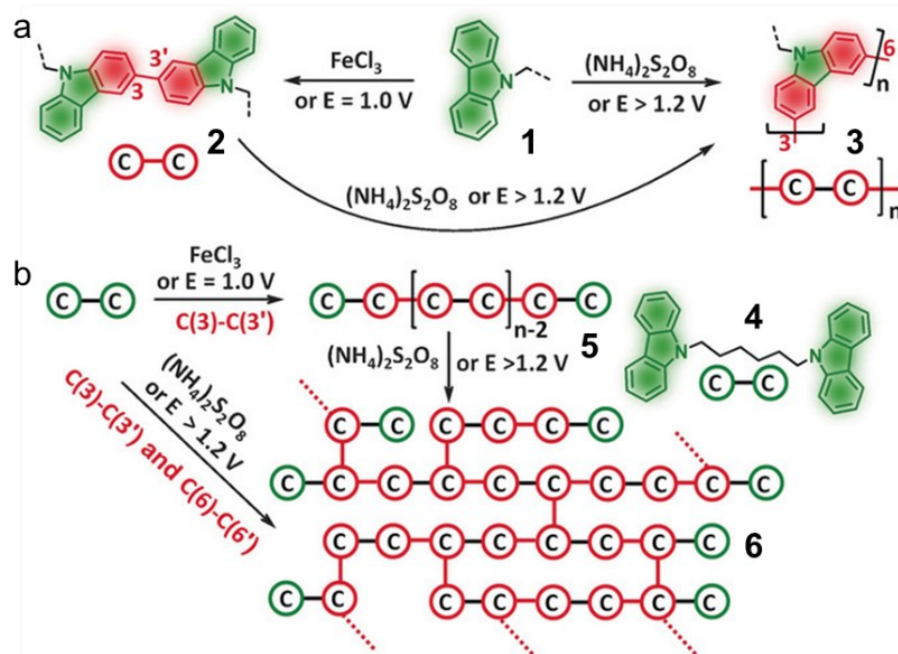


Figure 1.8. (a) C–C coupling mechanism of carbazoyl groups (**1**) under different oxidation conditions to form dimer (**2**) or polymer (**3**). (b) Radical initiated topological polymerizations of monomer containing two carbazoyl moieties (**4**) under different oxidation conditions to form linear polymer (**5**) or polymer network (**6**). Reproduced with permission from ref. 97. Copyright 2018, John Wiley and Sons

In chapter 3 of this dissertation, I will describe the synthesis of a new derivative of 4CzIPN, substituting one carbazole ring for an imidazole ligand group. Then, this coordinating chromophore will be polymerized at the carbazole rings, and the properties and utility of the resulting porous organic photoredox polymer will be illustrated.

The goal of the thesis is to find a stable binder that is multifunctional in alkaline OER and electropolymerizing of a 4CzIPN derivative 3CzImIPN.

1.4 References

- (1) Lewis, N. S. Toward Cost-Effective Solar Energy Use. *Science* **2007**, *315* (5813), 798–801. <https://doi.org/10.1126/science.1137014>.
- (2) Turner, J. A. Sustainable Hydrogen Production. *Science* **2004**, *305* (5686), 972–974. <https://doi.org/10.1126/science.1103197>.
- (3) Stott, R.; Arulkumaran, S.; Gilmore, I.; Godlee, F.; Page, L. Legislate for Carbon Net Zero by 2030. *The Lancet* **2019**, *393* (10175), 981. [https://doi.org/10.1016/S0140-6736\(19\)30048-0](https://doi.org/10.1016/S0140-6736(19)30048-0).
- (4) Mallapaty, S. How China Could Be Carbon Neutral by Mid-Century. *Nature* **2020**, *586* (7830), 482–483. <https://doi.org/10.1038/d41586-020-02927-9>.
- (5) IEA (2021), *World Energy Outlook 2021*, IEA, Paris <https://www.iea.org/reports/world-energy-outlook-2021>, License: CC BY 4.0.
- (6) Zhu, Z.; Wang, X.; Peng, Y.; Lei, H.; Fettingner, J. C.; Rivard, E.; Power, P. P. Addition of Hydrogen or Ammonia to a Low-Valent Group 13 Metal Species at 25 °C and 1 Atmosphere. *Angew. Chem. Int. Ed.* **2009**, *48* (11), 2031–2034. <https://doi.org/10.1002/anie.200805982>.
- (7) Graetz, J. New Approaches to Hydrogen Storage. *Chem Soc Rev* **2009**, *38* (1), 73–82. <https://doi.org/10.1039/B718842K>.
- (8) Aziz, M. Liquid Hydrogen: A Review on Liquefaction, Storage, Transportation, and Safety. *Energies* **2021**, *14* (18), 5917. <https://doi.org/10.3390/en14185917>.
- (9) Li, H.; Cao, X.; Liu, Y.; Shao, Y.; Nan, Z.; Teng, L.; Peng, W.; Bian, J. Safety of Hydrogen Storage and Transportation: An Overview on Mechanisms, Techniques, and Challenges. *Energy Rep.* **2022**, *8*, 6258–6269. <https://doi.org/10.1016/j.egy.2022.04.067>.
- (10) Yang, M.; Hunger, R.; Berrettoni, S.; Sprecher, B.; Wang, B. A Review of Hydrogen Storage and Transport Technologies. *Clean Energy* **2023**, *7* (1), 190–216. <https://doi.org/10.1093/ce/zkad021>.
- (11) Hoelzen, J.; Silberhorn, D.; Zill, T.; Bensmann, B.; Hanke-Rauschenbach, R. Hydrogen-Powered Aviation and Its Reliance on Green Hydrogen Infrastructure – Review and Research Gaps. *Int. J. Hydrog. Energy* **2022**, *47* (5), 3108–3130. <https://doi.org/10.1016/j.ijhydene.2021.10.239>.
- (12) Elrhoul, D.; Romero Gómez, M.; Naveiro, M. Review of Green Hydrogen Technologies Application in Maritime Transport. *Int. J. Green Energy* **2023**, 1–26. <https://doi.org/10.1080/15435075.2023.2194384>.
- (13) Choi, M.; Wang, L.; Stoerzinger, K. A.; Chung, S.; Chambers, S. A.; Du, Y. Epitaxial Design of Complex Nickelates as Electrocatalysts for the Oxygen Evolution Reaction. *Adv. Energy Mater.* **2023**, 2300239. <https://doi.org/10.1002/aenm.202300239>.
- (14) McHugh, P. J.; Stergiou, A. D.; Symes, M. D. Decoupled Electrochemical Water Splitting: From Fundamentals to Applications. *Adv. Energy Mater.* **2020**, *10* (44), 2002453. <https://doi.org/10.1002/aenm.202002453>.
- (15) Ifkovits, Z. P.; Evans, J. M.; Meier, M. C.; Papadantonakis, K. M.; Lewis, N. S. Decoupled Electrochemical Water-Splitting Systems: A Review and Perspective. *Energy Environ. Sci.* **2021**, *14* (9), 4740–4759. <https://doi.org/10.1039/D1EE01226F>.
- (16) Orhan, M. F.; Dincer, I.; Rosen, M. A.; Kanoglu, M. Integrated Hydrogen Production Options Based on Renewable and Nuclear Energy Sources. *Renew. Sustain. Energy Rev.* **2012**, *16* (8), 6059–6082. <https://doi.org/10.1016/j.rser.2012.06.008>.
- (17) Smith, C.; Hill, A. K.; Torrente-Murciano, L. Current and Future Role of Haber–Bosch Ammonia in a Carbon-Free Energy Landscape. *Energy Environ. Sci.* **2020**, *13* (2), 331–344. <https://doi.org/10.1039/C9EE02873K>.

- (18) Carmo, M.; Fritz, D. L.; Mergel, J.; Stolten, D. A Comprehensive Review on PEM Water Electrolysis. *Int. J. Hydrog. Energy* **2013**, *38* (12), 4901–4934. <https://doi.org/10.1016/j.ijhydene.2013.01.151>.
- (19) Wappler, M.; Unguder, D.; Lu, X.; Ohlmeyer, H.; Teschke, H.; Lueke, W. Building the Green Hydrogen Market – Current State and Outlook on Green Hydrogen Demand and Electrolyzer Manufacturing. *Int. J. Hydrog. Energy* **2022**, *47* (79), 33551–33570. <https://doi.org/10.1016/j.ijhydene.2022.07.253>.
- (20) Hossain, Md. B.; Islam, Md. R.; Muttaqi, K. M.; Sutanto, D.; Agalgaonkar, A. P. Advancement of Fuel Cells and Electrolyzers Technologies and Their Applications to Renewable-Rich Power Grids. *J. Energy Storage* **2023**, *62*, 106842. <https://doi.org/10.1016/j.est.2023.106842>.
- (21) Wang, T.; Cao, X.; Jiao, L. PEM Water Electrolysis for Hydrogen Production: Fundamentals, Advances, and Prospects. *Carbon Neutrality* **2022**, *1* (1), 21. <https://doi.org/10.1007/s43979-022-00022-8>.
- (22) Wang, S.; Lu, A.; Zhong, C.-J. Hydrogen Production from Water Electrolysis: Role of Catalysts. *Nano Converge* **2021**, *8* (1), 4. <https://doi.org/10.1186/s40580-021-00254-x>.
- (23) Zhai, W.; Ma, Y.; Chen, D.; Ho, J. C.; Dai, Z.; Qu, Y. Recent Progress on the Long - term Stability of Hydrogen Evolution Reaction Electrocatalysts. *InfoMat* **2022**, *4* (9). <https://doi.org/10.1002/inf2.12357>.
- (24) Suntivich, J.; May, K. J.; Gasteiger, H. A.; Goodenough, J. B.; Shao-Horn, Y. A Perovskite Oxide Optimized for Oxygen Evolution Catalysis from Molecular Orbital Principles. *Science* **2011**, *334* (6061), 1383–1385. <https://doi.org/10.1126/science.1212858>.
- (25) Zhang, Z.; Liu, P.; Song, Y.; Hou, Y.; Xu, B.; Liao, T.; Zhang, H.; Guo, J.; Sun, Z. Heterostructure Engineering of 2D Superlattice Materials for Electrocatalysis. *Adv. Sci.* **2022**, *9* (35), 2204297. <https://doi.org/10.1002/advs.202204297>.
- (26) Guo, B.; Ding, Y.; Huo, H.; Wen, X.; Ren, X.; Xu, P.; Li, S. Recent Advances of Transition Metal Basic Salts for Electrocatalytic Oxygen Evolution Reaction and Overall Water Electrolysis. *Nano-Micro Lett.* **2023**, *15* (1), 57. <https://doi.org/10.1007/s40820-023-01038-0>.
- (27) Zhang, Y.; Wu, J.; Guo, B.; Huo, H.; Niu, S.; Li, S.; Xu, P. Recent Advances of Transition - metal Metaphosphates for Efficient Electrocatalytic Water Splitting. *Carbon Energy* **2023**, e375. <https://doi.org/10.1002/cey2.375>.
- (28) Guo, B.; Huo, H.; Zhuang, Q.; Ren, X.; Wen, X.; Yang, B.; Huang, X.; Chang, Q.; Li, S. Iron Oxyhydroxide: Structure and Applications in Electrocatalytic Oxygen Evolution Reaction. *Adv. Funct. Mater.* **2023**, 2300557. <https://doi.org/10.1002/adfm.202300557>.
- (29) Liu, J.; Zhang, J.; Zhou, H.; Liu, B.; Dong, H.; Lin, X.; Qin, Y. Lignin-Derived Carbon-Supported MoC–FeNi Heterostructure as Efficient Electrocatalysts for Oxygen Evolution Reaction. *J. Colloid Interface Sci.* **2023**, *629*, 822–831. <https://doi.org/10.1016/j.jcis.2022.08.141>.
- (30) Shrestha, N. K.; Patil, S. A.; Han, J.; Cho, S.; Inamdar, A. I.; Kim, H.; Im, H. Chemical Etching Induced Microporous Nickel Backbones Decorated with Metallic Fe@hydroxide Nanocatalysts: An Efficient and Sustainable OER Anode toward Industrial Alkaline Water-Splitting. *J. Mater. Chem. A* **2022**, *10* (16), 8989–9000. <https://doi.org/10.1039/D1TA10103J>.
- (31) Chavan, H. S.; Lee, C. H.; Inamdar, A. I.; Han, J.; Park, S.; Cho, S.; Shrestha, N. K.; Lee, S. U.; Hou, B.; Im, H.; Kim, H. Designing and Tuning the Electronic Structure of Nickel–Vanadium Layered Double Hydroxides for Highly Efficient Oxygen Evolution Electrocatalysis. *ACS Catal.* **2022**, *12* (7), 3821–3831. <https://doi.org/10.1021/acscatal.1c05813>.

- (32) Nie, F.; Li, Z.; Dai, X.; Yin, X.; Gan, Y.; Yang, Z.; Wu, B.; Ren, Z.; Cao, Y.; Song, W. Interfacial Electronic Modulation on Heterostructured NiSe@CoFe LDH Nanoarrays for Enhancing Oxygen Evolution Reaction and Water Splitting by Facilitating the Deprotonation of OH to O. *Chem. Eng. J.* **2022**, *431*, 134080. <https://doi.org/10.1016/j.cej.2021.134080>.
- (33) Li, H.; Zhang, C.; Xiang, W.; Amin, M. A.; Na, J.; Wang, S.; Yu, J.; Yamauchi, Y. Efficient Electrocatalysis for Oxygen Evolution: W-Doped NiFe Nanosheets with Oxygen Vacancies Constructed by Facile Electrodeposition and Corrosion. *Chem. Eng. J.* **2023**, *452*, 139104. <https://doi.org/10.1016/j.cej.2022.139104>.
- (34) Zheng, X.; Cao, Y.; Wu, Z.; Ding, W.; Xue, T.; Wang, J.; Chen, Z.; Han, X.; Deng, Y.; Hu, W. Rational Design and Spontaneous Sulfurization of NiCo - (Oxy)Hydroxysulfides Nanosheets with Modulated Local Electronic Configuration for Enhancing Oxygen Electrocatalysis. *Adv. Energy Mater.* **2022**, *12* (15), 2103275. <https://doi.org/10.1002/aenm.202103275>.
- (35) Huang, W.; Li, J.; Liao, X.; Lu, R.; Ling, C.; Liu, X.; Meng, J.; Qu, L.; Lin, M.; Hong, X.; Zhou, X.; Liu, S.; Zhao, Y.; Zhou, L.; Mai, L. Ligand Modulation of Active Sites to Promote Electrocatalytic Oxygen Evolution. *Adv. Mater.* **2022**, *34* (18), 2200270. <https://doi.org/10.1002/adma.202200270>.
- (36) Chen, X.; Wang, Q.; Cheng, Y.; Xing, H.; Li, J.; Zhu, X.; Ma, L.; Li, Y.; Liu, D. S - Doping Triggers Redox Reactivities of Both Iron and Lattice Oxygen in FeOOH for Low - Cost and High - Performance Water Oxidation. *Adv. Funct. Mater.* **2022**, *32* (26), 2112674. <https://doi.org/10.1002/adfm.202112674>.
- (37) Zhang, B.; Wu, Z.; Shao, W.; Gao, Y.; Wang, W.; Ma, T.; Ma, L.; Li, S.; Cheng, C.; Zhao, C. Interfacial Atom - Substitution Engineered Transition - Metal Hydroxide Nanofibers with High - Valence Fe for Efficient Electrochemical Water Oxidation. *Angew. Chem. Int. Ed.* **2022**, *61* (13). <https://doi.org/10.1002/anie.202115331>.
- (38) He, Z.; Zhang, J.; Gong, Z.; Lei, H.; Zhou, D.; Zhang, N.; Mai, W.; Zhao, S.; Chen, Y. Activating Lattice Oxygen in NiFe-Based (Oxy)Hydroxide for Water Electrolysis. *Nat. Commun.* **2022**, *13* (1), 2191. <https://doi.org/10.1038/s41467-022-29875-4>.
- (39) Jiang, C.; Moniz, S. J. A.; Wang, A.; Zhang, T.; Tang, J. Photoelectrochemical Devices for Solar Water Splitting – Materials and Challenges. *Chem. Soc. Rev.* **2017**, *46* (15), 4645–4660. <https://doi.org/10.1039/C6CS00306K>.
- (40) Wei, C.; Xu, Z. J. The Comprehensive Understanding of 10 MA Cmgeo–2 as an Evaluation Parameter for Electrochemical Water Splitting. *Small Methods* **2018**, *2* (11), 1800168. <https://doi.org/10.1002/smtd.201800168>.
- (41) Antipin, D.; Risch, M. Calculation of the Tafel Slope and Reaction Order of the Oxygen Evolution Reaction between PH 12 and PH 14 for the Adsorbate Mechanism. *Electrochem. Sci. Adv.* **2022**, e2100213. <https://doi.org/10.1002/elsa.202100213>.
- (42) Suen, N.-T.; Hung, S.-F.; Quan, Q.; Zhang, N.; Xu, Y.-J.; Chen, H. M. Electrocatalysis for the Oxygen Evolution Reaction: Recent Development and Future Perspectives. *Chem. Soc. Rev.* **2017**, *46* (2), 337–365. <https://doi.org/10.1039/C6CS00328A>.
- (43) Fabbri, E.; Schmidt, T. J. Oxygen Evolution Reaction—The Enigma in Water Electrolysis. *ACS Catal.* **2018**, *8* (10), 9765–9774. <https://doi.org/10.1021/acscatal.8b02712>.
- (44) Pegis, M. L.; Roberts, J. A. S.; Wasylenko, D. J.; Mader, E. A.; Appel, A. M.; Mayer, J. M. Standard Reduction Potentials for Oxygen and Carbon Dioxide Couples in Acetonitrile and *N*, *N*-Dimethylformamide. *Inorg. Chem.* **2015**, *54* (24), 11883–11888. <https://doi.org/10.1021/acs.inorgchem.5b02136>.

- (45) Man, I. C.; Su, H.; Calle - Vallejo, F.; Hansen, H. A.; Martínez, J. I.; Inoglu, N. G.; Kitchin, J.; Jaramillo, T. F.; Nørskov, J. K.; Rossmeisl, J. Universality in Oxygen Evolution Electrocatalysis on Oxide Surfaces. *ChemCatChem* **2011**, *3* (7), 1159–1165. <https://doi.org/10.1002/cctc.201000397>.
- (46) Rossmeisl, J.; Logadottir, A.; Nørskov, J. K. Electrolysis of Water on (Oxidized) Metal Surfaces. *Chem. Phys.* **2005**, *319* (1–3), 178–184. <https://doi.org/10.1016/j.chemphys.2005.05.038>.
- (47) Wang, Q.; Cheng, Y.; Tao, H. B.; Liu, Y.; Ma, X.; Li, D.; Yang, H. B.; Liu, B. Long - Term Stability Challenges and Opportunities in Acidic Oxygen Evolution Electrocatalysis. *Angew. Chem. Int. Ed.* **2023**, *62* (11), e202216645. <https://doi.org/10.1002/anie.202216645>.
- (48) Zhang, R.; Xie, A.; Cheng, L.; Bai, Z.; Tang, Y.; Wan, P. Hydrogen Production by Traditional and Novel Alkaline Water Electrolysis on Nickel or Iron Based Electrocatalysts. *Chem. Commun.* **2023**, *59* (53), 8205–8221. <https://doi.org/10.1039/D3CC00996C>.
- (49) Zhang, N.; Chai, Y. Lattice Oxygen Redox Chemistry in Solid-State Electrocatalysts for Water Oxidation. *Energy Environ. Sci.* **2021**, *14* (9), 4647–4671. <https://doi.org/10.1039/D1EE01277K>.
- (50) Huang, Z.-F.; Song, J.; Du, Y.; Xi, S.; Dou, S.; Nsanzimana, J. M. V.; Wang, C.; Xu, Z. J.; Wang, X. Chemical and Structural Origin of Lattice Oxygen Oxidation in Co–Zn Oxyhydroxide Oxygen Evolution Electrocatalysts. *Nat. Energy* **2019**, *4* (4), 329–338. <https://doi.org/10.1038/s41560-019-0355-9>.
- (51) Xu, H.; Yuan, J.; He, G.; Chen, H. Current and Future Trends for Spinel-Type Electrocatalysts in Electrocatalytic Oxygen Evolution Reaction. *Coord. Chem. Rev.* **2023**, *475*, 214869. <https://doi.org/10.1016/j.ccr.2022.214869>.
- (52) Zhu, K.; Zhu, X.; Yang, W. Application of In Situ Techniques for the Characterization of NiFe-Based Oxygen Evolution Reaction (OER) Electrocatalysts. *Angew. Chem. Int. Ed.* **2019**, *58* (5), 1252–1265. <https://doi.org/10.1002/anie.201802923>.
- (53) Zhao, J.; Zhang, J.; Li, Z.; Bu, X. Recent Progress on NiFe - Based Electrocatalysts for the Oxygen Evolution Reaction. *Small* **2020**, *16* (51), 2003916. <https://doi.org/10.1002/smll.202003916>.
- (54) Bodhankar, P. M.; Sarawade, P. B.; Singh, G.; Vinu, A.; Dhawale, D. S. Recent Advances in Highly Active Nanostructured NiFe LDH Catalyst for Electrochemical Water Splitting. *J. Mater. Chem. A* **2021**, *9* (6), 3180–3208. <https://doi.org/10.1039/D0TA10712C>.
- (55) Speck, F. D.; Dettelbach, K. E.; Sherbo, R. S.; Salvatore, D. A.; Huang, A.; Berlinguette, C. P. On the Electrolytic Stability of Iron-Nickel Oxides. *Chem* **2017**, *2* (4), 590–597. <https://doi.org/10.1016/j.chempr.2017.03.006>.
- (56) Feng, C.; She, X.; Xiao, Y.; Li, Y. Direct Detection of Fe^{VI} Water Oxidation Intermediates in an Aqueous Solution. *Angew. Chem. Int. Ed.* **2023**, *62* (9), e202218738. <https://doi.org/10.1002/anie.202218738>.
- (57) Feng, C.; Wang, F.; Liu, Z.; Nakabayashi, M.; Xiao, Y.; Zeng, Q.; Fu, J.; Wu, Q.; Cui, C.; Han, Y.; Shibata, N.; Domen, K.; Sharp, I. D.; Li, Y. A Self-Healing Catalyst for Electrocatalytic and Photoelectrochemical Oxygen Evolution in Highly Alkaline Conditions. *Nat. Commun.* **2021**, *12* (1), 5980. <https://doi.org/10.1038/s41467-021-26281-0>.
- (58) Wu, C.; Zhang, X.; Xia, Z.; Shu, M.; Li, H.; Xu, X.; Si, R.; Rykov, A. I.; Wang, J.; Yu, S.; Wang, S.; Sun, G. Insight into the Role of Ni–Fe Dual Sites in the Oxygen Evolution Reaction Based on Atomically Metal-Doped Polymeric Carbon Nitride. *J. Mater. Chem. A* **2019**, *7* (23), 14001–14010. <https://doi.org/10.1039/C9TA03163D>.
- (59) Wang, H.-F.; Chen, L.; Pang, H.; Kaskel, S.; Xu, Q. MOF-Derived Electrocatalysts for Oxygen Reduction, Oxygen Evolution and Hydrogen Evolution Reactions. *Chem. Soc. Rev.* **2020**, *49* (5), 1414–1448. <https://doi.org/10.1039/C9CS00906J>.

- (60) Chandrasekaran, S.; Khandelwal, M.; Dayong, F.; Sui, L.; Chung, J. S.; Misra, R. D. K.; Yin, P.; Kim, E. J.; Kim, W.; Vanchiappan, A.; Liu, Y.; Hur, S. H.; Zhang, H.; Bowen, C. Developments and Perspectives on Robust Nano - and Microstructured Binder - Free Electrodes for Bifunctional Water Electrolysis and Beyond. *Adv. Energy Mater.* **2022**, *12* (23), 2200409. <https://doi.org/10.1002/aenm.202200409>.
- (61) Zeng, K.; Zhang, D. Recent Progress in Alkaline Water Electrolysis for Hydrogen Production and Applications. *Prog. Energy Combust. Sci.* **2010**, *36* (3), 307–326. <https://doi.org/10.1016/j.peccs.2009.11.002>.
- (62) Browne, M. P.; Mills, A. Determining the Importance of the Electrode Support and Fabrication Method during the Initial Screening Process of an Active Catalyst for the Oxygen Evolution Reaction. *J. Mater. Chem. A* **2018**, *6* (29), 14162–14169. <https://doi.org/10.1039/C8TA02908C>.
- (63) Hausmann, J. N.; Traynor, B.; Myers, R. J.; Driess, M.; Menezes, P. W. The PH of Aqueous NaOH/KOH Solutions: A Critical and Non-Trivial Parameter for Electrocatalysis. *ACS Energy Lett.* **2021**, *6* (10), 3567–3571. <https://doi.org/10.1021/acsenergylett.1c01693>.
- (64) Li, W.; Tian, H.; Ma, L.; Wang, Y.; Liu, X.; Gao, X. Low-Temperature Water Electrolysis: Fundamentals, Progress, and New Strategies. *Mater. Adv.* **2022**, *3* (14), 5598–5644. <https://doi.org/10.1039/D2MA00185C>.
- (65) Yan, Y.; Zhang, C.; Deng, X.; Zhang, J.; Xue, Y.; Zhang, J.; Luo, Y.; Yang, F.; Wang, G.; Wang, R.; Chen, J. Designing Superhydrophilic Hydrogels as Binder-Free Catalysts for Enhanced Oxygen Evolution Performance. *Ind. Eng. Chem. Res.* **2023**, *62* (13), 5543–5551. <https://doi.org/10.1021/acs.iecr.3c00281>.
- (66) Duan, Q.; Wang, H.; Benziger, J. Transport of Liquid Water through Nafion Membranes. *J. Membr. Sci.* **2012**, *392–393*, 88–94. <https://doi.org/10.1016/j.memsci.2011.12.004>.
- (67) Li, G.-F.; Yang, D.; Abel Chuang, P.-Y. Defining Nafion Ionomer Roles for Enhancing Alkaline Oxygen Evolution Electrocatalysis. *ACS Catal.* **2018**, *8* (12), 11688–11698. <https://doi.org/10.1021/acscatal.8b02217>.
- (68) Yan, X.; Biemolt, J.; Zhao, K.; Zhao, Y.; Cao, X.; Yang, Y.; Wu, X.; Rothenberg, G.; Yan, N. A Membrane-Free Flow Electrolyzer Operating at High Current Density Using Earth-Abundant Catalysts for Water Splitting. *Nat. Commun.* **2021**, *12* (1), 4143. <https://doi.org/10.1038/s41467-021-24284-5>.
- (69) Ruschhaupt, P.; Pohlmann, S.; Varzi, A.; Passerini, S. Determining Realistic Electrochemical Stability Windows of Electrolytes for Electrical Double - Layer Capacitors. *Batter. Supercaps* **2020**, *3* (8), 698–707. <https://doi.org/10.1002/batt.202000009>.
- (70) Bresser, D.; Buchholz, D.; Moretti, A.; Varzi, A.; Passerini, S. Alternative Binders for Sustainable Electrochemical Energy Storage – the Transition to Aqueous Electrode Processing and Bio-Derived Polymers. *Energy Environ. Sci.* **2018**, *11* (11), 3096–3127. <https://doi.org/10.1039/C8EE00640G>.
- (71) Tang, C.; Thomas, B.; Ramírez-Hernández, M.; Mikmeková, E. M.; Asefa, T. Metal-Functionalized Hydrogels as Efficient Oxygen Evolution Electrocatalysts. *ACS Appl. Mater. Interfaces* **2022**, *14* (18), 20919–20929. <https://doi.org/10.1021/acsaami.2c01667>.
- (72) Uoyama, H.; Goushi, K.; Shizu, K.; Nomura, H.; Adachi, C. Highly Efficient Organic Light-Emitting Diodes from Delayed Fluorescence. *Nature* **2012**, *492* (7428), 234–238. <https://doi.org/10.1038/nature11687>.
- (73) Wu, W.; Mao, D.; Xu, S.; Kenry; Hu, F.; Li, X.; Kong, D.; Liu, B. Polymerization-Enhanced Photosensitization. *Chem* **2018**, *4* (8), 1937–1951. <https://doi.org/10.1016/j.chempr.2018.06.003>.

- (74) Chen, W.; Song, F. Thermally Activated Delayed Fluorescence Molecules and Their New Applications aside from OLEDs. *Chin. Chem. Lett.* **2019**, *30* (10), 1717–1730. <https://doi.org/10.1016/j.ccllet.2019.08.032>.
- (75) Li, F.; Gillett, A. J.; Gu, Q.; Ding, J.; Chen, Z.; Hele, T. J. H.; Myers, W. K.; Friend, R. H.; Evans, E. W. Singlet and Triplet to Doublet Energy Transfer: Improving Organic Light-Emitting Diodes with Radicals. *Nat. Commun.* **2022**, *13* (1), 2744. <https://doi.org/10.1038/s41467-022-29759-7>.
- (76) Dias, F. B.; Penfold, T. J.; Monkman, A. P. Photophysics of Thermally Activated Delayed Fluorescence Molecules. *Methods Appl. Fluoresc.* **2017**, *5* (1), 012001. <https://doi.org/10.1088/2050-6120/aa537e>.
- (77) Castano, A. P.; Mroz, P.; Hamblin, M. R. Photodynamic Therapy and Anti-Tumour Immunity. *Nat. Rev. Cancer* **2006**, *6* (7), 535–545. <https://doi.org/10.1038/nrc1894>.
- (78) Li, J.; Pu, K. Development of Organic Semiconducting Materials for Deep-Tissue Optical Imaging, Phototherapy and Photoactivation. *Chem. Soc. Rev.* **2019**, *48* (1), 38–71. <https://doi.org/10.1039/C8CS00001H>.
- (79) Zhao, J.; Wu, W.; Sun, J.; Guo, S. Triplet Photosensitizers: From Molecular Design to Applications. *Chem. Soc. Rev.* **2013**, *42* (12), 5323. <https://doi.org/10.1039/c3cs35531d>.
- (80) Chi, Y.; Chou, P.-T. Transition-Metal Phosphors with Cyclometalating Ligands: Fundamentals and Applications. *Chem Soc Rev* **2010**, *39* (2), 638–655. <https://doi.org/10.1039/B916237B>.
- (81) Zhao, X.; Liu, J.; Fan, J.; Chao, H.; Peng, X. Recent Progress in Photosensitizers for Overcoming the Challenges of Photodynamic Therapy: From Molecular Design to Application. *Chem. Soc. Rev.* **2021**, *50* (6), 4185–4219. <https://doi.org/10.1039/D0CS00173B>.
- (82) Zhu, Z.; Tian, D.; Gao, P.; Wang, K.; Li, Y.; Shu, X.; Zhu, J.; Zhao, Q. Cell-Penetrating Peptides Transport Noncovalently Linked Thermally Activated Delayed Fluorescence Nanoparticles for Time-Resolved Luminescence Imaging. *J. Am. Chem. Soc.* **2018**, *140* (50), 17484–17491. <https://doi.org/10.1021/jacs.8b08438>.
- (83) Luo, J.; Zhang, J. Donor–Acceptor Fluorophores for Visible-Light-Promoted Organic Synthesis: Photoredox/Ni Dual Catalytic C(Sp³)–C(Sp²) Cross-Coupling. *ACS Catal.* **2016**, *6* (2), 873–877. <https://doi.org/10.1021/acscatal.5b02204>.
- (84) Shang, T.-Y.; Lu, L.-H.; Cao, Z.; Liu, Y.; He, W.-M.; Yu, B. Recent Advances of 1,2,3,5-Tetrakis(Carbazol-9-Yl)-4,6-Dicyanobenzene (4CzIPN) in Photocatalytic Transformations. *Chem. Commun.* **2019**, *55* (38), 5408–5419. <https://doi.org/10.1039/C9CC01047E>.
- (85) Chen J.; Li Y.; Mei L.; Wu H. Application of Photosensitizer 2, 4, 5, 6-Tetrakis(carbazol-9-yl)-1, 3-dicyanobenzene in Photo-induced Transition-Metal-Free Organic Synthesis. *Chin. J. Org. Chem.* **2019**, *39* (11), 3040. <https://doi.org/10.6023/cjoc201904022>.
- (86) Lévêque, C.; Cheneberg, L.; Corcé, V.; Ollivier, C.; Fensterbank, L. Organic Photoredox Catalysis for the Oxidation of Silicates: Applications in Radical Synthesis and Dual Catalysis. *Chem. Commun.* **2016**, *52* (64), 9877–9880. <https://doi.org/10.1039/C6CC04636C>.
- (87) Meng, Q.-Y.; Wang, S.; Huff, G. S.; König, B. Ligand-Controlled Regioselective Hydrocarboxylation of Styrenes with CO₂ by Combining Visible Light and Nickel Catalysis. *J. Am. Chem. Soc.* **2018**, *140* (9), 3198–3201. <https://doi.org/10.1021/jacs.7b13448>.
- (88) Rasu, L.; Amiri, M.; Bergens, S. H. Carbazole–Cyanobenzene Dyes Electrografted to Carbon or Indium-Doped Tin Oxide Supports for Visible Light-Driven Photoanodes and Olefin Isomerizations. *ACS Appl. Mater. Interfaces* **2021**, *13* (15), 17745–17752. <https://doi.org/10.1021/acsami.1c05064>.

- (89) Jiang, H.; Studer, A. Transition - Metal - Free Three - Component Radical 1,2 - Amidoalkynylation of Unactivated Alkenes. *Chem. – Eur. J.* **2018**, chem.201805490. <https://doi.org/10.1002/chem.201805490>.
- (90) Guo, J.; Wu, Q.-L.; Xie, Y.; Weng, J.; Lu, G. Visible-Light-Mediated Decarboxylative Benzoylation of Imines with Arylacetic Acids. *J. Org. Chem.* **2018**, *83* (20), 12559–12567. <https://doi.org/10.1021/acs.joc.8b01849>.
- (91) Liu, Y.; Chen, X.-L.; Li, X.-Y.; Zhu, S.-S.; Li, S.-J.; Song, Y.; Qu, L.-B.; Yu, B. 4CzIPN-^t Bu-Catalyzed Proton-Coupled Electron Transfer for Photosynthesis of Phosphorylated *N*-Heteroaromatics. *J. Am. Chem. Soc.* **2021**, *143* (2), 964–972. <https://doi.org/10.1021/jacs.0c11138>.
- (92) Sun, S.; Sun, S.; Liu, K.; Xiao, L.-P.; Ma, J.; Sun, R. Construction of a Metal-Free Photocatalyst *via* Encapsulation of 1,2,3,5-Tetrakis(Carbazole-9-Yl)-4,6-Dicyanobenzene in a Carboxymethylcellulose-Based Hydrogel for Photocatalytic Lactic Acid Production. *Green Chem.* **2023**, *25* (2), 736–745. <https://doi.org/10.1039/D2GC04336J>.
- (93) Bekkar, F.; Bettahar, F.; Moreno, I.; Meghabar, R.; Hamadouche, M.; Hernández, E.; Vilas-Vilela, J. L.; Ruiz-Rubio, L. Polycarbazole and Its Derivatives: Synthesis and Applications. A Review of the Last 10 Years. *Polymers* **2020**, *12* (10), 2227. <https://doi.org/10.3390/polym12102227>.
- (94) Nayana, V.; Kandasubramanian, B. Polycarbazole and Its Derivatives: Progress, Synthesis, and Applications. *J. Polym. Res.* **2020**, *27* (9), 285. <https://doi.org/10.1007/s10965-020-02254-7>.
- (95) Ates, M.; Uludag, N. Carbazole Derivative Synthesis and Their Electropolymerization. *J. Solid State Electrochem.* **2016**, *20* (10), 2599–2612. <https://doi.org/10.1007/s10008-016-3269-5>.
- (96) Mangione, M. I.; Spanevello, R. A.; Minudri, D.; Heredia, D.; Fernandez, L.; Otero, L.; Fungo, F. Electropolymerization of Functionalized Carbazole End-Capped Dendrimers. Formation of Conductive Films. *Electrochimica Acta* **2016**, *207*, 143–151. <https://doi.org/10.1016/j.electacta.2016.04.154>.
- (97) Li, M.; Kang, S.; Du, J.; Zhang, J.; Wang, J.; Ariga, K. Junction-Controlled Topological Polymerization. *Angew. Chem. Int. Ed.* **2018**, *57* (18), 4936–4939. <https://doi.org/10.1002/anie.201713026>.

CHAPTER 2

Electronically Conductive, Multifunctional Polymer Binder for Highly Active, Stable, and Abundant Composite Electrodes for Oxygen Evolution^a

2.1 Introduction

Solar and wind energy are diffuse and intermittent. Efficient, high-capacity, and output storage methods are needed to transition to carbon-zero energy production.^{1,2} Electrochemical water splitting to form hydrogen and oxygen is a promising approach.^{3,4} Unfortunately, the electrooxidation of water to oxygen, called the oxygen evolution reaction (OER), is slow, and it remains a significant challenge to develop low-cost, stable OER electrodes with low overpotentials and loadings at high current densities.^{5,6} Further, electrode preparations must be straightforward and utilize abundant starting materials for widespread, large-scale utilization.⁷

Non-precious metal OER electrocatalysts help fulfill these requirements. The reported systems are typically more active in the base.^{8,9} Cobalt and Nickel are common in OER electrocatalysts, and the performance of both is improved significantly when combined with even trace amounts of Fe.^{10,11} There have been several significant advances regarding the utilization and understanding of NiFe in the OER reaction.^{12–18} The mechanism by which Fe enhances the activity of Ni or Co towards the OER remains a topic of extensive investigation.^{19,20}

As stated above, a significant consideration of OER electrocatalysts is their stability.^{21,22} Strategies to improve their stability include coating them with thin layers of polymers or metal oxides by atomic-layer deposition.^{23–25} A significant challenge with these approaches is controlling the thickness of the coating to minimize charge- and mass-transfer resistances.²⁶ In principle, a polymer binder, which conducts both electrons and ions, which allows mass transport to and from the active sites, which is

^a A version of this chapter has been published as J. Liu, S. H. Bergens, *ACS Appl. Mater. Interfaces* **2023**, *15*, 25624–25632.

stable, and that promotes the OER reactions at the active sites would optimize the utilization, activity, and stability of OER catalysts. Polycarbazole (PCz) and its derivatives are well-known.^{27–31} Doped (partially oxidized) PCz transports ions and water, which are requirements of ionomers in OER electrodes; as well, PCz is a coordinating polymer. This raises the possibility that coordination between N sites in the polymer and metal ions either in solution or on the surfaces of nanoparticles will direct the location, activity, and stability of OER catalysts. Figure 2.1c illustrates the potential roles for PCz functional groups during the OER. We report the first polycarbazole-based OER electrodes. Active and stable OER electrodes were prepared in two simple procedures utilizing available materials.

2.2 Results and Discussion

2.2.1 Substrate Preparation

The electrode preparation begins with the electropolymerization of carbazole over carbon fiber paper (CF) in MeCN (0.1 M LiClO₄) with cyclic voltammetry (CV, –0.245 to 1.255 V vs. Fc/Fc⁺ (Fc = ferrocene), 100 mV s^{–1}, 45 cycles).^{32,33} Figure S2.1 shows the voltammograms recorded during the polymerization. Figure 2.1a shows the CV of the washed, isolated green (Figure S2.2) doped polycarbazole/carbon fiber paper electrode (PCz/CF) in MeCN (0.1 M LiClO₄).²⁷ There are only small differences between the final CV cycles during the polymerization and those of the isolated polymer.^{33,34} In the anodic sweep, the lower peak at ~0.55 V is attributed to one-electron oxidation (doping) to form a delocalized cationic radical.^{33,35} The higher peak (~0.94 V, Figure S2.1) is proposed to arise from further oxidation to a dicationic species.^{33,35,36} Doped-PCz is green and electronically conductive due to the presence of the conjugated polycations.²⁷ Assuming the area under the first peak in the positive-going sweeps arises from one-electron oxidation,^{33,35} the amount of electrochemically accessible carbazole groups is roughly estimated to be ~1 x 10^{–6} mol cm^{–2}. Figure 2.1b shows the Fourier-transform infrared spectrum (FTIR) of the PCz/CF. The spectrum is like those reported for doped polycarbazole.³⁷ The strong peak at ~1100 cm^{–1} arises from the perchlorate

counterion. The peak at $\sim 1550\text{ cm}^{-1}$ has been assigned to doped-PCz,³⁸ and the peak at $\sim 856\text{ cm}^{-1}$ is assigned to the substitution pattern of polymer.³⁹ See the supporting information (SI) for more details on the FTIR study. Figure 2.1c illustrates the structural features of doped-PCz and selected roles it may play as a multifunctional binder in OER electrodes.

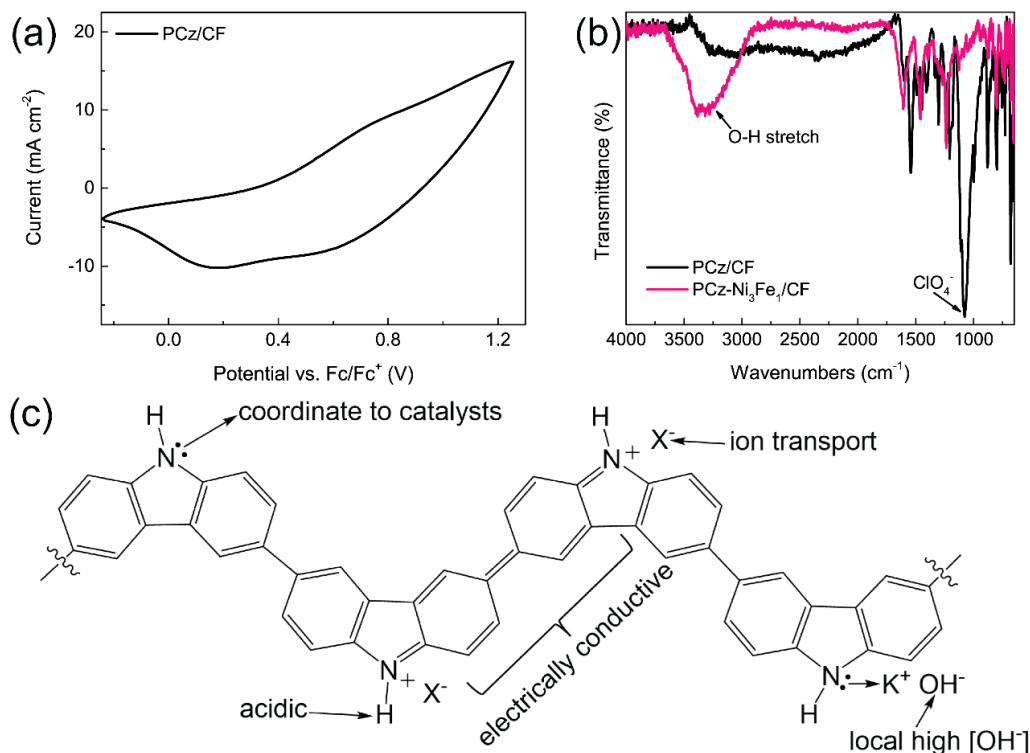


Figure 2.1. PCz characterization and structure. (a) CV of the isolated, washed PCz/CF electrode (MeCN, 0.1 M LiClO₄). (b) FTIR of PCz/CF and Ni₃Fe₁-PCz/CF. (c) The structure of doped polycarbazole illustrating the potential roles of the functional groups during the OER

2.2.2 Coordinative Deposition and OER Performance Over PCz/CF

The second step in the electrode preparation is the electrocatalyst deposition from NiCl₂·6H₂O, FeCl₂·4H₂O, or CoCl₂·6H₂O in methanol. Methanol was used as the solvent in part to swell the polymer film. The deposition is carried out under Ar for the first 24 h to avoid oxidation of Fe(II). These coordinative depositions likely begin with the coordination of Ni, Co, or Fe ions to the nitrogen sites on PCz (Figure 2.1c). For example, PCz sensors operate by different types of reactions at nitrogen.³⁷ After

24 h, the electrodes were left in the air overnight to oxidize the Fe(II) to Fe(III), washed with MeOH to remove any possible precursors, and utilized for the OER without further treatment.

Table S2.1 summarizes the concentrations of Ni(II), Fe(II), and Co(II) employed during the depositions and the amounts in the resulting M_xFe_y -PCz/CF electrodes ($M = Ni$ or Co), as determined by inductively-coupled plasma optical emission spectroscopy (ICP-OES). The total (Ni or Co + Fe) mole loadings in the OER electrodes ranged from 1.5 to $2.8 \times 10^{-6} \text{ mol cm}^{-2}$. The amount of electrochemically accessible carbazole in the PCz/CF deposit ($1 \times 10^{-6} \text{ mol cm}^{-2}$, Figure S2.3) resembles the amount of Ni + Fe ($2.8 \times 10^{-6} \text{ mol cm}^{-2}$) in the Ni_3Fe_1 -PCz/CF electrode. Further, the charge under the Ni(II) to Ni(III) oxidative wave in the linear sweep voltammogram of this electrode (Figure S2.4) corresponds to $1.3 \times 10^{-6} \text{ mol cm}^{-2}$ of Ni. The consistency among these rough estimates suggests that the deposition involves the coordination of Ni(II) and Fe(II) to the accessible nitrogen sites in PCz. The excess metal ions in the electrode (ICP-OES) suggest that catalyst growth proceeds further after coordination. Further studies are required to determine the exact mechanism of the coordinative deposition.

The OER activities were determined by linear sweep voltammetry (LSV) and galvanostatic experiments under alkaline conditions (Figure 2.2a, 1 mV s^{-1} , 1 M KOH , room temperature). The Ni_xFe_y electrodes were more active than Co_xFe_y . The Ni_xFe_y LSVs contained the known Ni^{2+} to Ni^{3+} oxidative wave that shifts in the positive direction with increasing amounts of Fe ($\sim 1.38 \text{ V}$ for Ni_9Fe_1 , $\sim 1.43 \text{ V}$ for Ni_3Fe_1 , obscured for Ni_1Fe_1).⁴⁰ We extrapolated the linear portion of the OER curve to the potential axis to estimate the onset potentials of the Ni_xFe_y -PCz/CF electrodes,⁴¹ giving 1.438 V , 1.452 V , and 1.461 V (vs RHE) for Ni_3Fe_1 -, Ni_9Fe_1 -, and Ni_1Fe_1 -PCz/CF, respectively, with Ni_3Fe_1 being the most active. The onset potential for Ni_3Fe_1 -PCz/CF is similar to the one we reported for Ni_3Fe_1 prepared by a different procedure.⁴¹ The onset potentials for Co_xFe_y were higher than Ni_xFe_y .

The LSV overpotentials at 10 mA cm^{-2} increased in the order Ni_3Fe_1 -PCz/CF (224 mV) < Ni_1Fe_1 -PCz/CF (245 mV) < Ni_9Fe_1 -PCz/CF (253 mV). The overpotential

at 10 mA cm^{-2} for the $\text{Ni}_3\text{Fe}_1\text{-PCz/CF}$ electrode is among the lowest reported in the literature, despite the relatively low loading of Ni + Fe in this electrode (Figure S2.5). The overpotentials for the Co-Fe electrodes increased in the order were $\text{Co}_3\text{Fe}_1\text{-PCz/CF}$ (283 mV) < $\text{Co}_9\text{Fe}_1\text{-PCz/CF}$ (289 mV) \sim $\text{Co}_1\text{Fe}_1\text{-PCz/CF}$ (291 mV). The control electrodes PCz/CF, $\text{Ni}_3\text{Fe}_1\text{-CF}$, and $\text{Co}_3\text{Fe}_1\text{-CF}$ were essentially inactive. The $\text{Ni}_3\text{Fe}_1\text{-PCz/CF}$ electrode was superior to the others in this study.

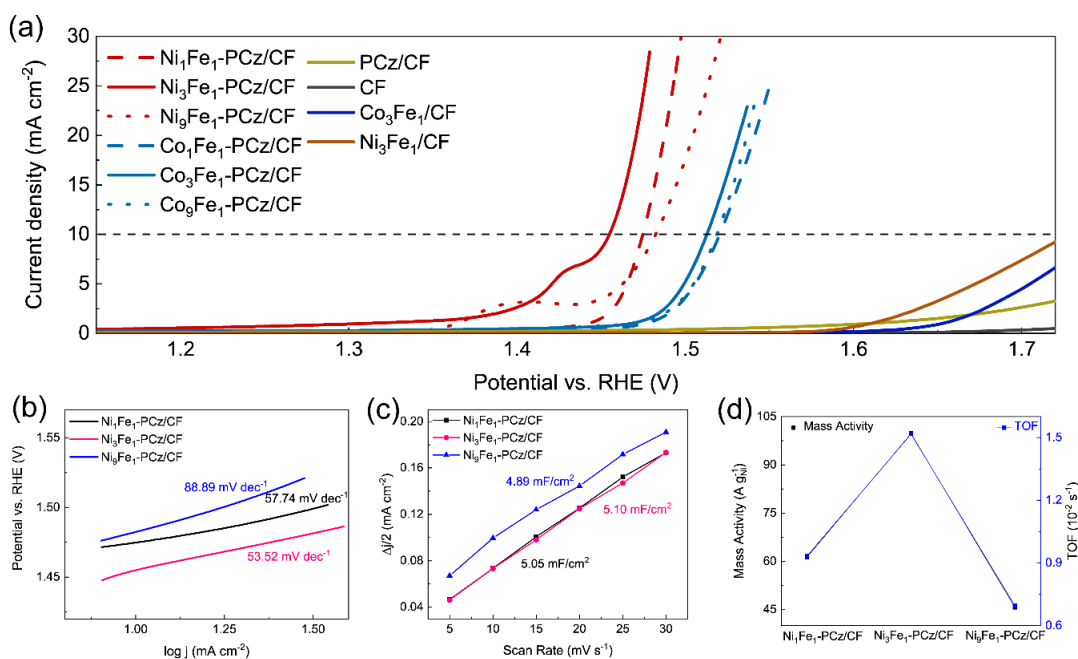


Figure 2.2. Performance of electrodes on PCz/CF. (a) OER LSV with different ratios of NiFe, CoFe, and control electrodes (CF, PCz/CF, and Co_3Fe_1 , Ni_3Fe_1 without PCz) in 1 M KOH at 1 mV s^{-1} . (b) Tafel slope, (c) double layer capacitance, and (d) mass activity (left) and TOF (right) at 1.454 V vs. RHE curves for Ni_1Fe_1 , Ni_3Fe_1 , $\text{Ni}_9\text{Fe}_1\text{-PCz/CF}$

Figure 2.2b shows Tafel plots for the electrodes. $\text{Ni}_3\text{Fe}_1\text{-PCz/CF}$ has the lowest Tafel slope among the Ni series, again demonstrating its high activity. Tafel slopes have been studied extensively in the literature for the OER.^{42,43} The Tafel slope for $\text{Ni}_3\text{Fe}_1\text{-PCz/CF}$ ($\sim 53.5 \text{ mV/dec}$) generally is accepted to indicate that the turnover limiting step is attacked by $\text{OH}^-_{(\text{aq})}$ on a surface oxide.^{44,45} This interpretation suggests that one role of the PCz may be to enhance the attack by OH^- , perhaps by increasing the local $[\text{OH}^-]$ (Figure 2.1c). This interpretation requires detailed mechanistic studies

to confirm. The slopes for the cobalt-based electrodes also indicate that the attack by hydroxide is turnover limiting.³⁵

The electrochemical surface areas (ECSAs) of the electrodes were investigated by comparing their double-layer capacitance (C_{dl}) in the non-Faradaic region (Figure 2.2c and Figures S2.6, S2.7, S2.31). Table S2.1 summarizes the results. The catalyst with the highest activity in this study, Ni₃Fe₁-PCz/CF, also has among the lowest C_{dl} . The high OER activity of the Ni₃Fe₁-PCz/CF is, therefore, more due to the intrinsic activity of the catalyst sites and less due to differences in ECSA.

High geometric activities with low catalyst mass loadings are desired in commercial systems to reduce cost and to simplify electrode preparation. Figure 2.2d shows the mass activities ($A\ g^{-1}(Ni + Fe)$) of the Ni_xFe_y-PCz/CF electrodes at 1.454 V vs. RHE, when the current density is 10 mA cm⁻² over Ni₃Fe₁-PCz/CF (Figure 2.2a). Again, Ni₃Fe₁-PCz/CF was significantly the most active CF-based electrode prepared in this study, with a mass activity of 99.73 A g⁻¹. Figure S2.5 plots overpotentials at 10 mA cm⁻² vs. catalyst mass loading for the most active earth-abundant OER catalysts in the literature. The Ni₃Fe₁-PCz/CF electrode is among those with the best combination of low overpotentials and mass loadings. A similar analysis also conducted using Co_xFe_y-PCz/CF electrodes can be found in the SI.

Figures 2.3 and S2.8 compare the OER activities of flat, well-defined glassy carbon electrodes (GC) with the same Ni₃Fe₁ loadings and prepared in the same manner with either electropolymerized carbazole or Nafion binders. This in-house, direct, well-defined comparison eliminates any effects of surface area and diffusion encountered with carbon felt. Figure 2.3a shows that during the galvanostatic OER (10 mA cm⁻², 1.0 M KOH), the Nafion-based electrode, Ni₃Fe₁-Nafion/GC, operated at significantly higher potentials, and it suffered a catastrophic failure after ~5 h. In contrast, the Ni₃Fe₁-PCz/GC operated at much lower potentials and was stable over the 24 h run, demonstrating that PCz is electrochemically stable and promotes the OER under these conditions. Figure 2.3b compares the LSV OER (1 M KOH) reactions over the Nafion-and PCz-based electrodes. The onset potential was much

lower over the Ni₃Fe₁-PCz/GC electrode, and the overpotential at 10 mA cm⁻² was only 272 mV. The overpotential at 10 mA cm⁻² over the Nafion-based electrode was 368 mV. Figure S2.8b shows that the LSV overpotential at 10 mA cm⁻² over Ni₃Fe₁-PCz/GC (272 mV), even was lower than a Nafion-based electrode with 5 X the mass loading of Ni₃Fe₁ (301 mV). Figure 2.3c shows the Nyquist plots (at 0.5 V vs. SCE) for the PCz- and Nafion-based electrodes before and after 24 h galvanostatic OER in 1 M KOH. As expected, the high-frequency resistance of Ni₃Fe₁-PCz/GC is much lower than the Nafion-based system, strongly indicating that the polycarbazole is electronically conductive at this potential. As well, there was little change in the Nyquist plot of the Ni₃Fe₁-PCz/GC electrode after the 24 h galvanostatic OER, again showing the stability of the polycarbazole binder under these conditions. As stated above, the Nafion-based electrode underwent catastrophic failure after ~5 h of the galvanostatic OER. While detailed investigations are required to determine the exact mechanisms responsible for the plots, it is clear that the PCz-binder significantly enhances and stabilizes the OER reaction. Figure S2.8c shows that the initial Nyquist plots of the PCz-based electrodes and that of a Nafion-based electrode with 5 X the mass loading of electrocatalyst (Ni₃Fe₁) were similar, but the higher loading Nafion-based electrode still underwent catastrophic failure during the galvanostatic OER. Figure 2.3d compares the Tafel slopes of the PCz- and Nafion-based glassy carbon electrodes with the same catalyst loadings. The Tafel slope (41.76 mV dec⁻¹) over Ni₃Fe₁-PCz/GC was significantly lower (41.76 mV dec⁻¹) than over the Nafion-based electrode (64.10 mV dec⁻¹), suggesting again that PCz enhances the OER reaction. Figure S2.8d shows that the Tafel slope of the PCz electrode (41.76 mV dec⁻¹) is similar to that of the Nafion-based electrode with 5 X the mass loading of electrocatalyst (41.64 mV dec⁻¹). We note that the 5 X mass loading of Ni₃Fe₁ on GC can be relatively stable until ~6 h. The 5 X higher loading of catalyst reduced the applied potential required to achieve the same current density (10 mA cm⁻²), improving its stability. Taken together, these results demonstrate that the polycarbazole binder increases both the OER performance and stability of Ni₃Fe₁-PCz/GC. Figure S2.9 shows similar enhancements in OER performance in

PCz vs Nafion electrodes on CF. Further, control experiments (details are in SI) showed there were no significant changes in the physical appearance of PCz on CF or Ni₃foam after soaking for 10 days in 6 or 1 M KOH. Moreover, chemical and electrochemical stability tests of PCz are described in detail in SI.

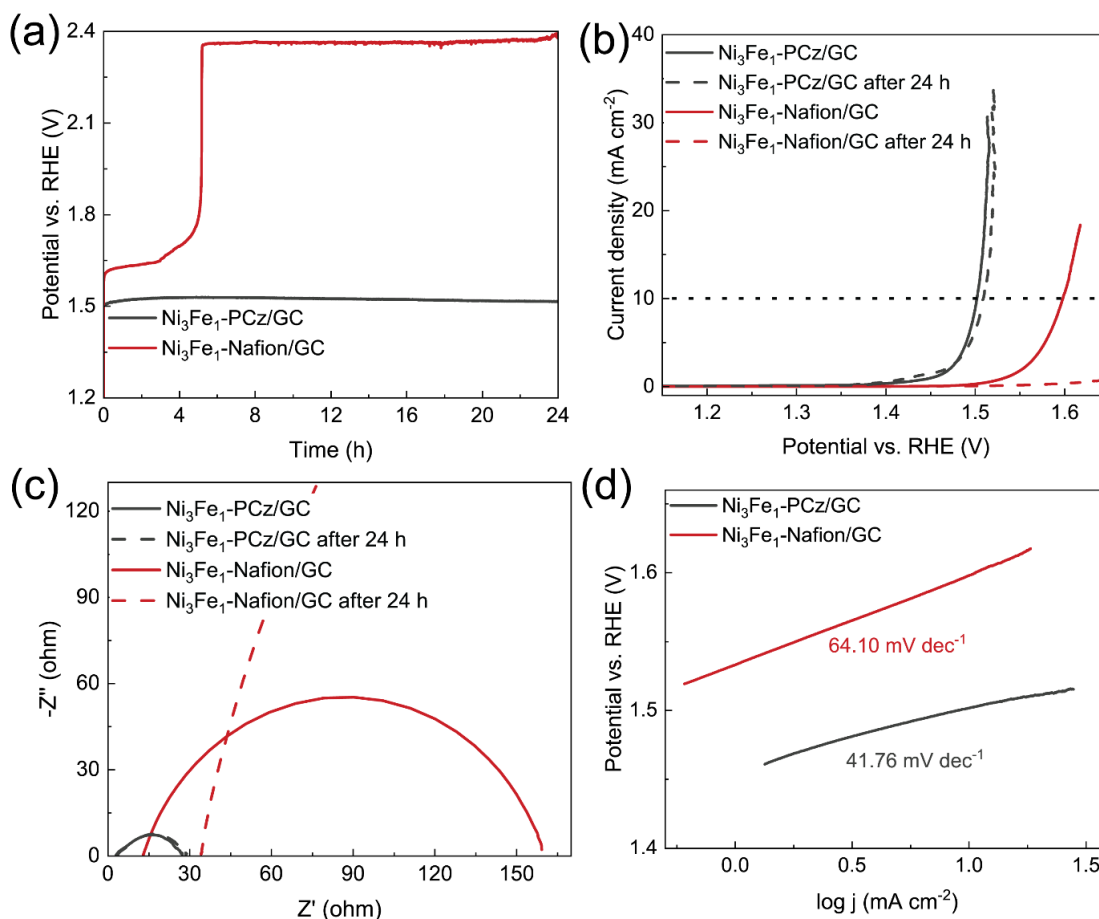


Figure 2.3. Stability of Ni₃Fe₁-PCz/GC and Ni₃Fe₁-Nafion/GC electrodes. (a) The galvanostatic OER over Ni₃Fe₁-PCz/GC and Ni₃Fe₁-Nafion/GC for 24 h at 10 mA cm⁻². (b) LSVs over Ni₃Fe₁-PCz/GC and Ni₃Fe₁-Nafion/GC before and after 24 h stability tests. (c) Nyquist plots (at 0.5 V vs. SCE) for Ni₃Fe₁-PCz/GC and Ni₃Fe₁-Nafion/GC before and after the 24 h stability tests. (d) Tafel slope of Ni₃Fe₁-PCz/GC and Ni₃Fe₁-Nafion/GC before stability tests

2.2.3 Structure of The Ni₃Fe₁-PCz/CF

Figure 2.1b shows the FTIR of the Ni₃Fe₁-PCz/CF deposit. The supplementary section contains the detailed assignments of other peaks in the FTIR, based upon comparisons to the literature. Notably, the large perchlorate signal in the FTIR of the unmetalled polymer, PCz/CF, is absent in the deposit. Thus, the polycarbazole was

either reduced during the deposition, or the perchlorate was exchanged with chloride. We note that the peak at 1554 cm^{-1} in the FTIR of PCz/CF, which was assigned to doped (partially oxidized) PCz,³¹ also is absent, suggesting that the oxidized polycarbazole was reduced at some stage during the deposition and handling. The uniform distributions of Cl and O observed in the EDX elemental mapping of Ni₃Fe₁-PCz/CF (Figures 2.4d and e) are, therefore, due to the presence of Cl⁻ and H₂O, OH⁻, or MeOH. The large broad peak at 3323 cm^{-1} in the FTIR spectrum of Ni₃Fe₁-PCz/CF is absent in the spectrum of PCz/CF. This peak is due to the presence of (Ni/Fe)-H₂O or -OH groups in the deposit.⁴⁶ Moreover, the peak at 733 cm^{-1} represents an Fe-O bond.⁴⁷

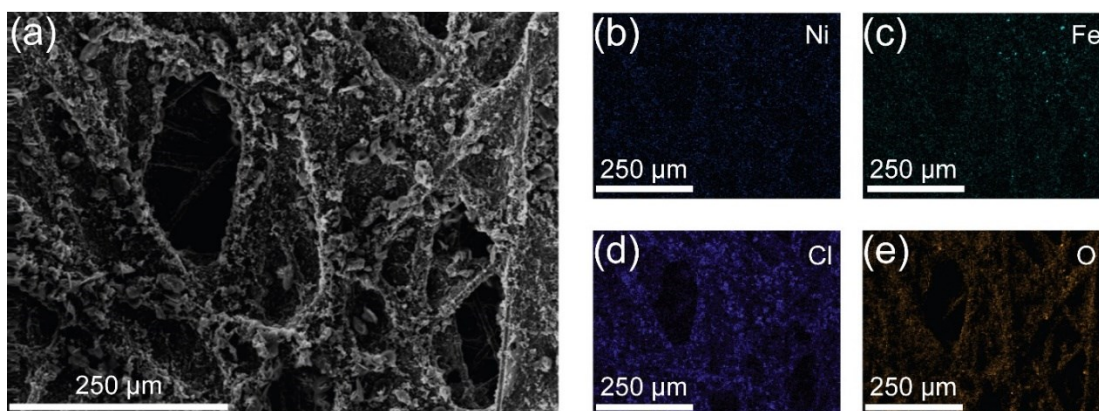


Figure 2.4. Morphology of Ni₃Fe₁-PCz/CF electrode. (a) SEM surface morphology of the Ni₃Fe₁-PCz/CF and EDX elemental mapping of (b) Ni, (c) Fe, (d) Cl, and (e) O

Figure S2.10 shows the high-resolution XPS spectra in the Ni *2p* and Fe *2p* regions for the Ni₃Fe₁-PCz/CF electrode. The 873.8 and 856.5 eV peaks correspond to Ni *2p*_{1/2} and *2p*_{3/2}, indicating that the oxidation state of Ni is +2.⁴⁸ The Fe *2p* peaks at 712.1 and 725.4 eV correspond to Fe(III), showing that, as expected, the Fe(II) was oxidized while the samples were left in the air overnight.⁴⁹ There were no significant changes to the XPS after the 20 h galvanostatic OER, again demonstrating the stability of the catalyst. The Ni *2p*_{1/2} and Ni *2p*_{3/2} peaks shifted by $\sim 0.48\text{ eV}$ in the positive direction, and the Fe *2p*_{1/2} and Fe *2p*_{3/2} shifted by $\sim 0.68\text{ eV}$ after the 20 h

OER. These slight shifts to higher energy are a common phenomenon for OER catalysts.^{41,50} See the SI for further details of the XPS analysis.

The absorbance by the CF support interfered with UV-Vis studies of Ni₃Fe₁-PCz/CF. As a result, control UV-Vis experiments were carried out with polycarbazole on ITO slides. Figure S2.11 showed that the doped polycarbazole indeed is reduced to the undoped form after soaking overnight in methanol, as indicated by the FTIR studies above. The spectra of Ni-PCz/ITO, and of Fe-PCz/ITO (Figure S2.12) contained new peaks due to interactions between the polycarbazole and the Ni and Fe ions during the coordinative deposition. The exact nature of these interactions requires further study.

2.2.4 Ni, Fe on PCz Coated Ni Foam Electrode

We next prepared the Ni₃Fe₁-PCz catalyst over Ni foam, an effective support for reported NiFe OER catalysts (Figure S2.13).^{51,52} Figure S2.14 shows the CV of the isolated PCz/Ni_{foam} (0.1 M *n*-Bu₄N⁺PF₆⁻ in CH₂Cl₂) that contains anodic waves due to oxidation of PCz and the Ni surface as well as reductive waves of the doped PCz. To our knowledge, this is the first report of the electropolymerization carbazole over Ni foam.

The PCz/Ni_{foam} electrode was treated with Ni(II) and Fe(II) in MeOH and then exposed to air, as was described previously (Figure S2.15). Figure S2.16 shows the SEM of Ni foam, PCz/Ni_{foam}, and Ni₃Fe₁-PCz/Ni_{foam}. The SEM of PCz/Ni_{foam} clearly shows a thick layer of PCz on Ni foam. The coverage of the Ni strands by the thick film of polycarbazole appears uniform, with some cracks and filaments of polymer that grew from the surface. The SEM recorded after the coordinative deposition of Ni₃Fe₁ (Ni₃Fe₁-PCz/Ni_{foam}) shows that the morphology of the deposit largely is the same as PCz/Ni_{foam}, perhaps with fewer filaments of polymer growing from the surface. EDX elemental mapping (Figure 2.5) shows a uniform distribution of N, Fe, and C throughout the deposit. The signal from the underlying Ni foam made conclusions about the distribution of Ni(II) unreliable.

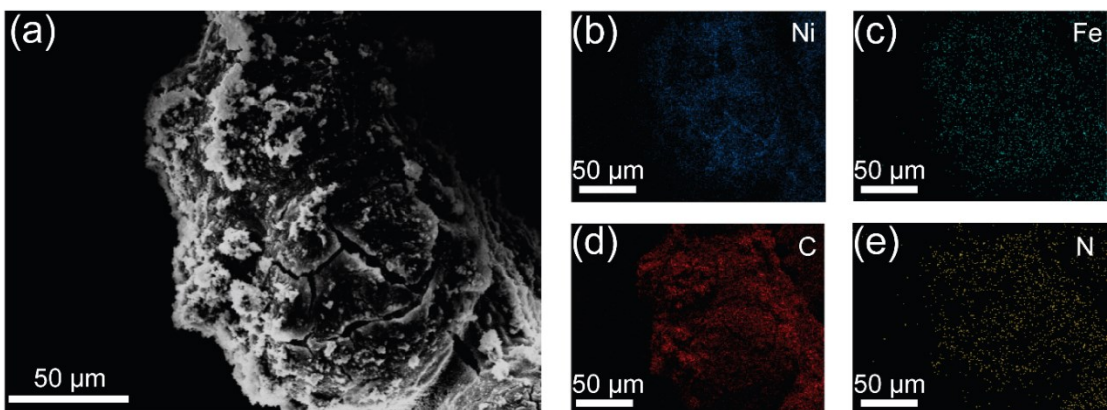


Figure 2.5. Morphology of $\text{Ni}_3\text{Fe}_1\text{-PCz/Ni}_{\text{foam}}$ electrode. (a) SEM surface morphology of the $\text{Ni}_3\text{Fe}_1\text{-PCz/Ni}_{\text{foam}}$ and EDX elemental mapping of (b) Ni, (c) Fe, (d) C, and (e) N

The FTIR of the $\text{PCz/Ni}_{\text{foam}}$ (Figure S2.17) contains peaks for the perchlorate anion and doped polycarbazole, the same as PCz/CF . The FTIR spectrum of $\text{Ni}_3\text{Fe}_1\text{-PCz/Ni}_{\text{foam}}$ (Figure S2.17b) was quite similar to that of $\text{Ni}_3\text{Fe}_1\text{-PCz/CF}$. The supplemental section details the FTIR analysis.

The XPS of spectrum $\text{PCz/Ni}_{\text{foam}}$ was typical for doped polycarbazole (Figure S2.18). As well, the Ni $2p_{1/2}$ and Ni $2p_{3/2}$ peaks (874.5 and 856.6 eV) and the Fe $2p_{1/2}$ and Fe $2p_{3/2}$ peaks (726.2 and 712.5 eV) in the XPS spectrum of $\text{Ni}_3\text{Fe}_1\text{-PCz/Ni}_{\text{foam}}$ were only of slightly higher energy than those in $\text{Ni}_3\text{Fe}_1\text{-PCz/CF}$ (Figure S2.19).

The amount of electrochemically accessible Ni in the $\text{Ni}_3\text{Fe}_1\text{-PCz/Ni}_{\text{foam}}$ deposit, as estimated from the Ni(II) to Ni(III) peak in the LSV (Figure S2.20), is $\sim 298 \mu\text{g cm}^{-2}$. This value, however, contains contributions from the Ni foam support. The amount of Fe in the $\text{Ni}_3\text{Fe}_1\text{-PCz/Ni}_{\text{foam}}$ deposit was $43 \mu\text{g cm}^{-2}$ (ICP-OES), a value similar to the $\text{Ni}_3\text{Fe}_1\text{-PCz/CF}$ deposit ($\sim 36 \mu\text{g cm}^{-2}$).

Figure 2.6a shows the LSVs for the OER over the $\text{Ni}_3\text{Fe}_1\text{-PCz/Ni}_{\text{foam}}$ electrode (1 mV s^{-1} , 1 M KOH , room temperature). To our delight, the $\text{Ni}_3\text{Fe}_1\text{-PCz/Ni}_{\text{foam}}$ was substantially more active than $\text{Ni}_3\text{Fe}_1\text{-PCz/CF}$. Although the onset potentials were similar over the Ni foam and CF-based electrodes, the potential at 10 mA cm^{-2} over the $\text{Ni}_3\text{Fe}_1\text{-PCz/Ni}_{\text{foam}}$ electrode was very low ($\sim 136 \text{ mV}$), despite the overlap with the Ni(II) to Ni(III) oxidation peak. The steady-state overpotential at 10 mA cm^{-2}

after 22 h was ~ 200 mV (Figure S2.21). This steady-state overpotential is primarily due to the OER, with little overlap by the Ni(II) to Ni(III) peak, and it is very low among the reported earth-abundant catalysts (Figure S2.5). The LSV overpotential at the much higher current density of 100 mA cm^{-2} was ~ 264 mV. At 500 mA cm^{-2} , the overpotential was 339 mV. The Tafel slope over $\text{Ni}_3\text{Fe}_1\text{-PCz/Ni}_{\text{foam}}$ was $61.83 \text{ mV dec}^{-1}$ (Figure S2.22), suggesting again that the turnover limiting step is attacked by $\text{OH}^{\text{(aq)}}$ on a surface oxide, although detailed studies are required to confirm this hypothesis. The control electrodes ($\text{Ni}_3\text{Fe}_1/\text{Ni}_{\text{foam}}$, $\text{PCz/Ni}_{\text{foam}}$, and Ni_{foam}) possessed little to no OER activity under these conditions. Figure 2.6a shows that the OER onset and overpotentials were much higher over a nickel foam electrode prepared with the same loading of Ni_3Fe_1 using only Nafion as binder, consistent with the comparisons over glassy carbon.

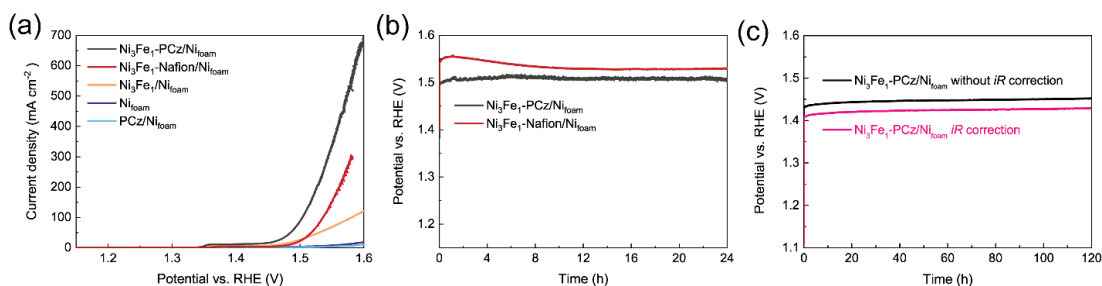


Figure 2.6. OER performance of $\text{Ni}_3\text{Fe}_1\text{-PCz/Ni}_{\text{foam}}$ electrode. (a) LSV curves of Ni_{foam} , $\text{PCz/Ni}_{\text{foam}}$, $\text{Ni}_3\text{Fe}_1/\text{Ni}_{\text{foam}}$, $\text{Ni}_3\text{Fe}_1\text{-Nafion/Ni}_{\text{foam}}$ and $\text{Ni}_3\text{Fe}_1\text{-PCz/Ni}_{\text{foam}}$ in 1 M KOH at 1 mV s^{-1} . (b) Galvanostatic tests of $\text{Ni}_3\text{Fe}_1\text{-Nafion/Ni}_{\text{foam}}$ and $\text{Ni}_3\text{Fe}_1\text{-PCz/Ni}_{\text{foam}}$ at 100 mA cm^{-2} over 24 h. (c) Galvanostatic tests of $\text{Ni}_3\text{Fe}_1\text{-PCz/Ni}_{\text{foam}}$ at 100 mA cm^{-2} over 120 h in 6 M KOH and at $85 \text{ }^\circ\text{C}$ versus RHE, without (black line) and with (red line) iR correction

At the much higher galvanostatic current density of 100 mA cm^{-2} , the overpotential was also essentially constant (~ 270 mV) over 24 h (Figure 2.6b). The LSV recorded afterwards showed a slight increase in performance over that recorded beforehand (Figure S2.23a), and the EIS recorded before and after almost unchanged (Figure S2.23b). Figure 2.6b also shows that the galvanostatic OER performance was significantly worse over a nickel foam electrode prepared with the same loading of Ni_3Fe_1 using Nafion as binder.

Figures 2.6c and 2.6d show the galvanostatic OER over the Ni₃Fe₁-PCz/Ni_{foam} electrode under harsh conditions (6 M KOH, 85 °C) at high current density (100 mA cm⁻²) over 120 h. The potential was measured versus the Hg/HgO reference electrode and converted to RHE using the method described in SI (Figure S2.24). The potential increased by only 0.69% over the first 14.5 h, then stabilized, increasing only 0.61% further during the remaining 105.5 h. The stabilized potential (after 14.5 h) vs. RHE without *iR* correction was 1.44 V. This is the lowest overpotential vs. RHE and the highest stability that we are aware of for an earth-abundant OER electrode under these harsh conditions. The *iR*-corrected stabilized potential was 1.42 V (Figure 2.6d).

2.3 Conclusions

This chapter combines a redox-active, conductive, polycationic, and coordinating polymer with a coordinative redox deposition to prepare electrodes for the OER. The new electrodes contain low loadings of earth-abundant catalysts, and they are highly active and stable under harsh conditions. The preparation is straightforward and can be utilized to prepare electrodes with different supports and metal ion precursors. The polycarbazole provides highly conductive, stable support for the OER catalysts. XPS and UV-Vis studies suggest that the deposition proceeds by coordination to the nitrogen sites in PCz. We propose that PCz provides a local high [OH⁻] for the turnover limiting step in the OER. Detailed mechanistic studies are required to investigate these interpretations. Such studies as well as the applicability of this system to other types of electrodes, are underway in our laboratories.

2.4 Experimental Section

2.4.1 Materials and Instrumentation

Potassium hydroxide (KOH, Aldrich, semiconductor grade, 99.99%); nickel(II) chloride hexahydrate (NiCl₂·6H₂O, Baker, 98%); iron(II) chloride tetrahydrate (FeCl₂·4H₂O, Aldrich, 99%); Cobalt(II) Chloride hexahydrate (CoCl₂·6H₂O, ACP, 98%); carbazole (C₁₂H₉N, Sigma, 95%); lithium perchlorate (LiClO₄; GFS);

acetonitrile (C_2H_3N , Sigma-Aldrich, 99.9%); methanol (CH_4O , Sigma-Aldrich, 99.8%); Ni foam (Ni, GoodFellow, 99.5%, porosity 95%, thickness 1.6 mm), hydrochloric acid (HCl, Fisher, 36.5%-38%, ACS grade); Toray carbon fiber paper (C, Fuel Cell Earth, P50); glassy carbon electrodes (5 mm diameter); and Nafion solution (Fuel Cell Earth, D1021, 10% wt.). All experiments use triple-distilled water. Electrochemical studies were carried out using a Solartron SI 1287 Electrochemical Interface. X-ray photoelectron spectroscopy (XPS) measurements were done using a Kratos AXIS Ultra. A monochromatized Al $K\alpha$ source ($h\nu = 1486.6$ eV) was used at 12 mA and 14 kV, while the pressure in the sample analytical chamber was maintained at $<1 \times 10^{-9}$ torr. Survey scans ran at 1100 to 0 eV binding energy, with an analyzer pass energy of 160 eV and 0.3 eV steps. All spectra are calibrated by the C 1s line at 284.8 eV for deconvolution. ICP-OES data are collected by Thermo iCAP6300 Duo (N. America). Thermo iCAP6300 Duo (N. America) inductively coupled plasma-optical emission spectrometer (ICP-OES) was used to characterize the concentration and amount of metal ions. Typically, the samples are weighed in concentrated trace metal grade HNO_3 , then left overnight. Before analysis, the final volume of the solution was 5mL and then digested using a modified EPA 3051a. In reflection mode, UV-Vis spectra were collected using the Cary 5000 UV-Vis spectrometer by ITO glasses as substrates. FTIR was measured by a Thermo Nicolet 8700 FTIR Spectrometer and Continuum FTIR Microscope on ATR. SEM images and EDX elemental mapping images were collected by Zeiss Sigma (Gemie) Field Emission Scanning Electron Microscope (FE-SEM) with EDX/EBSD; the system vacuum of FE-SEM is lower than 2×10^{-5} torr when acquiring images.

2.4.2 Preparation of Polycarbazole (PCz) on Carbon Fiber Paper (CF) (PCz/CF) or Glassy Carbon (GC)

The CF was cut into 1 cm x 2.5 cm, then sonicated in distilled water for 30 min. After drying in an oven at 60 °C for 30 min, the CF was ready to use for the next step. For GC electrodes, they first were polished with 5 μm , 0.3 μm , and 0.05 μm alumina, respectively. The GC electrodes were followed by being sonicated in water for a few seconds and washed with TD water, then dried with N_2 gas. Electropolymerization

was carried out in distilled acetonitrile (MeCN) solution, with 5 mM of carbazole and 0.1 M of LiClO₄.³⁵ CVs were acquired by sweeping 0–1.5 V vs. Ag wire (–0.245 to 1.255 V vs. Fc/Fc⁺, Fc=Ferrocene) at a scan rate of 100 mV s^{–1} for 45 cycles, with Ag wire as the reference electrode and graphite rod as the counter electrode. Ferrocene was added after the experiment as an internal reference. After polymerization, the electrodes were washed with MeCN and dried in the oven at 60 °C .

2.4.3 Preparation of Polycarbazole (PCz) on Ni Foam (PCz/Ni_{foam})

Ni foam was cut into 1 cm x 3 cm small pieces and soaked into 1 M HCl for 10 min to remove surface oxides and other impurities with sonication. After 10 min, the Ni foam was removed from the bath and washed with triple distilled water and ethanol. After drying in an oven at 60 °C for 30 min, the Ni foam was used for electropolymerization. The electropolymerization was carried out in freshly distilled acetonitrile (MeCN) solution, with 5 mM of carbazole as raw material and 0.1 M of LiClO₄ as electrolyte. CVs were operated by sweeping between –0.245 to 1.755V vs. Fc/Fc⁺ at a scan rate of 100 mV s^{–1} for 45 cycles, with Ag wire as the reference electrode and Pt mesh as the counter electrode. Ferrocene was added after the experiment to obtain a reference potential. After polymerization, the electrodes were washed with MeCN and dried in the oven at 60 °C .

2.4.4 Loading NiFe or CoFe Metal Ions on PCz/CF or PCz/Ni_{foam} (Ni_xFe_y-PCz/CF or Ni_xFe_y-PCz/Ni_{foam})

The PCz/Ni_{foam} or PCz/CF electrodes were transferred into Schlenk tubes, switched between vacuum (3 min) and argon gas (1 min) for three times to remove air, and left under argon gas environment. In individual containers, methanol and the metal salts were purged with argon for 30 min and then mixed to give solutions with a total concentration of metal salts of 0.2 M. The ratio of Ni to Fe is 3 to 1 for the most active electrodes. The different metal ion solutions were then transferred by syringe to Schlenk tubes containing the PCz/CF electrodes. The electrodes were exposed to the salt solution for 24 h under argon. The electrodes were then removed from the

solution and dried in air overnight to oxidize Fe^{2+} to Fe^{3+} . They were then washed with methanol in air before further use.

2.4.5 Loading NiFe or CoFe Metal Ions on CF or Ni_{foam} (Ni_xFe_y/CF or Ni_xFe_y/Ni_{foam})

The Ni_xFe_y/CF or Ni_xFe_y/Ni_{foam} electrodes were prepared by the same procedures above, except for replacing PCz/CF or PCz/ Ni_{foam} with CF or Ni_{foam}.

2.4.6 Loading Ni₃Fe₁ Metal Ions onto The Glassy Carbon Electrodes (GC), CF, or Ni_{foam} Control Electrodes Using Nafion as Binder

The Ni₃Fe₁ solutions (0.2 M) were prepared by dissolving the metal salts (NiCl₂ and FeCl₂ (as hydrates)) in triple-distilled water (TD water) and ethanol with a ratio of 5 to 1 under argon. Next, for each 1 mL of Ni₃Fe₁ solution, 10 μL 10 wt.% of Nafion was added, followed by sonication for 30 min to make the catalyst ink. Then, 15 μL of this solution were drop cast onto CF or Ni_{foam} to provide the same mass loading as the polycarbazole electrodes determined ICP-OES. Next, the electrodes were dried at 60 °C for ~30 min. The GC electrodes first were polished in sequence by 5 μm , 0.3 μm , and 0.05 μm alumina, then briefly sonicated in water, washed with TD water, and dried under a stream of N₂. To obtain Ni₃Fe₁-Nafion/GC electrodes with 5 x the mass loading of Ni₃Fe, 15 μL of the Ni₃Fe₁ (0.2 M) solution was drop cast onto GC, then left in air overnight before use. To obtain 1 equivalent catalyst amount of Ni₃Fe₁-Nafion/GC electrodes, 0.02 M Ni₃Fe₁ solution was prepared. The preparation procedures of 0.02 M Ni₃Fe₁ solution were the same as for the 0.2 M Ni₃Fe₁ solution except that the total metal ion concentrations changed to 0.02 M. Then, 30 μL of 0.02 M Ni₃Fe₁ solution were drop cast onto GC.

2.4.7 Electrochemical Measurements

For room temperature electrochemical studies, 1 M KOH solution was pretreated with solid Ni(OH)₂ to remove small traces of iron metals, prepared as described in the literature.⁴¹ A three-electrode system was used throughout the experiment, where the counter electrode was a graphite rod and the reference electrode was a saturated calomel electrode (SCE). The reaction flask was a 100 ml three-neck round bottom

flask. The linear sweep voltammetry (LSV) curves were measured at 1 mV s^{-1} . The current densities were iR corrected by the corresponding Electrochemical impedance spectroscopy (EIS). The reversible hydrogen electrode (RHE) voltage is calculated based on the equation: $E \text{ (vs. RHE)} = E \text{ (vs. SCE)} + 0.241 \text{ V} + 0.059 \times \text{pH}$. The Tafel slope is calculated using the equation $E = b \log j$, where E is the potential vs. RHE, b is the Tafel slope, and j is the current density. The following equation calculates the overpotential (η) for OER: $\eta = E \text{ (vs. RHE)} - 1.23 \text{ V}$. EIS was acquired with a frequency range of 0.1–100 kHz at a bias potential of 0.5 V vs. SCE. To investigate the electrochemical active surface area (ECSA), the electrochemical double-layer capacitance (C_{dl}) was measured over a range of 0.15–0.25 V vs. SCE, which was the non-Faradaic region, at the rate ranging from 10 to 30 mV s^{-1} at 5 mV increments. From the C_{dl} , the ECSA can be estimated using the equation $\text{ECSA} = C_{dl} / C_s$, where C_s is the specific capacitance of an atomically smooth material. Thus, ECSA is a linear relation to C_{dl} and can be used for comparison for a series of electrodes with a similar or same surface. For 6 M KOH at $85 \text{ }^\circ\text{C}$, a Hg/HgO reference electrode was used instead of SCE, and converted into RHE as described in the supporting information.

2.5 References

- (1) Kibsgaard, J.; Chorkendorff, I. Considerations for the Scaling-up of Water Splitting Catalysts. *Nat Energy* 2019, 4 (6), 430–433. <https://doi.org/10.1038/s41560-019-0407-1>.
- (2) Yan, Z.; Hitt, J. L.; Turner, J. A.; Mallouk, T. E. Renewable Electricity Storage Using Electrolysis. *Proc. Natl. Acad. Sci. U.S.A.* **2020**, 117 (23), 12558–12563. <https://doi.org/10.1073/pnas.1821686116>.
- (3) Subbaraman, R.; Tripkovic, D.; Strmcnik, D.; Chang, K.-C.; Uchimura, M.; Paulikas, A. P.; Stamenkovic, V.; Markovic, N. M. Enhancing Hydrogen Evolution Activity in Water Splitting by Tailoring $\text{Li}^+ \text{-Ni(OH)}_2 \text{-Pt}$ Interfaces. *Science* **2011**, 334 (6060), 1256–1260. <https://doi.org/10.1126/science.1211934>.
- (4) Nikolaidis, P.; Poullikkas, A. A Comparative Overview of Hydrogen Production Processes. *Renewable and Sustainable Energy Reviews* **2017**, 67, 597–611. <https://doi.org/10.1016/j.rser.2016.09.044>.
- (5) Zheng, X.; Tang, J.; Gallo, A.; Garrido Torres, J. A.; Yu, X.; Athanitis, C. J.; Been, E. M.; Ercius, P.; Mao, H.; Fakra, S. C.; Song, C.; Davis, R. C.; Reimer, J. A.; Vinson, J.; Bajdich, M.; Cui, Y. Origin of Enhanced Water Oxidation Activity in an Iridium Single Atom Anchored on NiFe Oxyhydroxide Catalyst. *Proc. Natl. Acad. Sci. U.S.A.* **2021**, 118 (36), e2101817118. <https://doi.org/10.1073/pnas.2101817118>.

- (6) Yu, M.; Weidenthaler, C.; Wang, Y.; Budiyo, E.; Onur Sahin, E.; Chen, M.; DeBeer, S.; Rüdiger, O.; Tüysüz, H. Surface Boron Modulation on Cobalt Oxide Nanocrystals for Electrochemical Oxygen Evolution Reaction. *Angew Chem Int Ed* **2022**. <https://doi.org/10.1002/anie.202211543>.
- (7) Zhang, B.; Wu, Z.; Shao, W.; Gao, Y.; Wang, W.; Ma, T.; Ma, L.; Li, S.; Cheng, C.; Zhao, C. Interfacial Atom - Substitution Engineered Transition - Metal Hydroxide Nanofibers with High - Valence Fe for Efficient Electrochemical Water Oxidation. *Angewandte Chemie* **2022**, *134* (13). <https://doi.org/10.1002/ange.202115331>.
- (8) Hunter, B. M.; Gray, H. B.; Müller, A. M. Earth-Abundant Heterogeneous Water Oxidation Catalysts. *Chem. Rev.* **2016**, *116* (22), 14120–14136. <https://doi.org/10.1021/acs.chemrev.6b00398>.
- (9) Li, S.; Gao, Y.; Li, N.; Ge, L.; Bu, X.; Feng, P. Transition Metal-Based Bimetallic MOFs and MOF-Derived Catalysts for Electrochemical Oxygen Evolution Reaction. *Energy Environ. Sci.* **2021**, *14* (4), 1897–1927. <https://doi.org/10.1039/D0EE03697H>.
- (10) Wu, Z.; Lu, X. F.; Zang, S.; Lou, X. W. (David). Non - Noble - Metal - Based Electrocatalysts toward the Oxygen Evolution Reaction. *Adv. Funct. Mater.* **2020**, *30* (15), 1910274. <https://doi.org/10.1002/adfm.201910274>.
- (11) Anantharaj, S.; Kundu, S.; Noda, S. “The Fe Effect”: A Review Unveiling the Critical Roles of Fe in Enhancing OER Activity of Ni and Co Based Catalysts. *Nano Energy* **2021**, *80*, 105514. <https://doi.org/10.1016/j.nanoen.2020.105514>.
- (12) Dang, L.; Liang, H.; Zhuo, J.; Lamb, B. K.; Sheng, H.; Yang, Y.; Jin, S. Direct Synthesis and Anion Exchange of Noncarbonate-Intercalated NiFe-Layered Double Hydroxides and the Influence on Electrocatalysis. *Chem. Mater.* **2018**, *30* (13), 4321–4330. <https://doi.org/10.1021/acs.chemmater.8b01334>.
- (13) Fan, L.; Zhang, P.; Zhang, B.; Daniel, Q.; Timmer, B. J. J.; Zhang, F.; Sun, L. 3D Core–Shell NiFeCr Catalyst on a Cu Nanoarray for Water Oxidation: Synergy between Structural and Electronic Modulation. *ACS Energy Lett.* **2018**, *3* (12), 2865–2874. <https://doi.org/10.1021/acsenergylett.8b01897>.
- (14) Niu, S.; Li, S.; Hu, J.; Li, Y.; Du, Y.; Han, X.; Xu, P. Fabrication of Uniform Ru-Doped NiFe₂O₄ Nanosheets as an Efficient Hydrogen Evolution Electrocatalyst. *Chem. Commun.* **2019**, *55* (97), 14649–14652. <https://doi.org/10.1039/C9CC07651D>.
- (15) Geng, S.-K.; Zheng, Y.; Li, S.-Q.; Su, H.; Zhao, X.; Hu, J.; Shu, H.-B.; Jaroniec, M.; Chen, P.; Liu, Q.-H.; Qiao, S.-Z. Nickel Ferrocyanide as a High-Performance Urea Oxidation Electrocatalyst. *Nat. Energy* **2021**, *6* (9), 904–912. <https://doi.org/10.1038/s41560-021-00899-2>.
- (16) Zhang, Y.; Guo, P.; Niu, S.; Wu, J.; Wang, W.; Song, B.; Wang, X.; Jiang, Z.; Xu, P. Magnetic Field Enhanced Electrocatalytic Oxygen Evolution of NiFe - LDH/Co₃O₄ P - n Heterojunction Supported on Nickel Foam. *Small Methods* **2022**, *6* (6), 2200084. <https://doi.org/10.1002/smt.202200084>.
- (17) Lyu, X.; Zhang, Y.; Wang, X.; Chen, H.; Li, S.; Zhang, W.; Hu, Y.; Li, F.; Li, D.; Yang, D. Electronic Structure Regulation of Nickel-Iron Layered Double Hydroxides by Tuning Ternary Component for Overall Water Splitting. *Mater. Today Sustain.* **2023**, *21*, 100295. <https://doi.org/10.1016/j.mtsust.2022.100295>.
- (18) Wan, W.; Wu, H.; Wang, Z.; Cai, G.; Li, D.; Zhong, H.; Jiang, T.; Jiang, C.; Ren, F. Tailoring Electronic Structure of Ni-Fe Oxide by V Incorporation for Effective Electrocatalytic Water Oxidation. *Appl. Surf. Sci.* **2023**, *611*, 155732. <https://doi.org/10.1016/j.apsusc.2022.155732>.

- (19) Xiao, H.; Shin, H.; Goddard, W. A. Synergy between Fe and Ni in the Optimal Performance of (Ni,Fe)OOH Catalysts for the Oxygen Evolution Reaction. *Proc. Natl. Acad. Sci. U.S.A.* **2018**, *115* (23), 5872–5877. <https://doi.org/10.1073/pnas.1722034115>.
- (20) Dionigi, F.; Zeng, Z.; Sinev, I.; Merzdorf, T.; Deshpande, S.; Lopez, M. B.; Kunze, S.; Zegkinoglou, I.; Sarodnik, H.; Fan, D.; Bergmann, A.; Drnec, J.; Araujo, J. F. de; Gliech, M.; Teschner, D.; Zhu, J.; Li, W.-X.; Greeley, J.; Cuenya, B. R.; Strasser, P. In-Situ Structure and Catalytic Mechanism of NiFe and CoFe Layered Double Hydroxides during Oxygen Evolution. *Nat Commun* **2020**, *11* (1), 2522. <https://doi.org/10.1038/s41467-020-16237-1>.
- (21) Chen, F.-Y.; Wu, Z.-Y.; Adler, Z.; Wang, H. Stability Challenges of Electrocatalytic Oxygen Evolution Reaction: From Mechanistic Understanding to Reactor Design. *Joule* **2021**, *5* (7), 1704–1731. <https://doi.org/10.1016/j.joule.2021.05.005>.
- (22) Zhao, S.; Yang, Y.; Tang, Z. Insight into Structural Evolution, Active Sites, and Stability of Heterogeneous Electrocatalysts. *Angew Chem Int Ed* **2022**, *61* (11). <https://doi.org/10.1002/anie.202110186>.
- (23) Xu, P.; Huang, T.; Huang, J.; Yan, Y.; Mallouk, T. E. Dye-Sensitized Photoelectrochemical Water Oxidation through a Buried Junction. *Proc. Natl. Acad. Sci. U.S.A.* **2018**, *115* (27), 6946–6951. <https://doi.org/10.1073/pnas.1804728115>.
- (24) Zhu, Y.; Wang, D.; Huang, Q.; Du, J.; Sun, L.; Li, F.; Meyer, T. J. Stabilization of a Molecular Water Oxidation Catalyst on a Dye-sensitized Photoanode by a Pyridyl Anchor. *Nat Commun* **2020**, *11* (1), 4610. <https://doi.org/10.1038/s41467-020-18417-5>.
- (25) Wang, D.; Huang, Q.; Shi, W.; You, W.; Meyer, T. J. Application of Atomic Layer Deposition in Dye-Sensitized Photoelectrosynthesis Cells. *Trends in Chemistry* **2021**, *3* (1), 59–71. <https://doi.org/10.1016/j.trechm.2020.11.002>.
- (26) Younus, H. A.; Vandichel, M.; Ahmad, N.; Ahlberg, E.; Busch, M.; Verpoort, F. Engineering of a Highly Stable Metal-Organic Co-Film for Efficient Electrocatalytic Water Oxidation in Acidic Media. *Materials Today Energy* **2020**, *17*, 100437. <https://doi.org/10.1016/j.mtener.2020.100437>.
- (27) Bekkar, F.; Bettahar, F.; Moreno, I.; Meghabar, R.; Hamadouche, M.; Hernández, E.; Vilas-Vilela, J. L.; Ruiz-Rubio, L. Polycarbazole and Its Derivatives: Synthesis and Applications. A Review of the Last 10 Years. *Polymers* **2020**, *12* (10), 2227. <https://doi.org/10.3390/polym12102227>.
- (28) Zaia, E. W.; Gordon, M. P.; Yuan, P.; Urban, J. J. Progress and Perspective: Soft Thermoelectric Materials for Wearable and Internet - of - Things Applications. *Adv. Electron. Mater.* **2019**, *5* (11), 1800823. <https://doi.org/10.1002/aelm.201800823>.
- (29) Sun, D.; Ren, Z.; Bryce, M. R.; Yan, S. Arylsilanes and Siloxanes as Optoelectronic Materials for Organic Light-Emitting Diodes (OLEDs). *Journal of Materials Chemistry C* **2015**, *13*.
- (30) Pernites, R.; Ponnampati, R.; Felipe, M. J.; Advincula, R. Electropolymerization Molecularly Imprinted Polymer (E-MIP) SPR Sensing of Drug Molecules: Pre-Polymerization Complexed Terthiophene and Carbazole Electroactive Monomers. *Biosensors and Bioelectronics* **2011**, *26* (5), 2766–2771. <https://doi.org/10.1016/j.bios.2010.10.027>.
- (31) Rice, N. A.; Bodnaryk, W. J.; Mirka, B.; Melville, O. A.; Adronov, A.; Lessard, B. H. Polycarbazole-Sorted Semiconducting Single-Walled Carbon Nanotubes for Incorporation into Organic Thin Film Transistors. *Adv. Electron. Mater.* **2019**, *5* (1), 1800539. <https://doi.org/10.1002/aelm.201800539>.
- (32) Zhou, Z.; Tian, Q.; Chai, L.; Chao, P.; Liu, S.; Wang, C. Construction of Nickel- and Iron-Coordinated Poly(5-Amino-1,10-Phenanthroline) Film for Electrocatalytic Water Oxidation

Reactions. *Journal of Power Sources* **2021**, *506*, 230109. <https://doi.org/10.1016/j.jpowsour.2021.230109>.

(33) Sezai Sarac, A.; Ates, M.; Parlak, E. A. Electrolyte and Solvent Effects of Electrocoated Polycarbazole Thin Films on Carbon Fiber Microelectrodes. *J Appl Electrochem* **2006**, *36* (8), 889–898. <https://doi.org/10.1007/s10800-006-9145-8>.

(34) Siove, A.; Ades, D.; N'gbilo, E.; Chevrot, C. Chain Length Effect on the Electroactivity of Poly(N-Alkyl-3,6-Carbazolediyl) Thin Films. *Synthetic Metals* **1990**, *38* (3), 331–340. [https://doi.org/10.1016/0379-6779\(90\)90086-Z](https://doi.org/10.1016/0379-6779(90)90086-Z).

(35) Macit, H.; Sen, S.; Saçak, M. Electrochemical Synthesis and Characterization of Polycarbazole: Electrochemical Synthesis and Characterization of Polycarbazole. *J. Appl. Polym. Sci.* **2005**, *96* (3), 894–898. <https://doi.org/10.1002/app.21532>.

(36) Ambrose, J. F.; Carpenter, L. L.; Nelson, R. F. Electrochemical and Spectroscopic Properties of Cation Radicals: III. Reaction Pathways of Carbazolium Radical Ions. *J. Electrochem. Soc.* **1975**, *122* (7), 876–894. <https://doi.org/10.1149/1.2134365>.

(37) Saxena, V.; Choudhury, S.; Jha, P.; Koiry, S. P.; Debnath, A. K.; Aswal, D. K.; Gupta, S. K.; Yakhmi, J. V. In Situ Spectroscopic Studies to Investigate Uncharacteristic NH₃ Sensing Behavior of Polycarbazole Langmuir–Blodgett Films. *Sensors and Actuators B: Chemical* **2010**, *150* (1), 7–11. <https://doi.org/10.1016/j.snb.2010.08.002>.

(38) Miyazaki, T.; Kim, S.-K.; Hoshino, K. Nanostructured Hybrid Materials Formed by Cell Reaction between Polycarbazole and Metals. *Chem. Mater.* **2006**, *18* (22), 5302–5311. <https://doi.org/10.1021/cm060613w>.

(39) Sun, W.; Sun, W.; Zhuo, Y.; Chu, Y. Facile Synthesis of Cu₂O Nanocube/Polycarbazole Composites and Their High Visible-Light Photocatalytic Properties. *Journal of Solid State Chemistry* **2011**, *184* (7), 1638–1643. <https://doi.org/10.1016/j.jssc.2011.03.055>.

(40) Trotochaud, L.; Young, S. L.; Ranney, J. K.; Boettcher, S. W. Nickel–Iron Oxyhydroxide Oxygen-Evolution Electrocatalysts: The Role of Intentional and Incidental Iron Incorporation. *J. Am. Chem. Soc.* **2014**, *136* (18), 6744–6753. <https://doi.org/10.1021/ja502379c>.

(41) Wang, C.; Moghaddam, R. B.; Brett, M. J.; Bergens, S. H. Simple Aqueous Preparation of High Activity and Stability NiFe Hydrous Oxide Catalysts for Water Oxidation. *ACS Sustainable Chem. Eng.* **2017**, *5* (1), 1106–1112. <https://doi.org/10.1021/acssuschemeng.6b02391>.

(42) Shinagawa, T.; Garcia-Esparza, A. T.; Takanabe, K. Insight on Tafel Slopes from a Microkinetic Analysis of Aqueous Electrocatalysis for Energy Conversion. *Sci Rep* **2015**, *5* (1), 13801. <https://doi.org/10.1038/srep13801>.

(43) Cheng, W.; Zhao, X.; Su, H.; Tang, F.; Che, W.; Zhang, H.; Liu, Q. Lattice-Strained Metal–Organic-Framework Arrays for Bifunctional Oxygen Electrocatalysis. *Nat Energy* **2019**, *4* (2), 115–122. <https://doi.org/10.1038/s41560-018-0308-8>.

(44) Louie, M. W.; Bell, A. T. An Investigation of Thin-Film Ni–Fe Oxide Catalysts for the Electrochemical Evolution of Oxygen. *J. Am. Chem. Soc.* **2013**, *135* (33), 12329–12337. <https://doi.org/10.1021/ja405351s>.

(45) Fan, K.; Chen, H.; Ji, Y.; Huang, H.; Claesson, P. M.; Daniel, Q.; Philippe, B.; Rensmo, H.; Li, F.; Luo, Y.; Sun, L. Nickel–Vanadium Monolayer Double Hydroxide for Efficient Electrochemical Water Oxidation. *Nat Commun* **2016**, *7* (1), 11981. <https://doi.org/10.1038/ncomms11981>.

(46) Netskina, O. V.; Pochtar, A. A.; Komova, O. V.; Simagina, V. I. Solid-State NaBH₄ Composites as Hydrogen Generation Material: Effect of Thermal Treatment of a Catalyst Precursor on the Hydrogen Generation Rate. *Catalysts* **2020**, *10* (2), 201. <https://doi.org/10.3390/catal10020201>.

- (47) Inam, M.; Khan, R.; Park, D.; Lee, Y.-W.; Yeom, I. Removal of Sb(III) and Sb(V) by Ferric Chloride Coagulation: Implications of Fe Solubility. *Water* **2018**, *10* (4), 418. <https://doi.org/10.3390/w10040418>.
- (48) Zhang, X.; Sun, X.; Li, Y.; Hu, F.; Xu, Y.; Tian, J.; Zhang, H.; Liu, Q.; Su, H.; Wei, S. Reduced Interfacial Tension on Ultrathin NiCr-LDH Nanosheet Arrays for Efficient Electrocatalytic Water Oxidation. *J. Mater. Chem. A* **2021**, *9* (31), 16706–16712. <https://doi.org/10.1039/D1TA03863J>.
- (49) Ning, F.; Shao, M.; Xu, S.; Fu, Y.; Zhang, R.; Wei, M.; Evans, D. G.; Duan, X. TiO₂/Graphene/NiFe-Layered Double Hydroxide Nanorod Array Photoanodes for Efficient Photoelectrochemical Water Splitting. *Energy Environ. Sci.* **2016**, *9* (8), 2633–2643. <https://doi.org/10.1039/C6EE01092J>.
- (50) Zhai, P.; Xia, M.; Wu, Y.; Zhang, G.; Gao, J.; Zhang, B.; Cao, S.; Zhang, Y.; Li, Z.; Fan, Z.; Wang, C.; Zhang, X.; Miller, J. T.; Sun, L.; Hou, J. Engineering Single-Atomic Ruthenium Catalytic Sites on Defective Nickel-Iron Layered Double Hydroxide for Overall Water Splitting. *Nat Commun* **2021**, *12* (1), 4587. <https://doi.org/10.1038/s41467-021-24828-9>.
- (51) Zheng, W.; Liu, M.; Lee, L. Y. S. Best Practices in Using Foam-Type Electrodes for Electrocatalytic Performance Benchmark. *ACS Energy Lett.* **2020**, *5* (10), 3260–3264. <https://doi.org/10.1021/acseenergylett.0c01958>.
- (52) Tang, C.; Thomas, B.; Ramírez-Hernández, M.; Mikmeková, E. M.; Asefa, T. Metal-Functionalized Hydrogels as Efficient Oxygen Evolution Electrocatalysts. *ACS Appl. Mater. Interfaces* **2022**, *14* (18), 20919–20929. <https://doi.org/10.1021/acsaami.2c01667>.

CHAPTER 3

A One-Step Electropolymerization of a Dicyanobenzene-Carbazole-Imidazole Dye for Photoelectrodes, Heterogeneous Photocatalysts, and Sensing Applications^a

3.1 Introduction

Molecular dyes are utilized in applications that include photocatalysis of organic reactions, as components of organic light emitting devices (OLEDs), in photodynamic cancer therapy, in dye-sensitized solar cells, and in photoelectrodes for solar fuels.^{1,2} Ru-³⁻⁵ and Ir-^{6,7} polypyridyl and related complexes are common molecular dyes because they have strong absorptions in the visible range (metal-to-ligand-charge transfer). Moreover, they are modified readily to tune the wavelengths of absorption and emission as well as the redox properties of the excited state, and readily undergo intersystem crossing to form relatively long-lived triplet excited states. There are inherent disadvantages with these compounds that include cost, toxicity, and low stability under certain reaction conditions that limit their large-scale application.⁸⁻¹⁰ Organic dyes that are abundant and easy to prepare offer a promising alternative to precious-metal-based systems.¹¹⁻¹³ The most studied organic dyes include perylene derivatives,¹⁴ porphyrins,¹⁵ triphenylamines,¹⁶ and subporphyrins.¹⁷ The excitation of push-pull dyes involves intramolecular charge transfer.³⁻⁵ The push-pull dye 1,2,3,5-tetrakis(carbazol-9-yl)-4,6-dicyanobenzene (4CzIPN),¹⁸⁻²⁰ has been utilized successfully in OLEDs,²¹⁻²³ as photocatalysts for organic reactions,²⁴⁻²⁸ the hydrogen photoevolution reaction,²⁹ and CO₂ photoreduction.^{30,31}

Our group and others have attached organic dyes to electrode surfaces by electrografting them with diazonium precursors.³²⁻³⁴ The resulting carbon(dye)-oxygen(semiconductor) bond shows promising stability under alkaline

^a A version of this chapter has been submitted in *Polymers* by J. Liu, O. M. Perez, D. Lavergne, L. Rasu, E. Murphy, A. G. Rodriguez, and S. H. Bergens, accepted.

conditions that exceed those of the carboxylate or phosphonate bridges typically used to attach molecular chromophore semiconductors.^{32,35} We previously reported the electrografting of 4CzIPN onto indium-doped tin oxide (ITO) or carbon electrodes using diazonium chemistry, and the system was more stable and active under basic conditions than the representative Ru-polypyridine complexes.³⁶

Porous organic polymers (POPs) offer several potential advantages over monolayers or near-monolayers of organic dyes attached to electrode surfaces.³⁷ For example, POPs have a three-dimensional, large surface area (i.e. high specific surface area) structures that may coordinate to redox catalysts or act as sensor detection sites. Also, 3-dimensional POPs made of dye monomers would offer larger cross sections for light absorption than their corresponding monolayers. As well, many POPs are grown directly from simple organic monomers that do not require synthetic modifications, greatly simplifying the preparation, processing, and purification steps for large-scale preparations.^{28,38} Carbazole-containing molecules have been studied extensively as electropolymerization monomers, and a wide variety of polycarbazole electropolymers have been developed for purposes that include organic light-emitting diodes (OLEDs), capacitors, and memory devices.³⁹ To our knowledge, there is one example of a POP made from a dicyanobenzene-carbazole chromophore.²⁸ In that report, the parent dye, 4CzIPN, was copolymerized with formaldehyde dimethyl acetal (FDA) using a Fe(III)-redox oxidant to effect the polymerization. The resulting polymer was evaluated as a heterogeneous photocatalyst for the C(sp³)-P bond construction and selective oxidation of sulfides in water under mild conditions.²⁸

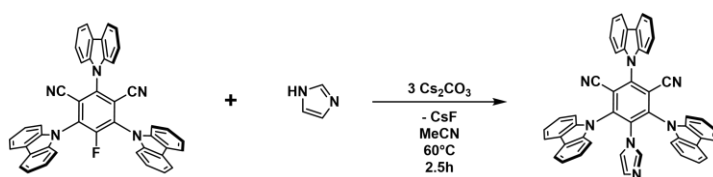
We now report the first direct electropolymerization of a dicyanobenzene-carbazole dye. Specifically, we prepared redox- and photoactive-POP films with controlled amount employing a new monomer, 1-imidazole-2,4,6-tri(carbazol-9-yl)-3,5-dicyanobenzene (**1**, 3CzImIPN). on ITO (**1**-ITO or **1**-ITO-NP) and carbon (**1**-CP) surfaces. Electrochemical polymerization is a simple, one-experimental-step process. We report the structure and activities of the POP films as photoelectrodes for electrooxidations, as heterogeneous photocatalysts

for photosynthetic olefin isomerizations, and as solid-state fluorescent metal ion sensors.

3.2 Results and Discussion

3.2.1 Preparation of Monomer

The imidazole-dye compound **1** was prepared by displacement of fluoride in the known precursor 1-fluoro-2,4,6-tri(carbazol-9-yl)-3,5-dicyanobenzene by cesium imidazolate in 95% yield (Scheme 3.1).



Scheme 3.1. Synthesis of the monomer 3CzImIPN (**1**)

Figure 3.1a shows the solid-state structure of **1**. As has been observed in related compounds,^{40,41} the dihedral angles between the benzene and carbazole rings range from 60 to 70° to relieve steric crowding. The dihedral angle between the benzene and imidazole ring is ~52°. Figure 3.1b shows the UV-Vis and steady-state photoluminescence spectra recorded in dichloromethane. As it is well-known for carbazole-dicyanobenzene dyes,⁴⁰ the excitation at ~421 nm results in a strong emission at ~543 nm. In keeping with the known photochemistry of this class of compounds, the excitation is a charge-transfer excitation from the highest occupied molecular orbital (HOMO), largely located on the carbazole rings, to the lowest unoccupied molecular orbital (LUMO), largely centered on the dicyanobenzene moiety. The S₁ and T₁ excited states are typically close in energy for this class of compounds, contributing to rapid intersystem crossing. Further, the T₁ excited state is sufficiently long-lived to promote photoredox and energy transfer organic photoreactions.^{42,43}

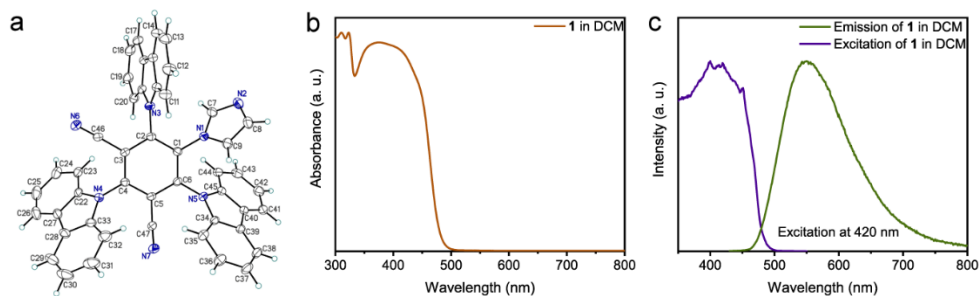


Figure 3.1. (a) The solid state structure of **1**, (b) absorbance UV-Vis spectrum of **1** (0.1 mM) in dichloromethane (DCM), and (c) the excitation and emission curve **1** (of 0.1 mM) in DCM

3.2.2 Electropolymerization of 3CzImIPN (**1**)

The electropolymerization of carbazole-containing molecules is well-known.^{44–46} Briefly, the carbazole ring undergoes one-electron oxidation to form the corresponding cationic radical, followed by carbon-carbon bond formation at the 3- or 6-positions. Proton loss then forms the neutral polymer. Figure 3.2a shows the cyclic voltammograms (CVs) for the 10-cycle potentiodynamic electropolymerization of **1** over ITO nanoparticles on ITO glass (the resulting polymer is designated as 10-**1**-ITO-NP) carried out in CH₂Cl₂ solution under air (0.1 M tetrabutyl ammonium hexafluorophosphate (TBAPF₆), 1.0 mM **1**, sweep rate 100 mV s⁻¹, 10 sweeps, sweep range from -0.55 to 1.45 vs Ferrocene/Ferrocene⁺ (Fc/Fc⁺, and unless stated otherwise, all potentials in this paper are relative to Fc/Fc⁺). The first positive-going sweep contains a strong anodic oxidation that commences at ~0.75 V vs Fc/Fc⁺ that corresponds to the one-electron oxidation of a carbazole ring (at nitrogen) to form the cationic radical that then undergoes the electropolymerization.

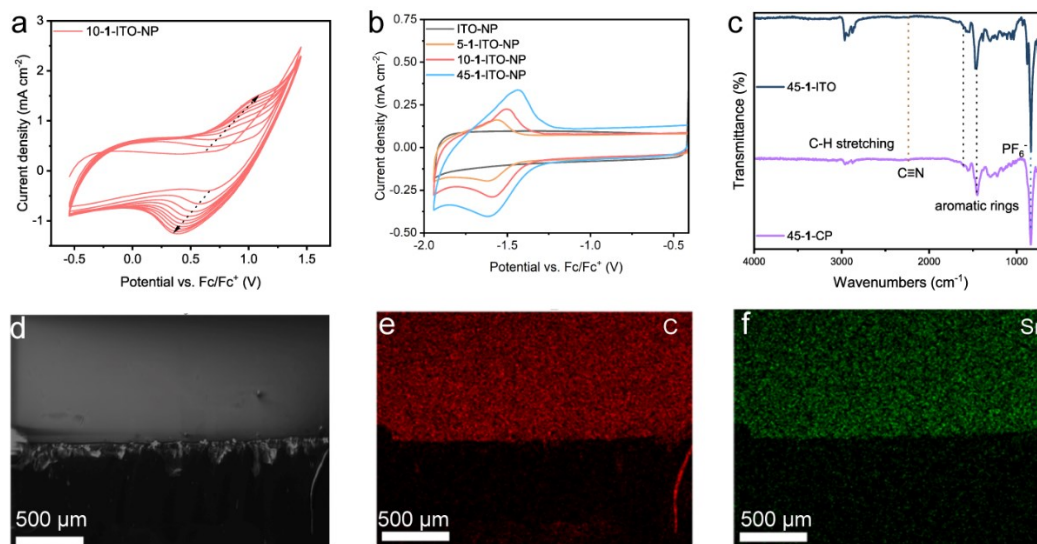
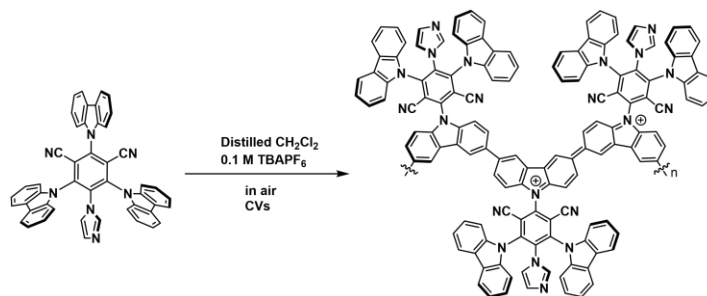


Figure 3.2. (a) CV curves of 10-1-ITO-NP in 0.1 M TBAPF₆ and 1mM of **1**. Sweep rate 100 mV s⁻¹, 10 sweeps, sweep range from -0.55 to 1.45 vs Fc/Fc⁺; (b) CV (sweep rate 10 mV s⁻¹; 5, 10, 45 sweeps; sweep range from -0.41 to -1.91 vs Fc/Fc⁺) curves of 5, 10, 45-1-ITO-NP compare with ITO-P in 0.1 M TBAPF₆ acetonitrile solution without monomer; (c) FT-IR of 45-1-ITO and 45-1-CP; (d) Tilted SEM of 45-1-ITO and corresponding (e) C and (f) Sn EDX mapping on ITO glass

The electropolymerization continues as the potential increases. The first negative going sweep contains a reductive wave at ~0.6 V that corresponds to the electroreduction of the POP deposited on the electrode during the first sweep. The second positive-going sweep contains a new peak at ~0.7 V that corresponds to the electrooxidation of the POP. Scheme 3.2 shows the proposed structure of the POP in both the reduced (neutral) and oxidized (polycationic) forms. The oxidative wave at ~0.7 V specifically arises from 1 e⁻ oxidation of the carbazole-nitrogen centers in the polymer to form the polycationic, conjugated polymer shown in Scheme 3.2. This behavior is typical of polycarbazoles, and the conjugated polycationic polymers are known to be electronically conductive. The reductive wave at ~0.6 V corresponds to the reduction of the positive nitrogen centers in the polycation to form the neutral polycarbazole structure shown in Scheme 3.2. These CVs are similar to the previous report by Li and his colleagues when obtaining polymers of carbazole derivatives.⁴⁷ Furthermore, under this high oxidation potential, a POP should be formed.⁴⁷ Again, this behavior is quite typical of polycarbazoles. The amount of the resulting polymer increases with each subsequent sweep, as shown by the increase in charge under the

redox peaks for the polymer and their potential shifts. Specifically, the cathodic peak shifts from ~ 0.65 V in the first negative going sweep to more reducing potentials, and the anodic peak shifts to more oxidizing potentials as the amount of polymer increases, slowing the rate of electron- and ion transfer through the POP. The resulting POP (10-1-ITO-NP) contains redox active groups in the backbone, photoactive groups in the polymerized monomer, and it is capable of reactions at the imide groups. The degree of crosslinking in the photoredox-POP is unknown.

Similar trends were observed during the 5- and 45-cycle electropolymerizations forming the 5-1-ITO-NP and 45-1-ITO-NP, respectively (Figure S3.1). Figure 3.2b shows the CV curves sweeping to negative potentials (sweep rate 10 mV s^{-1} ; 5, 10, 45 sweeps; sweep range from -0.41 to -1.91 vs Fc/Fc^+) for the isolated 5-, 10-, and 45-1-ITO-NP photoredox-POPs recorded in acetonitrile solution under N_2 (0.1 M TBAPF_6). The electrodes were removed from the electropolymerization solution and washed thoroughly with CH_2Cl_2 before the CVs were recorded. The photoredox-POPs all contain highly reversible reduction peaks at ~ -1.6 V vs Fc/Fc^+ .⁴⁸ The corresponding oxidation peak occurs ~ -1.5 V in the positive-going sweep. The CV of the free monomer **1** contains the corresponding 1 e^- reversible redox wave at ~ -1.5 V, and it corresponds to the 1 e^- reduction and oxidation of the dicyanobenzene ring.³⁶ The CVs of the electrodes (Figures 3.2b, S3.2) show that the dicyanobenzene rings in the photoredox-POPs undergo the same redox process. The charge under these peaks increased with increasing electropolymerization cycles, showing that the amount of the photoredox-POP is controlled by the number of potential sweeps during the polymerization. No oxidation or reduction peaks were detected in the control CVs of the bare ITO-NP electrode. Using the charges under the anodic peaks, the coverages are estimated to be 1.50×10^{-8} , 2.94×10^{-8} , and 4.74×10^{-8} moles cm^{-2} for 5-, 10-, and 45-1-ITO-NP, respectively.



Scheme 3.2. Proposed structure of the polymer in both the neutral and oxidized (doped) forms. This redox behavior is typical of polycarbazoles^{39,49,50}

The photoredox-POP can be grown over carbon paper and bare ITO slides as well (Figure S3.3). Figure 3.2c shows the reflectance Fourier Transform Infrared (FT-IR) spectra of both samples of the photoredox-POP films, recorded after thoroughly washing the films with CH_2Cl_2 . The peaks at about 1450 and 1610 cm^{-1} are attributed to the aromatic ring vibrations in **1**.²⁸ Figure S3.4 shows the weak signals at around 2237 cm^{-1} corresponding to the dicyano group on the central aromatic ring.⁴³ The strong peak at about 839 cm^{-1} is due to the hexafluorophosphate⁵¹ counterions to the cationic nitrogen centers formed during the oxidation of the carbazole groups in **1**. The C-H stretching appears around 3000 cm^{-1} .²⁸ The peak around 1554 cm^{-1} is a ring vibration band characteristic of the (partially) oxidized (doped) PCz.⁵² Similar observations are reported for polycarbazole prepared under the same conditions.³⁹

The morphology and elemental composition of 45-**1**-ITO were characterized by scanning electron microscopy (SEM) and energy dispersive X-ray spectroscopy (EDX) mapping. Figure 3.2d shows the edge-view SEM of a **1** film grown on an ITO slide. Figures 3.2e and 3.2f show the C and Sn elemental mappings, respectively. The SEM and EDX images all show a uniform distribution of the film and elements on the ITO surface.

Figure 3.3a shows the X-ray photoelectron spectroscopic (XPS) survey of both 45-**1**-ITO and 45-**1**-CP. C, N, O, P, F, and Cl are present on both photoredox-POP electrodes. The P and F signals probably arise from the presence of PF_6^- counter ions to the oxidized N centers present in the polymer (Scheme 3.2). The

Cl signal arises from residual CH₂Cl₂ solvent in the photoredox-POP. Figure 3.3b shows that deconvolution of the C 1s peak from 45-1-ITO revealed a prominent peak at 284.6 eV corresponding to sp² carbons. Two additional peaks at 285.6 eV and 286.7 eV were observed and attributed to C=N and C-N (or nitrile group), respectively.^{53,54} Figure 3.3c shows that deconvolution of the N 1s peak revealed three subpeaks at 399.4 eV, 400.6 eV, and 401.8 eV, which were assigned to nitrile nitrogen, pyrrolic nitrogen, and imidazole nitrogen or doped (oxidized) N sites, respectively. The deconvoluted XPS of elements on 45-1-CP is presented in Figure S3.5. Taken together, the CVs recorded during and after the electropolymerization, the SEM-EDX, the FTIR, and the XPS all confirm that the electropolymerization of the imidazole-dye **1** formed the photoredox-POP shown in Scheme 3.2.

3.2.3 Properties of The Polymer

Figure 3.3d shows the reflectance UV-Vis spectra of the photoredox-POPs on ITO-NP grown over 5, 10, and 45 cycles after subtracting the ITO-NP background. The lower limit is set to 400 nm to avoid the interference of ITO.⁵⁵ The observed increase in intensity as a function of the photoredox-POP amount may be attributed to the additional growth of the conjugated repeating units of the polymer, which could give rise to a band-like distribution of energy levels within the system.^{56,57} We assign this absorption to the well-known carbazole to dicyanobenzene intramolecular charge transfer.⁵⁸ The increase in wavelength of this absorption in the photoredox-POP compared with monomer **1** likely arises from either extended conjugation in the polymerized carbazole groups or, perhaps, some solid-state effect.^{59,60} The HOMO-LUMO gaps in the three photoredox-POPs were measured by applying Kubelka-Munk theory.⁶¹ Figure 3.3e shows that the HOMO and LUMO gaps were 2.53 eV (5 cycles), 2.49 eV (10 cycles), and 2.46 eV (45 cycles), respectively. As well, The energies of the LUMOs were estimated using the onset potential^{62,63} for the 1 e⁻ reduction of the dicyanobenzene rings in the photoredox-POPs. Figure S3.6 shows the CVs of the photoredox-POPs recorded with the photoredox-POP electrode immersed in CH₂Cl₂. The onsets for the reduction peaks were at -1.36 V, -1.33 V,

and -1.31 V vs. Fc/Fc^+ for the 5-, 10-, and 45-cycle photoredox-POPs, respectively. Figure 3.3f shows the results from using the reduction onset potentials measured by CV and adding the estimated difference in voltage based on the HOMO and LUMO band gap estimated from the Kubelka-Munk plots. We note that these results are tentative and rely on many factors.⁶⁴

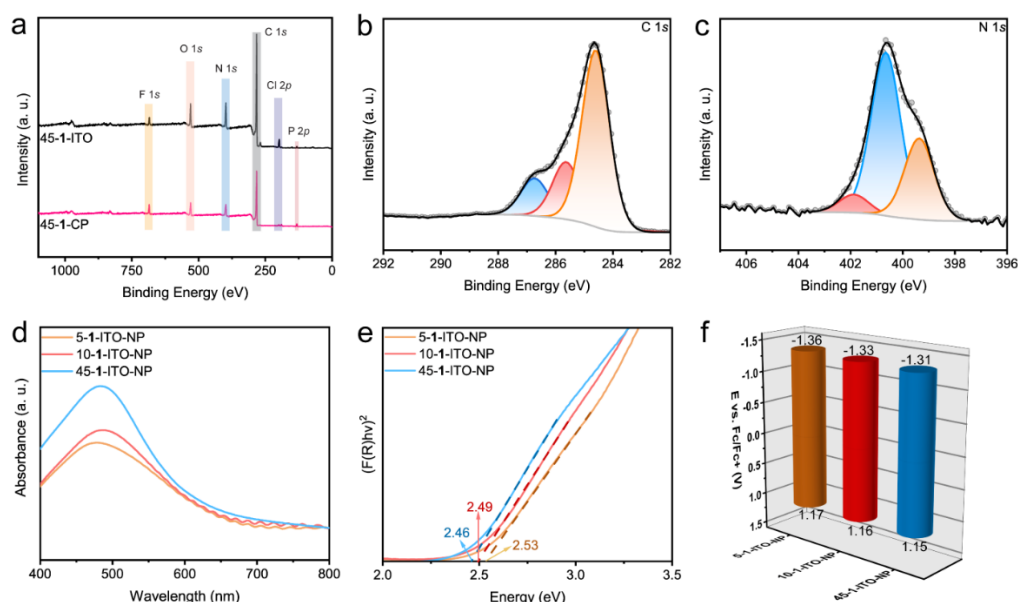


Figure 3.3. (a) XPS survey scans of 45-1-ITO and 45-1-CP and corresponding (b) C 1s and (c) N 1s of 45-1-ITO. (d) Reflectance UV-Vis of 5, 10, 45-1-ITO-NP by deduction of the ITO-NP substrates. (e) Optical band gap of 5, 10, 45-1-ITO-NP, and (f) LUMO and HOMO estimations

3.2.4 Utilization of Polymer Electrodes as Photoanodes

To investigate the photoactivity of the photoredox-POPs, we first measured the incident photon-to-current efficiencies (IPCEs) towards the photoelectrochemical oxidations of hydroquinone (HQ (0.02 M), 0.1 M NaClO_4 in H_2O , $\text{pH} = 7.0$) under neutral conditions and of triethylamine (TEA (0.5 M), 0.1 M NaClO_4 in H_2O , $\text{pH} = 12.6$) under alkaline conditions.

The experiments were performed in the visible light region (400–650 nm) using a 400 nm UV-light filter. Figure 3.4a shows the IPCEs for the oxidation of HQ by the **1** on ITO-NP deposited with 5, 10, and 45 sweeps under neutral conditions. Figure S3.7 shows that the photocurrent of a bare ITO-NP control electrode was negligible under neutral and alkaline conditions. The photoredox-POPs were

photoactive up to 550 nm (5-cycles), 560 nm (10 cycles), and 590 nm (45 cycles), showing that the activity extends further into the visible spectrum as the amount (i.e. the degree of conjugation) of the photoredox-POP increases. The maximum efficiency for all three photoredox-POPs occurs at 400 nm and decreases in the order of 15.9 % (10 cycles), 13.6 % (5 cycles), and 10.3 % (45 cycles). These efficiencies are high for organic dyes reported in the literature in the visible light region.^{65,66} It is likely that the efficiency of the 10-**1**-ITO-NP was higher than the 5-**1**-ITO-NP because of the higher amount of chromophores on the surface. The efficiency of the 45-**1**-ITO-NP was a little lower, likely because of increased resistance in the increasing amount photoredox-POP film. The 10-cycle electrode probably has the optimum balance between the number of chromophores per square centimeter versus electrical resistance among these three photoredox-POPs. The IPCE of the 45-cycle photoredox-POP, is, however, higher than the lower amount films at long wavelengths, likely due to increased conjugation in the longer polymer chain. Figure 3.4b shows that the most active 10-**1**-ITO-NP electrode is quite stable and active under AM 1.5G sunlight. Figure S3.8 shows that the other photoredox-POPs were appreciably stable under neutral or basic conditions. Figure 3.4c shows the IPCEs of the photoredox-POPs with Et₃N as an electron donor under basic conditions. In this case, the IPCE of the 45-**1**-ITO-NP electrode is slightly higher than the 10- or 5-**1**-ITO-NP electrodes at shorter- and longer- wavelengths. The maximum IPCE (~11%) and the steady-state currents were substantially higher than those we reported previously with 4CzIPN monolayer electrography to ITO nanoparticles using diazonium chemistry.³⁶ Further, chromophores attached by phosphonic- and carboxylic acid linkers tend to decompose quickly in the presence of base. The electropolymerization of the **1** occurs without derivatization, and it provides direct control over the amount of the resulting photoactive films.

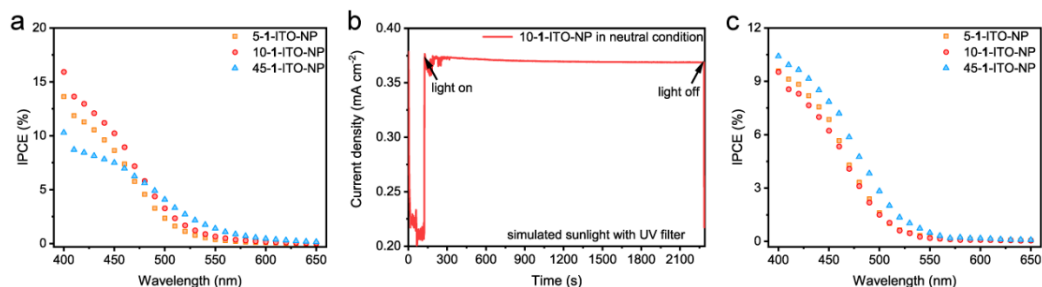
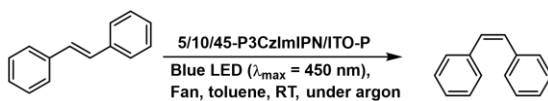


Figure 3.4. (a, c) IPCE tests of 5, 10, 45-1-ITO-NP in 0.1 M NaClO₄ dissolved in triple distilled water containing 0.02 M hydroquinone (pH = 7.0) (neutral condition) or 0.5 M Et₃N (pH = 12.6) (basic condition) at 0.25 V vs. SCE. (b) Stability test of 10-1-ITO-NP in the neutral conditions under simulated AM 1.5G sunlight with UV-light filter

3.2.5 Stilbene Isomerization

We next investigated the photosynthetic isomerization of *trans*- to *cis*-stilbene using the photoredox-POPs films as heterogeneous photocatalysts (Scheme 3.3). These isomerizations occur by the excited state of the dye undergoing Dexter energy transfer with stilbene. The resulting triplet state of stilbene collapses to either the *trans* or *cis* isomer. Dexter energy transfer between the excited dye occurs preferentially with *trans*-stilbene, eventually driving the reaction towards the *cis* isomer.^{40,67}



Scheme 3.3. Stilbene isomerization

We utilized 5-1-ITO-NP, 10-1-ITO-NP, 45-1-ITO-NP, and ITO-NP electrodes in toluene solvent under LED irradiation at 450 nm. The number of dye-catalyst on each photoredox-POP electrode was approximated by measuring the charge under the anodic peak for oxidation of the one-electron reduction of the dicyanobenzene groups in the CVs (Figure S3.9). The coverages by 5-1-ITO-NP, 10-1-ITO-NP, and 45-1-ITO-NP were estimated as 1.50×10^{-8} , 2.94×10^{-8} , and 4.74×10^{-8} moles cm⁻¹, respectively. These values are rough estimates because other charging/background currents could not be excluded wholly. Further, these values measure all the electrochemically accessible dye centers in the photoredox-POP, not just those on the

surface. Table 3.1 summarized the results utilizing an initial catalyst-to- stilbene ratio of 0.0060, 0.012, and 0.019, respectively. The 5-**1**-ITO-NP catalyst provided 5417.55 net turnovers from *trans*- to *cis*- after the first 16 h (32.49 % *cis*-), and 10365.60 after 48 h (67.57% *cis*-). For comparison, the 10-**1**-ITO-NP provided 1812.69 (21.34% *cis*-) after 16 h and 3993.05 (52.70 % *cis*-) after 48 h. The ratios of turnover numbers are lower than the ratios of % *cis*-, suggesting that while longer polymers are formed with more cycles, not all of the active sites in the longer photoredox-POPs are accessible to the reaction. The turnover numbers and % *cis*- obtained with the 45-**1**-ITO-NP (949.42 after 16 h (18.01 % *cis*-), 2194.55 after 48 h (46.67 % *cis*-) are consistent with this interpretation. The control ITO-NP electrode was essentially inactive (TON close to 0 in 48 h). We also note that the higher activity obtained with 5-**1**-ITO-NP is also consistent with the higher IPCE achieved with this electrode under neutral conditions, meaning this photoredox-POP demonstrates more effective light utilization. We next determined the photo-steady state by running a stilbene isomerization over 5-**1**-ITO-NP for a longer time. After 88 h, the conversion increased from 67.57% at 48 h to 83.33%. This photo steady state was similar to the one we reported previously with a different carbazole-dicyanobenzen catalyst,³⁶ and it results from the rate of the forward (*cis*-stilbene) and backward (*trans*-stilbene) reactions being the same. Reuse of the 5-**1**-ITO-NP photocatalyst resulted in a drop in efficiency by 74 % at 48 h.

The internal quantum yield on a solid electrode is extremely difficult to measure accurately because other factors, such as light scattering and reflections cannot be determined precisely, and vary from sample to sample.⁶⁸ We determined the apparent quantum efficiency, based on the number of photons impinging on the solid electrode, as detailed in the SI. To our delight, the net external quantum yields after 16 h for 5-**1**-ITO-NP, 10-**1**-ITO-NP, and 45-**1**-ITO-NP at 450 nm were 13.73 %, 9.02%, and 7.61%, respectively. These values do not include any reverse reaction that occurred during the isomerization, and so they are lower limits to the actual values. We note that these lower limits are roughly consistent with the IPCE values

indicating the inherent high performance for light utilization. These results demonstrate that the photoredox-POPs can be used as photocatalysts.

Table 3.1. Photosynthetic Isomerization of trans- to cis-Stilbene by different ITO-NP Electrodes.

Catalyst ¹	Mol % of catalyst	[stilbene]/%conv (16 h)	TON (16 h)	TOF/h (16 h)	%conv (48 h)	TON (48 h)	TOF/h (48 h)	%conv (88 h)
5-1-ITO-NP	0.0060	0.1	32.49	5417.55	338.60	67.57	10365.60	215.95
10-1-ITO-NP	0.012	0.1	21.34	1812.69	113.29	52.70	3993.05	83.19
45-1-ITO-NP	0.019	0.1	18.01	949.42	59.34	46.67	2194.55	45.72
ITO-NP	0	0.1	~0	~0	~0	~0	~0	~0
5-1-ITO-NP ²	0.0060	0.1						83.33
5-1-ITO-NP ³		0.1	4	666.98	41.69	17.63	2704.537	56.34

¹In the absence of any explicit notation to the contrary, the isomerization reactions were conducted using trans-stilbene as the substrate, toluene as the solvent, and an argon atmosphere at ambient temperature, with various cycles of photoredox-POPs serving as the catalyst. The % conversion, TON (with TONs being calculated after subtracting the amount of substrate removed in the preceding aliquots), and TOFs were determined through ¹H NMR spectroscopy. ²New run of a new 5-1-ITO-P electrode. ³Second run of the same 5-1-ITO-P electrode reused

3.2.6 Photoluminance Li Ion Response.

Figure 3.5a shows the reflectance UV-Vis spectra of 45-1-CP from 400 nm to 800 nm. A thick polymer coating (45 cycles, -0.55-2.45 V vs.Fc/Fc⁺) was utilized to maximize the signal from the polymer. The background absorbance of CP was subtracted, but there still were significant absorbances from the support below ~475 nm. There was a broad peak near 510 nm that was similar to that in the spectrum of the photoredox-POPs over ITO-NP (Figure 3.3d). Figure 3.5b shows the steady-state photoluminescence spectrum. There is a broad emission peak at ~650 nm resulting from excitation at 420 nm. The corresponding emission peak for the monomer in CH₂Cl₂ occurs at ~550 nm. The emission from polymerized **1** on CP is broader and shifted to a longer wavelength than the monomer (Figure 3.1). This shift to lower energies almost certainly results from factors that include conjugation in the polymer, solid-state interactions between the polymer and the support or other polymer chains, interactions between monomers in the polymers, and solid-state

packing effects on the molecular conformations. Detailed studies are required to understand this complex system fully. Regardless, the photoemission spectrum, the ICPE, and the stilbene isomerization results show that the photochemistry of the monomer is retained largely in the polymer, albeit with shifting to longer wavelengths and broadening. We also note the polycarbazole polymer has UV-Vis absorptions as well.

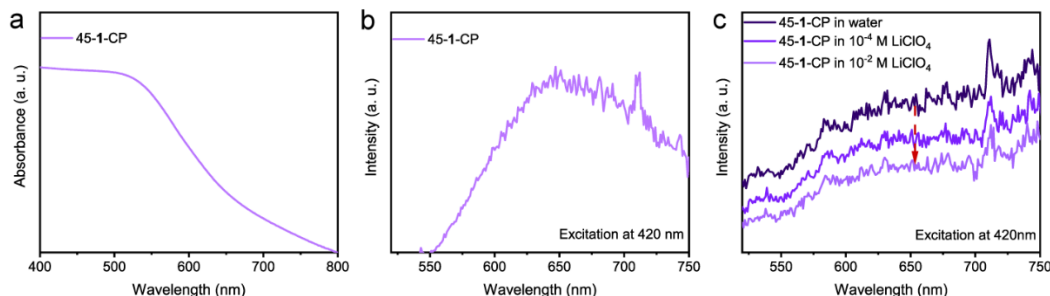


Figure 3.5. (a) Reflectance UV-Vis spectra and (b) emission light excited at 420 nm of 45-1-CP. (c) The prototype example of Li-ion detection of 45-1-CP

Considering the stability of the polymer in water and the widespread utilization of imidazole groups in sensors,^{52,69} we exposed the 45-1-CP to different concentrations of lithium in water to determine if the presence of Li affects the photoluminescence spectrum. Specifically, we soaked the 45-1-CP electrode in triple distilled water (TDW) for 2 h and measured the photoluminescence spectrum. We then exposed the electrode to 10⁻⁴ M LiClO₄ and 10⁻² M LiClO₄ aqueous solutions for 2 h. As shown in Figure 3.5c, the photoemission was partially quenched by the presence of lithium, with greater quenching at higher [Li⁺]. The quenching of the photoluminescence likely originated from the coordination of Li⁺ to the imidazole groups in the photoredox-POP,^{70,71} suggesting that they have applications as a solid-state ion sensor.

3.2.7 Understanding The Polymer

Preliminary TD-DFT calculations (Gaussian 16/B3LYP/6-31+G(d,p)) were carried out on **1** in the absence of solvent to provide insight into the photochemical processes reported in this paper. The calculated energy of the HOMO is -6.12 eV, and the

energy of the LUMO is -3.08 eV, giving a band gap of 3.04 eV. As shown in Figures 3.6a, b, the HOMO is localized on the carbazole groups, with the carbazole group between the cyano groups providing the highest contribution (LUMO, HOMO, and UV-Vis are drawn combined with Multiwfn⁷² or VMD⁷³). The LUMO is localized largely on the dicyanobenzene ring, and roughly can be viewed as a π^* aromatic orbital. As illustrated in Figure 3.6c, the calculated UV-Vis in the visible light region (>400 nm) is mainly a composite of 6 excitations. In Figure 3.6d, the vertical excitation energy from S_0 to S_1^* is 2.38 eV, and the fluorescence energy from S_1 to S_0^* is 1.84 eV (corresponding to 521 and 673.8 nm, respectively). The calculated difference in energy between S_1 and T_1 is small, ($\Delta E_{ST}^* \sim 0.18$ eV), and this small difference in energy is likely one reason why intersystem crossing is relatively fast for this type of molecule.⁷⁴

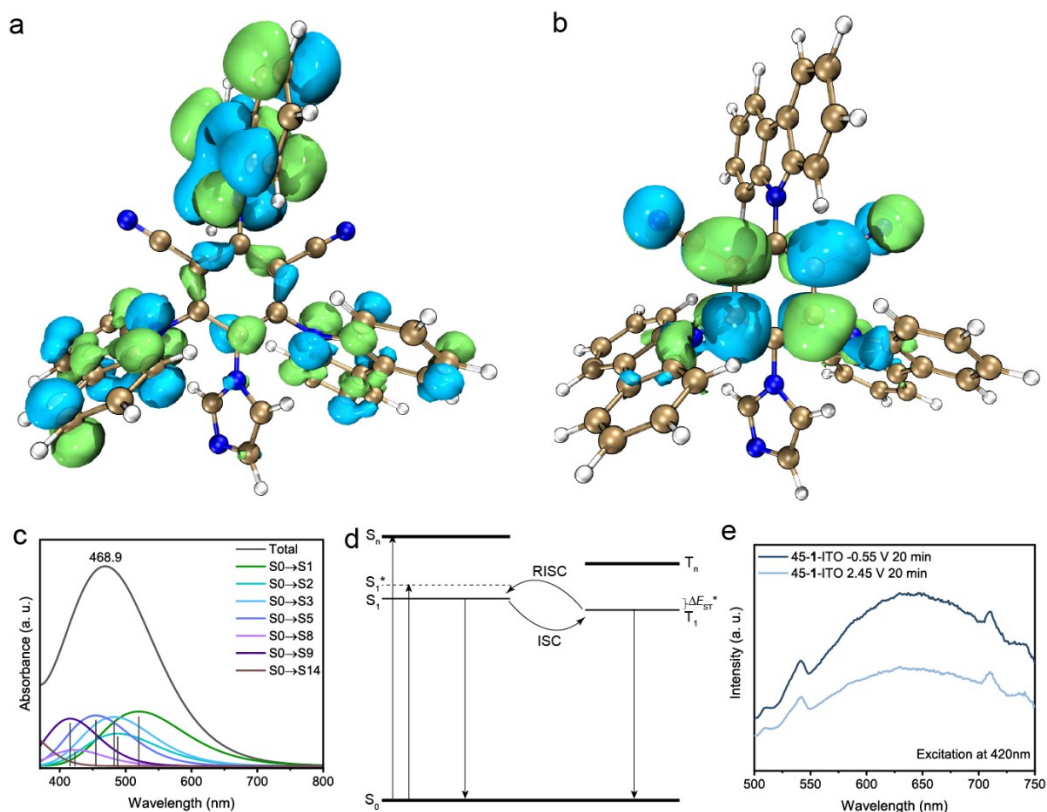


Figure 3.6. TD-DFT-calculated (a) HOMO and (b) LUMO wave functions of the geometry optimized structures; (c) calculated UV-Vis spectra; (d) a Jablonski diagram for **1**; (e) photoluminescence intensity with applied potential

Figure 3.6d shows the Jablonski diagram for **1**, which illustrates the potential photophysical pathways for **1**. These calculations support the results for similar compounds reported in the literature.⁴³ During photoexcitation, an electron is promoted from S_0 to a higher-energy singlet state. The electron then undergoes internal conversion (IC) to reach the lowest-energy singlet excited state S_1 . Two outcomes are possible: either the electron emits fluorescent light and returns to the ground state S_0 , or it undergoes intersystem crossing (ISC) to the lowest triplet excited state T_1 . The electron in state T_1 can either emit long-lived phosphorescent light and return to ground state S_0 , or it can undergo reverse intersystem crossing (RISC) and return to state S_1 . These calculations illustrate the photochemical processes that occur in **1** and in the photoredox-POPs.

A prediction made by combining the results from the calculations with the structure and redox functions of the polycarbazole (Scheme 3.2) is that there will be a partial depletion of the occupied molecular orbitals at higher potentials as the carbazole groups are electro-oxidized. Depletion of these orbitals will also decrease the photoluminescence. Indeed, Figure 3.6e shows that the photoluminescence intensity of the 45-**1**-ITO photoredox-POP is decreased significantly after oxidation at 2.45 V vs. Fc/Fc^+ for 20 min relative to the same photoredox-POP held at -0.55 V vs. Fc/Fc^+ for 20 min. We tend to explain this phenomenon by calculations. The occupied molecular orbitals in the visible range of our studied system are predominantly localized in the carbazole groups, whereas the excited state orbitals primarily reside in the dicyanobenzene ring. The effect of oxidation of the carbazole groups on the light emission of the system can be attributed potentially to the alteration of the electron transfer pathway. Specifically, upon oxidation of the carbazole groups, the excited electrons might be diverted from their original path to the center dicyanobenzene ring and instead trapped in the holes of the oxidized carbazole groups. These results show that the photoluminescence behavior of these types of photoredox POPs can to some extent be modulated by the applied potential.

3.3 Conclusions

A one-step preparation of the imidazole-functionalized, polycarbazole dicyanobenzene dye **1** is reported. The photophysical behavior of **1** dye is typical of this class of organic chromophore.¹⁰ The dye is electropolymerized readily in air at the carbazole rings to produce photoredox POPs on ITO glass, nanoparticles, and carbon paper. The resulting deposits are active photoanodes, photocatalysts for olefin isomerization reactions, and their photoluminescence behavior responds to lithium ions in solution, presumably through the coordinating imidazole groups. Studies are underway in our laboratories to fully investigate the photochemical properties and utility of these new photoredox POP deposits.

3.4 Experimental Section

3.4.1 Materials

The materials and chemicals were used without any further treatment, unless mentioned otherwise. The following compounds were purchased from Sigma Aldrich: hydroxypropyl cellulose (powder, 20 mesh particle size, Mw ~100,000), tetrabutylammonium hexafluorophosphate (TBAPF₆; for electrochemical analysis, ≥99.0%), hydroquinone (ReagentPlus, ≥99.5%), triethylamine, distilled (≥99.0%), acetonitrile, distilled (for HPLC, gradient grade, ≥99.9%), dichloromethane, distilled (DCM; ACS reagent, ≥99.5%), carbazole (≥95%), NaH (60% dispersion in mineral oil), NaCl, NaClO₄ (ACS reagent, ≥98.0%), calcium hydride (reagent grade, 95%), and trans-stilbene (96%). ITO nanoparticles were purchased from Fisher Scientific (17-28 nm APS Powder). Anhydrous ethanol was purchased from Greenfield Global. Tetrafluoroisophthalonitrile (>98.0%) was purchased from TCI chemicals. The solvents tetrahydrofuran (Na/benzophenone), toluene (CaH₂), DCM (CaH₂), and acetonitrile (CaH₂) were dried by distillation from the appropriate drying agent under N₂. Triple distilled water was used for all the glassware cleaning and preparation of aqueous solutions for electrochemistry experiments.

3.4.2 Fabrication of ITO Nanoparticles Coated ITO Glass Electrode (ITO-NP)

Indium tin oxide coated glass slides (ITO glass, Kaivo, surface resistivity $<7 \Omega/\text{sq}$) were cut into 1 cm x 2.5 cm, sonicated in ethanol, triple distilled water, and acetone for 30 min each, followed by drying in an oven at 60 °C. ITO nanoparticle paste was prepared following procedures: 1.32 g of hydroxypropyl cellulose (HPC) was placed in a vial with 15 mL of anhydrous ethanol and stirred overnight to obtain the HPC suspension. Next, 1.5 g of ITO nanoparticles were dispersed in 6.25 mL of anhydrous ethanol and sonicated for 40 min. After sonication, 3.75 mL of the HPC suspension was added to the ITO nanoparticle suspension, stirred overnight, followed by sonicating for 1 h before use to prepare the ITO paste. Then, the ITO paste was doctor-bladed on an ITO surface with four layers of scotch tape as a spacer. After drying in air, the prepared electrodes were heated from room temperature to 500 °C over 1 h and then kept at 500 °C for another 1 h in a furnace. The ITO-NP electrodes were collected after the furnace cooled down to room temperature.

3.4.3 Preparation of Poly 3CzImIPN (1) on ITO-NP, ITO Glass (ITO), or Carbon Fiber Paper (CP)

The ITO glass was cut into 1 cm x 2.5 cm small pieces, then sonicated in triple distilled water, ethanol, and acetone for 30 min, respectively. CP also was cut into 1 cm x 2.5 cm and sonicated in triple distilled water for 30 min. After drying in an oven at 60 °C for 30 min, the ITO or CF was ready to use for the next step. Electropolymerization was carried out in distilled dichloromethane (DCM) solution, with 1 mM of **1** and 0.1 M of TBAPF₆. CVs for ITO-NP electrodes were recorded by sweeping between 0 to 2 V vs. Ag wire (−0.55 to 1.45 V vs. Fc/Fc⁺, Fc = Ferrocene) at a scan rate of 100 mV s^{−1} for 5, 10, or 45 cycles (5/10/45-1-ITO-NP), with Ag wire as the reference electrode and platinum gauze as the counter electrode. CVs for ITO or CP electrodes were recorded by sweeping between 0 to 3 V vs. Ag wire (−0.55 to 2.45 V vs. Fc/Fc⁺, Fc = Ferrocene) at a scan rate of 100 mV s^{−1} for 45 cycles (45-1-ITO or 45-1-CP), with Ag wire as the reference electrode and platinum gauze as the counter electrode. Ferrocene was added after the experiment as an internal

reference. After polymerization, the electrodes were washed with DCM and dried in an oven at 60 °C for 45 min.

3.4.4 Stilbene Isomerization

In this experiment, *E*-Stilbene (45.1 mg, 0.25 mmol) was introduced into a custom-made test tube with a magnetic stir bar and polymer **1** on an ITO-NP electrode. Subsequently, the test tube was inserted into a side arm flask, which was connected to a Schlenk line, evacuated, and re-filled with argon for three cycles. Then, freshly distilled toluene (2.5 mL) was injected into the test tube using a gas-tight syringe under an argon atmosphere. Upon adding toluene, the resulting solution was stirred at room temperature under blue LED radiation with a fan. To monitor the reaction, 50 μ L of solutions were drawn from the vials, and ^1H NMR spectra were recorded using CDCl_3 as a solvent. 1,3,5-Trimethoxy benzene was added as an internal standard at the end of the reaction.

3.4.5 Photoluminescence Response to Lithium Ions

First, the 45-1-CP electrode was soaked in distilled water for 2 h. Subsequently, the electrode was taken out from the water without drying, and its photoluminescence spectrum was measured immediately (Figure 3.5c). Afterwards, the electrode was exposed to aqueous solutions containing 10^{-4} M and 10^{-2} M LiClO_4 , respectively for 120 min, and the photoluminescence spectrum was measured immediately, as described above (Figure 3.5c).

3.4.6 Characterization

The scanning electron microscope (SEM) with energy-dispersive X-ray spectroscopy (EDX) mapping measurements were done by a Zeiss EVO MA10 Scanning Electron Microscope with EDX. Typically, the system vacuum of SEM was lower than 2×10^{-5} torr when acquiring images. The X-ray photoelectron spectroscopy (XPS) measurements were done using a Kratos Axis Ultra. A monochromatized Al $K\alpha$ source ($h\nu = 1486.71$ eV) was used, while the pressure in the sample analytical chamber was maintained below 5×10^{-10} torr. Survey scans covered the binding

energies of 1100–0 eV with 160 eV analyzer pass energy. For the deconvolution process, the spectra were calibrated to position the C–C binding energy at 284.6 eV in order to correct the charge effect. Solid-state UV-Vis spectra were collected using the Cary 5000 UV-Vis spectrometer in reflection mode. Solid-state photo luminance was acquired by a Horiba-PTI QM-8075-11 Fluorescence System with a solid stand. FTIR was measured by Thermo Nicolet 8700 FTIR spectrometer and Continuum FTIR microscope on ATR. The ^1H NMR spectra were acquired using 400 MHz, 500 MHz, or 600 MHz Varian Inova, or Varian DD2 M2 400 MHz NMR spectrometers. The ^{13}C NMR spectra were acquired using a Varian VNMRS 500 MHz NMR spectrometer. The chemical shifts are reported in parts per million relative to TMS with the solvent as the internal standard. Abbreviations used in reporting of NMR data are s (singlet), d (doublet), t (triplet), q (quartet), dd (doublet of doublet), dq (doublet of quartet), and m (multiplet). HRMS spectra were acquired using either electrospray ionization in an Agilent 6220 oaTOF mass spectrometer or electron ionization on a Kratos Analytical MS50G double-focusing sector mass spectrometer. The experiment involving simulated sunlight was carried out using a 300 W Xenon light source solar simulator equipped with an AM 1.5G optical filter.

3.5 References

- (1) Chen, J.-R.; Hu, X.-Q.; Lu, L.-Q.; Xiao, W.-J. Visible Light Photoredox-Controlled Reactions of N-Radicals and Radical Ions. *Chem. Soc. Rev.* **2016**, *45* (8), 2044–2056. <https://doi.org/10.1039/C5CS00655D>.
- (2) Wang, Z.; Liu, Q.; Liu, R.; Ji, Z.; Li, Y.; Zhao, X.; Wei, W. Visible-Light-Initiated 4CzIPN Catalyzed Multi-Component Tandem Reactions to Assemble Sulfonated Quinoxalin-2(1H)-Ones. *Chin. Chem. Lett.* **2022**, *33* (3), 1479–1482. <https://doi.org/10.1016/j.ccl.2021.08.036>.
- (3) Mishra, A.; Fischer, M. K. R.; Bäuerle, P. Metal-Free Organic Dyes for Dye-Sensitized Solar Cells: From Structure: Property Relationships to Design Rules. *Angew. Chem. Int. Ed.* **2009**, *48* (14), 2474–2499. <https://doi.org/10.1002/anie.200804709>.
- (4) Hagfeldt, A.; Boschloo, G.; Sun, L.; Kloo, L.; Pettersson, H. Dye-Sensitized Solar Cells. *Chem. Rev.* **2010**, *110* (11), 6595–6663. <https://doi.org/10.1021/cr900356p>.
- (5) Giribabu, L.; Kanaparthi, R. K.; Velkannan, V. Molecular Engineering of Sensitizers for Dye-Sensitized Solar Cell Applications. *Chem. Rec.* **2012**, *12* (3), 306–328. <https://doi.org/10.1002/tcr.201100044>.
- (6) Wang, Y.; Zhao, X.; Zhao, Y.; Yang, T.; Liu, X.; Xie, J.; Li, G.; Zhu, D.; Tan, H.; Su, Z. Photosensitizers Based on Ir(III) Complexes for Highly Efficient Photocatalytic Hydrogen Generation. *Dyes Pigments* **2019**, *170*, 107547. <https://doi.org/10.1016/j.dyepig.2019.107547>.

- (7) Shon, J.-H.; Teets, T. S. Photocatalysis with Transition Metal Based Photosensitizers. *Comments Inorg. Chem.* **2020**, *40* (2), 53–85. <https://doi.org/10.1080/02603594.2019.1694517>.
- (8) Romero, N. A.; Nicewicz, D. A. Organic Photoredox Catalysis. *Chem. Rev.* **2016**, *116* (17), 10075–10166. <https://doi.org/10.1021/acs.chemrev.6b00057>.
- (9) Hossain, A.; Bhattacharyya, A.; Reiser, O. Copper's Rapid Ascent in Visible-Light Photoredox Catalysis. *Science* **2019**, *364* (6439), eaav9713. <https://doi.org/10.1126/science.aav9713>.
- (10) Liu, Y.; Chen, X.-L.; Li, X.-Y.; Zhu, S.-S.; Li, S.-J.; Song, Y.; Qu, L.-B.; Yu, B. 4CzIPN-^t Bu-Catalyzed Proton-Coupled Electron Transfer for Photosynthesis of Phosphorylated *N*-Heteroaromatics. *J. Am. Chem. Soc.* **2021**, *143* (2), 964–972. <https://doi.org/10.1021/jacs.0c11138>.
- (11) Joseph, M.; Haridas, S. Recent Progresses in Porphyrin Assisted Hydrogen Evolution. *Int. J. Hydrog. Energy* **2020**, *45* (21), 11954–11975. <https://doi.org/10.1016/j.ijhydene.2020.02.103>.
- (12) Fukuzumi, S.; Ohkubo, K. Organic Synthetic Transformations Using Organic Dyes as Photoredox Catalysts. *Org. Biomol. Chem.* **2014**, *12* (32), 6059–6071. <https://doi.org/10.1039/C4OB00843J>.
- (13) Decavoli, C.; Boldrini, C. L.; Manfredi, N.; Abbotto, A. Molecular Organic Sensitizers for Photoelectrochemical Water Splitting. *Eur. J. Inorg. Chem.* **2020**, *2020* (11–12), 978–999. <https://doi.org/10.1002/ejic.202000026>.
- (14) Ronconi, F.; Syrgiannis, Z.; Bonasera, A.; Prato, M.; Argazzi, R.; Caramori, S.; Cristino, V.; Bignozzi, C. A. Modification of Nanocrystalline WO₃ with a Dicationic Perylene Bisimide: Applications to Molecular Level Solar Water Splitting. *J. Am. Chem. Soc.* **2015**, *137* (14), 4630–4633. <https://doi.org/10.1021/jacs.5b01519>.
- (15) Yamamoto, M.; Wang, L.; Li, F.; Fukushima, T.; Tanaka, K.; Sun, L.; Imahori, H. Visible Light-Driven Water Oxidation Using a Covalently-Linked Molecular Catalyst–Sensitizer Dyad Assembled on a TiO₂ Electrode. *Chem. Sci.* **2016**, *7* (2), 1430–1439. <https://doi.org/10.1039/C5SC03669K>.
- (16) Windle, C. D.; Kumagai, H.; Higashi, M.; Brisse, R.; Bold, S.; Jusselme, B.; Chavarot-Kerlidou, M.; Maeda, K.; Abe, R.; Ishitani, O.; Artero, V. Earth-Abundant Molecular Z-Scheme Photoelectrochemical Cell for Overall Water-Splitting. *J. Am. Chem. Soc.* **2019**, *141* (24), 9593–9602. <https://doi.org/10.1021/jacs.9b02521>.
- (17) Shan, B.; Brennaman, M. K.; Troian-Gautier, L.; Liu, Y.; Nayak, A.; Klug, C. M.; Li, T.-T.; Bullock, R. M.; Meyer, T. J. A Silicon-Based Heterojunction Integrated with a Molecular Excited State in a Water-Splitting Tandem Cell. *J. Am. Chem. Soc.* **2019**, *141* (26), 10390–10398. <https://doi.org/10.1021/jacs.9b04238>.
- (18) Uoyama, H.; Goushi, K.; Shizu, K.; Nomura, H.; Adachi, C. Highly Efficient Organic Light-Emitting Diodes from Delayed Fluorescence. *Nature* **2012**, *492* (7428), 234–238. <https://doi.org/10.1038/nature11687>.
- (19) Forchetta, M.; Valentini, F.; Conte, V.; Galloni, P.; Sabuzi, F. Photocatalyzed Oxygenation Reactions with Organic Dyes: State of the Art and Future Perspectives. *Catalysts* **2023**, *13* (2), 220. <https://doi.org/10.3390/catal13020220>.
- (20) Yang, X.; Guo, Y.; Tong, H.; Liu, R.; Zhou, R. Metal-Free Acceptorless Dehydrogenative Cross-Coupling of Aldehydes/Alcohols with Alcohols. *Green Chem.* **2023**, *25* (4), 1672–1678. <https://doi.org/10.1039/D2GC04594J>.
- (21) Cardeynaels, T.; Etherington, M. K.; Paredis, S.; Batsanov, A. S.; Deckers, J.; Stavrou, K.; Vanderzande, D.; Monkman, A. P.; Champagne, B.; Maes, W. Dominant Dimer Emission Provides Colour Stability for Red Thermally Activated Delayed Fluorescence Emitter. *J. Mater. Chem. C* **2022**, *10* (15), 5840–5848. <https://doi.org/10.1039/D1TC04913E>.

- (22) Wu, S.; Kumar Gupta, A.; Yoshida, K.; Gong, J.; Hall, D.; Cordes, D. B.; Slawin, A. M. Z.; Samuel, I. D. W.; Zysman - Colman, E. Highly Efficient Green and Red Narrowband Emissive Organic Light - Emitting Diodes Employing Multi - Resonant Thermally Activated Delayed Fluorescence Emitters**. *Angew. Chem. Int. Ed.* **2022**, *61* (52). <https://doi.org/10.1002/anie.202213697>.
- (23) Li, F.; Gillett, A. J.; Gu, Q.; Ding, J.; Chen, Z.; Hele, T. J. H.; Myers, W. K.; Friend, R. H.; Evans, E. W. Singlet and Triplet to Doublet Energy Transfer: Improving Organic Light-Emitting Diodes with Radicals. *Nat. Commun.* **2022**, *13* (1), 2744. <https://doi.org/10.1038/s41467-022-29759-7>.
- (24) Badir, S. O.; Dumoulin, A.; Matsui, J. K.; Molander, G. A. Synthesis of Reversed C - Acyl Glycosides through Ni/Photoredox Dual Catalysis. *Angew. Chem. Int. Ed.* **2018**, *57* (22), 6610–6613. <https://doi.org/10.1002/anie.201800701>.
- (25) Shu, C.; Mega, R. S.; Andreassen, B. J.; Noble, A.; Aggarwal, V. K. Synthesis of Functionalized Cyclopropanes from Carboxylic Acids by a Radical Addition–Polar Cyclization Cascade. *Angew. Chem. Int. Ed.* **2018**, *57* (47), 15430–15434. <https://doi.org/10.1002/anie.201808598>.
- (26) Xu, J.; Cao, J.; Wu, X.; Wang, H.; Yang, X.; Tang, X.; Toh, R. W.; Zhou, R.; Yeow, E. K. L.; Wu, J. Unveiling Extreme Photoreduction Potentials of Donor–Acceptor Cyanoarenes to Access Aryl Radicals from Aryl Chlorides. *J. Am. Chem. Soc.* **2021**, *143* (33), 13266–13273. <https://doi.org/10.1021/jacs.1c05994>.
- (27) Liang, D.; Chen, J.-R.; Tan, L.-P.; He, Z.-W.; Xiao, W.-J. Catalytic Asymmetric Construction of Axially and Centrally Chiral Heterobiaryls by Minisci Reaction. *J. Am. Chem. Soc.* **2022**, *144* (13), 6040–6049. <https://doi.org/10.1021/jacs.2c01116>.
- (28) Zhu, S.-S.; Zuo, L.; Liu, Y.; Yu, B. 1,2,3,5-Tetrakis(Carbazol-9-Yl)-4,6-Dicyanobenzene (4CzIPN)-Based Porous Organic Polymers for Visible-Light-Driven Organic Transformations in Water under Aerobic Oxidation. *Green Chem.* **2022**, *24* (22), 8725–8732. <https://doi.org/10.1039/D2GC02950B>.
- (29) Yu, Z.-J.; Lou, W.-Y.; Junge, H.; Pöpcke, A.; Chen, H.; Xia, L.-M.; Xu, B.; Wang, M.-M.; Wang, X.-J.; Wu, Q.-A.; Lou, B.-Y.; Lochbrunner, S.; Beller, M.; Luo, S.-P. Thermally Activated Delayed Fluorescence (TADF) Dyes as Efficient Organic Photosensitizers for Photocatalytic Water Reduction. *Catal. Commun.* **2019**, *119*, 11–15. <https://doi.org/10.1016/j.catcom.2018.09.018>.
- (30) Fang, Y.; Liu, T.; Chen, L.; Chao, D. Exploiting Consecutive Photoinduced Electron Transfer (ConPET) in CO₂ Photoreduction. *Chem. Commun.* **2022**, *58* (57), 7972–7975. <https://doi.org/10.1039/D2CC02356C>.
- (31) Franceschi, P.; Rossin, E.; Goti, G.; Scopano, A.; Vega-Peñaloza, A.; Natali, M.; Singh, D.; Sartorel, A.; Dell’Amico, L. A Proton-Coupled Electron Transfer Strategy to the Redox-Neutral Photocatalytic CO₂ Fixation. *J. Org. Chem.* **2023**, *acs.joc.2c02952*. <https://doi.org/10.1021/acs.joc.2c02952>.
- (32) Wang, C.; Amiri, M.; Endean, R. T.; Martinez Perez, O.; Varley, S.; Rennie, B.; Rasu, L.; Bergens, S. H. Modular Construction of Photoanodes with Covalently Bonded Ru- and Ir-Polypyridyl Visible Light Chromophores. *ACS Appl. Mater. Interfaces* **2018**, *10* (29), 24533–24542. <https://doi.org/10.1021/acsami.8b06605>.
- (33) Çelik, H. H.; Özcan, S.; Mülazımoğlu, A. D.; Yılmaz, E.; Mercimek, B.; Çukurovalı, A.; Yılmaz, İ.; Solak, A. O.; Mülazımoğlu, İ. E. The Synthesis of a Novel DDPHC Diazonium Salt: Investigation of Its Usability in the Determination of Phenol and Chlorophenols Using CV, SWV and DPV Techniques. *Inorg. Chem. Commun.* **2020**, *116*, 107893. <https://doi.org/10.1016/j.inoche.2020.107893>.

- (34) Wu, T.; Fitchett, C. M.; Brooksby, P. A.; Downard, A. J. Building Tailored Interfaces through Covalent Coupling Reactions at Layers Grafted from Aryldiazonium Salts. *ACS Appl. Mater. Interfaces* **2021**, *13* (10), 11545–11570. <https://doi.org/10.1021/acsami.0c22387>.
- (35) Takijiri, K.; Morita, K.; Nakazono, T.; Sakai, K.; Ozawa, H. Highly Stable Chemisorption of Dyes with Pyridyl Anchors over TiO₂: Application in Dye-Sensitized Photoelectrochemical Water Reduction in Aqueous Media. *Chem. Commun.* **2017**, *53* (21), 3042–3045. <https://doi.org/10.1039/C6CC10321A>.
- (36) Rasu, L.; Amiri, M.; Bergens, S. H. Carbazole–Cyanobenzene Dyes Electrografted to Carbon or Indium-Doped Tin Oxide Supports for Visible Light-Driven Photoanodes and Olefin Isomerizations. *ACS Appl. Mater. Interfaces* **2021**, *13* (15), 17745–17752. <https://doi.org/10.1021/acsami.1c05064>.
- (37) Zhang, T.; Xing, G.; Chen, W.; Chen, L. Porous Organic Polymers: A Promising Platform for Efficient Photocatalysis. *Mater. Chem. Front.* **2020**, *4* (2), 332–353. <https://doi.org/10.1039/C9QM00633H>.
- (38) Zhang, Z.; Jia, J.; Zhi, Y.; Ma, S.; Liu, X. Porous Organic Polymers for Light-Driven Organic Transformations. *Chem. Soc. Rev.* **2022**, *51* (7), 2444–2490. <https://doi.org/10.1039/D1CS00808K>.
- (39) Bekkar, F.; Bettahar, F.; Moreno, I.; Meghabar, R.; Hamadouche, M.; Hernández, E.; Vilas-Vilela, J. L.; Ruiz-Rubio, L. Polycarbazole and Its Derivatives: Synthesis and Applications. A Review of the Last 10 Years. *Polymers* **2020**, *12* (10), 2227. <https://doi.org/10.3390/polym12102227>.
- (40) Shang, T.-Y.; Lu, L.-H.; Cao, Z.; Liu, Y.; He, W.-M.; Yu, B. Recent Advances of 1,2,3,5-Tetrakis(Carbazol-9-Yl)-4,6-Dicyanobenzene (4CzIPN) in Photocatalytic Transformations. *Chem. Commun.* **2019**, *55* (38), 5408–5419. <https://doi.org/10.1039/C9CC01047E>.
- (41) Speckmeier, E.; Fischer, T. G.; Zeitler, K. A Toolbox Approach To Construct Broadly Applicable Metal-Free Catalysts for Photoredox Chemistry: Deliberate Tuning of Redox Potentials and Importance of Halogens in Donor–Acceptor Cyanoarenes. *J. Am. Chem. Soc.* **2018**, *140* (45), 15353–15365. <https://doi.org/10.1021/jacs.8b08933>.
- (42) Lu, J.; Pattengale, B.; Liu, Q.; Yang, S.; Shi, W.; Li, S.; Huang, J.; Zhang, J. Donor–Acceptor Fluorophores for Energy-Transfer-Mediated Photocatalysis. *J. Am. Chem. Soc.* **2018**, *140* (42), 13719–13725. <https://doi.org/10.1021/jacs.8b07271>.
- (43) Zhu, S.-S.; Liu, Y.; Chen, X.-L.; Qu, L.-B.; Yu, B. Polymerization-Enhanced Photocatalysis for the Functionalization of C(Sp³)–H Bonds. *ACS Catal.* **2022**, *12* (1), 126–134. <https://doi.org/10.1021/acscatal.1c03765>.
- (44) Carbas, B. B.; Özbakır, S.; Kaya, Y. A Comprehensive Overview of Carbazole-EDOT Based Electrochromic Copolymers: A New Candidate for Carbazole-EDOT Based Electrochromic Copolymer. *Synth. Met.* **2023**, *293*, 117298. <https://doi.org/10.1016/j.synthmet.2023.117298>.
- (45) Gonzalez Lopez, E. J.; Renfige Rodriguez, M.; Santamarina, S. C.; Macor, L.; Otero, L. A.; Gervaldo, M. A.; Durantini, A. M.; Durantini, E. N.; Durantini, J. E.; Heredia, D. A. Light-Activated Antibacterial Polymeric Surface Based on Porphycene. *ACS Appl. Polym. Mater.* **2023**, *5* (1), 943–956. <https://doi.org/10.1021/acsapm.2c01890>.
- (46) Muras, K.; Kubicki, M.; Wałęsa-Chorab, M. Benzochalcodiazole-Based Donor-Acceptor-Donor Non-Symmetric Small Molecules as Dual-Functioning Electrochromic and Electrofluorochromic Materials. *Dyes Pigments* **2023**, *212*, 111098. <https://doi.org/10.1016/j.dyepig.2023.111098>.
- (47) Li, M.; Kang, S.; Du, J.; Zhang, J.; Wang, J.; Ariga, K. Junction-Controlled Topological Polymerization. *Angew. Chem. Int. Ed.* **2018**, *57* (18), 4936–4939. <https://doi.org/10.1002/anie.201713026>.

- (48) Ishimatsu, R.; Edura, T.; Adachi, C.; Nakano, K.; Imato, T. Photophysical Properties and Efficient, Stable, Electrogenerated Chemiluminescence of Donor-Acceptor Molecules Exhibiting Thermal Spin Upconversion. *Chem. - Eur. J.* **2016**, *22* (14), 4889–4898. <https://doi.org/10.1002/chem.201600077>.
- (49) Macit, H.; Sen, S.; Saçak, M. Electrochemical Synthesis and Characterization of Polycarbazole: Electrochemical Synthesis and Characterization of Polycarbazole. *J. Appl. Polym. Sci.* **2005**, *96* (3), 894–898. <https://doi.org/10.1002/app.21532>.
- (50) Sezai Sarac, A.; Ates, M.; Parlak, E. A. Electrolyte and Solvent Effects of Electrocoated Polycarbazole Thin Films on Carbon Fiber Microelectrodes. *J. Appl. Electrochem.* **2006**, *36* (8), 889–898. <https://doi.org/10.1007/s10800-006-9145-8>.
- (51) Adeloye, A. O.; Olomola, T. O.; Adebayo, A. I.; Ajibade, P. A. A High Molar Extinction Coefficient Bisterpyridyl Homoleptic Ru(II) Complex with Trans-2-Methyl-2-Butenoic Acid Functionality: Potential Dye for Dye-Sensitized Solar Cells. *Int. J. Mol. Sci.* **2012**, *13* (3), 3511–3526. <https://doi.org/10.3390/ijms13033511>.
- (52) Saxena, V.; Choudhury, S.; Jha, P.; Koiry, S. P.; Debnath, A. K.; Aswal, D. K.; Gupta, S. K.; Yakhmi, J. V. In Situ Spectroscopic Studies to Investigate Uncharacteristic NH₃ Sensing Behavior of Polycarbazole Langmuir–Blodgett Films. *Sens. Actuators B Chem.* **2010**, *150* (1), 7–11. <https://doi.org/10.1016/j.snb.2010.08.002>.
- (53) Schwinghammer, K.; Hug, S.; Mesch, M. B.; Senker, J.; Lotsch, B. V. Phenyl-Triazine Oligomers for Light-Driven Hydrogen Evolution. *Energy Environ. Sci.* **2015**, *8* (11), 3345–3353. <https://doi.org/10.1039/C5EE02574E>.
- (54) Ederer, J.; Janoš, P.; Ecorchard, P.; Tolasz, J.; Štengl, V.; Beneš, H.; Perchacz, M.; Pop-Georgievski, O. Determination of Amino Groups on Functionalized Graphene Oxide for Polyurethane Nanomaterials: XPS Quantitation vs. Functional Speciation. *RSC Adv.* **2017**, *7* (21), 12464–12473. <https://doi.org/10.1039/C6RA28745J>.
- (55) Lvova, L.; Paolesse, R.; Di Natale, C.; D'Amico, A.; Bergamini, A. Potentiometric Polymeric Film Sensors Based on 5,10,15-Tris(4-Aminophenyl) Porphyrinates of Co(II) and Cu(II) for Analysis of Biological Liquids. *Int. J. Electrochem.* **2011**, *2011*, 1–8. <https://doi.org/10.4061/2011/930203>.
- (56) Wu, W.; Mao, D.; Xu, S.; Kenry, Hu, F.; Li, X.; Kong, D.; Liu, B. Polymerization-Enhanced Photosensitization. *Chem* **2018**, *4* (8), 1937–1951. <https://doi.org/10.1016/j.chempr.2018.06.003>.
- (57) Wu, W.; Xu, S.; Qi, G.; Zhu, H.; Hu, F.; Liu, Z.; Zhang, D.; Liu, B. A Cross - linked Conjugated Polymer Photosensitizer Enables Efficient Sunlight - Induced Photooxidation. *Angew. Chem. Int. Ed.* **2019**, *58* (10), 3062–3066. <https://doi.org/10.1002/anie.201811067>.
- (58) Hosokai, T.; Matsuzaki, H.; Nakanotani, H.; Tokumaru, K.; Tsutsui, T.; Furube, A.; Nasu, K.; Nomura, H.; Yahiro, M.; Adachi, C. Evidence and Mechanism of Efficient Thermally Activated Delayed Fluorescence Promoted by Delocalized Excited States. *Sci. Adv.* **2017**, *3* (5), e1603282. <https://doi.org/10.1126/sciadv.1603282>.
- (59) Ling, S.; Schumacher, S.; Galbraith, I.; Paterson, M. J. Excited-State Absorption of Conjugated Polymers in the Near-Infrared and Visible: A Computational Study of Oligofluorenes. *J. Phys. Chem. C* **2013**, *117* (13), 6889–6895. <https://doi.org/10.1021/jp401359a>.
- (60) Halsey-Moore, C.; Jena, P.; McLeskey, J. T. Tuning Range-Separated DFT Functionals for Modeling the Peak Absorption of MEH-PPV Polymer in Various Solvents. *Comput. Theor. Chem.* **2019**, *1162*, 112506. <https://doi.org/10.1016/j.comptc.2019.112506>.
- (61) Makuła, P.; Pacia, M.; Macyk, W. How To Correctly Determine the Band Gap Energy of Modified Semiconductor Photocatalysts Based on UV–Vis Spectra. *J. Phys. Chem. Lett.* **2018**, *9* (23), 6814–6817. <https://doi.org/10.1021/acs.jpcclett.8b02892>.

- (62) Bredas, J. L.; Silbey, R.; Boudreaux, D. S.; Chance, R. R. Chain-Length Dependence of Electronic and Electrochemical Properties of Conjugated Systems: Polyacetylene, Polyphenylene, Polythiophene, and Polypyrrole. *J. Am. Chem. Soc.* **1983**, *105* (22), 6555–6559. <https://doi.org/10.1021/ja00360a004>.
- (63) Leonat, L.; Sbârcea, G.; Brânzoi, I. V. CYCLIC VOLTAMMETRY FOR ENERGY LEVELS ESTIMATION OF ORGANIC MATERIALS.
- (64) Nakata, M.; Shimazaki, T. PubChemQC Project: A Large-Scale First-Principles Electronic Structure Database for Data-Driven Chemistry. *J. Chem. Inf. Model.* **2017**, *57* (6), 1300–1308. <https://doi.org/10.1021/acs.jcim.7b00083>.
- (65) Wang, D.; Marquard, S. L.; Troian-Gautier, L.; Sheridan, M. V.; Sherman, B. D.; Wang, Y.; Eberhart, M. S.; Farnum, B. H.; Dares, C. J.; Meyer, T. J. Interfacial Deposition of Ru(II) Bipyridine-Dicarboxylate Complexes by Ligand Substitution for Applications in Water Oxidation Catalysis. *J. Am. Chem. Soc.* **2018**, *140* (2), 719–726. <https://doi.org/10.1021/jacs.7b10809>.
- (66) Zhu, Y.; Wang, D.; Huang, Q.; Du, J.; Sun, L.; Li, F.; Meyer, T. J. Stabilization of a Molecular Water Oxidation Catalyst on a Dye-sensitized Photoanode by a Pyridyl Anchor. *Nat. Commun.* **2020**, *11* (1), 4610. <https://doi.org/10.1038/s41467-020-18417-5>.
- (67) Xu, J.; Liu, N.; Lv, H.; He, C.; Liu, Z.; Shen, X.; Cheng, F.; Fan, B. Photocatalyst-Free Visible Light Promoted *E* → *Z* Isomerization of Alkenes. *Green Chem.* **2020**, *22* (9), 2739–2743. <https://doi.org/10.1039/C9GC04303A>.
- (68) Kisch, H.; Bahnemann, D. Best Practice in Photocatalysis: Comparing Rates or Apparent Quantum Yields? *J. Phys. Chem. Lett.* **2015**, *6* (10), 1907–1910. <https://doi.org/10.1021/acs.jpcclett.5b00521>.
- (69) Upadhyay, A. Synthesis and Photo Physical Properties of Carbazole Based Quinoxaline Conjugated Polymer for Fluorescent Detection of Ni²⁺. *Dyes Pigments* **2017**, *15*.
- (70) Yang, P.-C.; Li, S.-Q.; Chien, Y.-H.; Tao, T.-L.; Huang, R.-Y.; Chen, H.-Y. Synthesis, Chemosensory Properties, and Self-Assembly of Terpyridine-Containing Conjugated Polycarbazole through RAFT Polymerization and Heck Coupling Reaction. *Polymers* **2017**, *9* (9), 427. <https://doi.org/10.3390/polym9090427>.
- (71) Yu, H.; Fan, M.; Liu, Q.; Su, Z.; Li, X.; Pan, Q.; Hu, X. Two Highly Water-Stable Imidazole-Based Ln-MOFs for Sensing Fe³⁺, Cr₂O₇²⁻/CrO₄²⁻ in a Water Environment. *Inorg. Chem.* **2020**, *59* (3), 2005–2010. <https://doi.org/10.1021/acs.inorgchem.9b03364>.
- (72) Lu, T.; Chen, F. Multiwfn: A Multifunctional Wavefunction Analyzer. *J. Comput. Chem.* **2012**, *33* (5), 580–592. <https://doi.org/10.1002/jcc.22885>.
- (73) Humphrey, W.; Dalke, A.; Schulten, K. VMD: Visual Molecular Dynamics. *J. Mol. Graph.* **1996**, *14* (1), 33–38. [https://doi.org/10.1016/0263-7855\(96\)00018-5](https://doi.org/10.1016/0263-7855(96)00018-5).
- (74) Bryden, M. A.; Zysman-Colman, E. Organic Thermally Activated Delayed Fluorescence (TADF) Compounds Used in Photocatalysis. *Chem. Soc. Rev.* **2021**, *50* (13), 7587–7680. <https://doi.org/10.1039/D1CS00198A>.

CHAPTER 4

Conclusions and Outlook

This dissertation includes applying PCz as a multifunctional binder, subsequently coordinating with metal ions for electrochemical water oxidation, and a new method for direct one-step polymerization of 3CzImIPN. Both of the polymers can be polymerized on the surface of ITO and carbon-based surfaces by a one-step electropolymerization. Moreover, it is the first time that we reported directly polymerize carbazole on the surface of metal Ni, and it is the first time for straightforward electropolymerization of a 4CzIPN derivative. The polymers are characterized by FT-IR, SEM, XPS, UV-Vis, and electrochemistry methods, or PL and ICP-OES. The performance of polymers for different reactions is investigated briefly, and we have attempted to explain the mechanism behind reactions. Moreover, the OER performance of electrodes is compared with some of the best catalysts.

Chapter 2 introduces a new method for preparing PCz-based electrodes for OER reactions. PCz acts as a binder that is conductive, stable, and can coordinate with metal ions, such as Ni, Fe, and Co. The electrodes are prepared by electropolymerizing carbazole over CF or Ni_{foam}, and then depositing metal ions by coordination with PCz. We made and tested a series of CoFe- and NiFe-based electrodes, in which the Ni₃Fe₁-PCz/Ni_{foam} electrode is one of the best OER electrodes under alkaline conditions (~200 mV overpotential to reach a current density of 10 mA cm⁻² in 1.0 M KOH) and has a very low mass loading of catalysts among all OER catalysts. Moreover, this electrode can operate in harsh conditions (85 °C in 6 M KOH) with high current density (100 mA cm⁻²) for a relatively long time (120 h), with a minor decrease in performance. The function of PCz is to enhance the OER by providing a high local concentration of OH⁻ ions and facilitating charge and mass transport to the active sites. In summary, this method can provide a simple and low-cost way to prepare efficient and robust electrodes for water splitting, which is a promising technology for renewable energy storage and conversion. By using abundant and inexpensive materials and a straightforward procedure, we

demonstrate that our electrodes can achieve high OER performance and stability under harsh conditions. This could help overcome some of the challenges and barriers to the large-scale application of water splitting and hydrogen production.

Future work for PCz-based electrodes contain trying it in seawater with base, trying it as an HER electrode, and finding a commercial partner. To perform electrodes for water splitting in alkaline seawater, we need to consider some factors, such as the electrolyte, the separator, and especially the corrosion resistance. A possible technique is to use a two-cell configuration to separate the anode and cathode, with a gas-impermeable separator to prevent the product gases from mixing. Seawater contains various salts and impurities that can affect the electrode performance and stability, while it is a realistic condition if an electrode can perform for a long time and without decreasing in performance. For trying the electrode as an HER electrode, it is possible for the PCz binder to coordinate with some more efficient HER catalysts and improve the HER performance. Moreover, it is also possible to investigate the detailed mechanism of the coordinative deposition and the role of PCz in the OER reaction using spectroscopic and kinetic methods. For example, the conductivity should be measured in different potentials while operating in alkaline Conditions. The mechanistic unknowns to be investigated include how the catalysts and polycarbazole interact during the OER. Also, which pores are required to inject/expel counter ions, and the mechanism of electron conductivity through the electrode. Furthermore, we may explore other types of electrodes and metal ion precursors or nanomaterials that can benefit from the PCz binder, such as Ni-Co or Ni-V.

Chapter 3 reports the first direct electropolymerization of a dicyanobenzene-carbazole dye functionalized with an imidazole group (P3CzImIPN) to prepare photoredox- and photoactive POP films on carbon and ITO surface. The POP films have controlled amounts by different CV cycles, high stability under standard AM 1.5 G sunlight, and tunable properties for various applications. For example, the photoelectrodes in alkaline and neutral conditions that efficiently oxidize hydroquinone and triethylamine under visible light irradiation, which

increases their performance ~3–4 times compared to the electrografted 4CzIPN monomers we reported before. It is also a heterogeneous photocatalyst for stilbene isomerization to catalyze the photosynthetic isomerization of *trans*-stilbene to *cis*-stilbene. Moreover, it is a solid-state photoluminescence sensor for response to lithium ions by quenching their photoluminescence emission. We also provide some structural and spectroscopic characterizations of the POP films and the monomer, as well as some theoretical calculations to support the experimental results. In summary, we provide a novel and facile method to prepare redox- and photoactive POP films on various substrates, which can be used as photoelectrodes for solar energy conversion or storage or as photocatalysts for organic synthesis or environmental remediation.

Future work for P3CzImIPN includes incorporating catalysts for photoelectrochemical CO₂, N₂ reduction, the evolution of H₂, or maybe combine with polycarbazole and NiFe for photoelectrochemical OER. The imidazole group has the ability to coordinate or bond to different catalysts, such as Ru or Co catalysts for CO₂ reduction or water splitting to H₂. By binding water oxidation and reduction catalysts together with P3CzImIPN POPs, we may make new overall water-splitting catalysts for the generation of O₂ and H₂ without adding any sacrificial agent. It is also possible for us to explore other electropolymerization monomers with different functional groups or chromophores to obtain more diverse and versatile POP films with tailored properties. For example, adding an electron withdrawing or donating group may change the properties of the POP. Due to a relatively suitable redox window of the POP, future work also may incorporate an investigation of the mechanism and kinetics of the photoelectrochemical or photocatalytic organic reactions mediated by the POP films, as well as the factors affecting their efficiency and selectivity. Furthermore, we can optimize the fabrication and performance of the POP films as solid-state sensors for various metal ions or other analytes, such as Ni, Fe, and Co, and compare them with other existing sensing materials or methods.

In conclusion, this thesis focuses on the development of novel carbazole-based polymer catalysts and their direct integration onto various electrode surfaces. These electrodes exhibit exceptional performance as OER anodes,

surpassing conventional experimental conditions and demonstrating robustness in industrial-level harsh environments. The inherent characteristic attributes of the electrode possibly could be utilized in seawater environments. Moreover, these electrodes have the potential to application as HER electrodes. We already have submitted a patent application and are actively seeking a commercial partner for further advancement. The carbazole-imidazole-dicyanobenzene-based electrode, named P3CzImIPN, represents a versatile and multifunctional platform. It serves as a prototype electrode for future adornment and modification, enabling the incorporation of catalysts for photoelectrochemical carbon dioxide and nitrogen reduction, as well as hydrogen evolution. Additionally, the combination of polycarbazole and NiFe with this electrode holds promise for photoelectrochemical OER. With further development and enhanced understanding of these catalysts, we anticipate that their application will expand into broader domains.

Bibliography

- (1) Lewis, N. S. Toward Cost-Effective Solar Energy Use. *Science* **2007**, *315* (5813), 798–801. <https://doi.org/10.1126/science.1137014>.
- (2) Turner, J. A. Sustainable Hydrogen Production. *Science* **2004**, *305* (5686), 972–974. <https://doi.org/10.1126/science.1103197>.
- (3) Stott, R.; Arulkumaran, S.; Gilmore, I.; Godlee, F.; Page, L. Legislate for Carbon Net Zero by 2030. *The Lancet* **2019**, *393* (10175), 981. [https://doi.org/10.1016/S0140-6736\(19\)30048-0](https://doi.org/10.1016/S0140-6736(19)30048-0).
- (4) Mallapaty, S. How China Could Be Carbon Neutral by Mid-Century. *Nature* **2020**, *586* (7830), 482–483. <https://doi.org/10.1038/d41586-020-02927-9>.
- (5) IEA (2021), *World Energy Outlook 2021*, IEA, Paris <https://www.iea.org/reports/world-energy-outlook-2021>, License: CC BY 4.0.
- (6) Zhu, Z.; Wang, X.; Peng, Y.; Lei, H.; Fettinger, J. C.; Rivard, E.; Power, P. P. Addition of Hydrogen or Ammonia to a Low-Valent Group 13 Metal Species at 25 °C and 1 Atmosphere. *Angew. Chem. Int. Ed.* **2009**, *48* (11), 2031–2034. <https://doi.org/10.1002/anie.200805982>.
- (7) Graetz, J. New Approaches to Hydrogen Storage. *Chem Soc Rev* **2009**, *38* (1), 73–82. <https://doi.org/10.1039/B718842K>.
- (8) Aziz, M. Liquid Hydrogen: A Review on Liquefaction, Storage, Transportation, and Safety. *Energies* **2021**, *14* (18), 5917. <https://doi.org/10.3390/en14185917>.
- (9) Li, H.; Cao, X.; Liu, Y.; Shao, Y.; Nan, Z.; Teng, L.; Peng, W.; Bian, J. Safety of Hydrogen Storage and Transportation: An Overview on Mechanisms, Techniques, and Challenges. *Energy Rep.* **2022**, *8*, 6258–6269. <https://doi.org/10.1016/j.egy.2022.04.067>.
- (10) Yang, M.; Hunger, R.; Berrettoni, S.; Sprecher, B.; Wang, B. A Review of Hydrogen Storage and Transport Technologies. *Clean Energy* **2023**, *7* (1), 190–216. <https://doi.org/10.1093/ce/zkad021>.
- (11) Hoelzen, J.; Silberhorn, D.; Zill, T.; Bensmann, B.; Hanke-Rauschenbach, R. Hydrogen-Powered Aviation and Its Reliance on Green Hydrogen Infrastructure – Review and Research Gaps. *Int. J. Hydrog. Energy* **2022**, *47* (5), 3108–3130. <https://doi.org/10.1016/j.ijhydene.2021.10.239>.
- (12) Elrhoul, D.; Romero Gómez, M.; Naveiro, M. Review of Green Hydrogen Technologies Application in Maritime Transport. *Int. J. Green Energy* **2023**, 1–26. <https://doi.org/10.1080/15435075.2023.2194384>.
- (13) Choi, M.; Wang, L.; Stoerzinger, K. A.; Chung, S.; Chambers, S. A.; Du, Y. Epitaxial Design of Complex Nickelates as Electrocatalysts for the Oxygen Evolution Reaction. *Adv. Energy Mater.* **2023**, 2300239. <https://doi.org/10.1002/aenm.202300239>.
- (14) McHugh, P. J.; Stergiou, A. D.; Symes, M. D. Decoupled Electrochemical Water Splitting: From Fundamentals to Applications. *Adv. Energy Mater.* **2020**, *10* (44), 2002453. <https://doi.org/10.1002/aenm.202002453>.
- (15) Ifkovits, Z. P.; Evans, J. M.; Meier, M. C.; Papadantonakis, K. M.; Lewis, N. S. Decoupled Electrochemical Water-Splitting Systems: A Review and Perspective. *Energy Environ. Sci.* **2021**, *14* (9), 4740–4759. <https://doi.org/10.1039/D1EE01226F>.
- (16) Orhan, M. F.; Dincer, I.; Rosen, M. A.; Kanoglu, M. Integrated Hydrogen Production Options Based on Renewable and Nuclear Energy Sources. *Renew. Sustain. Energy Rev.* **2012**, *16* (8), 6059–6082. <https://doi.org/10.1016/j.rser.2012.06.008>.
- (17) Smith, C.; Hill, A. K.; Torrente-Murciano, L. Current and Future Role of Haber–Bosch Ammonia in a Carbon-Free Energy Landscape. *Energy Environ. Sci.* **2020**, *13* (2), 331–344. <https://doi.org/10.1039/C9EE02873K>.

- (18) Carmo, M.; Fritz, D. L.; Mergel, J.; Stolten, D. A Comprehensive Review on PEM Water Electrolysis. *Int. J. Hydrog. Energy* **2013**, *38* (12), 4901–4934. <https://doi.org/10.1016/j.ijhydene.2013.01.151>.
- (19) Wappler, M.; Unguder, D.; Lu, X.; Ohlmeyer, H.; Teschke, H.; Lueke, W. Building the Green Hydrogen Market – Current State and Outlook on Green Hydrogen Demand and Electrolyzer Manufacturing. *Int. J. Hydrog. Energy* **2022**, *47* (79), 33551–33570. <https://doi.org/10.1016/j.ijhydene.2022.07.253>.
- (20) Hossain, Md. B.; Islam, Md. R.; Muttaqi, K. M.; Sutanto, D.; Agalgaonkar, A. P. Advancement of Fuel Cells and Electrolyzers Technologies and Their Applications to Renewable-Rich Power Grids. *J. Energy Storage* **2023**, *62*, 106842. <https://doi.org/10.1016/j.est.2023.106842>.
- (21) Wang, T.; Cao, X.; Jiao, L. PEM Water Electrolysis for Hydrogen Production: Fundamentals, Advances, and Prospects. *Carbon Neutrality* **2022**, *1* (1), 21. <https://doi.org/10.1007/s43979-022-00022-8>.
- (22) Wang, S.; Lu, A.; Zhong, C.-J. Hydrogen Production from Water Electrolysis: Role of Catalysts. *Nano Converge* **2021**, *8* (1), 4. <https://doi.org/10.1186/s40580-021-00254-x>.
- (23) Zhai, W.; Ma, Y.; Chen, D.; Ho, J. C.; Dai, Z.; Qu, Y. Recent Progress on the Long - term Stability of Hydrogen Evolution Reaction Electrocatalysts. *InfoMat* **2022**, *4* (9). <https://doi.org/10.1002/inf2.12357>.
- (24) Suntivich, J.; May, K. J.; Gasteiger, H. A.; Goodenough, J. B.; Shao-Horn, Y. A Perovskite Oxide Optimized for Oxygen Evolution Catalysis from Molecular Orbital Principles. *Science* **2011**, *334* (6061), 1383–1385. <https://doi.org/10.1126/science.1212858>.
- (25) Zhang, Z.; Liu, P.; Song, Y.; Hou, Y.; Xu, B.; Liao, T.; Zhang, H.; Guo, J.; Sun, Z. Heterostructure Engineering of 2D Superlattice Materials for Electrocatalysis. *Adv. Sci.* **2022**, *9* (35), 2204297. <https://doi.org/10.1002/advs.202204297>.
- (26) Guo, B.; Ding, Y.; Huo, H.; Wen, X.; Ren, X.; Xu, P.; Li, S. Recent Advances of Transition Metal Basic Salts for Electrocatalytic Oxygen Evolution Reaction and Overall Water Electrolysis. *Nano-Micro Lett.* **2023**, *15* (1), 57. <https://doi.org/10.1007/s40820-023-01038-0>.
- (27) Zhang, Y.; Wu, J.; Guo, B.; Huo, H.; Niu, S.; Li, S.; Xu, P. Recent Advances of Transition - metal Metaphosphates for Efficient Electrocatalytic Water Splitting. *Carbon Energy* **2023**, e375. <https://doi.org/10.1002/cey2.375>.
- (28) Guo, B.; Huo, H.; Zhuang, Q.; Ren, X.; Wen, X.; Yang, B.; Huang, X.; Chang, Q.; Li, S. Iron Oxyhydroxide: Structure and Applications in Electrocatalytic Oxygen Evolution Reaction. *Adv. Funct. Mater.* **2023**, 2300557. <https://doi.org/10.1002/adfm.202300557>.
- (29) Liu, J.; Zhang, J.; Zhou, H.; Liu, B.; Dong, H.; Lin, X.; Qin, Y. Lignin-Derived Carbon-Supported MoC–FeNi Heterostructure as Efficient Electrocatalysts for Oxygen Evolution Reaction. *J. Colloid Interface Sci.* **2023**, *629*, 822–831. <https://doi.org/10.1016/j.jcis.2022.08.141>.
- (30) Shrestha, N. K.; Patil, S. A.; Han, J.; Cho, S.; Inamdar, A. I.; Kim, H.; Im, H. Chemical Etching Induced Microporous Nickel Backbones Decorated with Metallic Fe@hydroxide Nanocatalysts: An Efficient and Sustainable OER Anode toward Industrial Alkaline Water-Splitting. *J. Mater. Chem. A* **2022**, *10* (16), 8989–9000. <https://doi.org/10.1039/D1TA10103J>.
- (31) Chavan, H. S.; Lee, C. H.; Inamdar, A. I.; Han, J.; Park, S.; Cho, S.; Shrestha, N. K.; Lee, S. U.; Hou, B.; Im, H.; Kim, H. Designing and Tuning the Electronic Structure of Nickel–Vanadium Layered Double Hydroxides for Highly Efficient Oxygen Evolution Electrocatalysis. *ACS Catal.* **2022**, *12* (7), 3821–3831. <https://doi.org/10.1021/acscatal.1c05813>.

- (32) Nie, F.; Li, Z.; Dai, X.; Yin, X.; Gan, Y.; Yang, Z.; Wu, B.; Ren, Z.; Cao, Y.; Song, W. Interfacial Electronic Modulation on Heterostructured NiSe@CoFe LDH Nanoarrays for Enhancing Oxygen Evolution Reaction and Water Splitting by Facilitating the Deprotonation of OH to O. *Chem. Eng. J.* **2022**, *431*, 134080. <https://doi.org/10.1016/j.cej.2021.134080>.
- (33) Li, H.; Zhang, C.; Xiang, W.; Amin, M. A.; Na, J.; Wang, S.; Yu, J.; Yamauchi, Y. Efficient Electrocatalysis for Oxygen Evolution: W-Doped NiFe Nanosheets with Oxygen Vacancies Constructed by Facile Electrodeposition and Corrosion. *Chem. Eng. J.* **2023**, *452*, 139104. <https://doi.org/10.1016/j.cej.2022.139104>.
- (34) Zheng, X.; Cao, Y.; Wu, Z.; Ding, W.; Xue, T.; Wang, J.; Chen, Z.; Han, X.; Deng, Y.; Hu, W. Rational Design and Spontaneous Sulfurization of NiCo - (Oxy)Hydroxysulfides Nanosheets with Modulated Local Electronic Configuration for Enhancing Oxygen Electrocatalysis. *Adv. Energy Mater.* **2022**, *12* (15), 2103275. <https://doi.org/10.1002/aenm.202103275>.
- (35) Huang, W.; Li, J.; Liao, X.; Lu, R.; Ling, C.; Liu, X.; Meng, J.; Qu, L.; Lin, M.; Hong, X.; Zhou, X.; Liu, S.; Zhao, Y.; Zhou, L.; Mai, L. Ligand Modulation of Active Sites to Promote Electrocatalytic Oxygen Evolution. *Adv. Mater.* **2022**, *34* (18), 2200270. <https://doi.org/10.1002/adma.202200270>.
- (36) Chen, X.; Wang, Q.; Cheng, Y.; Xing, H.; Li, J.; Zhu, X.; Ma, L.; Li, Y.; Liu, D. S - Doping Triggers Redox Reactivities of Both Iron and Lattice Oxygen in FeOOH for Low - Cost and High - Performance Water Oxidation. *Adv. Funct. Mater.* **2022**, *32* (26), 2112674. <https://doi.org/10.1002/adfm.202112674>.
- (37) Zhang, B.; Wu, Z.; Shao, W.; Gao, Y.; Wang, W.; Ma, T.; Ma, L.; Li, S.; Cheng, C.; Zhao, C. Interfacial Atom - Substitution Engineered Transition - Metal Hydroxide Nanofibers with High - Valence Fe for Efficient Electrochemical Water Oxidation. *Angew. Chem. Int. Ed.* **2022**, *61* (13). <https://doi.org/10.1002/anie.202115331>.
- (38) He, Z.; Zhang, J.; Gong, Z.; Lei, H.; Zhou, D.; Zhang, N.; Mai, W.; Zhao, S.; Chen, Y. Activating Lattice Oxygen in NiFe-Based (Oxy)Hydroxide for Water Electrolysis. *Nat. Commun.* **2022**, *13* (1), 2191. <https://doi.org/10.1038/s41467-022-29875-4>.
- (39) Jiang, C.; Moniz, S. J. A.; Wang, A.; Zhang, T.; Tang, J. Photoelectrochemical Devices for Solar Water Splitting – Materials and Challenges. *Chem. Soc. Rev.* **2017**, *46* (15), 4645–4660. <https://doi.org/10.1039/C6CS00306K>.
- (40) Wei, C.; Xu, Z. J. The Comprehensive Understanding of 10 MA Cmgeo–2 as an Evaluation Parameter for Electrochemical Water Splitting. *Small Methods* **2018**, *2* (11), 1800168. <https://doi.org/10.1002/smtd.201800168>.
- (41) Antipin, D.; Risch, M. Calculation of the Tafel Slope and Reaction Order of the Oxygen Evolution Reaction between PH 12 and PH 14 for the Adsorbate Mechanism. *Electrochem. Sci. Adv.* **2022**, e2100213. <https://doi.org/10.1002/elsa.202100213>.
- (42) Suen, N.-T.; Hung, S.-F.; Quan, Q.; Zhang, N.; Xu, Y.-J.; Chen, H. M. Electrocatalysis for the Oxygen Evolution Reaction: Recent Development and Future Perspectives. *Chem. Soc. Rev.* **2017**, *46* (2), 337–365. <https://doi.org/10.1039/C6CS00328A>.
- (43) Fabbri, E.; Schmidt, T. J. Oxygen Evolution Reaction—The Enigma in Water Electrolysis. *ACS Catal.* **2018**, *8* (10), 9765–9774. <https://doi.org/10.1021/acscatal.8b02712>.
- (44) Pegis, M. L.; Roberts, J. A. S.; Wasylenko, D. J.; Mader, E. A.; Appel, A. M.; Mayer, J. M. Standard Reduction Potentials for Oxygen and Carbon Dioxide Couples in Acetonitrile and *N*, *N*-Dimethylformamide. *Inorg. Chem.* **2015**, *54* (24), 11883–11888. <https://doi.org/10.1021/acs.inorgchem.5b02136>.

- (45) Man, I. C.; Su, H.; Calle - Vallejo, F.; Hansen, H. A.; Martínez, J. I.; Inoglu, N. G.; Kitchin, J.; Jaramillo, T. F.; Nørskov, J. K.; Rossmeisl, J. Universality in Oxygen Evolution Electrocatalysis on Oxide Surfaces. *ChemCatChem* **2011**, *3* (7), 1159–1165. <https://doi.org/10.1002/cctc.201000397>.
- (46) Rossmeisl, J.; Logadottir, A.; Nørskov, J. K. Electrolysis of Water on (Oxidized) Metal Surfaces. *Chem. Phys.* **2005**, *319* (1–3), 178–184. <https://doi.org/10.1016/j.chemphys.2005.05.038>.
- (47) Wang, Q.; Cheng, Y.; Tao, H. B.; Liu, Y.; Ma, X.; Li, D.; Yang, H. B.; Liu, B. Long - Term Stability Challenges and Opportunities in Acidic Oxygen Evolution Electrocatalysis. *Angew. Chem. Int. Ed.* **2023**, *62* (11), e202216645. <https://doi.org/10.1002/anie.202216645>.
- (48) Zhang, R.; Xie, A.; Cheng, L.; Bai, Z.; Tang, Y.; Wan, P. Hydrogen Production by Traditional and Novel Alkaline Water Electrolysis on Nickel or Iron Based Electrocatalysts. *Chem. Commun.* **2023**, *59* (53), 8205–8221. <https://doi.org/10.1039/D3CC00996C>.
- (49) Zhang, N.; Chai, Y. Lattice Oxygen Redox Chemistry in Solid-State Electrocatalysts for Water Oxidation. *Energy Environ. Sci.* **2021**, *14* (9), 4647–4671. <https://doi.org/10.1039/D1EE01277K>.
- (50) Huang, Z.-F.; Song, J.; Du, Y.; Xi, S.; Dou, S.; Nsanzimana, J. M. V.; Wang, C.; Xu, Z. J.; Wang, X. Chemical and Structural Origin of Lattice Oxygen Oxidation in Co–Zn Oxyhydroxide Oxygen Evolution Electrocatalysts. *Nat. Energy* **2019**, *4* (4), 329–338. <https://doi.org/10.1038/s41560-019-0355-9>.
- (51) Xu, H.; Yuan, J.; He, G.; Chen, H. Current and Future Trends for Spinel-Type Electrocatalysts in Electrocatalytic Oxygen Evolution Reaction. *Coord. Chem. Rev.* **2023**, *475*, 214869. <https://doi.org/10.1016/j.ccr.2022.214869>.
- (52) Zhu, K.; Zhu, X.; Yang, W. Application of In Situ Techniques for the Characterization of NiFe-Based Oxygen Evolution Reaction (OER) Electrocatalysts. *Angew. Chem. Int. Ed.* **2019**, *58* (5), 1252–1265. <https://doi.org/10.1002/anie.201802923>.
- (53) Zhao, J.; Zhang, J.; Li, Z.; Bu, X. Recent Progress on NiFe - Based Electrocatalysts for the Oxygen Evolution Reaction. *Small* **2020**, *16* (51), 2003916. <https://doi.org/10.1002/smll.202003916>.
- (54) Bodhankar, P. M.; Sarawade, P. B.; Singh, G.; Vinu, A.; Dhawale, D. S. Recent Advances in Highly Active Nanostructured NiFe LDH Catalyst for Electrochemical Water Splitting. *J. Mater. Chem. A* **2021**, *9* (6), 3180–3208. <https://doi.org/10.1039/D0TA10712C>.
- (55) Speck, F. D.; Dettelbach, K. E.; Sherbo, R. S.; Salvatore, D. A.; Huang, A.; Berlinguette, C. P. On the Electrolytic Stability of Iron-Nickel Oxides. *Chem* **2017**, *2* (4), 590–597. <https://doi.org/10.1016/j.chempr.2017.03.006>.
- (56) Feng, C.; She, X.; Xiao, Y.; Li, Y. Direct Detection of Fe^{VI} Water Oxidation Intermediates in an Aqueous Solution. *Angew. Chem. Int. Ed.* **2023**, *62* (9), e202218738. <https://doi.org/10.1002/anie.202218738>.
- (57) Feng, C.; Wang, F.; Liu, Z.; Nakabayashi, M.; Xiao, Y.; Zeng, Q.; Fu, J.; Wu, Q.; Cui, C.; Han, Y.; Shibata, N.; Domen, K.; Sharp, I. D.; Li, Y. A Self-Healing Catalyst for Electrocatalytic and Photoelectrochemical Oxygen Evolution in Highly Alkaline Conditions. *Nat. Commun.* **2021**, *12* (1), 5980. <https://doi.org/10.1038/s41467-021-26281-0>.
- (58) Wu, C.; Zhang, X.; Xia, Z.; Shu, M.; Li, H.; Xu, X.; Si, R.; Rykov, A. I.; Wang, J.; Yu, S.; Wang, S.; Sun, G. Insight into the Role of Ni–Fe Dual Sites in the Oxygen Evolution Reaction Based on Atomically Metal-Doped Polymeric Carbon Nitride. *J. Mater. Chem. A* **2019**, *7* (23), 14001–14010. <https://doi.org/10.1039/C9TA03163D>.
- (59) Wang, H.-F.; Chen, L.; Pang, H.; Kaskel, S.; Xu, Q. MOF-Derived Electrocatalysts for Oxygen Reduction, Oxygen Evolution and Hydrogen Evolution Reactions. *Chem. Soc. Rev.* **2020**, *49* (5), 1414–1448. <https://doi.org/10.1039/C9CS00906J>.

- (60) Chandrasekaran, S.; Khandelwal, M.; Dayong, F.; Sui, L.; Chung, J. S.; Misra, R. D. K.; Yin, P.; Kim, E. J.; Kim, W.; Vanchiappan, A.; Liu, Y.; Hur, S. H.; Zhang, H.; Bowen, C. Developments and Perspectives on Robust Nano - and Microstructured Binder - Free Electrodes for Bifunctional Water Electrolysis and Beyond. *Adv. Energy Mater.* **2022**, *12* (23), 2200409. <https://doi.org/10.1002/aenm.202200409>.
- (61) Zeng, K.; Zhang, D. Recent Progress in Alkaline Water Electrolysis for Hydrogen Production and Applications. *Prog. Energy Combust. Sci.* **2010**, *36* (3), 307–326. <https://doi.org/10.1016/j.peccs.2009.11.002>.
- (62) Browne, M. P.; Mills, A. Determining the Importance of the Electrode Support and Fabrication Method during the Initial Screening Process of an Active Catalyst for the Oxygen Evolution Reaction. *J. Mater. Chem. A* **2018**, *6* (29), 14162–14169. <https://doi.org/10.1039/C8TA02908C>.
- (63) Hausmann, J. N.; Traynor, B.; Myers, R. J.; Driess, M.; Menezes, P. W. The PH of Aqueous NaOH/KOH Solutions: A Critical and Non-Trivial Parameter for Electrocatalysis. *ACS Energy Lett.* **2021**, *6* (10), 3567–3571. <https://doi.org/10.1021/acseenergylett.1c01693>.
- (64) Li, W.; Tian, H.; Ma, L.; Wang, Y.; Liu, X.; Gao, X. Low-Temperature Water Electrolysis: Fundamentals, Progress, and New Strategies. *Mater. Adv.* **2022**, *3* (14), 5598–5644. <https://doi.org/10.1039/D2MA00185C>.
- (65) Yan, Y.; Zhang, C.; Deng, X.; Zhang, J.; Xue, Y.; Zhang, J.; Luo, Y.; Yang, F.; Wang, G.; Wang, R.; Chen, J. Designing Superhydrophilic Hydrogels as Binder-Free Catalysts for Enhanced Oxygen Evolution Performance. *Ind. Eng. Chem. Res.* **2023**, *62* (13), 5543–5551. <https://doi.org/10.1021/acs.iecr.3c00281>.
- (66) Duan, Q.; Wang, H.; Benziger, J. Transport of Liquid Water through Nafion Membranes. *J. Membr. Sci.* **2012**, *392–393*, 88–94. <https://doi.org/10.1016/j.memsci.2011.12.004>.
- (67) Li, G.-F.; Yang, D.; Abel Chuang, P.-Y. Defining Nafion Ionomer Roles for Enhancing Alkaline Oxygen Evolution Electrocatalysis. *ACS Catal.* **2018**, *8* (12), 11688–11698. <https://doi.org/10.1021/acscatal.8b02217>.
- (68) Yan, X.; Biemolt, J.; Zhao, K.; Zhao, Y.; Cao, X.; Yang, Y.; Wu, X.; Rothenberg, G.; Yan, N. A Membrane-Free Flow Electrolyzer Operating at High Current Density Using Earth-Abundant Catalysts for Water Splitting. *Nat. Commun.* **2021**, *12* (1), 4143. <https://doi.org/10.1038/s41467-021-24284-5>.
- (69) Ruschhaupt, P.; Pohlmann, S.; Varzi, A.; Passerini, S. Determining Realistic Electrochemical Stability Windows of Electrolytes for Electrical Double - Layer Capacitors. *Batter. Supercaps* **2020**, *3* (8), 698–707. <https://doi.org/10.1002/batt.202000009>.
- (70) Bresser, D.; Buchholz, D.; Moretti, A.; Varzi, A.; Passerini, S. Alternative Binders for Sustainable Electrochemical Energy Storage – the Transition to Aqueous Electrode Processing and Bio-Derived Polymers. *Energy Environ. Sci.* **2018**, *11* (11), 3096–3127. <https://doi.org/10.1039/C8EE00640G>.
- (71) Tang, C.; Thomas, B.; Ramírez-Hernández, M.; Mikmeková, E. M.; Asefa, T. Metal-Functionalized Hydrogels as Efficient Oxygen Evolution Electrocatalysts. *ACS Appl. Mater. Interfaces* **2022**, *14* (18), 20919–20929. <https://doi.org/10.1021/acsmi.2c01667>.
- (72) Uoyama, H.; Goushi, K.; Shizu, K.; Nomura, H.; Adachi, C. Highly Efficient Organic Light-Emitting Diodes from Delayed Fluorescence. *Nature* **2012**, *492* (7428), 234–238. <https://doi.org/10.1038/nature11687>.
- (73) Wu, W.; Mao, D.; Xu, S.; Kenry; Hu, F.; Li, X.; Kong, D.; Liu, B. Polymerization-Enhanced Photosensitization. *Chem* **2018**, *4* (8), 1937–1951. <https://doi.org/10.1016/j.chempr.2018.06.003>.

- (74) Chen, W.; Song, F. Thermally Activated Delayed Fluorescence Molecules and Their New Applications aside from OLEDs. *Chin. Chem. Lett.* **2019**, *30* (10), 1717–1730. <https://doi.org/10.1016/j.ccllet.2019.08.032>.
- (75) Li, F.; Gillett, A. J.; Gu, Q.; Ding, J.; Chen, Z.; Hele, T. J. H.; Myers, W. K.; Friend, R. H.; Evans, E. W. Singlet and Triplet to Doublet Energy Transfer: Improving Organic Light-Emitting Diodes with Radicals. *Nat. Commun.* **2022**, *13* (1), 2744. <https://doi.org/10.1038/s41467-022-29759-7>.
- (76) Dias, F. B.; Penfold, T. J.; Monkman, A. P. Photophysics of Thermally Activated Delayed Fluorescence Molecules. *Methods Appl. Fluoresc.* **2017**, *5* (1), 012001. <https://doi.org/10.1088/2050-6120/aa537e>.
- (77) Castano, A. P.; Mroz, P.; Hamblin, M. R. Photodynamic Therapy and Anti-Tumour Immunity. *Nat. Rev. Cancer* **2006**, *6* (7), 535–545. <https://doi.org/10.1038/nrc1894>.
- (78) Li, J.; Pu, K. Development of Organic Semiconducting Materials for Deep-Tissue Optical Imaging, Phototherapy and Photoactivation. *Chem. Soc. Rev.* **2019**, *48* (1), 38–71. <https://doi.org/10.1039/C8CS00001H>.
- (79) Zhao, J.; Wu, W.; Sun, J.; Guo, S. Triplet Photosensitizers: From Molecular Design to Applications. *Chem. Soc. Rev.* **2013**, *42* (12), 5323. <https://doi.org/10.1039/c3cs35531d>.
- (80) Chi, Y.; Chou, P.-T. Transition-Metal Phosphors with Cyclometalating Ligands: Fundamentals and Applications. *Chem Soc Rev* **2010**, *39* (2), 638–655. <https://doi.org/10.1039/B916237B>.
- (81) Zhao, X.; Liu, J.; Fan, J.; Chao, H.; Peng, X. Recent Progress in Photosensitizers for Overcoming the Challenges of Photodynamic Therapy: From Molecular Design to Application. *Chem. Soc. Rev.* **2021**, *50* (6), 4185–4219. <https://doi.org/10.1039/D0CS00173B>.
- (82) Zhu, Z.; Tian, D.; Gao, P.; Wang, K.; Li, Y.; Shu, X.; Zhu, J.; Zhao, Q. Cell-Penetrating Peptides Transport Noncovalently Linked Thermally Activated Delayed Fluorescence Nanoparticles for Time-Resolved Luminescence Imaging. *J. Am. Chem. Soc.* **2018**, *140* (50), 17484–17491. <https://doi.org/10.1021/jacs.8b08438>.
- (83) Luo, J.; Zhang, J. Donor–Acceptor Fluorophores for Visible-Light-Promoted Organic Synthesis: Photoredox/Ni Dual Catalytic C(Sp³)–C(Sp²) Cross-Coupling. *ACS Catal.* **2016**, *6* (2), 873–877. <https://doi.org/10.1021/acscatal.5b02204>.
- (84) Shang, T.-Y.; Lu, L.-H.; Cao, Z.; Liu, Y.; He, W.-M.; Yu, B. Recent Advances of 1,2,3,5-Tetrakis(Carbazol-9-Yl)-4,6-Dicyanobenzene (4CzIPN) in Photocatalytic Transformations. *Chem. Commun.* **2019**, *55* (38), 5408–5419. <https://doi.org/10.1039/C9CC01047E>.
- (85) Chen J.; Li Y.; Mei L.; Wu H. Application of Photosensitizer 2, 4, 5, 6-Tetrakis(carbazol-9-yl)-1, 3-dicyanobenzene in Photo-induced Transition-Metal-Free Organic Synthesis. *Chin. J. Org. Chem.* **2019**, *39* (11), 3040. <https://doi.org/10.6023/cjoc201904022>.
- (86) Lévêque, C.; Cheneberg, L.; Corcé, V.; Ollivier, C.; Fensterbank, L. Organic Photoredox Catalysis for the Oxidation of Silicates: Applications in Radical Synthesis and Dual Catalysis. *Chem. Commun.* **2016**, *52* (64), 9877–9880. <https://doi.org/10.1039/C6CC04636C>.
- (87) Meng, Q.-Y.; Wang, S.; Huff, G. S.; König, B. Ligand-Controlled Regioselective Hydrocarboxylation of Styrenes with CO₂ by Combining Visible Light and Nickel Catalysis. *J. Am. Chem. Soc.* **2018**, *140* (9), 3198–3201. <https://doi.org/10.1021/jacs.7b13448>.
- (88) Rasu, L.; Amiri, M.; Bergens, S. H. Carbazole–Cyanobenzene Dyes Electrografted to Carbon or Indium-Doped Tin Oxide Supports for Visible Light-Driven Photoanodes and Olefin Isomerizations. *ACS Appl. Mater. Interfaces* **2021**, *13* (15), 17745–17752. <https://doi.org/10.1021/acsami.1c05064>.

- (89) Jiang, H.; Studer, A. Transition - Metal - Free Three - Component Radical 1,2 - Amidoalkynylation of Unactivated Alkenes. *Chem. – Eur. J.* **2018**, chem.201805490. <https://doi.org/10.1002/chem.201805490>.
- (90) Guo, J.; Wu, Q.-L.; Xie, Y.; Weng, J.; Lu, G. Visible-Light-Mediated Decarboxylative Benzoylation of Imines with Arylacetic Acids. *J. Org. Chem.* **2018**, *83* (20), 12559–12567. <https://doi.org/10.1021/acs.joc.8b01849>.
- (91) Liu, Y.; Chen, X.-L.; Li, X.-Y.; Zhu, S.-S.; Li, S.-J.; Song, Y.; Qu, L.-B.; Yu, B. 4CzIPN-Bu-Catalyzed Proton-Coupled Electron Transfer for Photosynthesis of Phosphorylated *N*-Heteroaromatics. *J. Am. Chem. Soc.* **2021**, *143* (2), 964–972. <https://doi.org/10.1021/jacs.0c11138>.
- (92) Sun, S.; Sun, S.; Liu, K.; Xiao, L.-P.; Ma, J.; Sun, R. Construction of a Metal-Free Photocatalyst via Encapsulation of 1,2,3,5-Tetrakis(Carbazole-9-Yl)-4,6-Dicyanobenzene in a Carboxymethylcellulose-Based Hydrogel for Photocatalytic Lactic Acid Production. *Green Chem.* **2023**, *25* (2), 736–745. <https://doi.org/10.1039/D2GC04336J>.
- (93) Bekkar, F.; Bettahar, F.; Moreno, I.; Meghabar, R.; Hamadouche, M.; Hernáez, E.; Vilas-Vilela, J. L.; Ruiz-Rubio, L. Polycarbazole and Its Derivatives: Synthesis and Applications. A Review of the Last 10 Years. *Polymers* **2020**, *12* (10), 2227. <https://doi.org/10.3390/polym12102227>.
- (94) Nayana, V.; Kandasubramanian, B. Polycarbazole and Its Derivatives: Progress, Synthesis, and Applications. *J. Polym. Res.* **2020**, *27* (9), 285. <https://doi.org/10.1007/s10965-020-02254-7>.
- (95) Ates, M.; Uludag, N. Carbazole Derivative Synthesis and Their Electropolymerization. *J. Solid State Electrochem.* **2016**, *20* (10), 2599–2612. <https://doi.org/10.1007/s10008-016-3269-5>.
- (96) Mangione, M. I.; Spanevello, R. A.; Minudri, D.; Heredia, D.; Fernandez, L.; Otero, L.; Fungo, F. Electropolymerization of Functionalized Carbazole End-Capped Dendrimers. Formation of Conductive Films. *Electrochimica Acta* **2016**, *207*, 143–151. <https://doi.org/10.1016/j.electacta.2016.04.154>.
- (97) Li, M.; Kang, S.; Du, J.; Zhang, J.; Wang, J.; Ariga, K. Junction-Controlled Topological Polymerization. *Angew. Chem. Int. Ed.* **2018**, *57* (18), 4936–4939. <https://doi.org/10.1002/anie.201713026>.
- (98) Kibsgaard, J.; Chorkendorff, I. Considerations for the Scaling-up of Water Splitting Catalysts. *Nat Energy* **2019**, *4* (6), 430–433. <https://doi.org/10.1038/s41560-019-0407-1>.
- (99) Yan, Z.; Hitt, J. L.; Turner, J. A.; Mallouk, T. E. Renewable Electricity Storage Using Electrolysis. *Proc. Natl. Acad. Sci. U.S.A.* **2020**, *117* (23), 12558–12563. <https://doi.org/10.1073/pnas.1821686116>.
- (100) Subbaraman, R.; Tripkovic, D.; Strmcnik, D.; Chang, K.-C.; Uchimura, M.; Paulikas, A. P.; Stamenkovic, V.; Markovic, N. M. Enhancing Hydrogen Evolution Activity in Water Splitting by Tailoring Li^+ -Ni(OH)₂-Pt Interfaces. *Science* **2011**, *334* (6060), 1256–1260. <https://doi.org/10.1126/science.1211934>.
- (101) Nikolaidis, P.; Poullikkas, A. A Comparative Overview of Hydrogen Production Processes. *Renewable and Sustainable Energy Reviews* **2017**, *67*, 597–611. <https://doi.org/10.1016/j.rser.2016.09.044>.
- (102) Zheng, X.; Tang, J.; Gallo, A.; Garrido Torres, J. A.; Yu, X.; Athanitis, C. J.; Been, E. M.; Ercius, P.; Mao, H.; Fakra, S. C.; Song, C.; Davis, R. C.; Reimer, J. A.; Vinson, J.; Bajdich, M.; Cui, Y. Origin of Enhanced Water Oxidation Activity in an Iridium Single Atom Anchored on NiFe Oxyhydroxide Catalyst. *Proc. Natl. Acad. Sci. U.S.A.* **2021**, *118* (36), e2101817118. <https://doi.org/10.1073/pnas.2101817118>.

- (103) Yu, M.; Weidenthaler, C.; Wang, Y.; Budiyo, E.; Onur Sahin, E.; Chen, M.; DeBeer, S.; Rüdiger, O.; Tüysüz, H. Surface Boron Modulation on Cobalt Oxide Nanocrystals for Electrochemical Oxygen Evolution Reaction. *Angew Chem Int Ed* **2022**. <https://doi.org/10.1002/anie.202211543>.
- (104) Hunter, B. M.; Gray, H. B.; Müller, A. M. Earth-Abundant Heterogeneous Water Oxidation Catalysts. *Chem. Rev.* **2016**, *116* (22), 14120–14136. <https://doi.org/10.1021/acs.chemrev.6b00398>.
- (105) Li, S.; Gao, Y.; Li, N.; Ge, L.; Bu, X.; Feng, P. Transition Metal-Based Bimetallic MOFs and MOF-Derived Catalysts for Electrochemical Oxygen Evolution Reaction. *Energy Environ. Sci.* **2021**, *14* (4), 1897–1927. <https://doi.org/10.1039/D0EE03697H>.
- (106) Wu, Z.; Lu, X. F.; Zang, S.; Lou, X. W. (David). Non - Noble - Metal - Based Electrocatalysts toward the Oxygen Evolution Reaction. *Adv. Funct. Mater.* **2020**, *30* (15), 1910274. <https://doi.org/10.1002/adfm.201910274>.
- (107) Anantharaj, S.; Kundu, S.; Noda, S. “The Fe Effect”: A Review Unveiling the Critical Roles of Fe in Enhancing OER Activity of Ni and Co Based Catalysts. *Nano Energy* **2021**, *80*, 105514. <https://doi.org/10.1016/j.nanoen.2020.105514>.
- (108) Dang, L.; Liang, H.; Zhuo, J.; Lamb, B. K.; Sheng, H.; Yang, Y.; Jin, S. Direct Synthesis and Anion Exchange of Noncarbonate-Intercalated NiFe-Layered Double Hydroxides and the Influence on Electrocatalysis. *Chem. Mater.* **2018**, *30* (13), 4321–4330. <https://doi.org/10.1021/acs.chemmater.8b01334>.
- (109) Fan, L.; Zhang, P.; Zhang, B.; Daniel, Q.; Timmer, B. J. J.; Zhang, F.; Sun, L. 3D Core–Shell NiFeCr Catalyst on a Cu Nanoarray for Water Oxidation: Synergy between Structural and Electronic Modulation. *ACS Energy Lett.* **2018**, *3* (12), 2865–2874. <https://doi.org/10.1021/acsenergylett.8b01897>.
- (110) Niu, S.; Li, S.; Hu, J.; Li, Y.; Du, Y.; Han, X.; Xu, P. Fabrication of Uniform Ru-Doped NiFe₂O₄ Nanosheets as an Efficient Hydrogen Evolution Electrocatalyst. *Chem. Commun.* **2019**, *55* (97), 14649–14652. <https://doi.org/10.1039/C9CC07651D>.
- (111) Geng, S.-K.; Zheng, Y.; Li, S.-Q.; Su, H.; Zhao, X.; Hu, J.; Shu, H.-B.; Jaroniec, M.; Chen, P.; Liu, Q.-H.; Qiao, S.-Z. Nickel Ferrocyanide as a High-Performance Urea Oxidation Electrocatalyst. *Nat. Energy* **2021**, *6* (9), 904–912. <https://doi.org/10.1038/s41560-021-00899-2>.
- (112) Zhang, Y.; Guo, P.; Niu, S.; Wu, J.; Wang, W.; Song, B.; Wang, X.; Jiang, Z.; Xu, P. Magnetic Field Enhanced Electrocatalytic Oxygen Evolution of NiFe - LDH/Co₃O₄ P - n Heterojunction Supported on Nickel Foam. *Small Methods* **2022**, *6* (6), 2200084. <https://doi.org/10.1002/smt.202200084>.
- (113) Lyu, X.; Zhang, Y.; Wang, X.; Chen, H.; Li, S.; Zhang, W.; Hu, Y.; Li, F.; Li, D.; Yang, D. Electronic Structure Regulation of Nickel-Iron Layered Double Hydroxides by Tuning Ternary Component for Overall Water Splitting. *Mater. Today Sustain.* **2023**, *21*, 100295. <https://doi.org/10.1016/j.mtsust.2022.100295>.
- (114) Wan, W.; Wu, H.; Wang, Z.; Cai, G.; Li, D.; Zhong, H.; Jiang, T.; Jiang, C.; Ren, F. Tailoring Electronic Structure of Ni-Fe Oxide by V Incorporation for Effective Electrocatalytic Water Oxidation. *Appl. Surf. Sci.* **2023**, *611*, 155732. <https://doi.org/10.1016/j.apsusc.2022.155732>.
- (115) Xiao, H.; Shin, H.; Goddard, W. A. Synergy between Fe and Ni in the Optimal Performance of (Ni,Fe)OOH Catalysts for the Oxygen Evolution Reaction. *Proc. Natl. Acad. Sci. U.S.A.* **2018**, *115* (23), 5872–5877. <https://doi.org/10.1073/pnas.1722034115>.
- (116) Dionigi, F.; Zeng, Z.; Sinev, I.; Merzdorf, T.; Deshpande, S.; Lopez, M. B.; Kunze, S.; Zegkinoglou, I.; Sarodnik, H.; Fan, D.; Bergmann, A.; Drnec, J.; Araujo, J. F. de; Gliech, M.; Teschner, D.; Zhu, J.; Li, W.-X.; Greeley, J.; Cuenya, B. R.; Strasser, P. In-Situ Structure and Catalytic

- Mechanism of NiFe and CoFe Layered Double Hydroxides during Oxygen Evolution. *Nat Commun* **2020**, *11* (1), 2522. <https://doi.org/10.1038/s41467-020-16237-1>.
- (117) Chen, F.-Y.; Wu, Z.-Y.; Adler, Z.; Wang, H. Stability Challenges of Electrocatalytic Oxygen Evolution Reaction: From Mechanistic Understanding to Reactor Design. *Joule* **2021**, *5* (7), 1704–1731. <https://doi.org/10.1016/j.joule.2021.05.005>.
- (118) Zhao, S.; Yang, Y.; Tang, Z. Insight into Structural Evolution, Active Sites, and Stability of Heterogeneous Electrocatalysts. *Angew Chem Int Ed* **2022**, *61* (11). <https://doi.org/10.1002/anie.202110186>.
- (119) Xu, P.; Huang, T.; Huang, J.; Yan, Y.; Mallouk, T. E. Dye-Sensitized Photoelectrochemical Water Oxidation through a Buried Junction. *Proc. Natl. Acad. Sci. U.S.A.* **2018**, *115* (27), 6946–6951. <https://doi.org/10.1073/pnas.1804728115>.
- (120) Zhu, Y.; Wang, D.; Huang, Q.; Du, J.; Sun, L.; Li, F.; Meyer, T. J. Stabilization of a Molecular Water Oxidation Catalyst on a Dye-sensitized Photoanode by a Pyridyl Anchor. *Nat Commun* **2020**, *11* (1), 4610. <https://doi.org/10.1038/s41467-020-18417-5>.
- (121) Wang, D.; Huang, Q.; Shi, W.; You, W.; Meyer, T. J. Application of Atomic Layer Deposition in Dye-Sensitized Photoelectrosynthesis Cells. *Trends in Chemistry* **2021**, *3* (1), 59–71. <https://doi.org/10.1016/j.trechm.2020.11.002>.
- (122) Younus, H. A.; Vandichel, M.; Ahmad, N.; Ahlberg, E.; Busch, M.; Verpoort, F. Engineering of a Highly Stable Metal-Organic Co-Film for Efficient Electrocatalytic Water Oxidation in Acidic Media. *Materials Today Energy* **2020**, *17*, 100437. <https://doi.org/10.1016/j.mtener.2020.100437>.
- (123) Zaia, E. W.; Gordon, M. P.; Yuan, P.; Urban, J. J. Progress and Perspective: Soft Thermoelectric Materials for Wearable and Internet - of - Things Applications. *Adv. Electron. Mater.* **2019**, *5* (11), 1800823. <https://doi.org/10.1002/aelm.201800823>.
- (124) Sun, D.; Ren, Z.; Bryce, M. R.; Yan, S. Arylsilanes and Siloxanes as Optoelectronic Materials for Organic Light-Emitting Diodes (OLEDs). *Journal of Materials Chemistry C* **2015**, *13*.
- (125) Pernites, R.; Ponnampati, R.; Felipe, M. J.; Advincula, R. Electropolymerization Molecularly Imprinted Polymer (E-MIP) SPR Sensing of Drug Molecules: Pre-Polymerization Complexed Terthiophene and Carbazole Electroactive Monomers. *Biosensors and Bioelectronics* **2011**, *26* (5), 2766–2771. <https://doi.org/10.1016/j.bios.2010.10.027>.
- (126) Rice, N. A.; Bodnaryk, W. J.; Mirka, B.; Melville, O. A.; Adronov, A.; Lessard, B. H. Polycarbazole-Sorted Semiconducting Single-Walled Carbon Nanotubes for Incorporation into Organic Thin Film Transistors. *Adv. Electron. Mater.* **2019**, *5* (1), 1800539. <https://doi.org/10.1002/aelm.201800539>.
- (127) Zhou, Z.; Tian, Q.; Chai, L.; Chao, P.; Liu, S.; Wang, C. Construction of Nickel- and Iron-Coordinated Poly(5-Amino-1,10-Phenanthroline) Film for Electrocatalytic Water Oxidation Reactions. *Journal of Power Sources* **2021**, *506*, 230109. <https://doi.org/10.1016/j.jpowsour.2021.230109>.
- (128) Sezai Sarac, A.; Ates, M.; Parlak, E. A. Electrolyte and Solvent Effects of Electrocoated Polycarbazole Thin Films on Carbon Fiber Microelectrodes. *J Appl Electrochem* **2006**, *36* (8), 889–898. <https://doi.org/10.1007/s10800-006-9145-8>.
- (129) Siove, A.; Ades, D.; N'gbilo, E.; Chevrot, C. Chain Length Effect on the Electroactivity of Poly(N-Alkyl-3,6-Carbazolediyl) Thin Films. *Synthetic Metals* **1990**, *38* (3), 331–340. [https://doi.org/10.1016/0379-6779\(90\)90086-Z](https://doi.org/10.1016/0379-6779(90)90086-Z).

- (130) Macit, H.; Sen, S.; Saçak, M. Electrochemical Synthesis and Characterization of Polycarbazole: Electrochemical Synthesis and Characterization of Polycarbazole. *J. Appl. Polym. Sci.* **2005**, *96* (3), 894–898. <https://doi.org/10.1002/app.21532>.
- (131) Ambrose, J. F.; Carpenter, L. L.; Nelson, R. F. Electrochemical and Spectroscopic Properties of Cation Radicals: III . Reaction Pathways of Carbazolium Radical Ions. *J. Electrochem. Soc.* **1975**, *122* (7), 876–894. <https://doi.org/10.1149/1.2134365>.
- (132) Saxena, V.; Choudhury, S.; Jha, P.; Koiry, S. P.; Debnath, A. K.; Aswal, D. K.; Gupta, S. K.; Yakhmi, J. V. In Situ Spectroscopic Studies to Investigate Uncharacteristic NH₃ Sensing Behavior of Polycarbazole Langmuir–Blodgett Films. *Sensors and Actuators B: Chemical* **2010**, *150* (1), 7–11. <https://doi.org/10.1016/j.snb.2010.08.002>.
- (133) Miyazaki, T.; Kim, S.-K.; Hoshino, K. Nanostructured Hybrid Materials Formed by Cell Reaction between Polycarbazole and Metals. *Chem. Mater.* **2006**, *18* (22), 5302–5311. <https://doi.org/10.1021/cm060613w>.
- (134) Sun, W.; Sun, W.; Zhuo, Y.; Chu, Y. Facile Synthesis of Cu₂O Nanocube/Polycarbazole Composites and Their High Visible-Light Photocatalytic Properties. *Journal of Solid State Chemistry* **2011**, *184* (7), 1638–1643. <https://doi.org/10.1016/j.jssc.2011.03.055>.
- (135) Trotochaud, L.; Young, S. L.; Ranney, J. K.; Boettcher, S. W. Nickel–Iron Oxyhydroxide Oxygen-Evolution Electrocatalysts: The Role of Intentional and Incidental Iron Incorporation. *J. Am. Chem. Soc.* **2014**, *136* (18), 6744–6753. <https://doi.org/10.1021/ja502379c>.
- (136) Wang, C.; Moghaddam, R. B.; Brett, M. J.; Bergens, S. H. Simple Aqueous Preparation of High Activity and Stability NiFe Hydrous Oxide Catalysts for Water Oxidation. *ACS Sustainable Chem. Eng.* **2017**, *5* (1), 1106–1112. <https://doi.org/10.1021/acssuschemeng.6b02391>.
- (137) Shinagawa, T.; Garcia-Esparza, A. T.; Takane, K. Insight on Tafel Slopes from a Microkinetic Analysis of Aqueous Electrocatalysis for Energy Conversion. *Sci Rep* **2015**, *5* (1), 13801. <https://doi.org/10.1038/srep13801>.
- (138) Cheng, W.; Zhao, X.; Su, H.; Tang, F.; Che, W.; Zhang, H.; Liu, Q. Lattice-Strained Metal–Organic-Framework Arrays for Bifunctional Oxygen Electrocatalysis. *Nat Energy* **2019**, *4* (2), 115–122. <https://doi.org/10.1038/s41560-018-0308-8>.
- (139) Louie, M. W.; Bell, A. T. An Investigation of Thin-Film Ni–Fe Oxide Catalysts for the Electrochemical Evolution of Oxygen. *J. Am. Chem. Soc.* **2013**, *135* (33), 12329–12337. <https://doi.org/10.1021/ja405351s>.
- (140) Fan, K.; Chen, H.; Ji, Y.; Huang, H.; Claesson, P. M.; Daniel, Q.; Philippe, B.; Rensmo, H.; Li, F.; Luo, Y.; Sun, L. Nickel–Vanadium Monolayer Double Hydroxide for Efficient Electrochemical Water Oxidation. *Nat Commun* **2016**, *7* (1), 11981. <https://doi.org/10.1038/ncomms11981>.
- (141) Netskina, O. V.; Pochtar, A. A.; Komova, O. V.; Simagina, V. I. Solid-State NaBH₄ Composites as Hydrogen Generation Material: Effect of Thermal Treatment of a Catalyst Precursor on the Hydrogen Generation Rate. *Catalysts* **2020**, *10* (2), 201. <https://doi.org/10.3390/catal10020201>.
- (142) Inam, M.; Khan, R.; Park, D.; Lee, Y.-W.; Yeom, I. Removal of Sb(III) and Sb(V) by Ferric Chloride Coagulation: Implications of Fe Solubility. *Water* **2018**, *10* (4), 418. <https://doi.org/10.3390/w10040418>.
- (143) Zhang, X.; Sun, X.; Li, Y.; Hu, F.; Xu, Y.; Tian, J.; Zhang, H.; Liu, Q.; Su, H.; Wei, S. Reduced Interfacial Tension on Ultrathin NiCr-LDH Nanosheet Arrays for Efficient Electrocatalytic Water Oxidation. *J. Mater. Chem. A* **2021**, *9* (31), 16706–16712. <https://doi.org/10.1039/D1TA03863J>.
- (144) Ning, F.; Shao, M.; Xu, S.; Fu, Y.; Zhang, R.; Wei, M.; Evans, D. G.; Duan, X. TiO₂/Graphene/NiFe-Layered Double Hydroxide Nanorod Array Photoanodes for Efficient

- Photoelectrochemical Water Splitting. *Energy Environ. Sci.* **2016**, *9* (8), 2633–2643. <https://doi.org/10.1039/C6EE01092J>.
- (145) Zhai, P.; Xia, M.; Wu, Y.; Zhang, G.; Gao, J.; Zhang, B.; Cao, S.; Zhang, Y.; Li, Z.; Fan, Z.; Wang, C.; Zhang, X.; Miller, J. T.; Sun, L.; Hou, J. Engineering Single-Atomic Ruthenium Catalytic Sites on Defective Nickel-Iron Layered Double Hydroxide for Overall Water Splitting. *Nat Commun* **2021**, *12* (1), 4587. <https://doi.org/10.1038/s41467-021-24828-9>.
- (146) Zheng, W.; Liu, M.; Lee, L. Y. S. Best Practices in Using Foam-Type Electrodes for Electrocatalytic Performance Benchmark. *ACS Energy Lett.* **2020**, *5* (10), 3260–3264. <https://doi.org/10.1021/acsenerylett.0c01958>.
- (147) Chen, J.-R.; Hu, X.-Q.; Lu, L.-Q.; Xiao, W.-J. Visible Light Photoredox-Controlled Reactions of N-Radicals and Radical Ions. *Chem. Soc. Rev.* **2016**, *45* (8), 2044–2056. <https://doi.org/10.1039/C5CS00655D>.
- (148) Wang, Z.; Liu, Q.; Liu, R.; Ji, Z.; Li, Y.; Zhao, X.; Wei, W. Visible-Light-Initiated 4CzIPN Catalyzed Multi-Component Tandem Reactions to Assemble Sulfonated Quinoxalin-2(1H)-Ones. *Chin. Chem. Lett.* **2022**, *33* (3), 1479–1482. <https://doi.org/10.1016/j.ccl.2021.08.036>.
- (149) Mishra, A.; Fischer, M. K. R.; Bäuerle, P. Metal-Free Organic Dyes for Dye-Sensitized Solar Cells: From Structure: Property Relationships to Design Rules. *Angew. Chem. Int. Ed.* **2009**, *48* (14), 2474–2499. <https://doi.org/10.1002/anie.200804709>.
- (150) Hagfeldt, A.; Boschloo, G.; Sun, L.; Kloo, L.; Pettersson, H. Dye-Sensitized Solar Cells. *Chem. Rev.* **2010**, *110* (11), 6595–6663. <https://doi.org/10.1021/cr900356p>.
- (151) Giribabu, L.; Kanaparthi, R. K.; Velkannan, V. Molecular Engineering of Sensitizers for Dye-Sensitized Solar Cell Applications. *Chem. Rec.* **2012**, *12* (3), 306–328. <https://doi.org/10.1002/tcr.201100044>.
- (152) Wang, Y.; Zhao, X.; Zhao, Y.; Yang, T.; Liu, X.; Xie, J.; Li, G.; Zhu, D.; Tan, H.; Su, Z. Photosensitizers Based on Ir(III) Complexes for Highly Efficient Photocatalytic Hydrogen Generation. *Dyes Pigments* **2019**, *170*, 107547. <https://doi.org/10.1016/j.dyepig.2019.107547>.
- (153) Shon, J.-H.; Teets, T. S. Photocatalysis with Transition Metal Based Photosensitizers. *Comments Inorg. Chem.* **2020**, *40* (2), 53–85. <https://doi.org/10.1080/02603594.2019.1694517>.
- (154) Romero, N. A.; Nicewicz, D. A. Organic Photoredox Catalysis. *Chem. Rev.* **2016**, *116* (17), 10075–10166. <https://doi.org/10.1021/acs.chemrev.6b00057>.
- (155) Hossain, A.; Bhattacharyya, A.; Reiser, O. Copper's Rapid Ascent in Visible-Light Photoredox Catalysis. *Science* **2019**, *364* (6439), eaav9713. <https://doi.org/10.1126/science.aav9713>.
- (156) Joseph, M.; Haridas, S. Recent Progresses in Porphyrin Assisted Hydrogen Evolution. *Int. J. Hydrog. Energy* **2020**, *45* (21), 11954–11975. <https://doi.org/10.1016/j.ijhydene.2020.02.103>.
- (157) Fukuzumi, S.; Ohkubo, K. Organic Synthetic Transformations Using Organic Dyes as Photoredox Catalysts. *Org. Biomol. Chem.* **2014**, *12* (32), 6059–6071. <https://doi.org/10.1039/C4OB00843J>.
- (158) Decavoli, C.; Boldrini, C. L.; Manfredi, N.; Abboto, A. Molecular Organic Sensitizers for Photoelectrochemical Water Splitting. *Eur. J. Inorg. Chem.* **2020**, *2020* (11–12), 978–999. <https://doi.org/10.1002/ejic.202000026>.
- (159) Ronconi, F.; Syrgiannis, Z.; Bonasera, A.; Prato, M.; Argazzi, R.; Caramori, S.; Cristino, V.; Bignozzi, C. A. Modification of Nanocrystalline WO₃ with a Dicationic Perylene Bisimide: Applications to Molecular Level Solar Water Splitting. *J. Am. Chem. Soc.* **2015**, *137* (14), 4630–4633. <https://doi.org/10.1021/jacs.5b01519>.

- (160) Yamamoto, M.; Wang, L.; Li, F.; Fukushima, T.; Tanaka, K.; Sun, L.; Imahori, H. Visible Light-Driven Water Oxidation Using a Covalently-Linked Molecular Catalyst–Sensitizer Dyad Assembled on a TiO₂ Electrode. *Chem. Sci.* **2016**, *7* (2), 1430–1439. <https://doi.org/10.1039/C5SC03669K>.
- (161) Windle, C. D.; Kumagai, H.; Higashi, M.; Brisse, R.; Bold, S.; Jusselme, B.; Chavarot-Kerlidou, M.; Maeda, K.; Abe, R.; Ishitani, O.; Artero, V. Earth-Abundant Molecular Z-Scheme Photoelectrochemical Cell for Overall Water-Splitting. *J. Am. Chem. Soc.* **2019**, *141* (24), 9593–9602. <https://doi.org/10.1021/jacs.9b02521>.
- (162) Shan, B.; Brennaman, M. K.; Troian-Gautier, L.; Liu, Y.; Nayak, A.; Klug, C. M.; Li, T.-T.; Bullock, R. M.; Meyer, T. J. A Silicon-Based Heterojunction Integrated with a Molecular Excited State in a Water-Splitting Tandem Cell. *J. Am. Chem. Soc.* **2019**, *141* (26), 10390–10398. <https://doi.org/10.1021/jacs.9b04238>.
- (163) Forchetta, M.; Valentini, F.; Conte, V.; Galloni, P.; Sabuzi, F. Photocatalyzed Oxygenation Reactions with Organic Dyes: State of the Art and Future Perspectives. *Catalysts* **2023**, *13* (2), 220. <https://doi.org/10.3390/catal13020220>.
- (164) Yang, X.; Guo, Y.; Tong, H.; Liu, R.; Zhou, R. Metal-Free Acceptorless Dehydrogenative Cross-Coupling of Aldehydes/Alcohols with Alcohols. *Green Chem.* **2023**, *25* (4), 1672–1678. <https://doi.org/10.1039/D2GC04594J>.
- (165) Cardeynaels, T.; Etherington, M. K.; Paredis, S.; Batsanov, A. S.; Deckers, J.; Stavrou, K.; Vanderzande, D.; Monkman, A. P.; Champagne, B.; Maes, W. Dominant Dimer Emission Provides Colour Stability for Red Thermally Activated Delayed Fluorescence Emitter. *J. Mater. Chem. C* **2022**, *10* (15), 5840–5848. <https://doi.org/10.1039/D1TC04913E>.
- (166) Wu, S.; Kumar Gupta, A.; Yoshida, K.; Gong, J.; Hall, D.; Cordes, D. B.; Slawin, A. M. Z.; Samuel, I. D. W.; Zysman - Colman, E. Highly Efficient Green and Red Narrowband Emissive Organic Light - Emitting Diodes Employing Multi - Resonant Thermally Activated Delayed Fluorescence Emitters**. *Angew. Chem. Int. Ed.* **2022**, *61* (52). <https://doi.org/10.1002/anie.202213697>.
- (167) Badir, S. O.; Dumoulin, A.; Matsui, J. K.; Molander, G. A. Synthesis of Reversed C - Acyl Glycosides through Ni/Photoredox Dual Catalysis. *Angew. Chem. Int. Ed.* **2018**, *57* (22), 6610–6613. <https://doi.org/10.1002/anie.201800701>.
- (168) Shu, C.; Mega, R. S.; Andreassen, B. J.; Noble, A.; Aggarwal, V. K. Synthesis of Functionalized Cyclopropanes from Carboxylic Acids by a Radical Addition–Polar Cyclization Cascade. *Angew. Chem. Int. Ed.* **2018**, *57* (47), 15430–15434. <https://doi.org/10.1002/anie.201808598>.
- (169) Xu, J.; Cao, J.; Wu, X.; Wang, H.; Yang, X.; Tang, X.; Toh, R. W.; Zhou, R.; Yeow, E. K. L.; Wu, J. Unveiling Extreme Photoreduction Potentials of Donor–Acceptor Cyanoarenes to Access Aryl Radicals from Aryl Chlorides. *J. Am. Chem. Soc.* **2021**, *143* (33), 13266–13273. <https://doi.org/10.1021/jacs.1c05994>.
- (170) Liang, D.; Chen, J.-R.; Tan, L.-P.; He, Z.-W.; Xiao, W.-J. Catalytic Asymmetric Construction of Axially and Centrally Chiral Heterobiaryls by Minisci Reaction. *J. Am. Chem. Soc.* **2022**, *144* (13), 6040–6049. <https://doi.org/10.1021/jacs.2c01116>.
- (171) Zhu, S.-S.; Zuo, L.; Liu, Y.; Yu, B. 1,2,3,5-Tetrakis(Carbazol-9-Yl)-4,6-Dicyanobenzene (4CzIPN)-Based Porous Organic Polymers for Visible-Light-Driven Organic Transformations in Water under Aerobic Oxidation. *Green Chem.* **2022**, *24* (22), 8725–8732. <https://doi.org/10.1039/D2GC02950B>.

- (172) Yu, Z.-J.; Lou, W.-Y.; Junge, H.; Pöpcke, A.; Chen, H.; Xia, L.-M.; Xu, B.; Wang, M.-M.; Wang, X.-J.; Wu, Q.-A.; Lou, B.-Y.; Lochbrunner, S.; Beller, M.; Luo, S.-P. Thermally Activated Delayed Fluorescence (TADF) Dyes as Efficient Organic Photosensitizers for Photocatalytic Water Reduction. *Catal. Commun.* **2019**, *119*, 11–15. <https://doi.org/10.1016/j.catcom.2018.09.018>.
- (173) Fang, Y.; Liu, T.; Chen, L.; Chao, D. Exploiting Consecutive Photoinduced Electron Transfer (ConPET) in CO₂ Photoreduction. *Chem. Commun.* **2022**, *58* (57), 7972–7975. <https://doi.org/10.1039/D2CC02356C>.
- (174) Franceschi, P.; Rossin, E.; Goti, G.; Scopano, A.; Vega-Peñaloza, A.; Natali, M.; Singh, D.; Sartorel, A.; Dell'Amico, L. A Proton-Coupled Electron Transfer Strategy to the Redox-Neutral Photocatalytic CO₂ Fixation. *J. Org. Chem.* **2023**, *acs.joc.2c02952*. <https://doi.org/10.1021/acs.joc.2c02952>.
- (175) Wang, C.; Amiri, M.; Edean, R. T.; Martinez Perez, O.; Varley, S.; Rennie, B.; Rasu, L.; Bergens, S. H. Modular Construction of Photoanodes with Covalently Bonded Ru- and Ir-Polypyridyl Visible Light Chromophores. *ACS Appl. Mater. Interfaces* **2018**, *10* (29), 24533–24542. <https://doi.org/10.1021/acsami.8b06605>.
- (176) Çelik, H. H.; Özcan, S.; Mülazimoğlu, A. D.; Yılmaz, E.; Mercimek, B.; Çukurovalı, A.; Yılmaz, İ.; Solak, A. O.; Mülazimoğlu, İ. E. The Synthesis of a Novel DDPHC Diazonium Salt: Investigation of Its Usability in the Determination of Phenol and Chlorophenols Using CV, SWV and DPV Techniques. *Inorg. Chem. Commun.* **2020**, *116*, 107893. <https://doi.org/10.1016/j.inoche.2020.107893>.
- (177) Wu, T.; Fitchett, C. M.; Brooksby, P. A.; Downard, A. J. Building Tailored Interfaces through Covalent Coupling Reactions at Layers Grafted from Aryldiazonium Salts. *ACS Appl. Mater. Interfaces* **2021**, *13* (10), 11545–11570. <https://doi.org/10.1021/acsami.0c22387>.
- (178) Takijiri, K.; Morita, K.; Nakazono, T.; Sakai, K.; Ozawa, H. Highly Stable Chemisorption of Dyes with Pyridyl Anchors over TiO₂: Application in Dye-Sensitized Photoelectrochemical Water Reduction in Aqueous Media. *Chem. Commun.* **2017**, *53* (21), 3042–3045. <https://doi.org/10.1039/C6CC10321A>.
- (179) Zhang, T.; Xing, G.; Chen, W.; Chen, L. Porous Organic Polymers: A Promising Platform for Efficient Photocatalysis. *Mater. Chem. Front.* **2020**, *4* (2), 332–353. <https://doi.org/10.1039/C9QM00633H>.
- (180) Zhang, Z.; Jia, J.; Zhi, Y.; Ma, S.; Liu, X. Porous Organic Polymers for Light-Driven Organic Transformations. *Chem. Soc. Rev.* **2022**, *51* (7), 2444–2490. <https://doi.org/10.1039/D1CS00808K>.
- (181) Speckmeier, E.; Fischer, T. G.; Zeitler, K. A Toolbox Approach To Construct Broadly Applicable Metal-Free Catalysts for Photoredox Chemistry: Deliberate Tuning of Redox Potentials and Importance of Halogens in Donor–Acceptor Cyanoarenes. *J. Am. Chem. Soc.* **2018**, *140* (45), 15353–15365. <https://doi.org/10.1021/jacs.8b08933>.
- (182) Lu, J.; Pattengale, B.; Liu, Q.; Yang, S.; Shi, W.; Li, S.; Huang, J.; Zhang, J. Donor–Acceptor Fluorophores for Energy-Transfer-Mediated Photocatalysis. *J. Am. Chem. Soc.* **2018**, *140* (42), 13719–13725. <https://doi.org/10.1021/jacs.8b07271>.
- (183) Zhu, S.-S.; Liu, Y.; Chen, X.-L.; Qu, L.-B.; Yu, B. Polymerization-Enhanced Photocatalysis for the Functionalization of C(Sp³)–H Bonds. *ACS Catal.* **2022**, *12* (1), 126–134. <https://doi.org/10.1021/acscatal.1c03765>.
- (184) Carbas, B. B.; Özbakır, S.; Kaya, Y. A Comprehensive Overview of Carbazole-EDOT Based Electrochromic Copolymers: A New Candidate for Carbazole-EDOT Based Electrochromic Copolymer. *Synth. Met.* **2023**, *293*, 117298. <https://doi.org/10.1016/j.synthmet.2023.117298>.

- (185) Gonzalez Lopez, E. J.; Renfige Rodriguez, M.; Santamarina, S. C.; Macor, L.; Otero, L. A.; Gervaldo, M. A.; Durantini, A. M.; Durantini, E. N.; Durantini, J. E.; Heredia, D. A. Light-Activated Antibacterial Polymeric Surface Based on Porphycene. *ACS Appl. Polym. Mater.* **2023**, *5* (1), 943–956. <https://doi.org/10.1021/acsapm.2c01890>.
- (186) Muras, K.; Kubicki, M.; Wałęsa-Chorab, M. Benzochalcodiazole-Based Donor-Acceptor-Donor Non-Symmetric Small Molecules as Dual-Functioning Electrochromic and Electrofluorochromic Materials. *Dyes Pigments* **2023**, *212*, 111098. <https://doi.org/10.1016/j.dyepig.2023.111098>.
- (187) Ishimatsu, R.; Edura, T.; Adachi, C.; Nakano, K.; Imato, T. Photophysical Properties and Efficient, Stable, Electrogenerated Chemiluminescence of Donor-Acceptor Molecules Exhibiting Thermal Spin Upconversion. *Chem. - Eur. J.* **2016**, *22* (14), 4889–4898. <https://doi.org/10.1002/chem.201600077>.
- (188) Adeloye, A. O.; Olomola, T. O.; Adebayo, A. I.; Ajibade, P. A. A High Molar Extinction Coefficient Bisterpyridyl Homoleptic Ru(II) Complex with Trans-2-Methyl-2-Butenoic Acid Functionality: Potential Dye for Dye-Sensitized Solar Cells. *Int. J. Mol. Sci.* **2012**, *13* (3), 3511–3526. <https://doi.org/10.3390/ijms13033511>.
- (189) Schwinghammer, K.; Hug, S.; Mesch, M. B.; Senker, J.; Lotsch, B. V. Phenyl-Triazine Oligomers for Light-Driven Hydrogen Evolution. *Energy Environ. Sci.* **2015**, *8* (11), 3345–3353. <https://doi.org/10.1039/C5EE02574E>.
- (190) Ederer, J.; Janoš, P.; Ecorchard, P.; Tolasz, J.; Štengl, V.; Beneš, H.; Perchacz, M.; Pop-Georgievski, O. Determination of Amino Groups on Functionalized Graphene Oxide for Polyurethane Nanomaterials: XPS Quantitation vs. Functional Speciation. *RSC Adv.* **2017**, *7* (21), 12464–12473. <https://doi.org/10.1039/C6RA28745J>.
- (191) Lvova, L.; Paolesse, R.; Di Natale, C.; D'Amico, A.; Bergamini, A. Potentiometric Polymeric Film Sensors Based on 5,10,15-Tris(4-Aminophenyl) Porphyrinates of Co(II) and Cu(II) for Analysis of Biological Liquids. *Int. J. Electrochem.* **2011**, *2011*, 1–8. <https://doi.org/10.4061/2011/930203>.
- (192) Wu, W.; Xu, S.; Qi, G.; Zhu, H.; Hu, F.; Liu, Z.; Zhang, D.; Liu, B. A Cross - linked Conjugated Polymer Photosensitizer Enables Efficient Sunlight - Induced Photooxidation. *Angew. Chem. Int. Ed.* **2019**, *58* (10), 3062–3066. <https://doi.org/10.1002/anie.201811067>.
- (193) Hosokai, T.; Matsuzaki, H.; Nakanotani, H.; Tokumaru, K.; Tsutsui, T.; Furube, A.; Nasu, K.; Nomura, H.; Yahiro, M.; Adachi, C. Evidence and Mechanism of Efficient Thermally Activated Delayed Fluorescence Promoted by Delocalized Excited States. *Sci. Adv.* **2017**, *3* (5), e1603282. <https://doi.org/10.1126/sciadv.1603282>.
- (194) Ling, S.; Schumacher, S.; Galbraith, I.; Paterson, M. J. Excited-State Absorption of Conjugated Polymers in the Near-Infrared and Visible: A Computational Study of Oligofluorenes. *J. Phys. Chem. C* **2013**, *117* (13), 6889–6895. <https://doi.org/10.1021/jp401359a>.
- (195) Halsey-Moore, C.; Jena, P.; McLeskey, J. T. Tuning Range-Separated DFT Functionals for Modeling the Peak Absorption of MEH-PPV Polymer in Various Solvents. *Comput. Theor. Chem.* **2019**, *1162*, 112506. <https://doi.org/10.1016/j.comptc.2019.112506>.
- (196) Makuła, P.; Pacia, M.; Macyk, W. How To Correctly Determine the Band Gap Energy of Modified Semiconductor Photocatalysts Based on UV-Vis Spectra. *J. Phys. Chem. Lett.* **2018**, *9* (23), 6814–6817. <https://doi.org/10.1021/acs.jpcclett.8b02892>.
- (197) Bredas, J. L.; Silbey, R.; Boudreaux, D. S.; Chance, R. R. Chain-Length Dependence of Electronic and Electrochemical Properties of Conjugated Systems: Polyacetylene, Polyphenylene, Polythiophene, and Polypyrrole. *J. Am. Chem. Soc.* **1983**, *105* (22), 6555–6559. <https://doi.org/10.1021/ja00360a004>.

- (198) Leonat, L.; Sbârcea, G.; Brânzoi, I. V. CYCLIC VOLTAMMETRY FOR ENERGY LEVELS ESTIMATION OF ORGANIC MATERIALS.
- (199) Nakata, M.; Shimazaki, T. PubChemQC Project: A Large-Scale First-Principles Electronic Structure Database for Data-Driven Chemistry. *J. Chem. Inf. Model.* **2017**, *57* (6), 1300–1308. <https://doi.org/10.1021/acs.jcim.7b00083>.
- (200) Wang, D.; Marquard, S. L.; Troian-Gautier, L.; Sheridan, M. V.; Sherman, B. D.; Wang, Y.; Eberhart, M. S.; Farnum, B. H.; Dares, C. J.; Meyer, T. J. Interfacial Deposition of Ru(II) Bipyridine-Dicarboxylate Complexes by Ligand Substitution for Applications in Water Oxidation Catalysis. *J. Am. Chem. Soc.* **2018**, *140* (2), 719–726. <https://doi.org/10.1021/jacs.7b10809>.
- (201) Xu, J.; Liu, N.; Lv, H.; He, C.; Liu, Z.; Shen, X.; Cheng, F.; Fan, B. Photocatalyst-Free Visible Light Promoted $E \rightarrow Z$ Isomerization of Alkenes. *Green Chem.* **2020**, *22* (9), 2739–2743. <https://doi.org/10.1039/C9GC04303A>.
- (202) Kisch, H.; Bahnemann, D. Best Practice in Photocatalysis: Comparing Rates or Apparent Quantum Yields? *J. Phys. Chem. Lett.* **2015**, *6* (10), 1907–1910. <https://doi.org/10.1021/acs.jpcelett.5b00521>.
- (203) Upadhyay, A. Synthesis and Photo Physical Properties of Carbazole Based Quinoxaline Conjugated Polymer for Fluorescent Detection of Ni²⁺. *Dyes Pigments* **2017**, 15.
- (204) Yang, P.-C.; Li, S.-Q.; Chien, Y.-H.; Tao, T.-L.; Huang, R.-Y.; Chen, H.-Y. Synthesis, Chemosensory Properties, and Self-Assembly of Terpyridine-Containing Conjugated Polycarbazole through RAFT Polymerization and Heck Coupling Reaction. *Polymers* **2017**, *9* (9), 427. <https://doi.org/10.3390/polym9090427>.
- (205) Yu, H.; Fan, M.; Liu, Q.; Su, Z.; Li, X.; Pan, Q.; Hu, X. Two Highly Water-Stable Imidazole-Based Ln-MOFs for Sensing Fe³⁺, Cr₂O₇²⁻/CrO₄²⁻ in a Water Environment. *Inorg. Chem.* **2020**, *59* (3), 2005–2010. <https://doi.org/10.1021/acs.inorgchem.9b03364>.
- (206) Lu, T.; Chen, F. Multiwfn: A Multifunctional Wavefunction Analyzer. *J. Comput. Chem.* **2012**, *33* (5), 580–592. <https://doi.org/10.1002/jcc.22885>.
- (207) Humphrey, W.; Dalke, A.; Schulten, K. VMD: Visual Molecular Dynamics. *J. Mol. Graph.* **1996**, *14* (1), 33–38. [https://doi.org/10.1016/0263-7855\(96\)00018-5](https://doi.org/10.1016/0263-7855(96)00018-5).
- (208) Bryden, M. A.; Zysman-Colman, E. Organic Thermally Activated Delayed Fluorescence (TADF) Compounds Used in Photocatalysis. *Chem. Soc. Rev.* **2021**, *50* (13), 7587–7680. <https://doi.org/10.1039/D1CS00198A>.
- (209) Nickell, R. A.; Zhu, W. H.; Payne, R. U.; Cahela, D. R.; Tatarchuk, B. J. Hg/HgO Electrode and Hydrogen Evolution Potentials in Aqueous Sodium Hydroxide. *Journal of Power Sources* **2006**, *161* (2), 1217–1224. <https://doi.org/10.1016/j.jpowsour.2006.05.028>.
- (210) Zhang, J.; Hu, Y.; Liu, D.; Yu, Y.; Zhang, B. Enhancing Oxygen Evolution Reaction at High Current Densities on Amorphous-Like Ni-Fe-S Ultrathin Nanosheets via Oxygen Incorporation and Electrochemical Tuning. *Adv. Sci.* **2017**, *4* (3), 1600343. <https://doi.org/10.1002/advs.201600343>.
- (211) Ates, M.; Sarac, A. S.; Turhan, C. M.; Ayaz, N. E. Polycarbazole Modified Carbon Fiber Microelectrode: Surface Characterization and Dopamine Sensor. *Fibers Polym* **2009**, *10* (1), 46–52. <https://doi.org/10.1007/s12221-009-0046-4>.
- (212) Bernede, J. C.; Taoudi, H.; Bonnet, A.; Molinie, P.; Morsli, M.; De Valle, M. A.; Diaz, F. XPS and ESR Studies of Electrochemically Synthesized Polycarbazole Post-Doped with Iodine. *J. Appl. Polym. Sci.* **1999**, *71* (1), 115–124. [https://doi.org/10.1002/\(SICI\)1097-4628\(19990103\)71:1<115::AID-APP14>3.0.CO;2-Y](https://doi.org/10.1002/(SICI)1097-4628(19990103)71:1<115::AID-APP14>3.0.CO;2-Y).

- (213) Primbs, M.; Sun, Y.; Roy, A.; Malko, D.; Mehmood, A.; Sougrati, M.-T.; Blanchard, P.-Y.; Granozzi, G.; Kosmala, T.; Daniel, G.; Atanassov, P.; Sharman, J.; Durante, C.; Kucernak, A.; Jones, D.; Jaouen, F.; Strasser, P. Establishing Reactivity Descriptors for Platinum Group Metal (PGM)-Free Fe–N–C Catalysts for PEM Fuel Cells. *Energy Environ. Sci.* **2020**, *13* (8), 2480–2500. <https://doi.org/10.1039/D0EE01013H>.
- (214) Qiu, Z.; Tai, C.-W.; Niklasson, G. A.; Edvinsson, T. Direct Observation of Active Catalyst Surface Phases and the Effect of Dynamic Self-Optimization in NiFe-Layered Double Hydroxides for Alkaline Water Splitting. *Energy Environ. Sci.* **2019**, *12* (2), 572–581. <https://doi.org/10.1039/C8EE03282C>.
- (215) Zahoor, A.; Qiu, T.; Zhang, J.; Li, X. Synthesis and Characterization of Ag@polycarbazole Nanoparticles and Their Novel Optical Behavior. *J Mater Sci* **2009**, *44* (22), 6054–6059. <https://doi.org/10.1007/s10853-009-3831-y>.
- (216) Zhao, Y.; Dongfang, N.; Triana, C. A.; Huang, C.; Erni, R.; Wan, W.; Li, J.; Stoian, D.; Pan, L.; Zhang, P.; Lan, J.; Iannuzzi, M.; Patzke, G. R. Dynamics and Control of Active Sites in Hierarchically Nanostructured Cobalt Phosphide/Chalcogenide-Based Electrocatalysts for Water Splitting. *Energy Environ. Sci.* **2022**, *15* (2), 727–739. <https://doi.org/10.1039/D1EE02249K>.
- (217) Zhang, J.; Quast, T.; He, W.; Dieckhöfer, S.; Junqueira, J. R. C.; Öhl, D.; Wilde, P.; Jambrec, D.; Chen, Y.; Schuhmann, W. In Situ Carbon Corrosion and Cu Leaching as a Strategy for Boosting Oxygen Evolution Reaction in Multimetal Electrocatalysts. *Advanced Materials* **2022**, 2109108. <https://doi.org/10.1002/adma.202109108>.
- (218) Wang, Y.; Liu, B.; Shen, X.; Arandiyani, H.; Zhao, T.; Li, Y.; Garbrecht, M.; Su, Z.; Han, L.; Tricoli, A.; Zhao, C. Engineering the Activity and Stability of MOF - Nanocomposites for Efficient Water Oxidation. *Adv. Energy Mater.* **2021**, *11* (16), 2003759. <https://doi.org/10.1002/aenm.202003759>.
- (219) Peng, L.; Yang, N.; Yang, Y.; Wang, Q.; Xie, X.; Sun - Waterhouse, D.; Shang, L.; Zhang, T.; Waterhouse, G. I. N. Atomic Cation - Vacancy Engineering of NiFe - Layered Double Hydroxides for Improved Activity and Stability towards the Oxygen Evolution Reaction. *Angew. Chem. Int. Ed.* **2021**, *60* (46), 24612–24619. <https://doi.org/10.1002/anie.202109938>.
- (220) Li, W.; Chen, S.; Zhong, M.; Wang, C.; Lu, X. Synergistic Coupling of NiFe Layered Double Hydroxides with Co-C Nanofibers for High-Efficiency Oxygen Evolution Reaction. *Chemical Engineering Journal* **2021**, *415*, 128879. <https://doi.org/10.1016/j.cej.2021.128879>.
- (221) Gong, Z.; Liu, R.; Gong, H.; Ye, G.; Liu, J.; Dong, J.; Liao, J.; Yan, M.; Liu, J.; Huang, K.; Xing, L.; Liang, J.; He, Y.; Fei, H. Constructing a Graphene-Encapsulated Amorphous/Crystalline Heterophase NiFe Alloy by Microwave Thermal Shock for Boosting the Oxygen Evolution Reaction. *ACS Catal.* **2021**, *11* (19), 12284–12292. <https://doi.org/10.1021/acscatal.1c03333>.
- (222) Wang, C.; Yang, H.; Zhang, Y.; Wang, Q. NiFe Alloy Nanoparticles with Hcp Crystal Structure Stimulate Superior Oxygen Evolution Reaction Electrocatalytic Activity. *Angew. Chem. Int. Ed.* **2019**, *58* (18), 6099–6103. <https://doi.org/10.1002/anie.201902446>.
- (223) Song, F.; Hu, X. Exfoliation of Layered Double Hydroxides for Enhanced Oxygen Evolution Catalysis. *Nat Commun* **2014**, *5* (1), 4477. <https://doi.org/10.1038/ncomms5477>.
- (224) Gong, M.; Li, Y.; Wang, H.; Liang, Y.; Wu, J. Z.; Zhou, J.; Wang, J.; Regier, T.; Wei, F.; Dai, H. An Advanced Ni–Fe Layered Double Hydroxide Electrocatalyst for Water Oxidation. *J. Am. Chem. Soc.* **2013**, *135* (23), 8452–8455. <https://doi.org/10.1021/ja4027715>.
- (225) Zhang, N.; Brugger, J.; Etschmann, B.; Ngothai, Y.; Zeng, D. Thermodynamic Modeling of Poorly Complexing Metals in Concentrated Electrolyte Solutions: An X-Ray Absorption and UV-Vis

Spectroscopic Study of Ni(II) in the NiCl₂-MgCl₂-H₂O System. *PLoS ONE* **2015**, *10* (4), e0119805. <https://doi.org/10.1371/journal.pone.0119805>.

(226) Liu, W.; Etschmann, B.; Brugger, J.; Spiccia, L.; Foran, G.; McInnes, B. UV-Vis Spectrophotometric and XAFS Studies of Ferric Chloride Complexes in Hyper-Saline LiCl Solutions at 25–90 °C. *Chemical Geology* **2006**, *231* (4), 326–349. <https://doi.org/10.1016/j.chemgeo.2006.02.005>.

(227) M. A. Robb, J. R. Cheeseman, G. Scalmani, V. Barone, G. A. Petersson, H. Nakatsuji, X. Li, M. Caricato, A. V. Marenich, J. Bloino, B. G. Janesko, R. Gomperts, B. Mennucci, H. P. Hratchian, J. V. Ortiz, A. F. Izmaylov, J. L. Sonnenberg, D. Williams-Young, F. Ding, F. Lipparini, F. Egidi, J. Goings, B. Peng, A. Petrone, T. Henderson, D. Ranasinghe, V. G. Zakrzewski, J. Gao, N. Rega, G. Zheng, W. Liang, M. Hada, M. Ehara, K. Toyota, R. Fukuda, J. Hasegawa, M. Ishida, T. Nakajima, Y. Honda, O. Kitao, H. Nakai, T. Vreven, K. Throssell, J. A. Montgomery, Jr., J. E. Peralta, F. Ogliaro, M. J. Bearpark, J. J. Heyd, E. N. Brothers, K. N. Kudin, V. N. Staroverov, T. A. Keith, R. Kobayashi, J. Normand, K. Raghavachari, A. P. Rendell, J. C. Burant, S. S. Iyengar, J. Tomasi, M. Cossi, J. M. Millam, M. Klene, C. Adamo, R. Cammi, J. W. Ochterski, R. L. Martin, K. Morokuma, O. Farkas, J. B. Foresman, and D. J. Fox, Gaussian, Inc., Wallingford CT, 2016.

(228) Devlin, F. J.; Finley, J. W.; Stephens, P. J.; Frisch, M. J. Ab Initio Calculation of Vibrational Absorption and Circular Dichroism Spectra Using Density Functional Force Fields: A Comparison of Local, Nonlocal, and Hybrid Density Functionals. *J. Phys. Chem.* **1995**, *99* (46), 16883–16902. <https://doi.org/10.1021/j100046a014>.

(229) McLean, A. D.; Chandler, G. S. Contracted Gaussian Basis Sets for Molecular Calculations. I. Second Row Atoms, $Z = 11-18$. *J. Chem. Phys.* **1980**, *72* (10), 5639–5648. <https://doi.org/10.1063/1.438980>.

APPENDIX A

Supporting Information for Electronically Conductive, Multifunctional Polymer Binder for Highly Active, Stable, and Abundant Composite Electrodes for Oxygen Evolution

Supplementary Notes

Conversion of Hg/HgO Voltage to RHE Voltage at 85 °C in 6 M KOH

According to J. Niklas Hausmann *et al.*,¹ the pH of 6 M KOH at 85 °C is estimated to be 13.59. The reversible hydrogen electrode (RHE) voltage is calculated based on the equation:

$$E (\text{vs.RHE}) = E (\text{vs. Hg/HgO}) + 0.098 \text{ V}^* + 0.059 \times 13.59 \quad \text{S2.1}$$

According to Ryan A. Nickell *et al.*,² for the same concentration of NaOH (OH⁻), the increasing temperature may reduce the reference potential of Hg/HgO vs. NHE. Thus, the standard potential (E°) may be lower than 0.098 V, possibly underestimating the performance of the electrodes. Furthermore, the filling solution in Hg/HgO reference electrode is 4.24 M KOH, which is lower than the outside environment of 6 M KOH. As time passes, water may leak from the inside reference electrode to the outside environment. Consequently, the concentration of KOH inside the reference electrode may rise, which may cause interference. However, more investigations are needed to solve the questions above.

iR Correction

We use the corresponding Nyquist plot to do *iR* correction. In brief, the intercept of the X axis is identified as the solution resistance (R_s) and multiplied by the current to obtain the shifted voltage (V_{shift}). The *iR*-corrected new voltage is the untreated voltage that subtracts the V_{shift} .

Estimation of Turnover Frequency (TOF)

Suppose Faraday efficiency is 100%, and Ni and Co are the active centers in the reaction. Therefore, The TOF can be estimated as below:

$$\text{TOF} = jA/4Fn \quad \text{S2.2}$$

Where j is the geometric current density at a given potential, A is the geometrical area, F is the Faraday constant, and n is the moles of Ni or Co on the electrodes.³

Estimation of the Amount of Ni and Accessible PCz on the Electrodes Using Cyclic Voltammetry (CV)

Firstly, the I-t curves are plotted by the corresponding CV curves. Then, the total charge in Coulombs (Q) is calculated by integrating the corresponding peak in the I-t curve derived from the CV. Moreover, the moles of content on the electrodes (*mole*) can be calculated as follows:

$$\text{mole} = Q/ N_A e \quad \text{S2.3}$$

Where Q is the total charge of Coulomb calculated from Figures S2.3, S2.4, and S20, N_A is the Avogadro constant, and e is the Coulomb number for one electron. The mass content was estimated by multiplication by the molar mass.

Identification of Growth Polycarbazole on Carbon Fiber Paper (CF)

The first sweep proceeds in the positive-going direction and contains one anodic peak at ~ 0.92 V vs. Fc/Fc⁺ (Figure S2.1). This peak likely corresponds to the oxidation of dissolved carbazole to form the mono-cationic radical.⁴ This radical either bonds to the carbon surface or reacts with carbazole in solution to form the 3,3'-dimer eventually.⁵ The electropolymerization commences and propagates with this oxidation and proceeds as the voltage increases higher than ~ 0.92 V in the positive-going sweep. The subsequent cycles contain two anodic waves in the positive direction and two cathodic waves in the negative. With each subsequent sweep, these peaks grow, broaden, and shift to higher (anodic) or lower (cathodic) potentials. This is typical behavior for the electropolymerization of carbazole.^{4,6} The lower peak (~ 0.75 V) in the anodic sweep likely arises from oxidation of the polycarbazole form to a mono-cationic radical. The higher peak (~ 0.92 V) likely arises from further oxidation

to a dicationic (~ 0.92 V) species, along with oxidation of carbazole in solution as part of polymer growth.⁴ The color of the electrode turns dark green as the polymerization proceeds, and the green color persists after washing with MeCN (Figure S2.3). It is well known that polycarbazole turns green upon oxidation (doping) to form conjugated polycations.⁷ The shifting and broadening of these peaks during the polymerization arise, forming a thicker polymer layer. These effects include changes in electronic and ionic conductivity through the growing film.

Performance of The Ni₃Fe₁-PCz/CF and Ni₃Fe₁-Nafion/CF Electrodes

Figure S2.9 compares Ni₃Fe₁ electrodes with the same mass loadings on CF prepared with polycarbazole and Nafion as binders. Figure S2.9a shows the long-term galvanostatic OER at 10 mA cm^{-2} with the Ni₃Fe₁-PCz/CF and Ni₃Fe₁-Nafion/CF electrodes (1.0 M KOH, room temperature). The potential of the PCz-based electrode rose slightly over 5 h and then stabilized at ~ 1.46 V (vs. RHE) over the remainder of the 20 h, demonstrating the stability of this system towards the OER. The slight increase in potential over the first 5 h may have resulted from a minor reconstruction of the electrode. In contrast, the Nafion-based electrodes operated at higher, much less stable potentials throughout the experiment. Figure S2.9b shows the LSV curves before and after the 20 h OER. The before and after LSVs of the PCz electrode are quite comparable, with the curve actually being more defined after the 20 h reaction. There are positive currents at low potentials in the LSV of the Ni₃Fe₁-PCz/CF electrode before the long-term reaction. These currents likely arose from the electrooxidation (doping) of the polycarbazole support. There was almost no decrease in the LSV current densities after the 20 h reaction. The corresponding LSVs of the Nafion electrode showed significant degradation of activity. Figure S2.9c shows the Nyquist plots (at 0.5 V vs. SCE) for the PCz- and Nafion-based electrodes before and after the 20 h reaction. The high-frequency resistance of the PCz-based electrode is low, indicating the polycarbazole is electronically conductive at this potential. There are very few resistances at low frequencies, and there is little change in the plot after the 20 h OER. We note that the charge transfer resistance (R_{ct}) decreased slightly

after 20 h. In contrast, the high-frequency resistance of the Nafion-based electrode is much higher, there are significant low-frequency resistances, and the Nyquist plot changes significantly after 20 h. While detailed investigations are required to determine the exact mechanisms responsible for the plots, it is clear that the PCz-binder significantly enhances and stabilizes the OER reaction.

Identification of Growth Polycarbazole on Ni Foam

Figure S2.13 shows the CVs of Ni foam in MeCN (0.1 M LiClO₄) both in the absence of carbazole and during the electropolymerization (0.005 M carbazole). The CV of the Ni foam in the absence of carbazole contains large, linear oxidative waves starting at 0.6 V in the forward and reverse directions caused by Ni oxidation, presumably forming [Ni(MeCN)₄]²⁺. Similar waves are present in the first sweeps of the CVs recorded during the carbazole electropolymerization. These waves decreased as the surface was covered by polycarbazole, leaving only waves for the polymerization of carbazole in the final sweeps.

XPS Identification

Figure S2.18 shows the C, N, and O regions of the XPS spectra of PCz/Ni_{foam} (A-C) and Ni₃Fe₁-PCz/Ni_{foam} after (D-F). The C 1s region of PCz/Ni_{foam} (Figure S2.18a) contains peaks at 284.8 and 285.8 eV that may be assigned to the sp² carbons bonded to -carbon and -nitrogen, respectively, in the PCz rings. There is only one signal in the O 1s region at 533.1 eV, which may be assigned to the ClO₄⁻ counter ion resulting from the doping (Figure S2.18b). There are two peaks in the N 1s region in the XPS spectrum of PCz/Ni_{foam} (Figure S2.18c), one at 400.4 eV that may be assigned to neutral nitrogen in the polycarbazole rings (Figure S2.26a), and a smaller peak at 402.6 eV that may be assigned to N⁺ present because of partial doping of the polymer (Figure S2.26b). These tentative assignments are in line with those reported for partially doped PCz in the literature.⁸ We cannot rule out the presence of trace MeCN in the PCz/Ni_{foam}.

The new C 1s peaks in the XPS spectrum of Ni₃Fe₁-PCz/Ni_{foam} (287.0 eV and 288.3 eV) likely arise from methanol in the deposit left over from the coordinative

deposition (Figure S2.18d). The new peak in the N 1s region at 401.2 eV may arise from nitrogen bonded to Ni or Fe (Figure S2.18e, S2.26c). This tentative assignment is in-line with polypyridily-metal complexes in the literature.⁹ The peak assigned to N from partially doped PCz in the XPS spectrum of PCz/Ni_{foam} is absent with Ni₃Fe₁-PCz/Ni_{foam}. The O 1s region of the XPS spectrum of Ni₃Fe₁-PCz/Ni_{foam} (Figure S2.18f) contains peaks ~533.6 eV that may arise from methanol in the deposit, and peaks at ~532.4 eV that may arise from metal hydrates or hydroxides, consistent with literature assignments.¹⁰ These assignments are tentative because specific reference spectra are not available.

Similar tentative assignments are shown for the C, N, and O regions of the XPS spectra of Ni₃Fe₁-PCz/CF and Co₃Fe₁-PCz/CF (Figure S2.25a-c, and Figure S2.25d-f). The XPS survey data is shown in Figure S2.27.

FTIR Identification

For polycarbazole on carbon paper, the bands present at 728, 755, 800, and 880 cm⁻¹ relate to the C-H bonds. An intense peak at 1100 cm⁻¹ corresponds to ClO₄⁻ ions. Moreover, the peak at 1238 cm⁻¹ represents the N-H stretching. A C=C peak locates positions at 1449 and 1461 cm⁻¹. The peak at 1605 cm⁻¹ is the C-C peak. A broad peak at 3280 cm⁻¹ may result from N-H stretching. The proof for 3, 6 polycarbazole is the peak at 856 cm⁻¹.^{11,12} The peak at 1554 cm⁻¹ is a ring vibration band characteristic of the (partially) oxidized (doped) PCz.¹³ The band that appeared at approximately ~3250 cm⁻¹ is assigned to O-H stretching vibrations. After soaking in MeOH with metal chloride hydrates salts, washing and drying in the air for 24 h, peaks at 1100 and 1554 cm⁻¹ disappear, meaning the absence of ClO₄⁻ ions and reduced (undoped) PCz. In addition, a higher intensity broad peak around 3400 cm⁻¹ represents the presence of Ni salt,¹⁴ and a new peak at 733 cm⁻¹ represents the Fe-O bond.¹⁵

Chemical and Electrochemical Stability Tests of Polycarbazole (PCz)

To examine whether polycarbazole is chemically stable in the alkaline OER conditions or not, carbazole is polymerized on carbon fiber paper and Ni foam electrodes first, then soaked in 1 M KOH and 6 M KOH for 240 h at room temperature. As shown in Figure S2.28, there are no precipitates present or color change of the KOH solution after 240 h soaking, meaning that the PCz is stable to dissolution under the alkaline conditions. Furthermore, after 15 CVs in acetonitrile, the color of PCz changes from brown (undoped) back to dark green (doped), indicating that the electrochemical properties of PCz had not significantly changed, and the PCz remained on the electrode surface (Figure S2.29). The CVs of PCz on CF after 240 h soaking in 1.0 and 6.0 M KOH was not significantly different than before (Figure S2.30). We note that the anion in the polymer would have changed from perchlorate to hydroxide, some surface restructuring inevitably occurring during the long-term exposure to base, and the stability of the CF support to base is unknown under these conditions. Regardless, these findings, along with the stability of the operating OER electrode in 6M KOH, 85 °C, and 120 h, strongly indicate that polycarbazole is chemically stable under alkaline OER conditions.

Next, the electrochemical stability of PCz is checked by the galvanostatic tests on GC, CF, and Ni_{foam} with Ni₃Fe₁. Notably, If the binder is not electrochemically stable, the performance of electrodes for OER will drop. The Ni₃Fe₁ with Nafion binder is only electrochemically stable on the Ni_{foam} electrode in this paper (Figure 2.6b). The other Nafion binder on GC (Figures 2.3a,b; S2.8a,b) and CF (Figures S2.9a,b) fail to pass the galvanostatic tests. Impressively, all electrodes with PCz as a binder show good electrochemical stability during the OER tests (Figures 2.3a, 2.6b, S2.8a, S2.9a), and the CVs (Figures 2.3b, S2.8b, S2.9b, S2.23) change a little before and after the galvanostatic tests.

Supplementary Figures

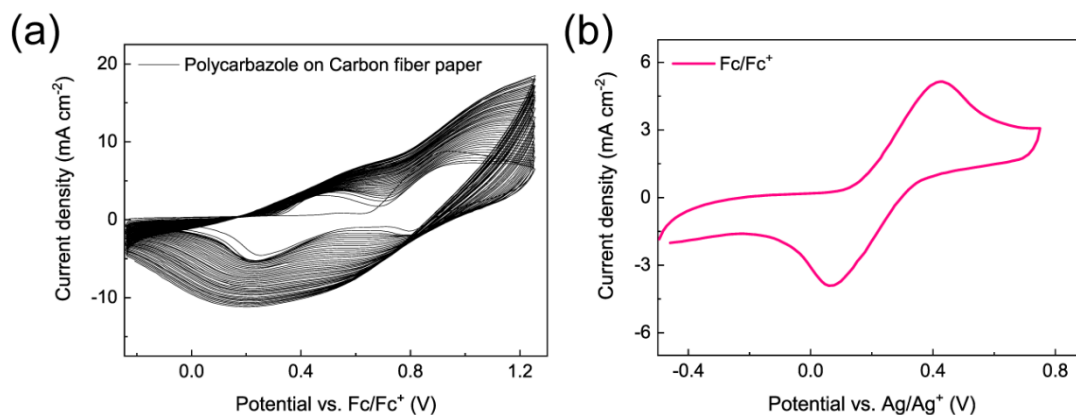


Figure S2.1. Growth of polycarbazole on carbon fiber paper (CF). (a) 45 cycles CV of CF electrode (area ~ 1 cm x 1 cm) in MeCN (0.1 M LiClO₄ and 0.005 M carbazole). (b) Corresponding of determining $E_{1/2}$ Fc/Fc⁺ reference in the same solution. The oxidation peak is at 0.423 V, and the reduction peak is at 0.0674 V vs. Ag/Ag⁺, $E_{1/2} = 0.245$ V

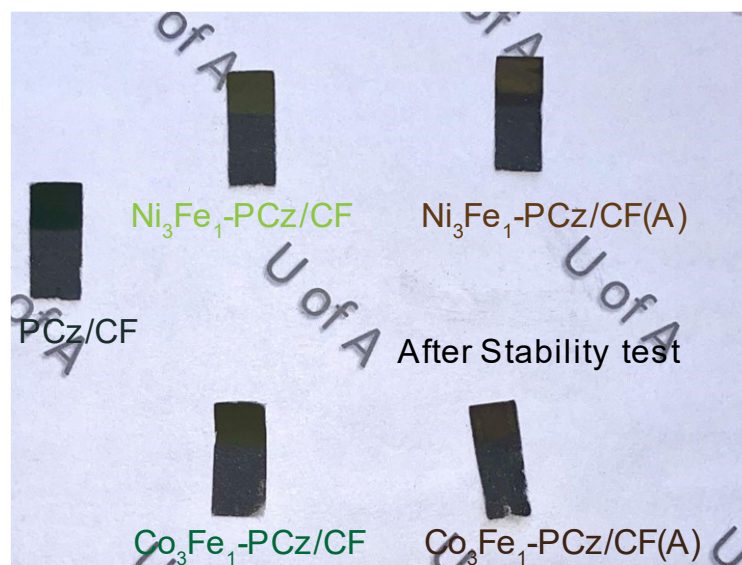


Figure S2.2. Picture of the CF electrodes. Polycarbazole grown on carbon fiber paper (PCz/CF), NiFe-PCz/CF, CoFe-PCz/CF, and the NiFe-PCz/CF(A), CoFe-PCz/CF(A) after 20 h stability test. The color changes from green (PCz/CF) to yellow (NiFe-PCz/CF) and green-yellow (CoFe-PCz/CF) after coordinating metal ions on the surface. NiFe-PCz/CF and CoFe-PCz/CF turn brown after 20 h stability test at 10 mA cm⁻²

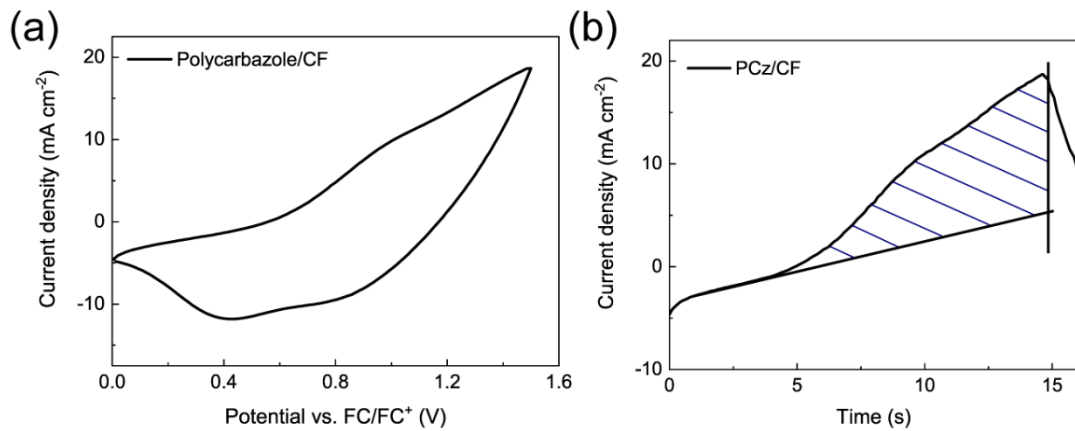


Figure S2.3. Estimation of polymer amount on PCz/CF electrode. (b) I-t curve and (a) corresponding LSV curve; Scan rate 100 mV s⁻¹

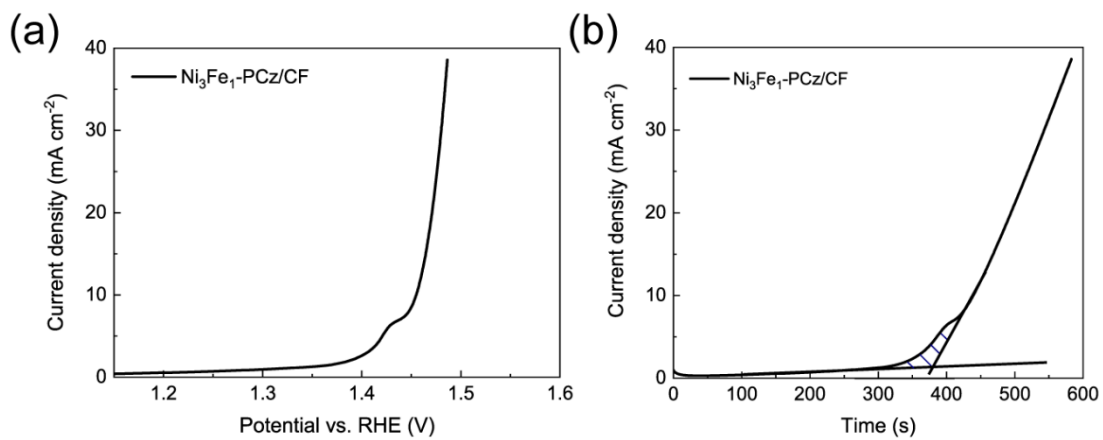


Figure S2.4. Estimation of Ni amount on Ni₃Fe₁-PCz/CF electrode. (b) I-t curve and (a) corresponding LSV curve; Scan rate 1 mV s⁻¹

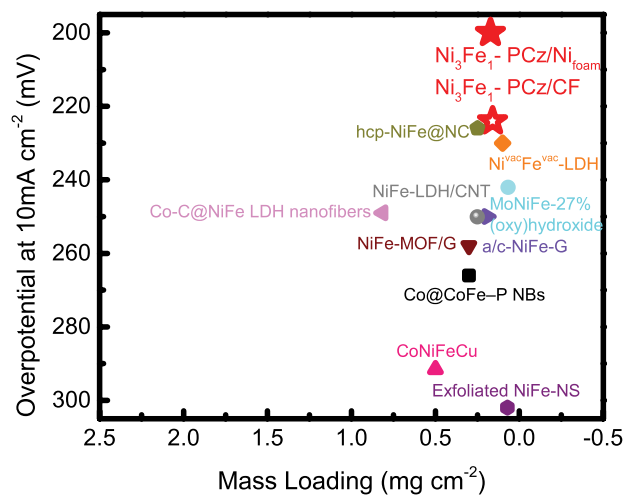


Figure S2.5. Comparison of literature with relatively low catalyst mass loading vs. OER overpotential. The mass loading of Ni₃Fe₁-PCz/Ni_{foam} is estimated from the Fe amount in ICP-OES supposing the ratio of Ni to Fe is 3 :1. The comparison is according to these references^{16–25}

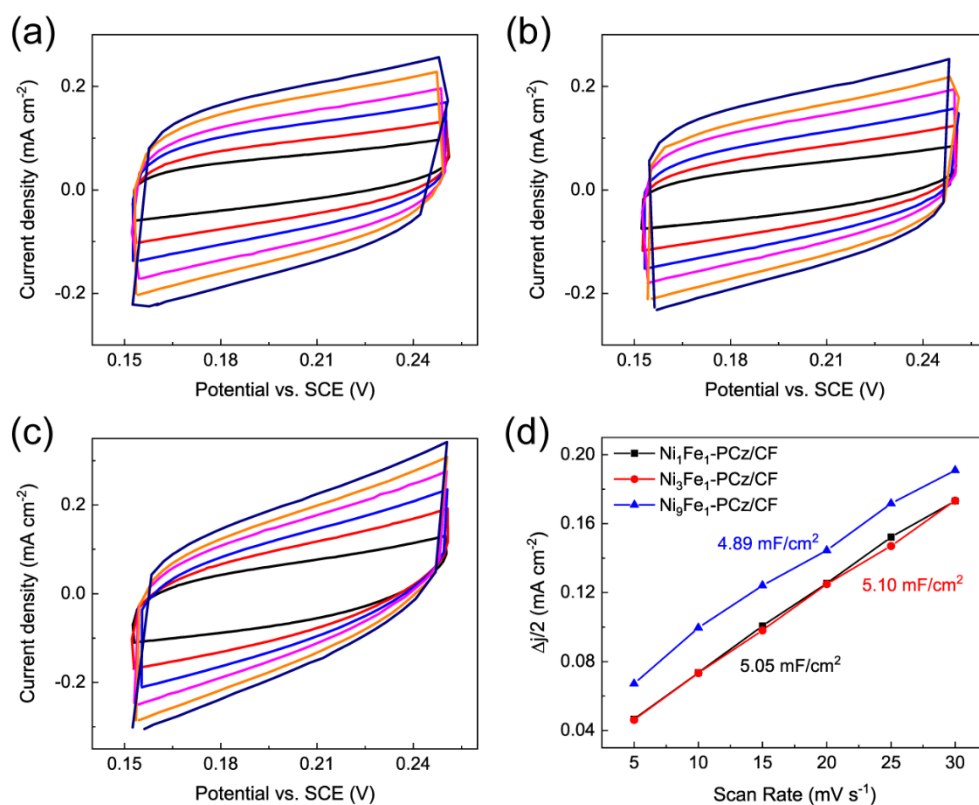


Figure S2.6. Determine double layer capacitance (C_{dl}) of Ni_xFe_y -PCz/CF electrodes. (a) CV scanning of Ni_1Fe_1 -PCz/CF, (b) Ni_3Fe_1 -PCz/CF, and (c) Ni_9Fe_1 -PCz/CF for ECSA estimation. (d) The corresponding C_{dl} numbers are shown in the graph

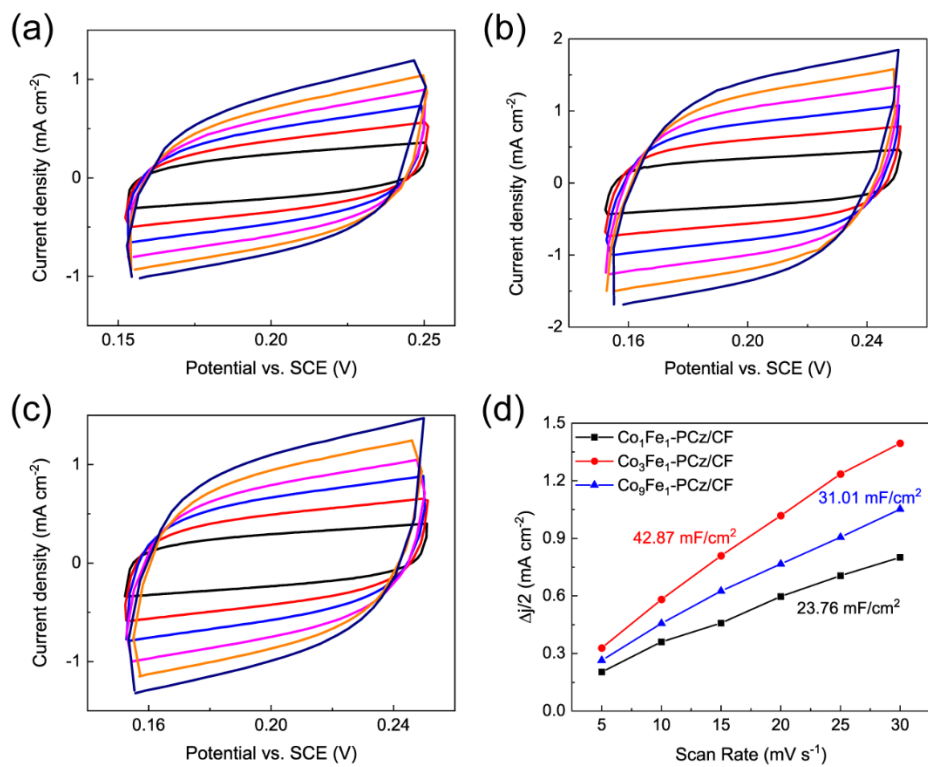


Figure S2.7. Determine double layer capacitance (C_{dl}) of $\text{Co}_x\text{Fe}_y\text{-PCz/CF}$ electrodes. (a) CV scanning of $\text{Co}_1\text{Fe}_1\text{-PCz/CF}$, (b) $\text{Co}_3\text{Fe}_1\text{-PCz/CF}$, and (c) $\text{Co}_9\text{Fe}_1\text{-PCz/CF}$ for ECSA estimation. (d) The corresponding C_{dl} numbers are shown in the graph

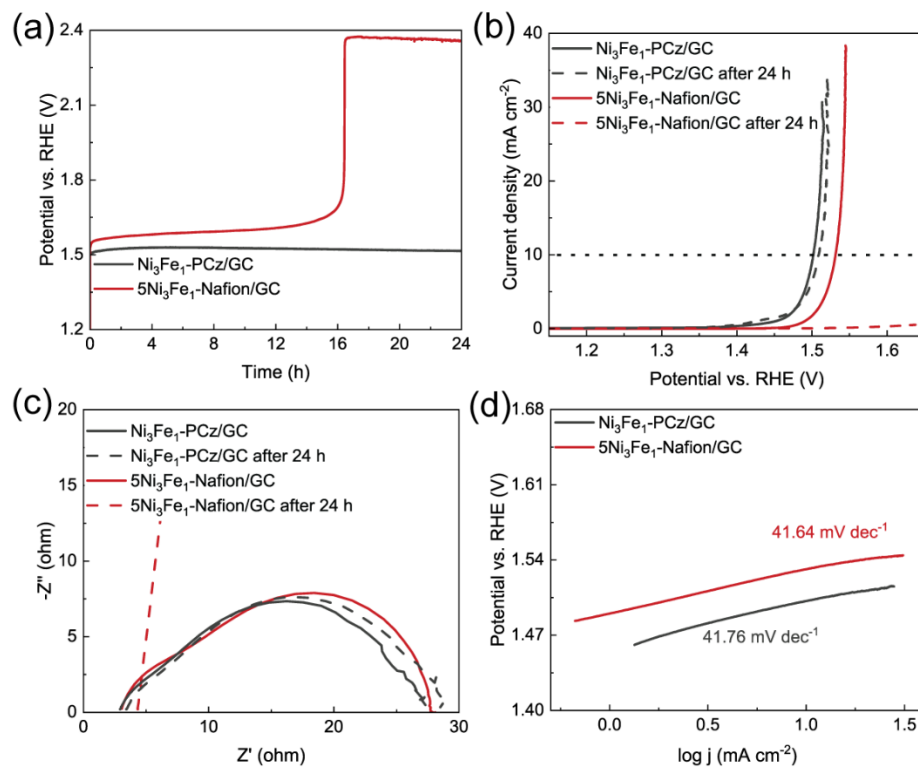


Figure S2.8. Stability of $\text{Ni}_3\text{Fe}_1\text{-PCz/GC}$ and $5\text{Ni}_3\text{Fe}_1\text{-Nafion/GC}$ electrodes. (a) The galvanostatic OER over $\text{Ni}_3\text{Fe}_1\text{-PCz/GC}$ and $5\text{Ni}_3\text{Fe}_1\text{-Nafion/GC}$ for 24 h at 10 mA cm^{-2} . (b) LSVs over $\text{Ni}_3\text{Fe}_1\text{-PCz/GC}$ and $5\text{Ni}_3\text{Fe}_1\text{-Nafion/GC}$ before and after 24 h stability tests. (c) Nyquist plots (at 0.5 V vs. SCE) for $\text{Ni}_3\text{Fe}_1\text{-PCz/GC}$ and $5\text{Ni}_3\text{Fe}_1\text{-Nafion/GC}$ before and after the 24 h stability tests. (d) Tafel slope of $\text{Ni}_3\text{Fe}_1\text{-PCz/GC}$ and $5\text{Ni}_3\text{Fe}_1\text{-Nafion/GC}$ before stability tests

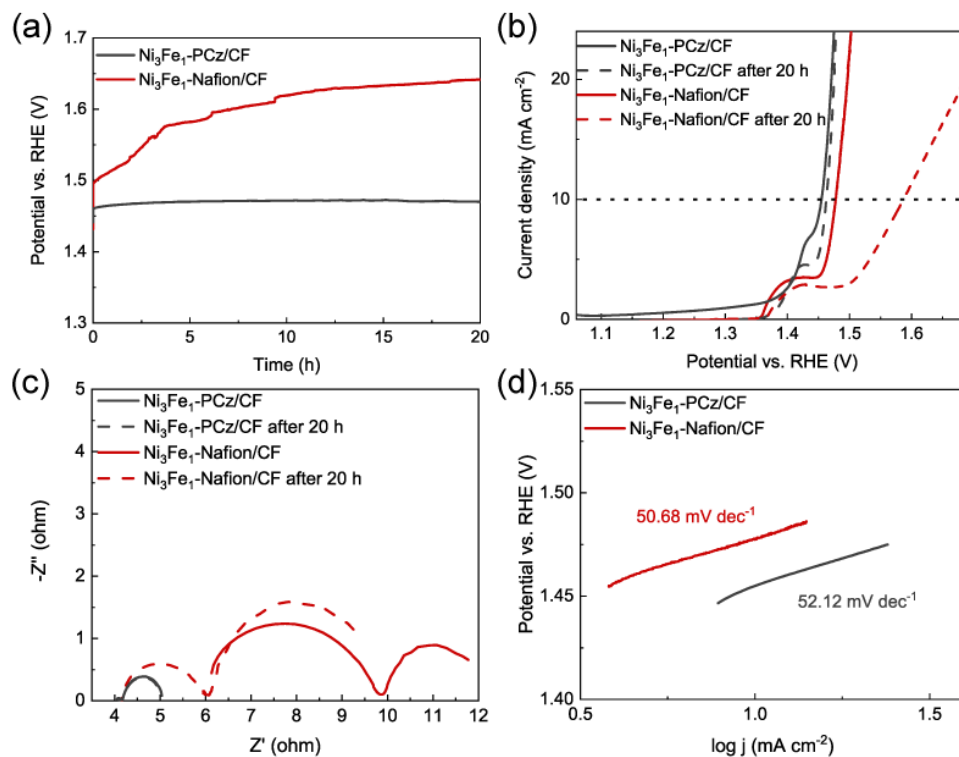


Figure S2.9. Performance of $\text{Ni}_3\text{Fe}_1\text{-PCz/CF}$ and $\text{Ni}_3\text{Fe}_1\text{-Nafion/CF}$ electrodes. (a) The galvanostatic OER over $\text{Ni}_3\text{Fe}_1\text{-PCz/CF}$ and $\text{Ni}_3\text{Fe}_1\text{-Nafion/CF}$ for 20 h at 10 mA cm^{-2} . (b) LSVs over $\text{Ni}_3\text{Fe}_1\text{-PCz/CF}$ and $\text{Ni}_3\text{Fe}_1\text{-Nafion/CF}$ before and after 20 h stability tests. (c) Nyquist plots (at 0.5 V vs. SCE) for $\text{Ni}_3\text{Fe}_1\text{-PCz/CF}$ and $\text{Ni}_3\text{Fe}_1\text{-Nafion/CF}$ before and after the 20 h stability tests. (d) Tafel slope of $\text{Ni}_3\text{Fe}_1\text{-PCz/CF}$ and $\text{Ni}_3\text{Fe}_1\text{-Nafion/CF}$ before stability tests. The Nyquist plots clearly show a difference in the impedance behavior of the polymer. A parent difference in initial activity between polymer carbazole and Nafion electrodes is minimized by the large range of the X-axis

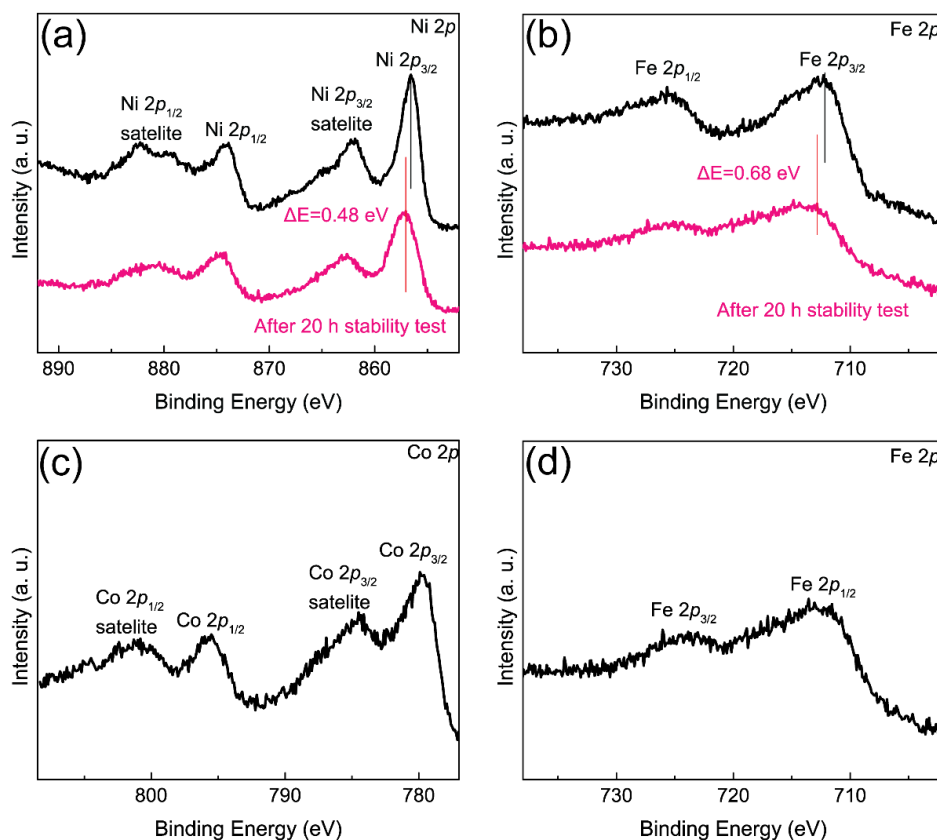


Figure S2.10. XPS of the electrodes on CF. (a) The Ni 2p and (b) Fe 2p regions in the high-resolution XPS spectra of Ni₃Fe₁-PCz/CF before (black line), and after the long-term galvanostatic OER (pink line) (conditions: Time, 20 h; current, 10 mA/cm²; solution, 1 M KOH). (c) and (d) are the Co 2p and Fe 2p regions in the high-resolution XPS spectra of Co₃Fe₁-PCz/CF

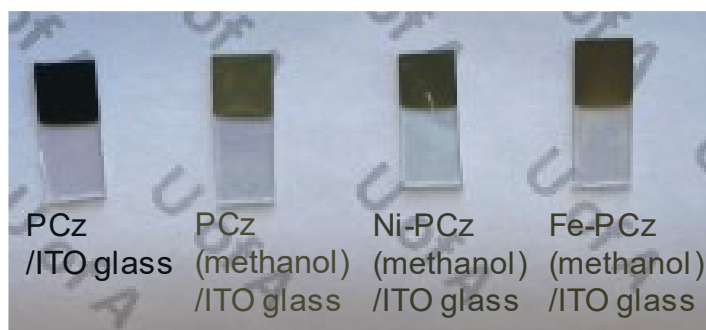


Figure S2.11. Picture of glass electrodes. Picture of polycarbazole grown on ITO glass (PCz/ITO); after soaking PCz/ITO in methanol for 24 h and dry (PCz (methanol)/ITO glass); after soaking PCz/ITO in methanol with Ni²⁺ ions for 24 h (Ni-PCz (methanol)/ITO glass) and after soaking PCz/ITO in methanol with Fe²⁺ ions for 24 h (Fe-PCz (methanol)/ITO glass) and dry

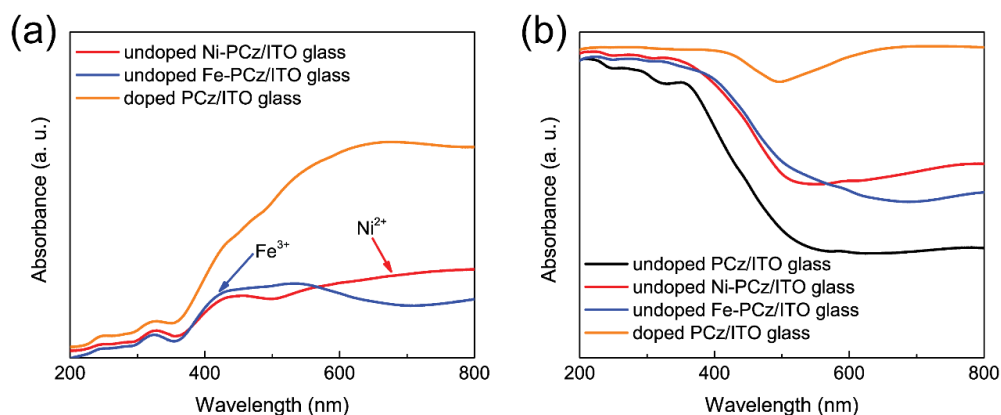


Figure S2.12. UV-Vis of different polycarbazole electrodes on ITO glass. (a) The UV-Vis graph subtracts undoped PCz/ITO glass as blank: Polycarbazole on ITO glass without soaking in methanol (doped PCz/ITO glass); Polycarbazole on ITO glass after soaking with Ni ions (undoped Ni-PCz/ITO glass); Polycarbazole on ITO glass after soaking with Fe ions (undoped Fe-PCz/ITO glass) and Polycarbazole on ITO glass after soaking in methanol without metal ions (undoped PCz/ITO glass). (b) The original UV-Vis graph without subtraction. The peak around 700 nm in undoped Ni-PCz/ITO glass represents the presence of Ni ions. The peak around 400 nm in both undoped Ni or Fe-PCz/ITO glass represents the presence of Ni and Fe ions. However, the Fe-PCz/ITO glass peak starts earlier and is stronger^{26,27}

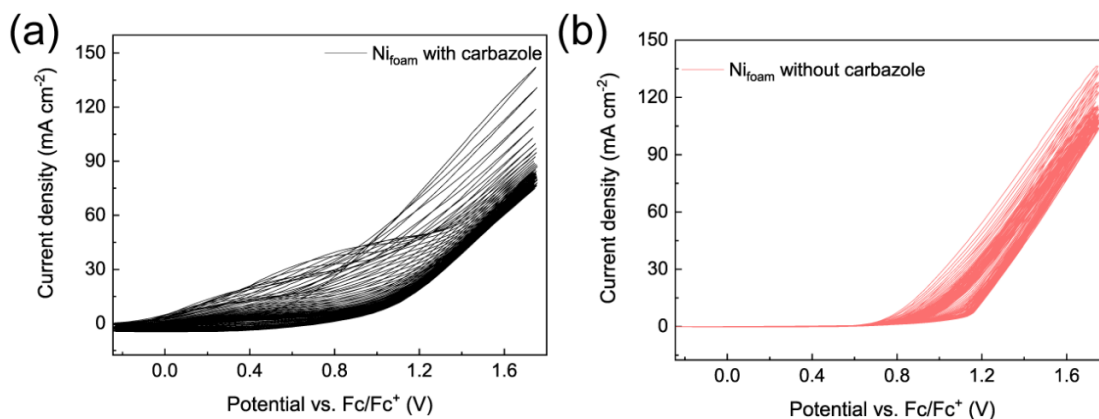


Figure S2.13. Comparison of CVs with or without carbazole on Ni foam. (a) 45 cycles CV of electropolymerization carbazole on Ni foam with 0.0050 M carbazoles and (b) without carbazole in 0.10 M LiClO₄ MeCN solution

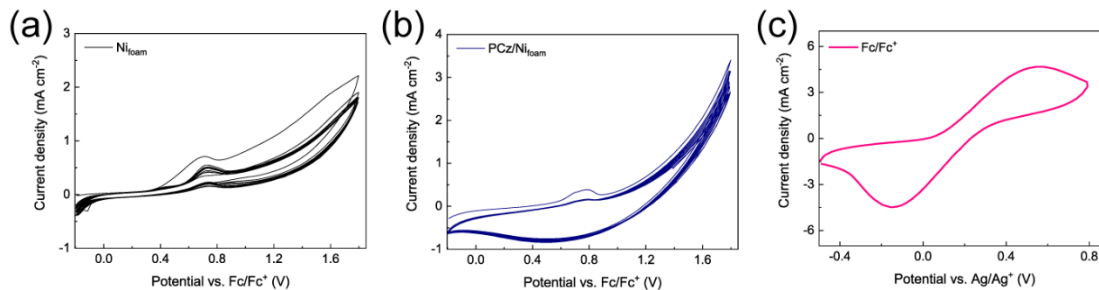


Figure S2.14. Comparison of Ni_{foam} and PCz/Ni_{foam} electrodes. (a) 10 cycles CV of Ni_{foam} and (b) PCz/Ni_{foam} electrode (area ~1 cm x 1 cm) in DCM with 0.1 M TBAPF₆. (c) Corresponding of determining $E_{1/2}$ of Fc/Fc⁺ reference in the same solution. The oxidation peak is at 0.555 V, and the reduction peak is at -0.149 V vs. Ag/Ag⁺. Therefore, $E_{1/2} = 0.203$ V

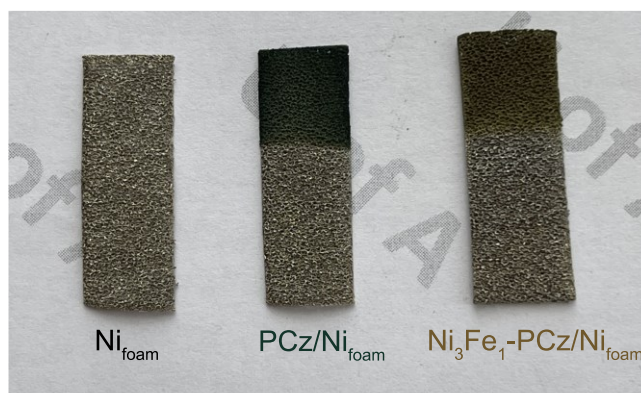


Figure S2.15. Picture of Ni foam (Ni_{foam}) electrodes. Picture of Ni_{foam}, polycarbazole grew on Ni_{foam} (PCz/Ni_{foam}), and NiFe metal ions coordinate on the polycarbazole (Ni₃Fe₁-PCz/Ni_{foam})

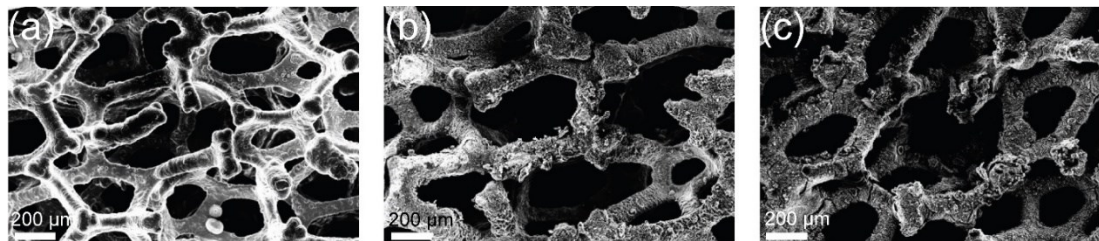


Figure S2.16. Morphology of Ni_{foam} electrodes. SEM surface morphology of the (a) Ni_{foam}, (b) PCz/Ni_{foam}, and (c) Ni₃Fe₁-PCz/Ni_{foam}

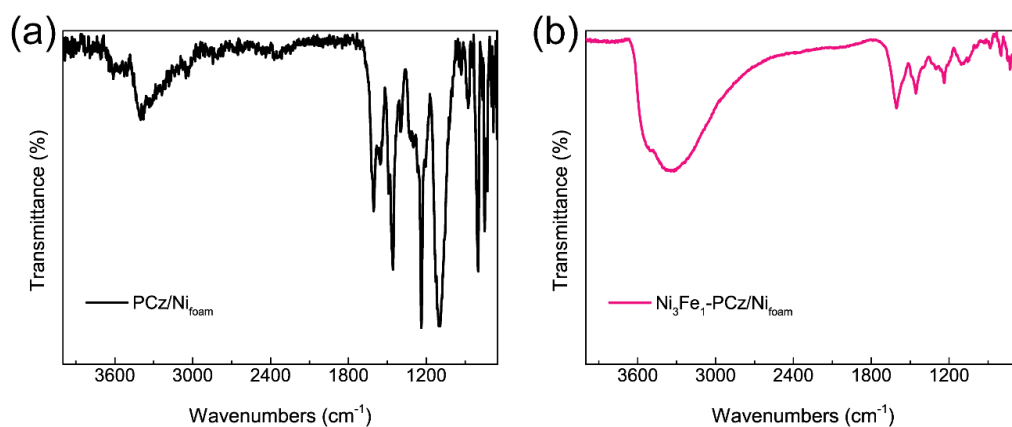


Figure S2.17. Comparison FTIR of Ni_{foam} electrodes. (a) FTIR spectra of the PCz/Ni_{foam} and (b) Ni₃Fe₁-PCz/Ni_{foam} electrodes

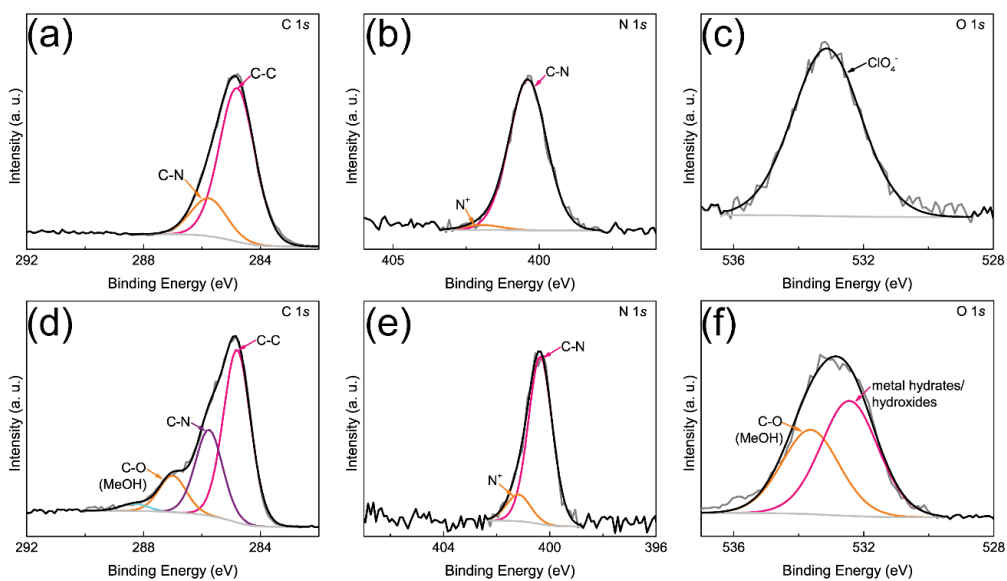


Figure S2.18. Comparison XPS of Ni_{foam} electrodes. XPS of (a) C 1s, (b) N 1s, and (c) O 1s in PCz/Ni_{foam}; XPS of (d) C 1s, (e) N 1s, and (f) O 1s in Ni₃Fe₁-PCz/Ni_{foam}

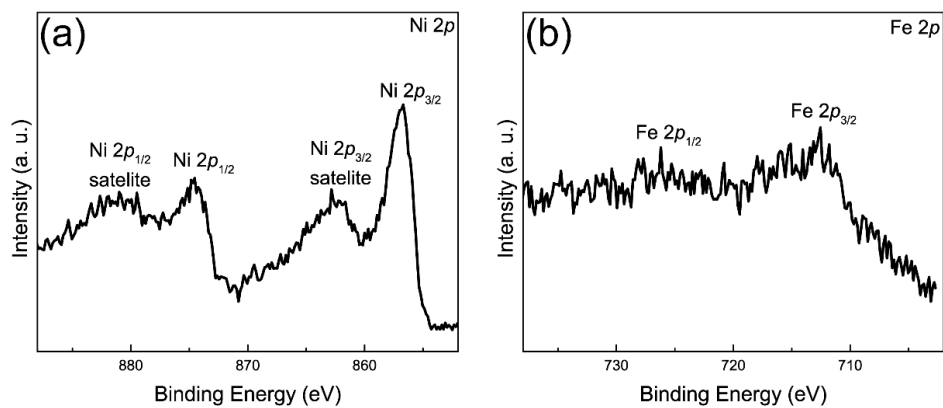


Figure S2.19. Ni, Fe XPS in $\text{Ni}_3\text{Fe}_1\text{-PCz/Ni}_{\text{foam}}$. (a) The Ni 2p and (b) Fe 2p regions in the high-resolution XPS spectra of $\text{Ni}_3\text{Fe}_1\text{-PCz/Ni}_{\text{foam}}$

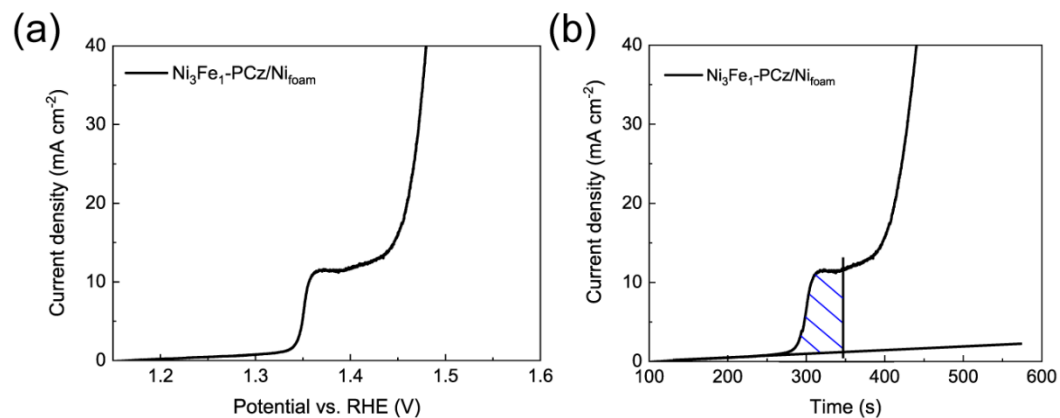


Figure S2.20. Estimation of Ni amount on $\text{Ni}_3\text{Fe}_1\text{-PCz/Ni}_{\text{foam}}$ electrode. (b) $I-t$ curve and (a) corresponding LSV curve ; Scan rate 1 mV s^{-1}

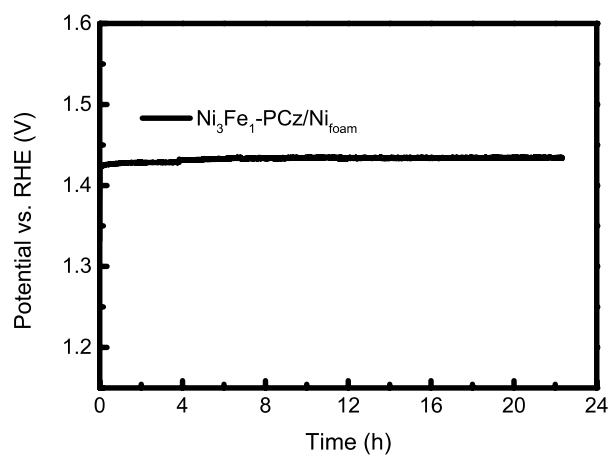


Figure S2.21. Galvanostatic stability test of $\text{Ni}_3\text{Fe}_1\text{-PCz/Ni}_{\text{foam}}$ at 10 mA cm^{-2} over 22 h. The performance of $\text{Ni}_3\text{Fe}_1\text{-PCz/Ni}_{\text{foam}}$ at 10 mA cm^{-2} was read after the stability test

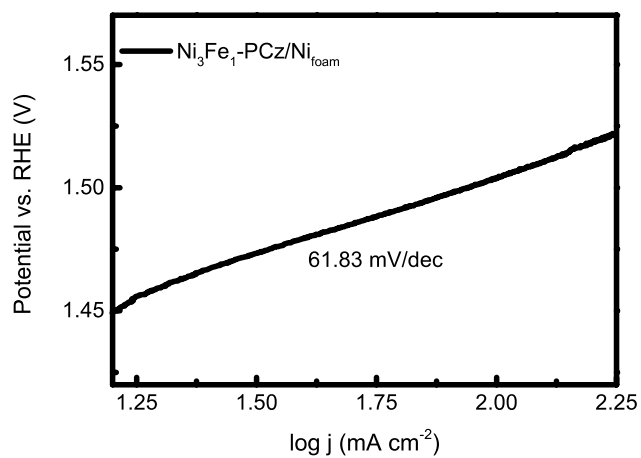


Figure S2.22. Tafel slope of $\text{Ni}_3\text{Fe}_1\text{-PCz/Ni}_{\text{foam}}$ electrode. Conditions: in 1 M KOH and scan rate of 1 mV s^{-1}

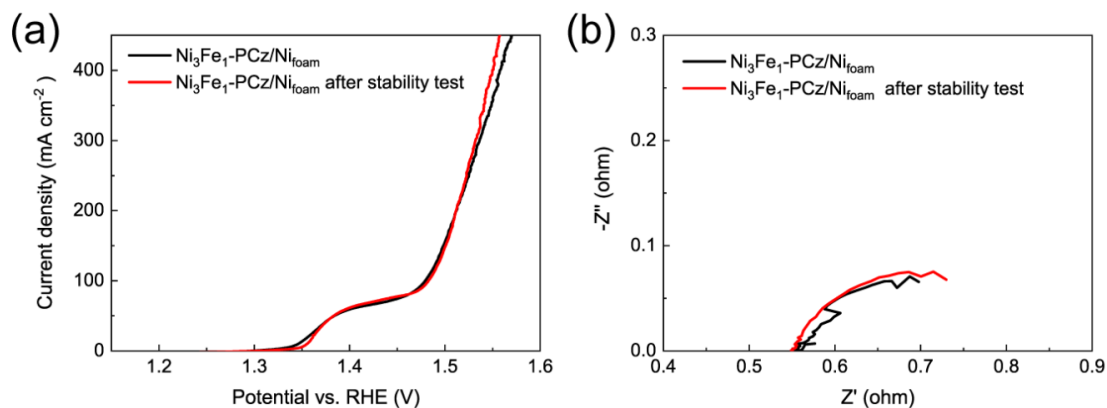


Figure S2.23. Stability test of Ni₃Fe₁-PCz/Ni_{foam}. (a) The LSV curves of Ni₃Fe₁-PCz/Ni_{foam} electrode before and after 24 h stability test 1 M KOH, scan rate 5 mV s⁻¹. (b) Nyquist plots of the Ni₃Fe₁-PCz/Ni_{foam} electrode before and after the 24 h stability test at 0.5 V vs. SCE. The curves are not in perfect shapes and may originate from O₂ bubble interference at this relatively high voltage

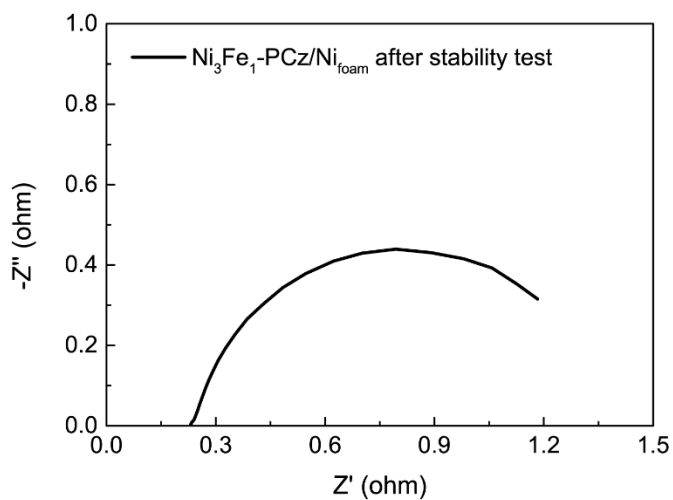


Figure S2.24. Stability test of Ni₃Fe₁-PCz/Ni_{foam} electrode under harsh conditions. Nyquist plot of the Ni₃Fe₁-PCz/Ni_{foam} electrode after 120 h stability test in 6 M KOH and 85 °C at 0.5 V vs. Hg/HgO reference electrode. The conversion from Hg/HgO to RHE is described in the supplementary text

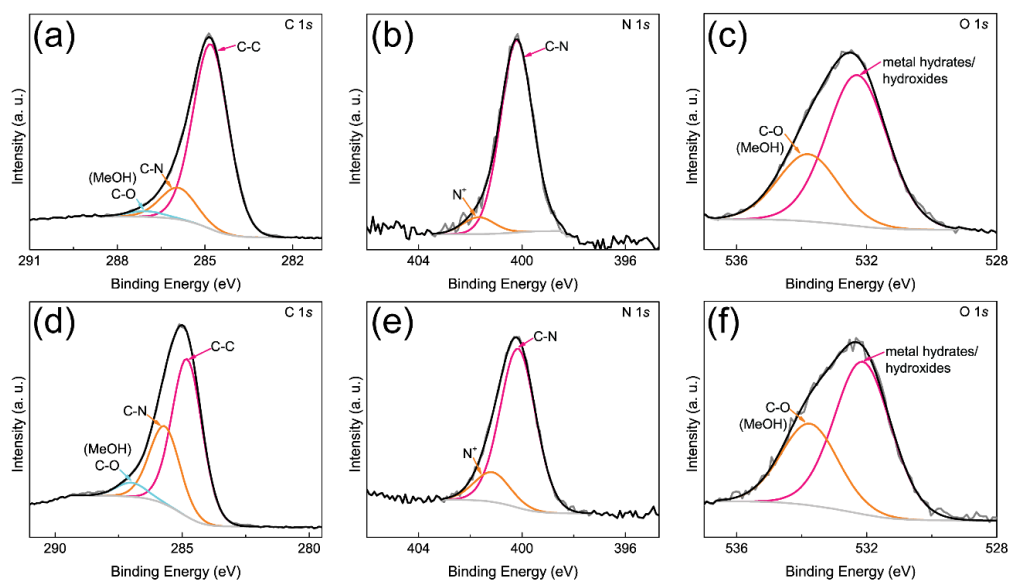


Figure S2.25. XPS of CF substrate electrodes. XPS of (a) C 1s, (b) N 1s, and (c) O 1s in $\text{Ni}_3\text{Fe}_1\text{-PCz/CF}$; XPS of (d) C 1s, (e) N 1s, and (f) O 1s in $\text{Co}_3\text{Fe}_1\text{-PCz/CF}$

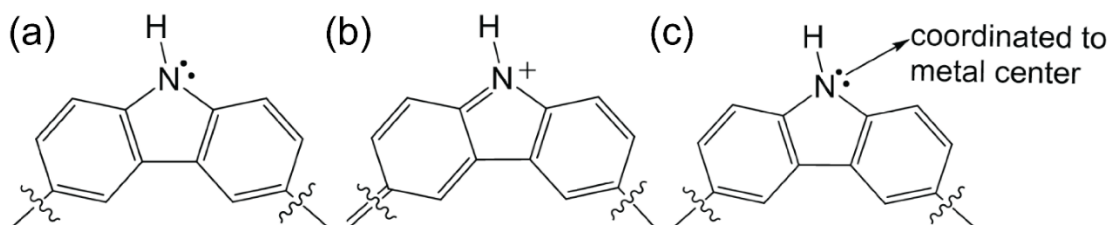


Figure S2.26. Illustration of different N sites of polycarbazole. (a) sp^2 C bonded to -C and -N, (b) N^+ in doped polycarbazole, (c) N coordinated to the metal

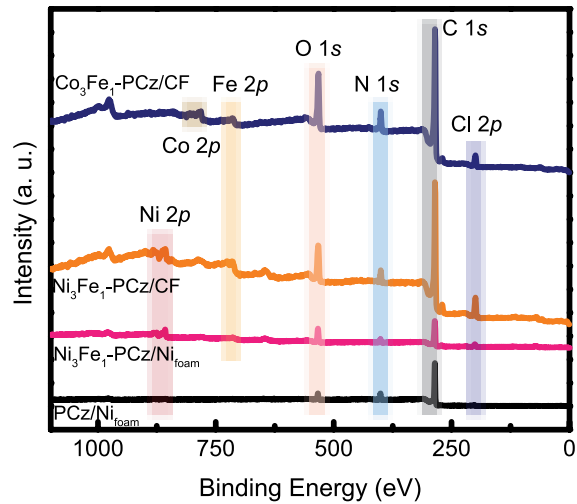


Figure S2.27. XPS survey spectra. From top to bottom: $\text{Co}_3\text{Fe}_1\text{-PCz/CF}$; $\text{Ni}_3\text{Fe}_1\text{-PCz/CF}$; $\text{Ni}_3\text{Fe}_1\text{-PCz/Ni}_{\text{foam}}$; $\text{PCz/Ni}_{\text{foam}}$

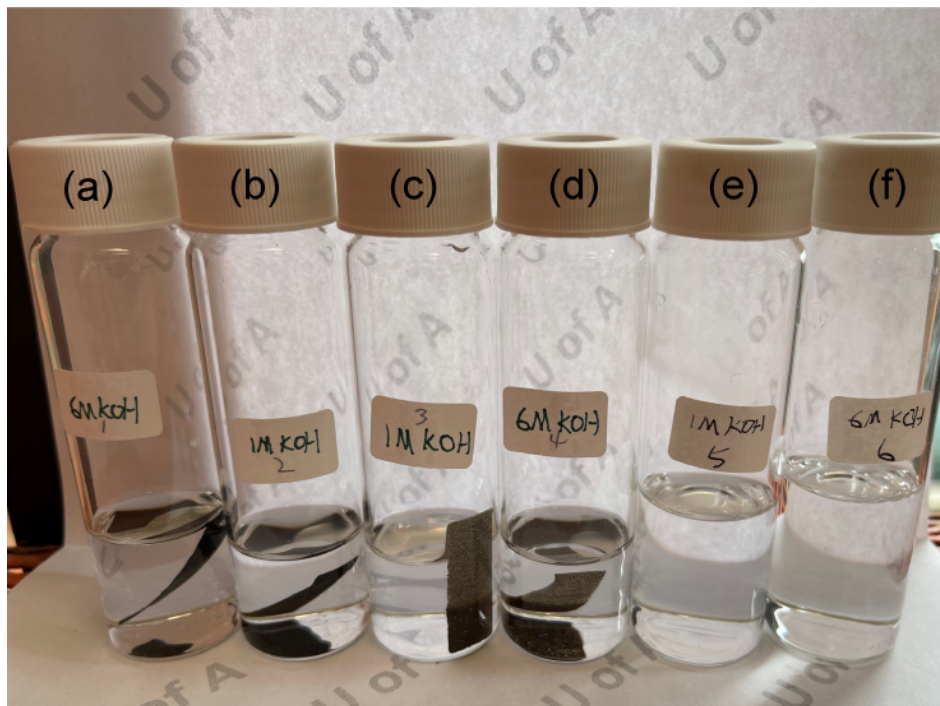


Figure S2.28. Chemical stability test of PCz. (a, b) PCz/CF in 6 M KOH and 1 M KOH over 240 h. (c, d) PCz/ Ni_{foam} in 1 M KOH and 6 M KOH over 240 h. (e, f) 1 M KOH and 6 M KOH without any electrode

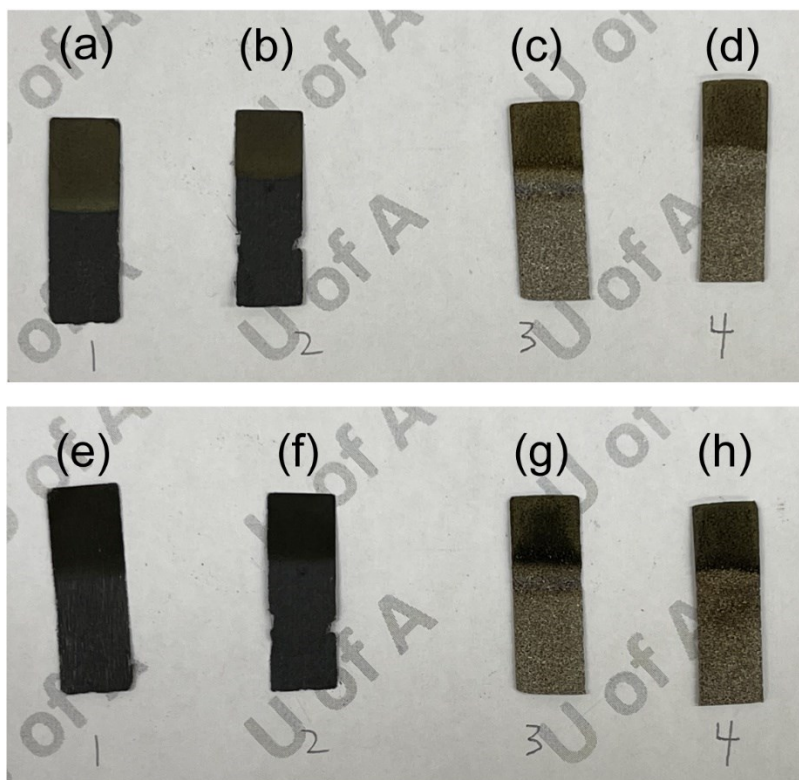


Figure S2.29. Electrodes before and after CV tests. (a, b) After soaking the PCz/CF electrodes in 6 M KOH or 1 M KOH for 240 h, then washing with triple-distilled water before CV tests. (c, d) After soaking the PCz/CF electrodes in 6 M KOH or 1 M KOH for 240 h, then washing with triple-distilled water before CV tests. (e – h) a, b, c, and d electrodes after CV tests

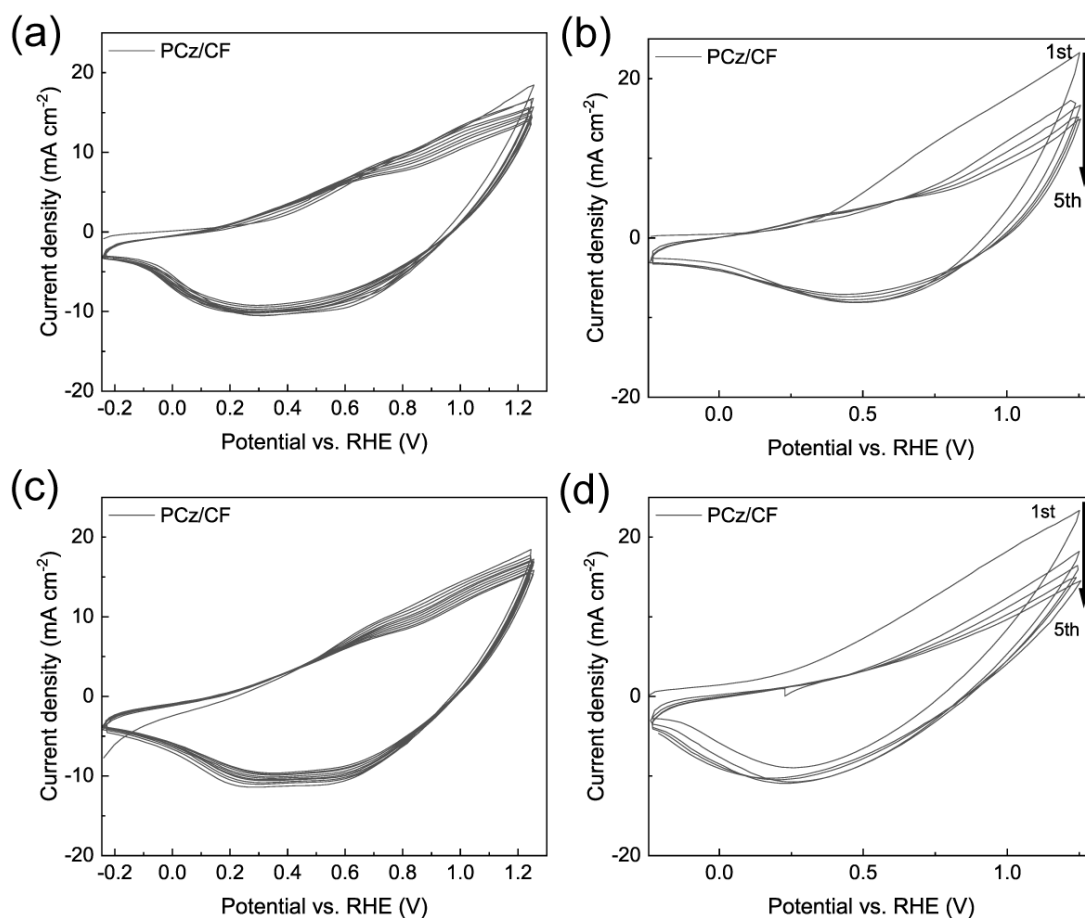


Figure S2.30. CVs before and after soaking in KOH. (a, b) CVs of PCz/CF electrodes before and after 1 M KOH soaking over 240 h. (c, d) CVs of PCz/CF electrodes before and after 6 M KOH soaking over 240 h

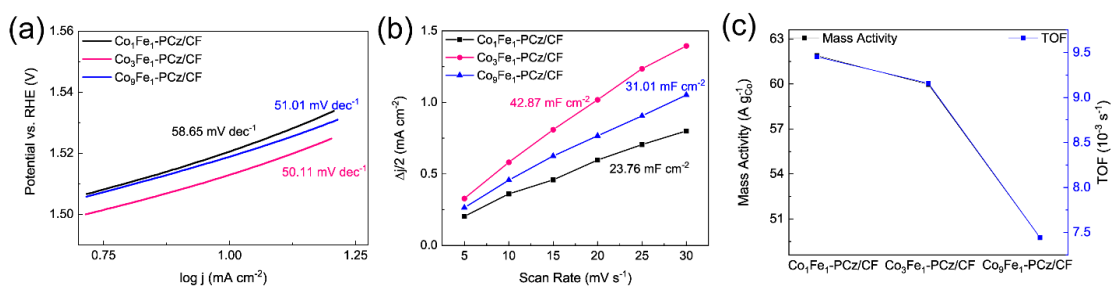


Figure S2.31. Performance of electrodes on PCz/CF substrates. (a) Tafel slope, (b) double layer capacitance, and (c) mass activity (left) and TOF (right) at 1.50 V vs. RHE curves for Co_1Fe_1 , Co_3Fe_1 , and Co_9Fe_1 -PCz/CF

Supplementary Tables

Table S2.1. ICP-OES Results of Different Ratios of Ni, Fe and Ni, Co Electrodes. The Mole Ratios and Double Layer Capacitance (C_{dl}) Numbers are Calculated and Shown in the Table.

Label	Co (μg)	Fe (μg)	The ratio of Co to Fe	Co ($\mu\text{ Moles}$)	Fe ($\mu\text{ Moles}$)	C_{dl} (mF)
Co ₁ Fe ₁	57.91	64.41	0.853: 1	0.983	1.153	23.76
Co ₃ Fe ₁	86.45	32.12	2.55: 1	1.467	0.575	42.87
Co ₉ Fe ₁	77.9	10.03	7.39: 1	1.322	0.179	31.01
Label	Ni (μg)	Fe (μg)	The ratio of Ni to Fe	Ni ($\mu\text{ Moles}$)	Fe ($\mu\text{ Moles}$)	C_{dl} (mF)
Ni ₁ Fe ₁	53.3	50.4	1.01: 1	0.908	0.902	5.05
Ni ₃ Fe ₁	124.43	35.75	3.31: 1	2.12	0.64	5.10
Ni ₉ Fe ₁	100.89	17.47	5.51: 1	1.719	0.312	4.89

Table S2.2. Table for Comparisons of the Output Results for Electrochemical Water Oxidation.

Catalyst	Support	overpotential@ 10 mA cm ²	Stability test time	overpotential@ 100 mA cm ²	Stability test time
Co ₁ Fe ₁ -PCz	CF	291 mV			
Co ₃ Fe ₁ -PCz	CF	283 mV			
Co ₉ Fe ₁ -PCz	CF	289 mV			
Ni ₁ Fe ₁ -PCz	CF	245 mV			
Ni ₃ Fe ₁ -PCz	CF	224 mV	20 h		
Ni ₉ Fe ₁ -PCz	CF	253 mV			
Ni ₃ Fe ₁ -PCz	GC	272 mV	24 h		
Ni ₃ Fe ₁ -PCz	Ni foam	~200 mV	22 h	264 mV	24 h
Ni ₃ Fe ₁ -PCz ^a	Ni foam			~210 mV	120 h

^a Ni₃Fe₁-PCz/Ni_{foam} electrode under harsh conditions (6 M KOH, 85 °C) without *iR* compensation.

Supplementary References

- (1) Hausmann, J. N.; Traynor, B.; Myers, R. J.; Driess, M.; Menezes, P. W. The PH of Aqueous NaOH/KOH Solutions: A Critical and Non-Trivial Parameter for Electrocatalysis. *ACS Energy Lett.* **2021**, *6* (10), 3567–3571. <https://doi.org/10.1021/acseenergylett.1c01693>.
- (2) Nickell, R. A.; Zhu, W. H.; Payne, R. U.; Cahela, D. R.; Tatarchuk, B. J. Hg/HgO Electrode and Hydrogen Evolution Potentials in Aqueous Sodium Hydroxide. *Journal of Power Sources* **2006**, *161* (2), 1217–1224. <https://doi.org/10.1016/j.jpowsour.2006.05.028>.
- (3) Zhang, J.; Hu, Y.; Liu, D.; Yu, Y.; Zhang, B. Enhancing Oxygen Evolution Reaction at High Current Densities on Amorphous-Like Ni-Fe-S Ultrathin Nanosheets via Oxygen Incorporation and Electrochemical Tuning. *Adv. Sci.* **2017**, *4* (3), 1600343. <https://doi.org/10.1002/adv.201600343>.
- (4) Sezai Sarac, A.; Ates, M.; Parlak, E. A. Electrolyte and Solvent Effects of Electrocoated Polycarbazole Thin Films on Carbon Fiber Microelectrodes. *J Appl Electrochem* **2006**, *36* (8), 889–898. <https://doi.org/10.1007/s10800-006-9145-8>.
- (5) Ambrose, J. F.; Carpenter, L. L.; Nelson, R. F. Electrochemical and Spectroscopic Properties of Cation Radicals: III. Reaction Pathways of Carbazolium Radical Ions. *J. Electrochem. Soc.* **1975**, *122* (7), 876–894. <https://doi.org/10.1149/1.2134365>.
- (6) Ates, M.; Sarac, A. S.; Turhan, C. M.; Ayaz, N. E. Polycarbazole Modified Carbon Fiber Microelectrode: Surface Characterization and Dopamine Sensor. *Fibers Polym* **2009**, *10* (1), 46–52. <https://doi.org/10.1007/s12221-009-0046-4>.
- (7) Bekkar, F.; Bettahar, F.; Moreno, I.; Meghabar, R.; Hamadouche, M.; Hernández, E.; Vilas-Vilela, J. L.; Ruiz-Rubio, L. Polycarbazole and Its Derivatives: Synthesis and Applications. A Review of the Last 10 Years. *Polymers* **2020**, *12* (10), 2227. <https://doi.org/10.3390/polym12102227>.
- (8) Bernede, J. C.; Taoudi, H.; Bonnet, A.; Molinie, P.; Morsli, M.; De Valle, M. A.; Diaz, F. XPS and ESR Studies of Electrochemically Synthesized Polycarbazole Post-Doped with Iodine. *J. Appl. Polym. Sci.* **1999**, *71* (1), 115–124. [https://doi.org/10.1002/\(SICI\)1097-4628\(19990103\)71:1<115::AID-APP14>3.0.CO;2-Y](https://doi.org/10.1002/(SICI)1097-4628(19990103)71:1<115::AID-APP14>3.0.CO;2-Y).
- (9) Primbs, M.; Sun, Y.; Roy, A.; Malko, D.; Mehmood, A.; Sougrati, M.-T.; Blanchard, P.-Y.; Granozzi, G.; Kosmala, T.; Daniel, G.; Atanassov, P.; Sharman, J.; Durante, C.; Kucernak, A.; Jones, D.; Jaouen, F.; Strasser, P. Establishing Reactivity Descriptors for Platinum Group Metal (PGM)-Free Fe–N–C Catalysts for PEM Fuel Cells. *Energy Environ. Sci.* **2020**, *13* (8), 2480–2500. <https://doi.org/10.1039/D0EE01013H>.
- (10) Qiu, Z.; Tai, C.-W.; Niklasson, G. A.; Edvinsson, T. Direct Observation of Active Catalyst Surface Phases and the Effect of Dynamic Self-Optimization in NiFe-Layered Double Hydroxides for Alkaline Water Splitting. *Energy Environ. Sci.* **2019**, *12* (2), 572–581. <https://doi.org/10.1039/C8EE03282C>.
- (11) Sun, W.; Sun, W.; Zhuo, Y.; Chu, Y. Facile Synthesis of Cu₂O Nanocube/Polycarbazole Composites and Their High Visible-Light Photocatalytic Properties. *Journal of Solid State Chemistry* **2011**, *184* (7), 1638–1643. <https://doi.org/10.1016/j.jssc.2011.03.055>.
- (12) Zahoor, A.; Qiu, T.; Zhang, J.; Li, X. Synthesis and Characterization of Ag@polycarbazole Nanoparticles and Their Novel Optical Behavior. *J Mater Sci* **2009**, *44* (22), 6054–6059. <https://doi.org/10.1007/s10853-009-3831-y>.
- (13) Saxena, V.; Choudhury, S.; Jha, P.; Koiry, S. P.; Debnath, A. K.; Aswal, D. K.; Gupta, S. K.; Yakhmi, J. V. In Situ Spectroscopic Studies to Investigate Uncharacteristic NH₃ Sensing Behavior of

- Polycarbazole Langmuir–Blodgett Films. *Sensors and Actuators B: Chemical* **2010**, *150* (1), 7–11. <https://doi.org/10.1016/j.snb.2010.08.002>.
- (14) Netskina, O. V.; Pochtar, A. A.; Komova, O. V.; Simagina, V. I. Solid-State NaBH₄ Composites as Hydrogen Generation Material: Effect of Thermal Treatment of a Catalyst Precursor on the Hydrogen Generation Rate. *Catalysts* **2020**, *10* (2), 201. <https://doi.org/10.3390/catal10020201>.
- (15) Inam, M.; Khan, R.; Park, D.; Lee, Y.-W.; Yeom, I. Removal of Sb(III) and Sb(V) by Ferric Chloride Coagulation: Implications of Fe Solubility. *Water* **2018**, *10* (4), 418. <https://doi.org/10.3390/w10040418>.
- (16) Zhao, Y.; Dongfang, N.; Triana, C. A.; Huang, C.; Erni, R.; Wan, W.; Li, J.; Stoian, D.; Pan, L.; Zhang, P.; Lan, J.; Iannuzzi, M.; Patzke, G. R. Dynamics and Control of Active Sites in Hierarchically Nanostructured Cobalt Phosphide/Chalcogenide-Based Electrocatalysts for Water Splitting. *Energy Environ. Sci.* **2022**, *15* (2), 727–739. <https://doi.org/10.1039/D1EE02249K>.
- (17) Zhang, J.; Quast, T.; He, W.; Dieckhöfer, S.; Junqueira, J. R. C.; Öhl, D.; Wilde, P.; Jambrec, D.; Chen, Y.; Schuhmann, W. In Situ Carbon Corrosion and Cu Leaching as a Strategy for Boosting Oxygen Evolution Reaction in Multimetal Electrocatalysts. *Advanced Materials* **2022**, 2109108. <https://doi.org/10.1002/adma.202109108>.
- (18) He, Z.; Zhang, J.; Gong, Z.; Lei, H.; Zhou, D.; Zhang, N.; Mai, W.; Zhao, S.; Chen, Y. Activating Lattice Oxygen in NiFe-Based (Oxy)Hydroxide for Water Electrolysis. *Nat Commun* **2022**, *13* (1), 2191. <https://doi.org/10.1038/s41467-022-29875-4>.
- (19) Wang, Y.; Liu, B.; Shen, X.; Arandiyana, H.; Zhao, T.; Li, Y.; Garbrecht, M.; Su, Z.; Han, L.; Tricoli, A.; Zhao, C. Engineering the Activity and Stability of MOF - Nanocomposites for Efficient Water Oxidation. *Adv. Energy Mater.* **2021**, *11* (16), 2003759. <https://doi.org/10.1002/aenm.202003759>.
- (20) Peng, L.; Yang, N.; Yang, Y.; Wang, Q.; Xie, X.; Sun - Waterhouse, D.; Shang, L.; Zhang, T.; Waterhouse, G. I. N. Atomic Cation - Vacancy Engineering of NiFe - Layered Double Hydroxides for Improved Activity and Stability towards the Oxygen Evolution Reaction. *Angew. Chem. Int. Ed.* **2021**, *60* (46), 24612–24619. <https://doi.org/10.1002/anie.202109938>.
- (21) Li, W.; Chen, S.; Zhong, M.; Wang, C.; Lu, X. Synergistic Coupling of NiFe Layered Double Hydroxides with Co-C Nanofibers for High-Efficiency Oxygen Evolution Reaction. *Chemical Engineering Journal* **2021**, *415*, 128879. <https://doi.org/10.1016/j.cej.2021.128879>.
- (22) Gong, Z.; Liu, R.; Gong, H.; Ye, G.; Liu, J.; Dong, J.; Liao, J.; Yan, M.; Liu, J.; Huang, K.; Xing, L.; Liang, J.; He, Y.; Fei, H. Constructing a Graphene-Encapsulated Amorphous/Crystalline Heterophase NiFe Alloy by Microwave Thermal Shock for Boosting the Oxygen Evolution Reaction. *ACS Catal.* **2021**, *11* (19), 12284–12292. <https://doi.org/10.1021/acscatal.1c03333>.
- (23) Wang, C.; Yang, H.; Zhang, Y.; Wang, Q. NiFe Alloy Nanoparticles with Hcp Crystal Structure Stimulate Superior Oxygen Evolution Reaction Electrocatalytic Activity. *Angew. Chem. Int. Ed.* **2019**, *58* (18), 6099–6103. <https://doi.org/10.1002/anie.201902446>.
- (24) Song, F.; Hu, X. Exfoliation of Layered Double Hydroxides for Enhanced Oxygen Evolution Catalysis. *Nat Commun* **2014**, *5* (1), 4477. <https://doi.org/10.1038/ncomms5477>.
- (25) Gong, M.; Li, Y.; Wang, H.; Liang, Y.; Wu, J. Z.; Zhou, J.; Wang, J.; Regier, T.; Wei, F.; Dai, H. An Advanced Ni–Fe Layered Double Hydroxide Electrocatalyst for Water Oxidation. *J. Am. Chem. Soc.* **2013**, *135* (23), 8452–8455. <https://doi.org/10.1021/ja4027715>.
- (26) Zhang, N.; Brugger, J.; Etschmann, B.; Ngothai, Y.; Zeng, D. Thermodynamic Modeling of Poorly Complexing Metals in Concentrated Electrolyte Solutions: An X-Ray Absorption and UV-Vis

Spectroscopic Study of Ni(II) in the NiCl₂-MgCl₂-H₂O System. *PLoS ONE* **2015**, *10* (4), e0119805.
<https://doi.org/10.1371/journal.pone.0119805>.

(27) Liu, W.; Etschmann, B.; Brugger, J.; Spiccia, L.; Foran, G.; McInnes, B. UV-Vis Spectrophotometric and XAFS Studies of Ferric Chloride Complexes in Hyper-Saline LiCl Solutions at 25–90 °C. *Chemical Geology* **2006**, *231* (4), 326–349.
<https://doi.org/10.1016/j.chemgeo.2006.02.005>.

APPENDIX B

Supporting Information for A One-Step Electropolymerization of a Dicyanobenzene-Carbazole-Imidazole Dye for Photoelectrodes, Heterogeneous Photocatalysts, and Sensing Applications

General Information

Photoelectrochemistry

The photoactivity of the electrodes was investigated in two different PH solutions: a 0.1 M NaClO₄ water solution containing 0.02 M hydroquinone (pH = 7.0), and a 0.1 M NaClO₄ water solution containing 0.5 M triethylamine (pH = 12.6). The reference and counter electrodes were saturated calomel electrode (SCE) and high surface area platinum gauze, respectively. The reaction was carried out in a four-neck quartz flask (total volume of 100 mL), and a flat window was used as the reaction flask. The electrolyte was stirred using a magnetic bar during the measurements. Before each experiment, the electrolyte was purged with argon for 20 min, and an argon gas atmosphere was maintained on top of the solution throughout the studies. The light source was a 300 W Xe lamp equipped with a Cornerstone M 260 QEPVSI-b monochromator from Newport. The incident light intensity was determined by a Thorlab S121C light meter at each wavelength. The incident photon to current conversion efficiencies (IPCEs) at any given wavelength was calculated using the following equation:

$$IPCE (\%) = (1240i / (P\lambda)) \times 100 \quad S3.1$$

where λ is the specific wavelength of irradiated light (nm), P is light power density (mW cm⁻²), and i is the measured photocurrent density (mA cm⁻²). For electrochemical studies, a Solartron SI 1287 potentiostat equipped with Frequency Response Analyzer SI 1260 was used.

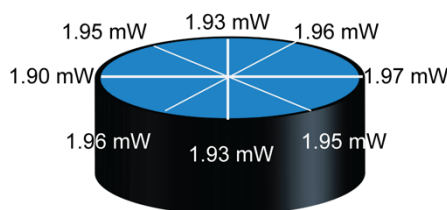
Estimation of Surface Coverage on The Electrodes Using Cyclic Voltammetry (CV)

Initially, the $I-t$ curves were generated based on the corresponding CV curves with known scan rates. The total charge in Coulombs (Q) subsequently was calculated by integrating the dicyanobenzene oxidation peak. Additionally, the number of moles of the substance on the electrodes (*mole*) was determined using the following equation:

$$\text{mole} = Q/N_A e \quad \text{S3.2}$$

where Q is the total charge of Coulomb, N_A is the Avogadro constant, and e is the Coulomb number for one electron.

Determine Apparent Quantum Efficiency



Average power in the middle: 1.94 mW

Photodiode Power Sensor (S121C)

Actual detector area:
 $\pi \cdot (0.95/2) \cdot (0.95/2) \text{ cm}^2 = 0.71 \text{ cm}^2$

Average intensity in the middle:
 $1.94 \text{ mW} / 0.71 \text{ cm}^2 = 2.73 \text{ mW cm}^{-2}$

Surface area of an electrode: $\sim 1 \text{ cm}^2$

The reactor apparatus was prepared with either a 1-ITO-NP glass slide electrodes or ITO-NP glass slide electrode in a glass vial, which was filled with a solution of *trans*-stilbene at the start of the experiment. To ensure an argon atmosphere, the vial containing the sample was transferred to a larger Schlenk line side arm flask, which then was positioned at the center of a glass cylinder wrapped with LED tape emitting at 450 nm. The intensity of the light was measured at 45° intervals, with a photodiode power sensor positioned at the center of the vial. The average intensity in the middle of the vial was found to be 2.73 mW cm⁻², and the surface area of one electrode was approximately 1 cm². Based on these values, the total energy of the incident photon flux over 16 h was calculated as 157.25 J, by the formula $1.94 \times 10^{-3} \text{ (J s}^{-1}) \text{ (cm}^{-2}) \times 1 \text{ cm}^2 \times (16 \times 60 \times 60) \text{ s}$. This result corresponds to 0.59 mmol photons (by $157.25 \text{ J} / 4.41424 \times 10^{-19} \text{ J} / N_A$; the energy of one photon at 450 nm is $4.41424 \times 10^{-19} \text{ J}$; N_A is Avogadro constant). Apparent quantum efficiency (AQE) = # of moles of *cis*-stilbene produced/# of moles of photons

AQY = 0.25 mmol x 32.49%/0.59154 mmol = 13.73% (5 cycles); 9.02% (10 cycles); 7.61% (45 cycles).

Calculation Method

We employed the Gaussian 16 software¹ package to conduct the Time-Dependent Density Functional Theory (TD-DFT) calculations. Specifically, the molecular structures were computed using the B3LYP (Becke, three-parameter, Lee-Yang-Parr) hybrid functional² to describe the exchange-correlation energies. Basis sets were implemented to enable high-level B3LYP calculations at 6-31+G(d,p)³ for atoms, including C, N, and H. Vibrational frequency calculations were performed on all minima states, and each minimum was identified to have no imaginary frequencies. Prior to energy-related calculations, the ground state was stabilized to the minimum energy point. Notably, all excited state energies were found to be positive during the calculation process. To determine the T1 energy, we first optimized it using the Unrestricted Kohn-Sham (UKS) method. Additionally, LUMO and HOMO were drawn using Gaussian 16, Multiwfn (Multiwfn_3.8_dev_bin_Win64), and VMD (1.9.3). Furthermore, the UV-Vis was calculated via Gaussian 16 (nstates = 80) and was subsequently read and exported by Multiwfn (Multiwfn_3.8_dev_bin_Win64).

Supplementary Figures

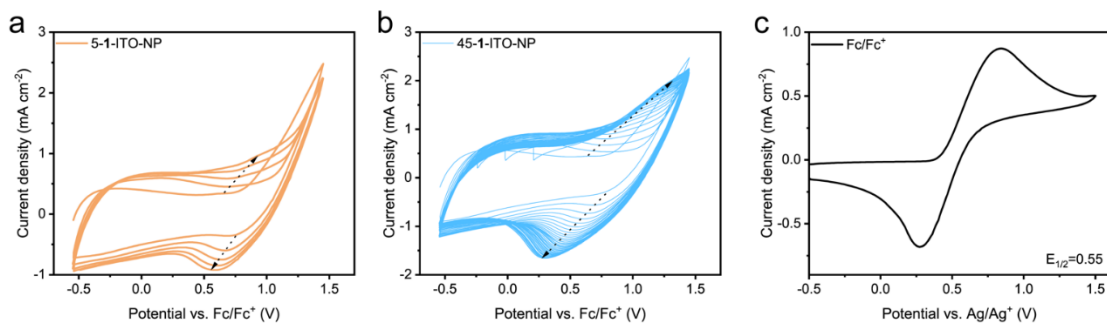


Figure S3.1. (a) CV curves of 5-1-ITO-NP in 0.1 M TBAPF₆ and 1 mM **1** in DCM. (b) CV curves of 45-1-ITO-NP in 0.1 M TBAPF₆ and 1 mM **1**. Sweep rate 100 mV s⁻¹, 5 or 45 sweeps, sweep range from -0.55 to 1.45 vs Fc/Fc⁺. (c) Determination of E_{1/2} for Fc/Fc⁺ reference in the same solution

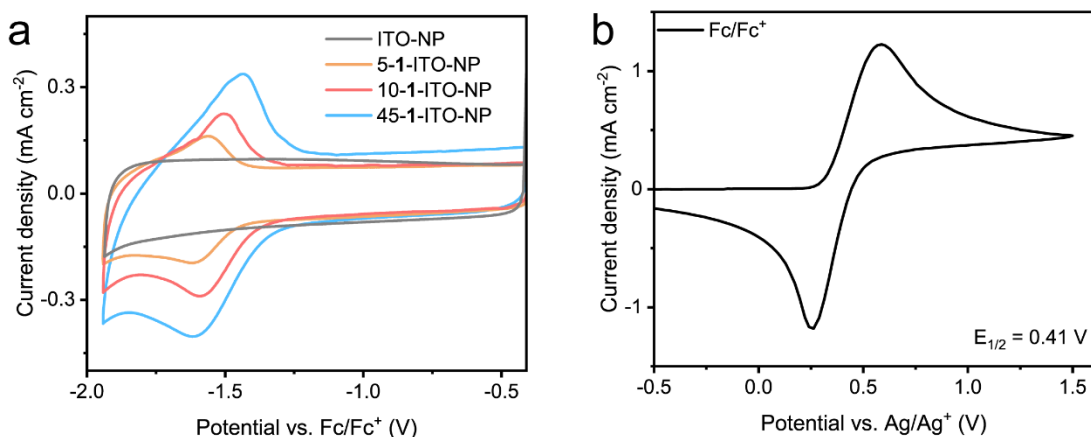


Figure S3.2. (a) Negative region CV curves for isolated 5-, 10-, and 45-1-ITO-NP compared to an ITO-NP blank showing the 1 e⁻ redox wave for the dicyanobenzene groups in the polymers (0.1 M TBAPF₆ in MeCN, sweep rate 10 mV s⁻¹ from -0.41 to -1.91 vs Fc/Fc⁺); (b) Determination of E_{1/2} for Fc/Fc⁺ reference in the same solution

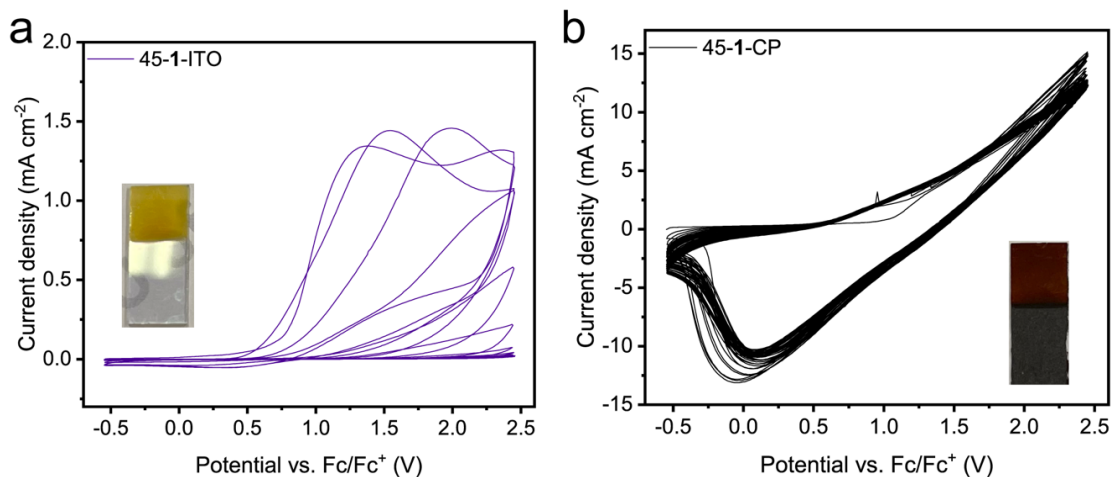


Figure S3.3. (a) CV curves for electropolymerization of **1** to prepare 45-1-ITO and (b) 45-1-CP in 0.1 M TBAPF₆ and 1mM **1** in DCM (45 sweeps, sweep rate 100 mV s⁻¹ from -0.55 to 2.45 vs Fc/Fc⁺)

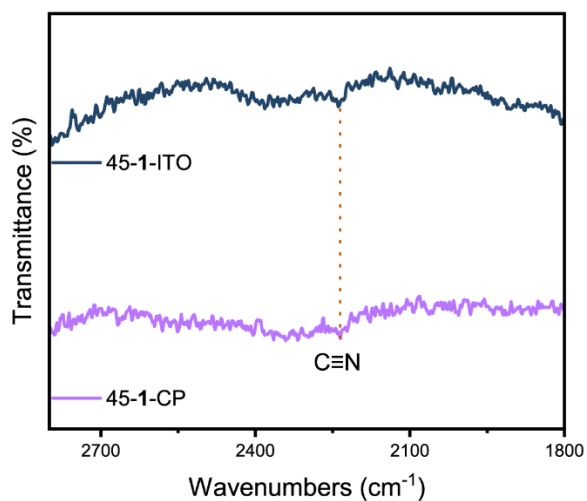


Figure S3.4. Enlarged FT-IR region with putative assignments of the weak stretching peaks for the dicyano groups on the central aromatic ring in 45-1-ITO and 45-1-CP

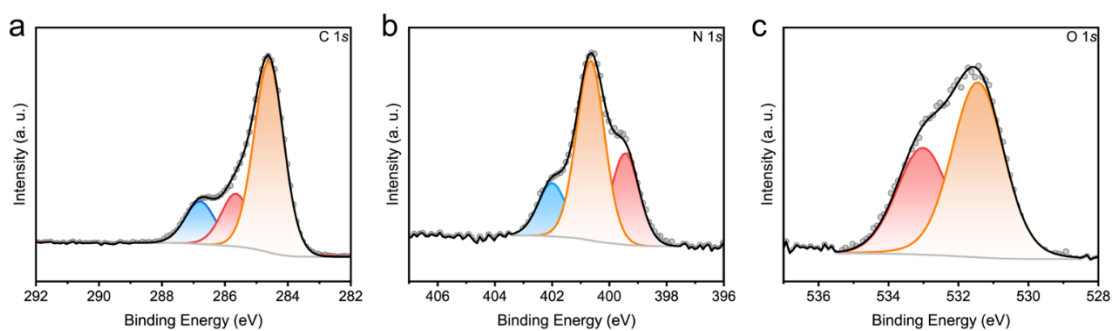


Figure S3.5. The deconvoluted XPS of elements (a) C 1s, (b) N 1s, and (c) O 1s on 45-1-CP

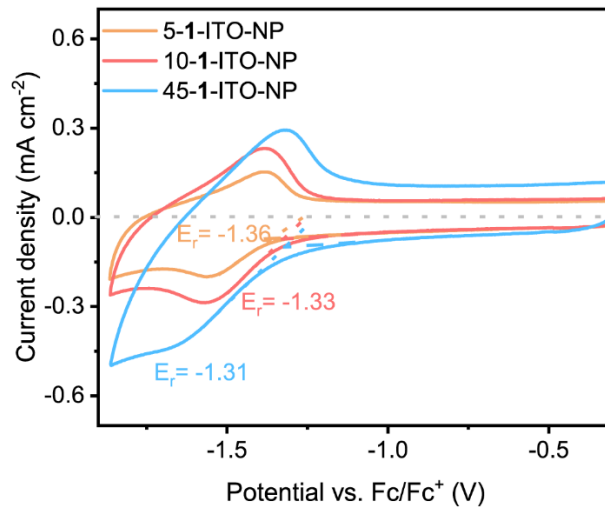


Figure S3.6. CVs (sweep rate 10 mV s^{-1} from -0.30 to -1.86 vs Fc/Fc^+) of the 5, 10, or 45-1-ITO-NP electrodes immersed in CH_2Cl_2 with 0.1 M TABPF_6 . The onset potentials were determined, as shown in the figure

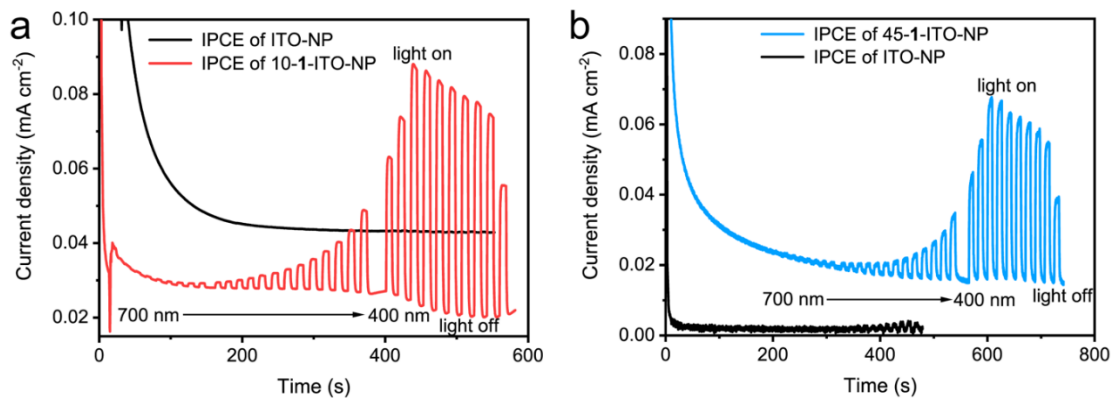


Figure S3.7. IPCE measurements with the ITO-NP control, and (a) 10-1-ITO-NP electrodes under neutral and (b) 45-1-ITO-NP electrodes under alkaline conditions. 0.02 M hydroquinone ($\text{pH} = 7.0$) (neutral condition) or $0.5 \text{ M Et}_3\text{N}$ ($\text{pH} = 12.6$) (basic condition) in triple distilled water at 0.25 V vs. SCE. Each spike in current corresponds to a decrease in wavelength by 10 nm , starting at 700 nm , then down to 400 nm . The light was held at each wavelength for $\sim 8 \text{ sec}$

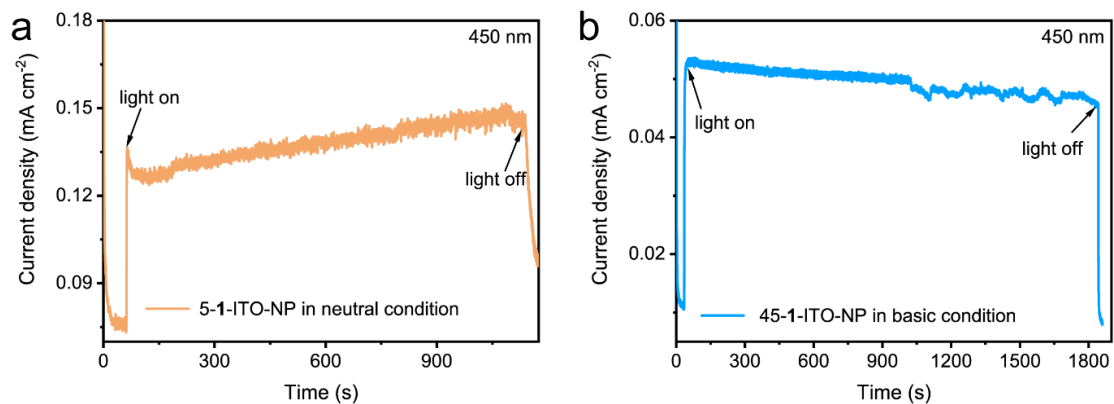


Figure S3.8. (a) The steady-state potentiostatic photoelectrooxidation of hydroquinone over 10-1-ITO-NP under neutral conditions, and of triethyl amine over 45-1-ITO-NP under basic conditions. 0.02 M hydroquinone (pH = 7.0) (neutral condition) or 0.5 M Et₃N (pH = 12.6) (basic condition) in triple distilled water at 0.25 V vs. SCE

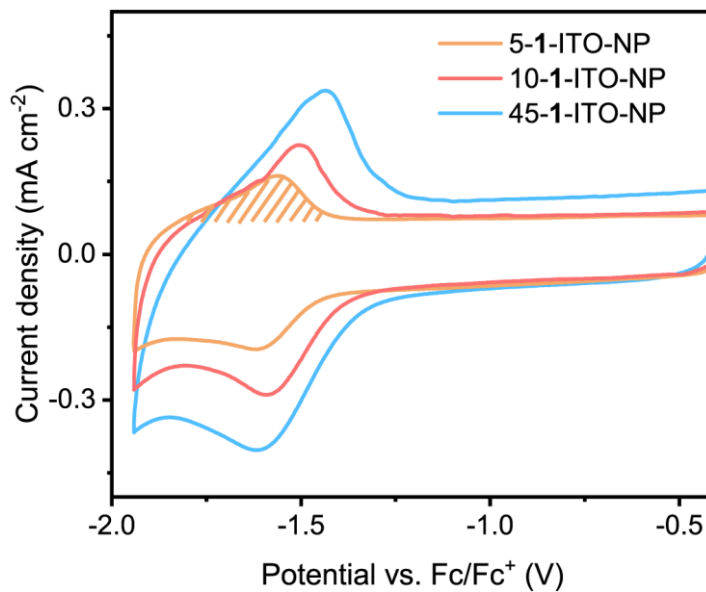
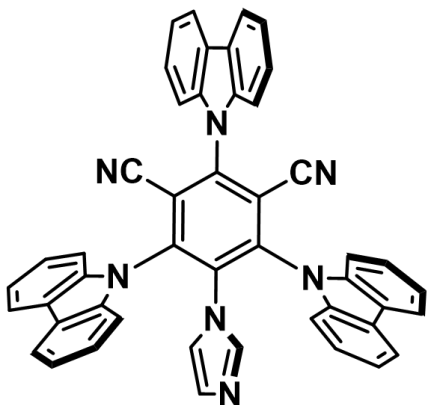


Figure S3.9. Estimation of electrochemically accessible surface coverage of poly **1** from the charge under the one-electron redox wave for the dicyanobenzene moieties in the polymer. 5-1-ITO-NP: 1.50×10^{-8} mol; 10-1-ITO-NP: 2.94×10^{-8} mol; 45-1-ITO-NP: 4.74×10^{-8} mol

Synthesis of Target Compounds

5-fluoro-2,4,6-tri(9H-carbazol-9-yl)benzene-1,3-dicarbonitrile (3CzFIPN) was prepared as described in our previous report.⁴

1-imidazole-2,4,6-tri(carbazol-9-yl)-3,5-dicyanobenzene (3CzImIPN) (1)



Imidazole (106.1 mg, 1.56 mmol) and Cs_2CO_3 (1.52 g, 4.67 mmol) were weighed into a side arm flask. Then, the flask was connected to a Schlenk line, evacuated, and refilled with argon for three cycles. Next, acetonitrile (CH_3CN , 30 mL, dried over molecular sieves and bubbled with N_2 for 30 min) was added into the flask, and the resulted suspension was stirred at 50 °C for 30 min.

Meantime, the monofluoro compound, 3CzFIPN (1.06 g, 1.56 mmol) was dissolved in 10 mL of CH_3CN and added slowly into the flask containing imidazole and base at room temperature. Additional CH_3CN (10 mL) was used for quantitative transfer of 3CzFIPN, and then the contents in the flask were stirred at 50 °C. An aliquot after three hours showed the completion of the reaction with no starting materials remaining. The reaction flask was cooled down and filtered with an additional wash with CH_3CN (100 mL). The combined filtrate was concentrated under reduced pressure using a rotavap to give yellow solid products. Next, the crude product was dissolved in DCM (50 mL) and washed with water (3×50 mL). After washing with saturated NaCl, the organic layer was dried over anhydrous Na_2SO_4 , filtered, and concentrated again using a rotavap to give the target product as a yellow powder in 95% yield. ^1H NMR (499.789 MHz, CD_3CN , 27.7 °C): δ 6.11 (1H, s), 6.21 (1H, t, $J=1.3$ Hz), 6.73 (1H, s), 7.39 (4H, t, $J = 7.5$ Hz), 7.49–7.55 (6H, m), 7.62 (4H, d, $J = 8.1$), 7.73 (1H, dt, $J = 8.0$ Hz, $J = 1.1$ Hz), 7.86 (1H, d, $J = 8.2$ Hz), 8.17 (2H, d, $J = 7.8$ Hz), 8.30 (2H, d, $J = 7.8$ Hz). $^{13}\text{C}\{^1\text{H}\}$ NMR (125.685 MHz, CD_3CN , 27.7 °C): δ 110.1, 110.6, 111.8, 117.8, 118.2, 120.8, 121.0, 122.1, 122.4, 123.9, 124.2, 126.9, 127.1,

129.3, 135.4, 137.3, 139.4, 139.7, 143.2, 145.3. HRMS (ESI) m/z Calcd. for $C_{47}H_{27}N_7$ (M+H)⁺: 690.2401. Found: 690.2404.

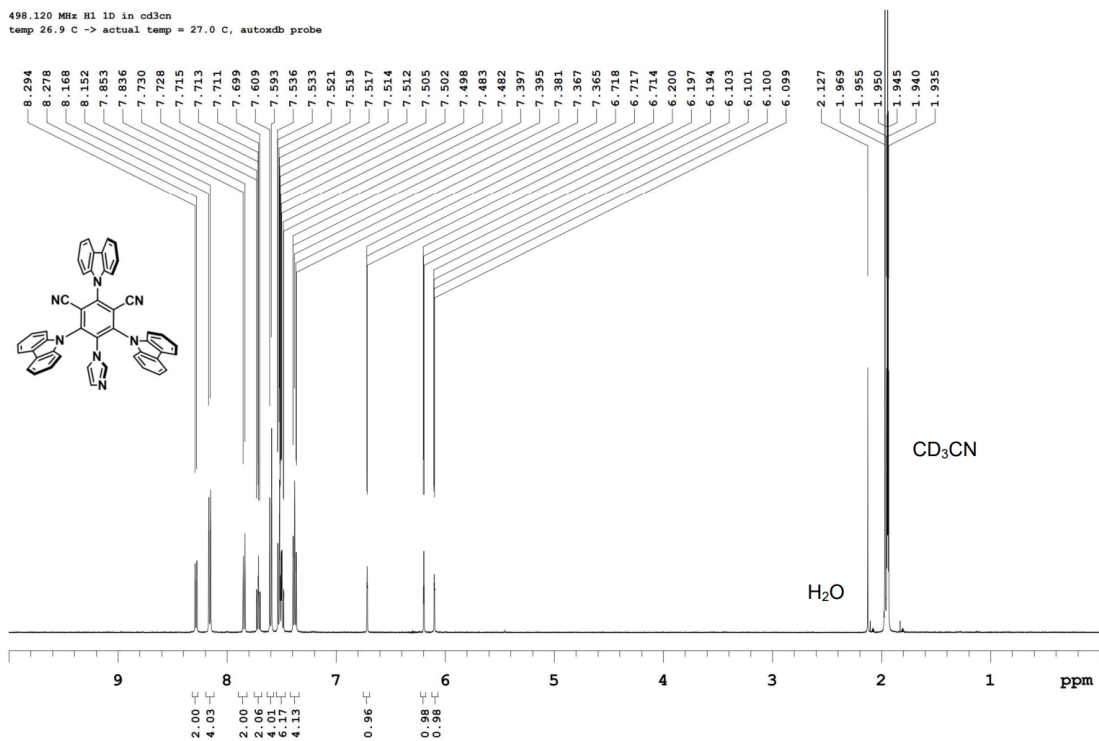


Figure S3.10. ¹H NMR of 3CzImIPN (**1**). The δ region from 10 to 1 ppm showing the ¹H NMR. The spectrum is acquired in CD₃CN with 500 MHz Varian Inova

498.120 MHz H1 1D in cd3cn
temp 26.9 C -> actual temp = 27.0 C, autoxdb probe

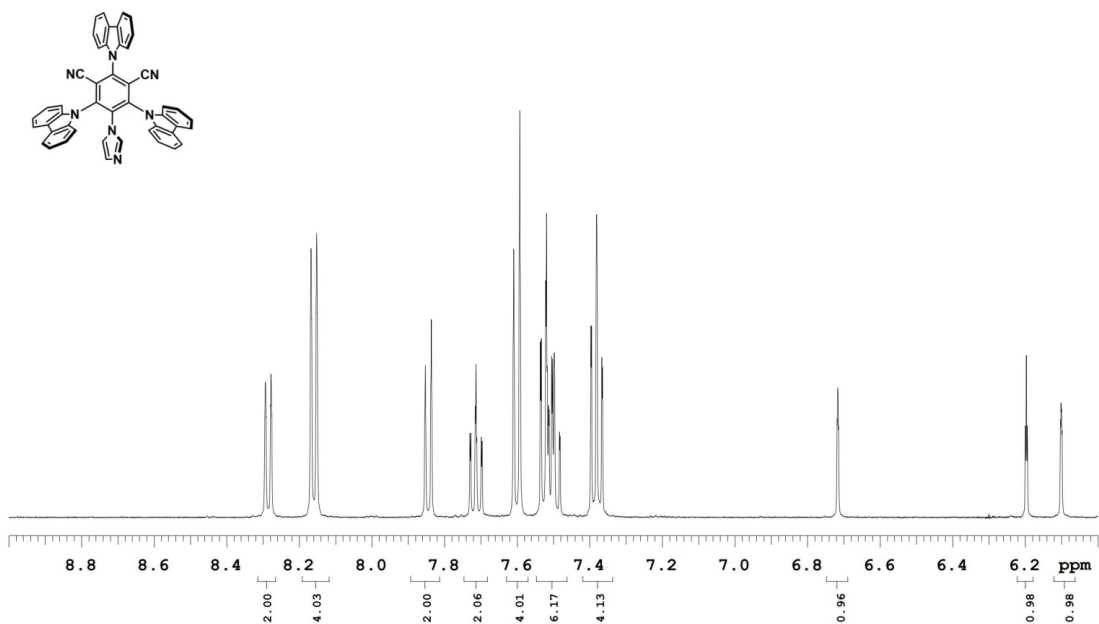


Figure S3.11. Zoom in ¹H NMR of 3CzImIPN (1). The δ region from 9 to 6 ppm showing the ¹H NMR. The spectrum is acquired in CD₃CN with 500 MHz Varian Inova

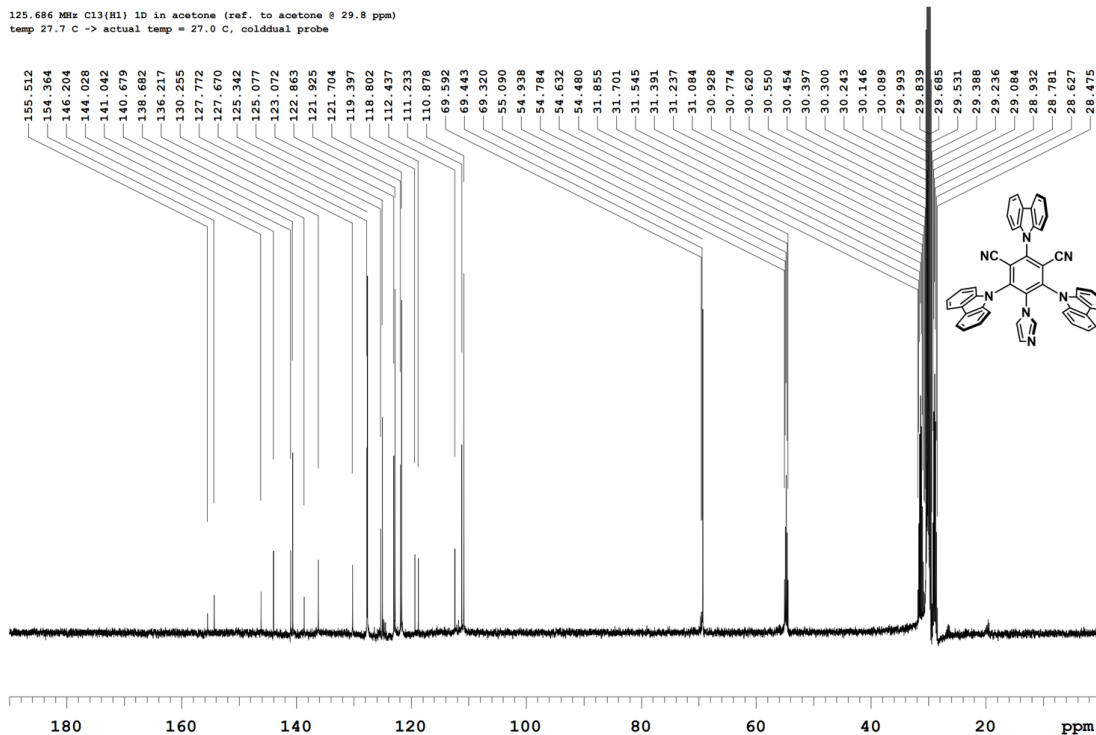


Figure S3.12. ^{13}C NMR of 3CzImIPN (**1**), from 0 to 190 ppm. The spectrum is acquired in acetone by Varian VNMRS 500 MHz NMR spectrometer

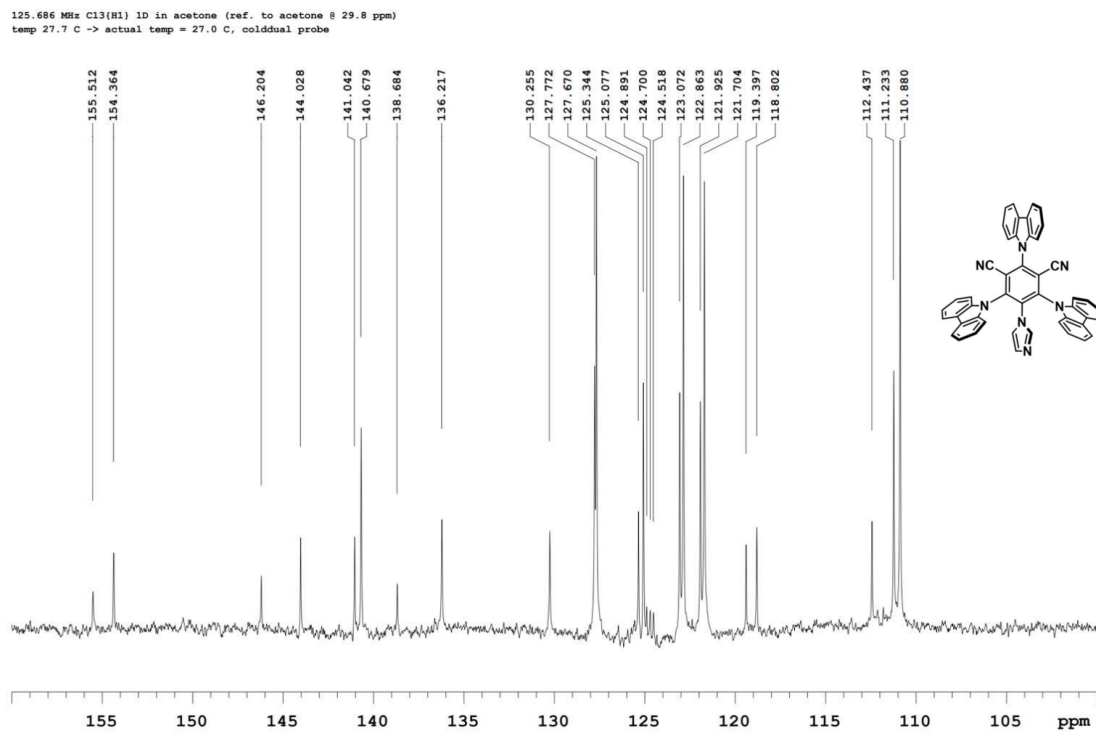


Figure S3.13. Zoom in ^{13}C NMR of 3CzImIPN (**1**), from 100 to 160 ppm. The spectrum is acquired in acetone by Varian VNMRS 500 MHz NMR spectrometer

Stilbene Isomerization

Trans reactants denoted by (T); cis-products denoted by (*); internal standard denoted by (IS)

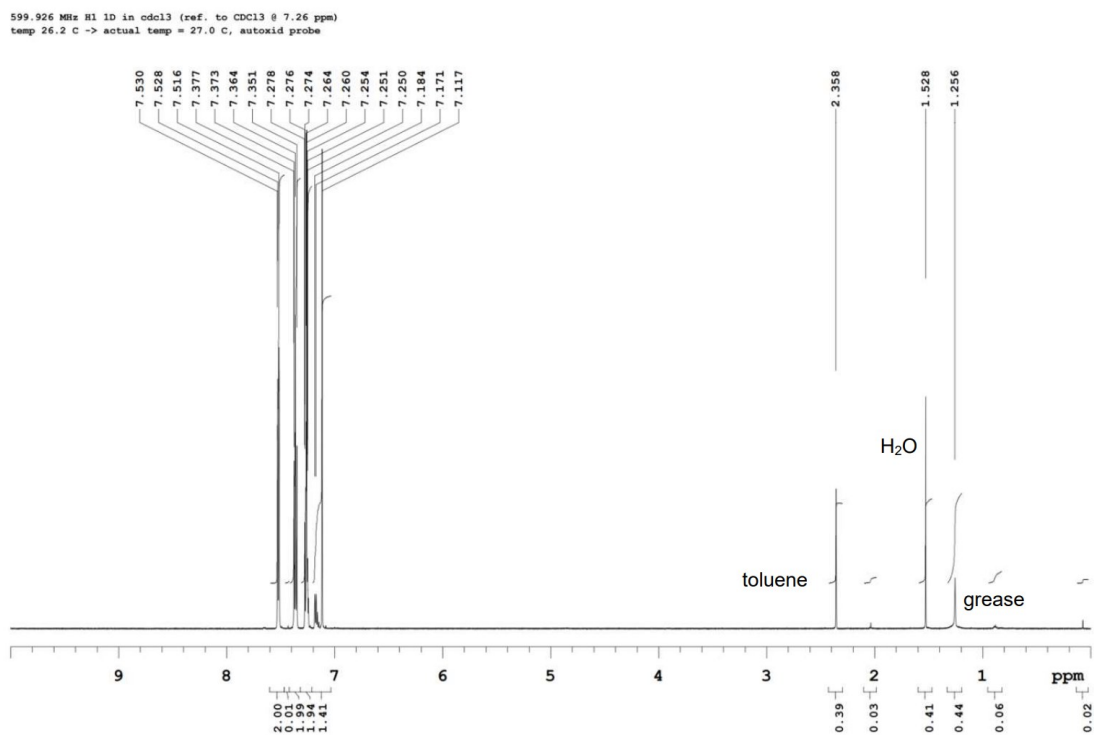


Figure S3.14. ¹H NMR of stilbene isomerization by ITO-NP for 16 h; the δ region from 10 to 0 ppm

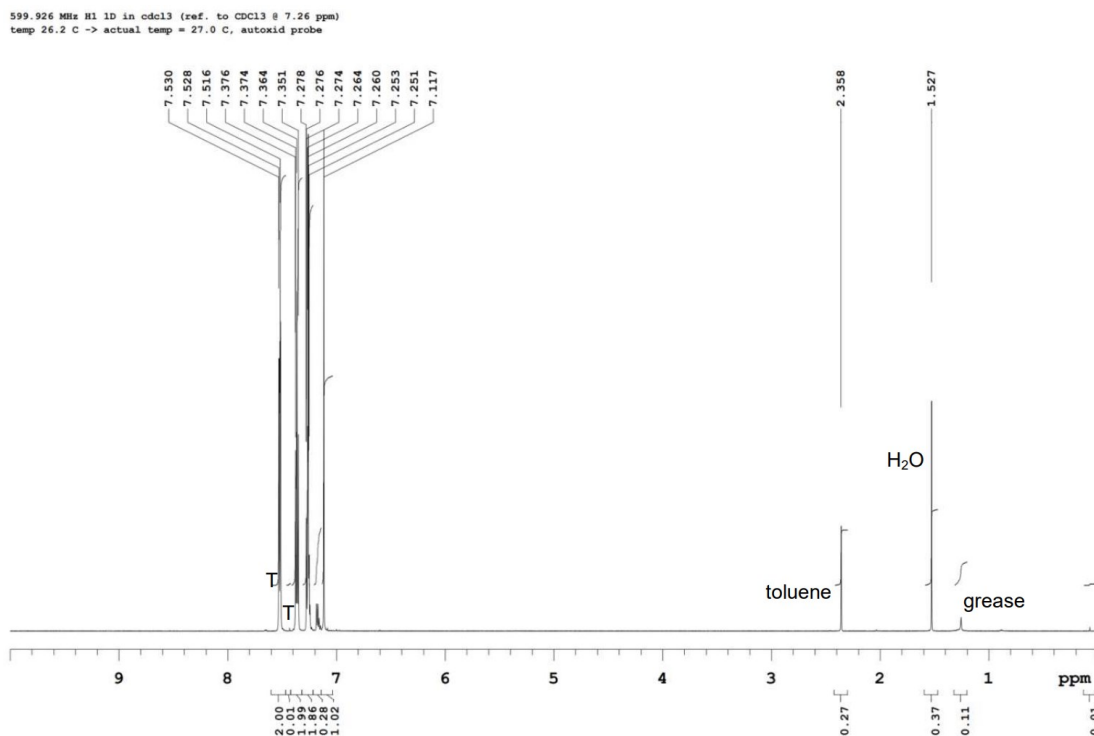


Figure S3.15. ^1H NMR of stilbene isomerization by ITO-NP for 48 h; the δ region from 10 to 0 ppm

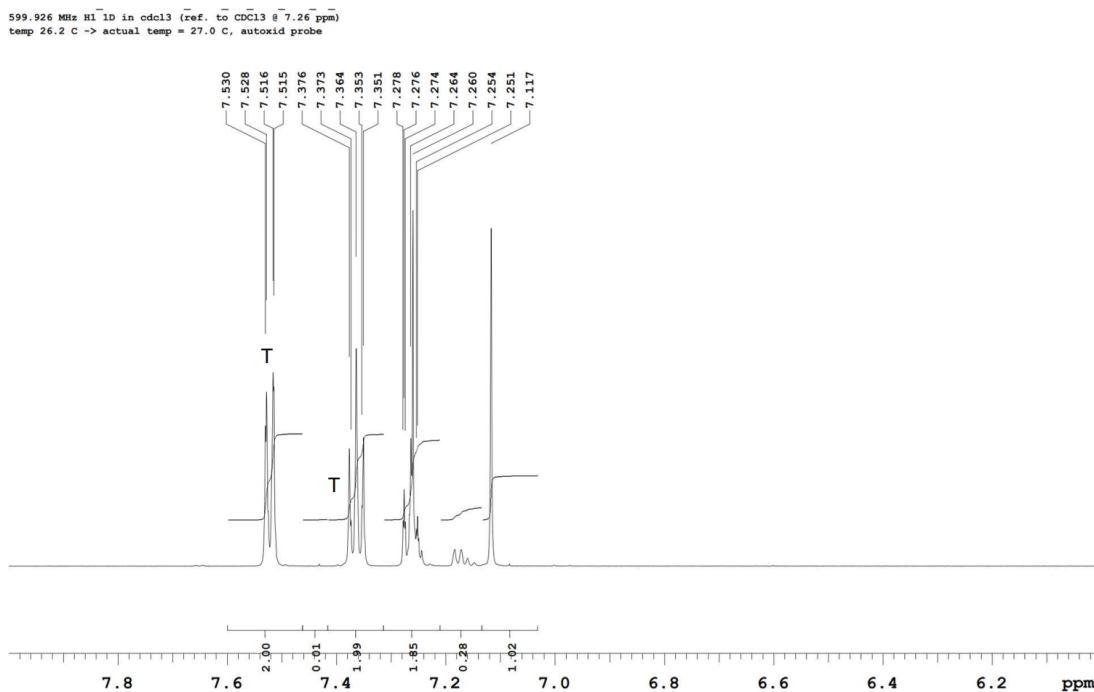


Figure S3.16. Zoom in ^1H NMR of stilbene isomerization by new ITO-NP for 48 h; the δ region from 6 to 8 ppm

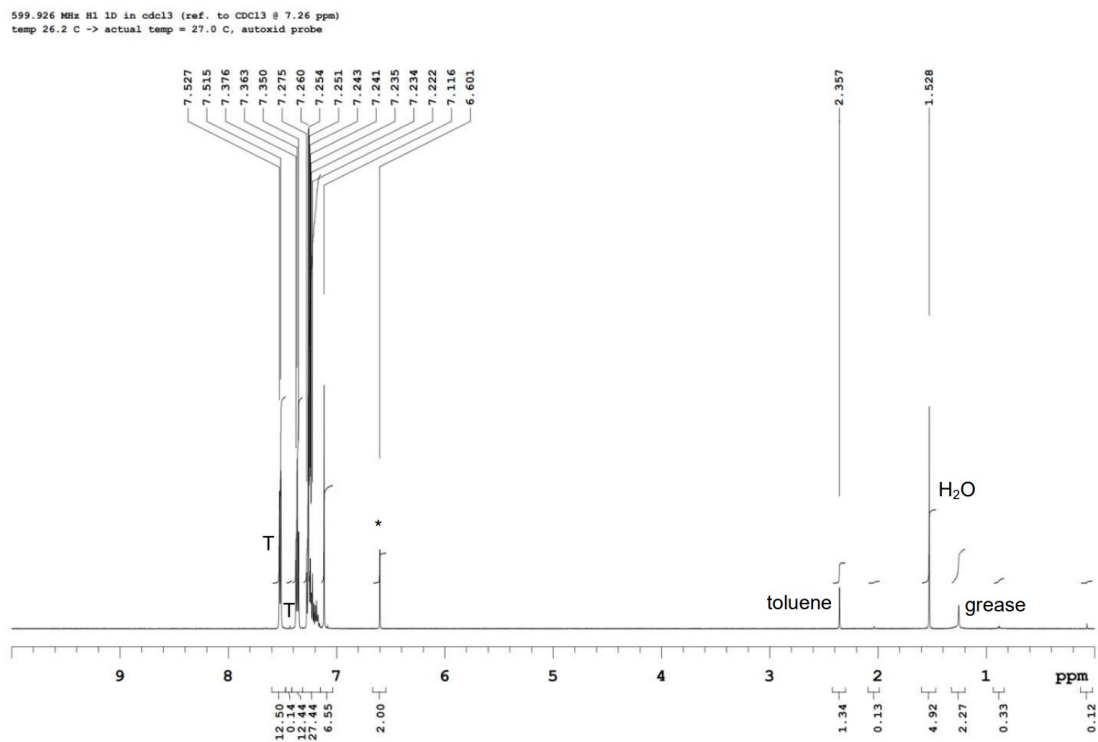


Figure S3.17. ¹H NMR of stilbene isomerization by 5-1-ITO-NP for 16 h; the δ region from 10 to 0 ppm

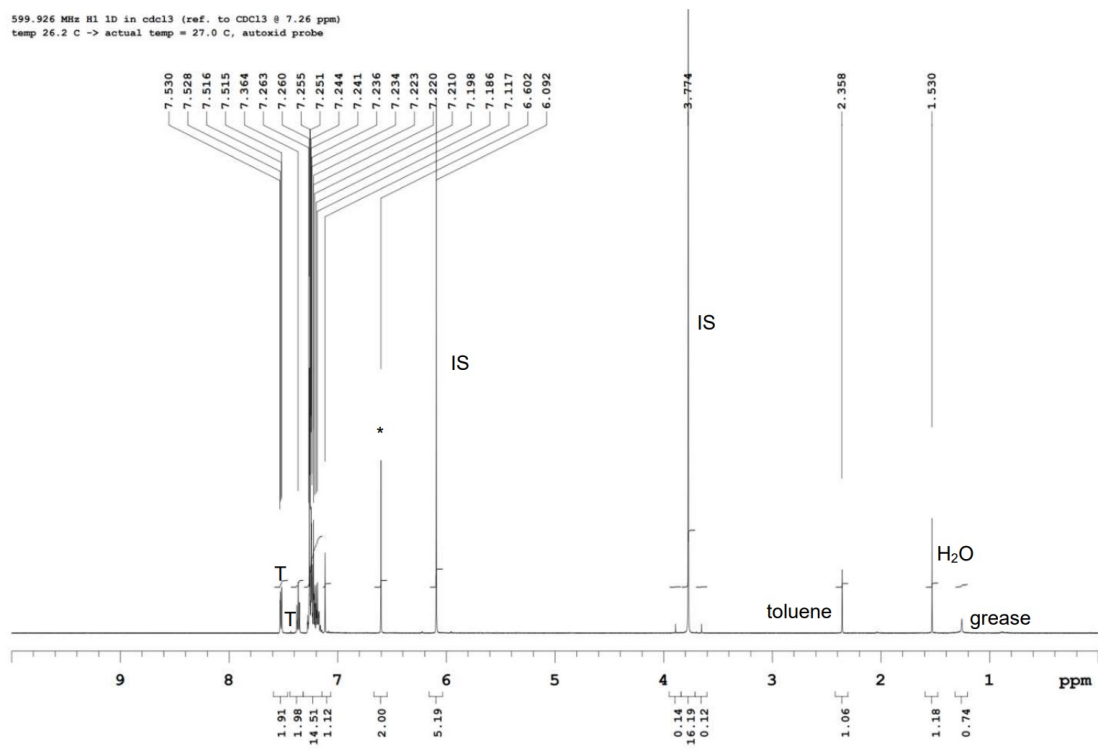


Figure S3.18. ¹H NMR of stilbene isomerization by 5-1-ITO-NP for 48 h; the δ region from 10 to 0 ppm

599.926 MHz ¹H 1D in cdcl3 (ref. to CDCl3 @ 7.26 ppm)
temp 26.2 C -> actual temp = 27.0 C, autoxid probe

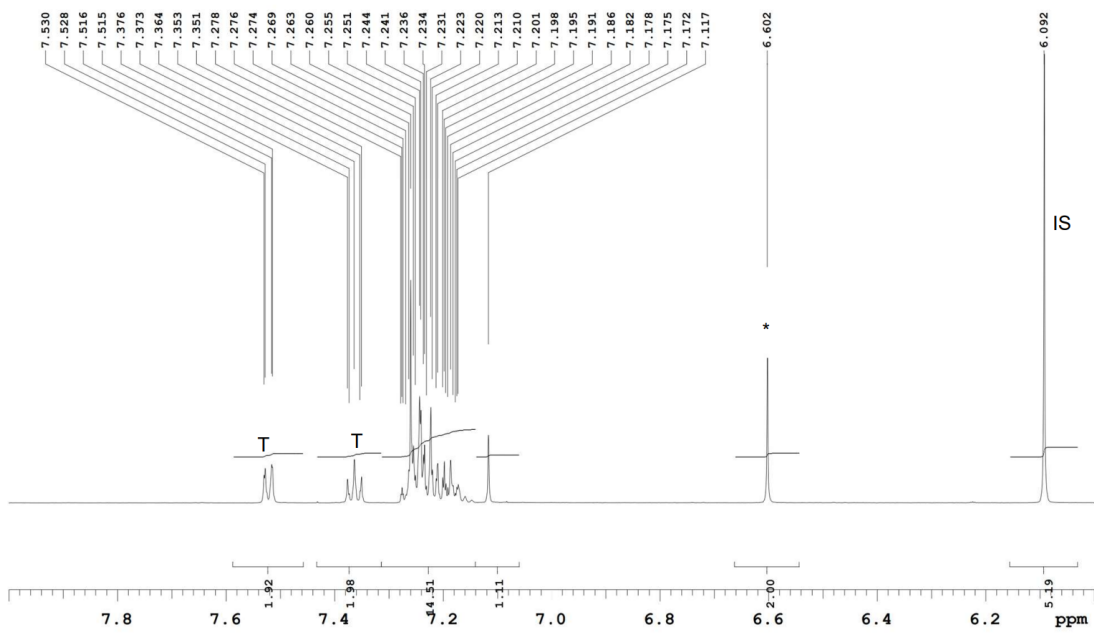


Figure S3.19. Zoom in ¹H NMR of stilbene isomerization by 5-1-ITO-NP for 48 h; the δ region from 6 to 8 ppm

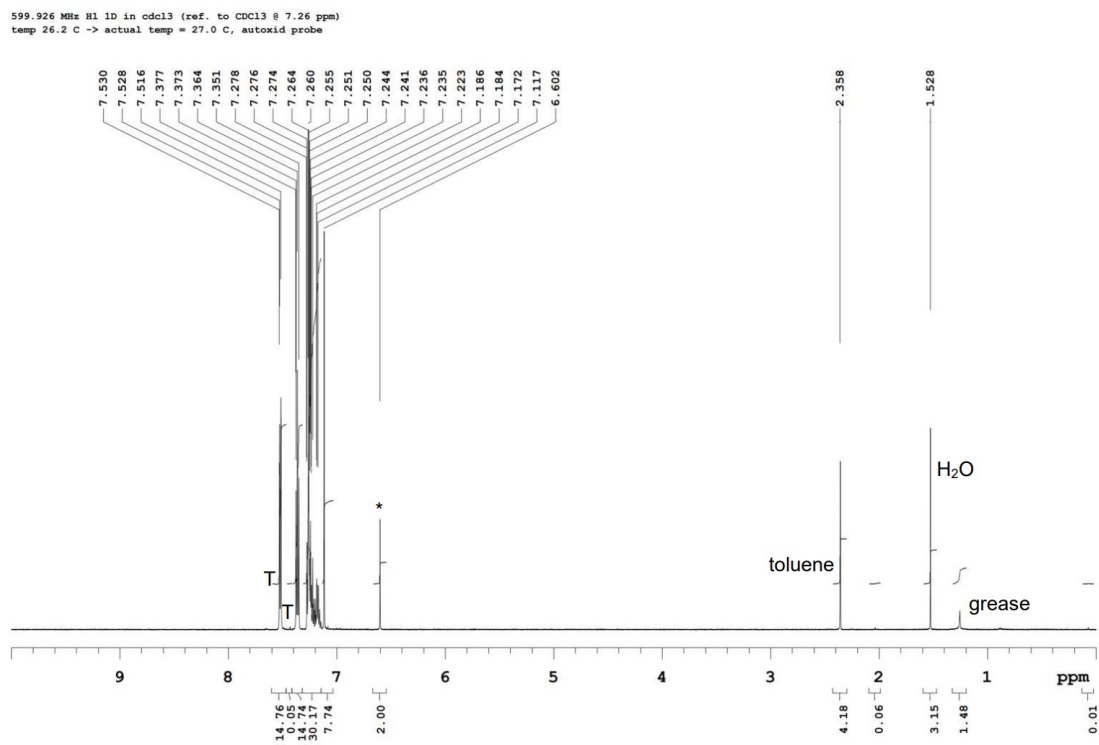


Figure S3.20. ¹H NMR of stilbene isomerization by 10-1-ITO-NP for 16 h; the δ region from 10 to 0 ppm

599.926 MHz ¹H 1D in cdcl3 (ref. to CDCl3 @ 7.26 ppm)
temp 26.2 C -> actual temp = 27.0 C, autoxid probe

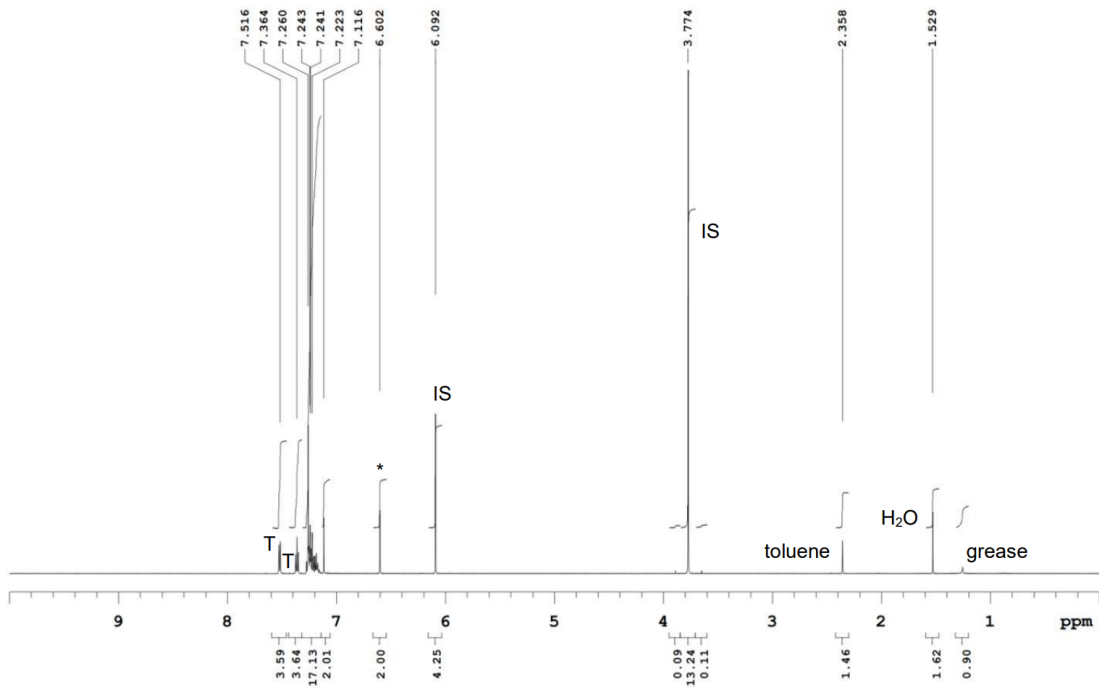


Figure S3.21. ¹H NMR of stilbene isomerization by 10-1-ITO-NP for 48 h; the δ region from 10 to 0 ppm

599.926 MHz ^1H 1D in cdcl_3 (ref. to CDCl_3 @ 7.26 ppm)
temp 26.2 C -> actual temp = 27.0 C, autoxid probe

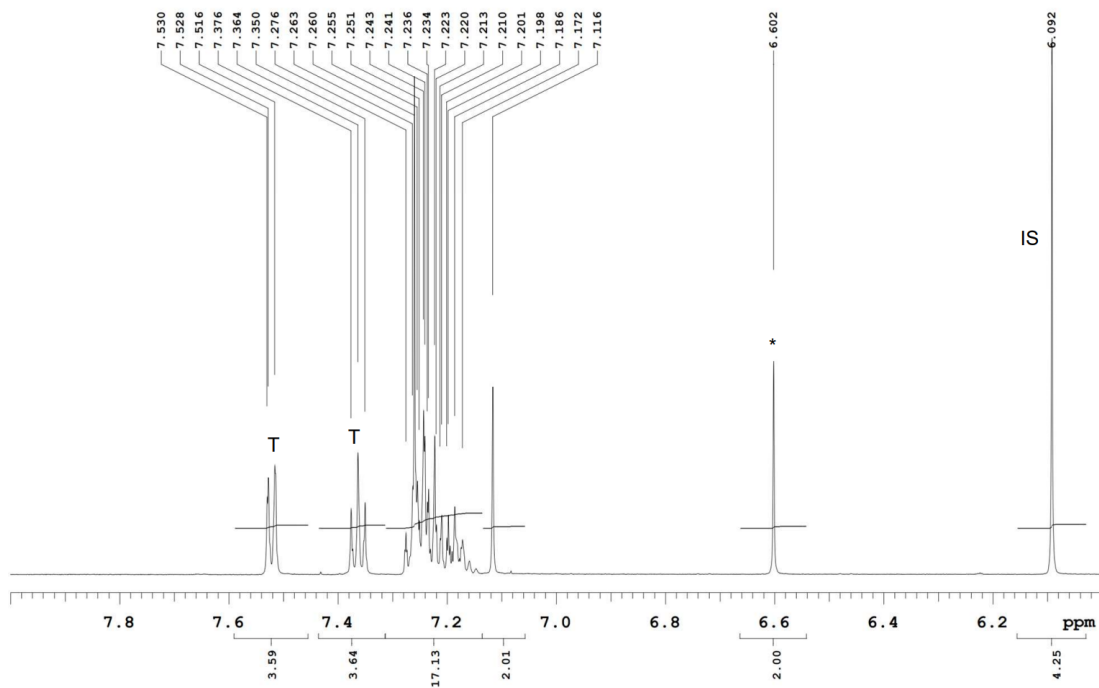


Figure S3.22. Zoom in ^1H NMR of stilbene isomerization by 10-1-ITO-NP for 48 h; the δ region from 6 to 8 ppm

599.926 MHz ¹H 1D in cdcl3 (ref. to CDCl3 @ 7.26 ppm)
temp 26.2 C -> actual temp = 27.0 C, autoxid probe

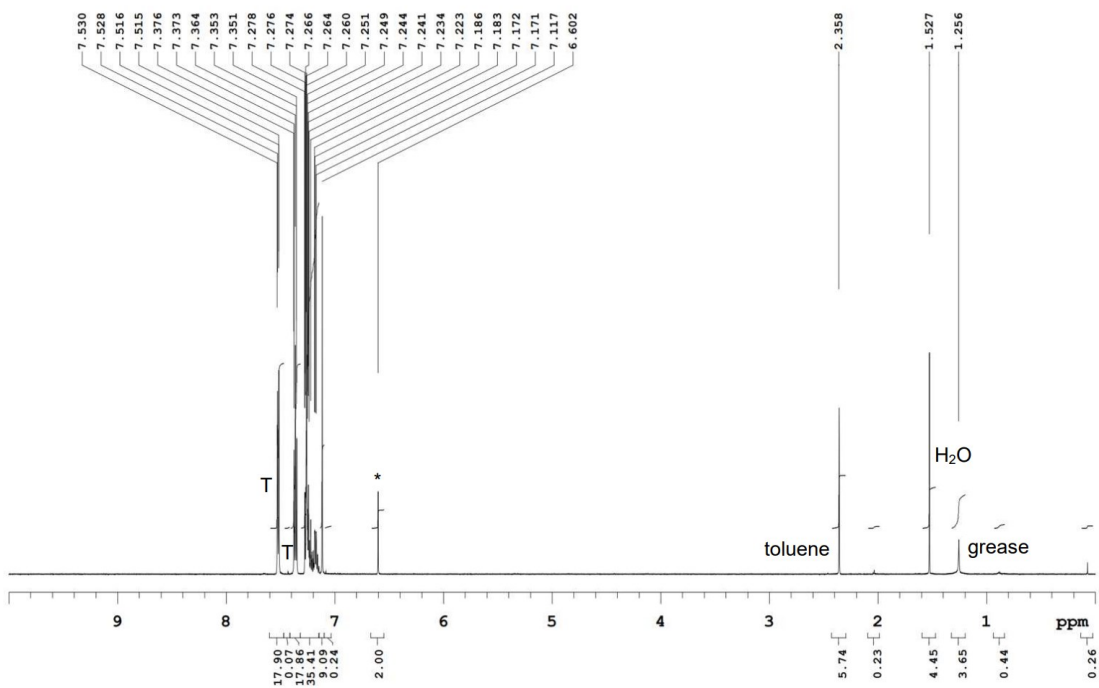


Figure S3.23. ¹H NMR of stilbene isomerization by 45-1-ITO-NP for 16 h; the δ region from 10 to 0 ppm

599.926 MHz H1 1D in cdcl3 (ref. to CDCl3 @ 7.26 ppm)
temp 26.2 C -> actual temp = 27.0 C, autoxid probe

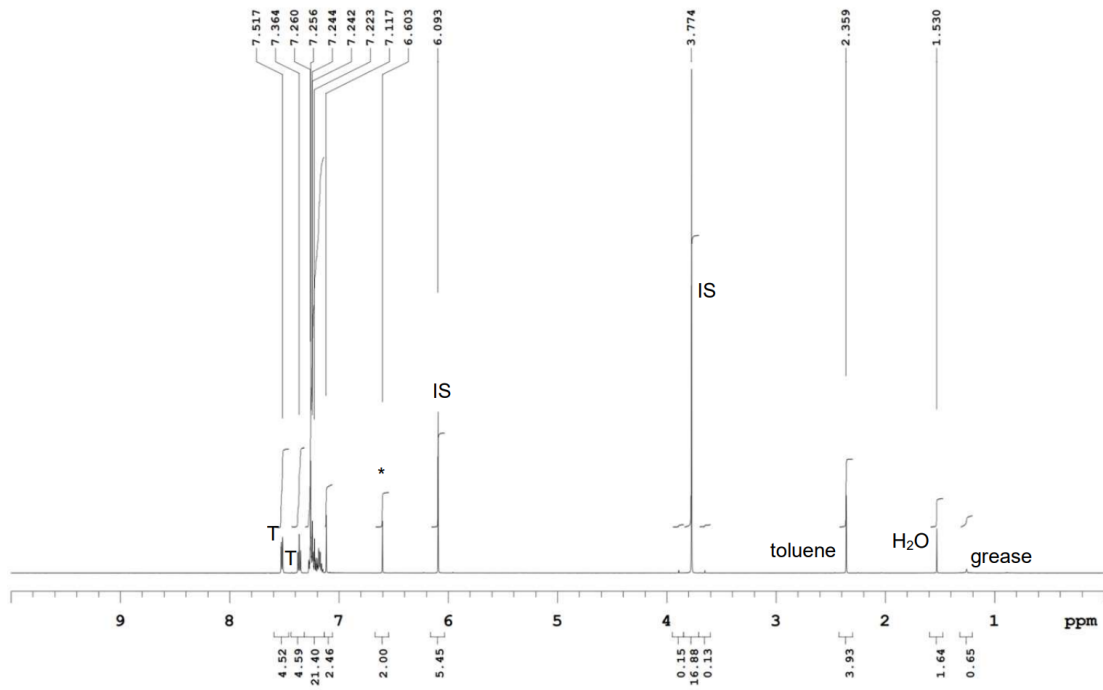


Figure S3.24. ¹H NMR of stilbene isomerization by 45-1-ITO-NP for 48 h; the δ region from 10 to 0 ppm

599.926 MHz ^1H 1D in cdcl_3 (ref. to CDCl_3 @ 7.26 ppm)
temp 26.2 C -> actual temp = 27.0 C, autoxid probe

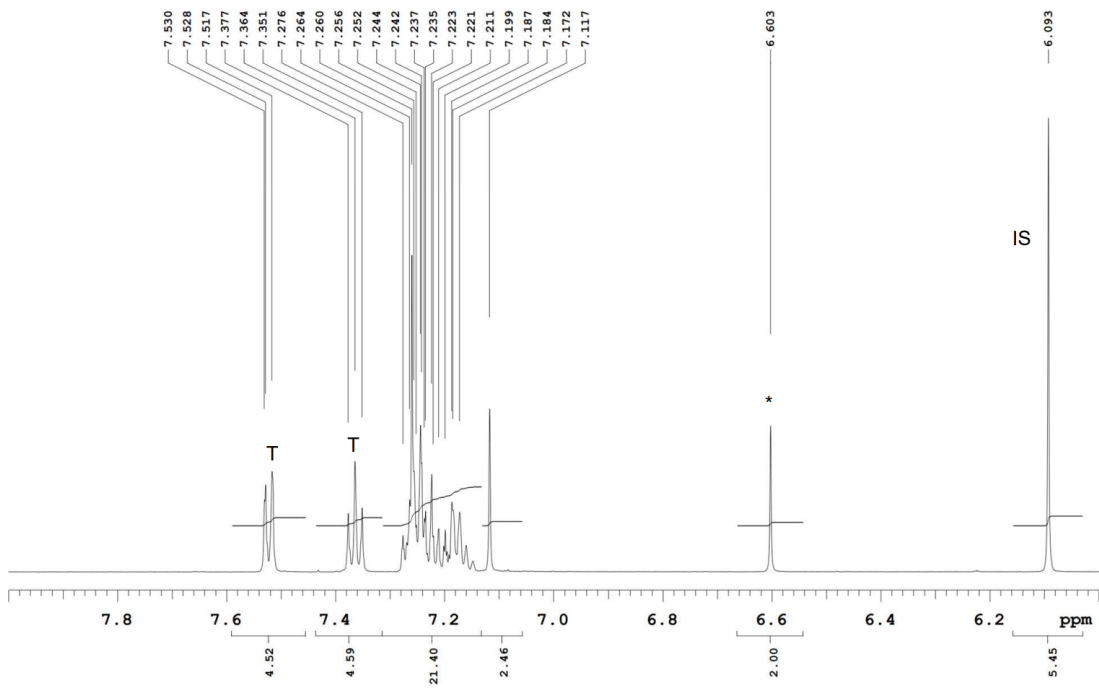


Figure S3.25. Zoom in ^1H NMR of stilbene isomerization by 45-1-ITO-NP for 48 h; the δ region from 6 to 8 ppm

599.926 MHz ¹H 1D in cdcl3 (ref. to CDCl3 @ 7.26 ppm)
temp 26.2 C -> actual temp = 27.0 C, autoxid probe

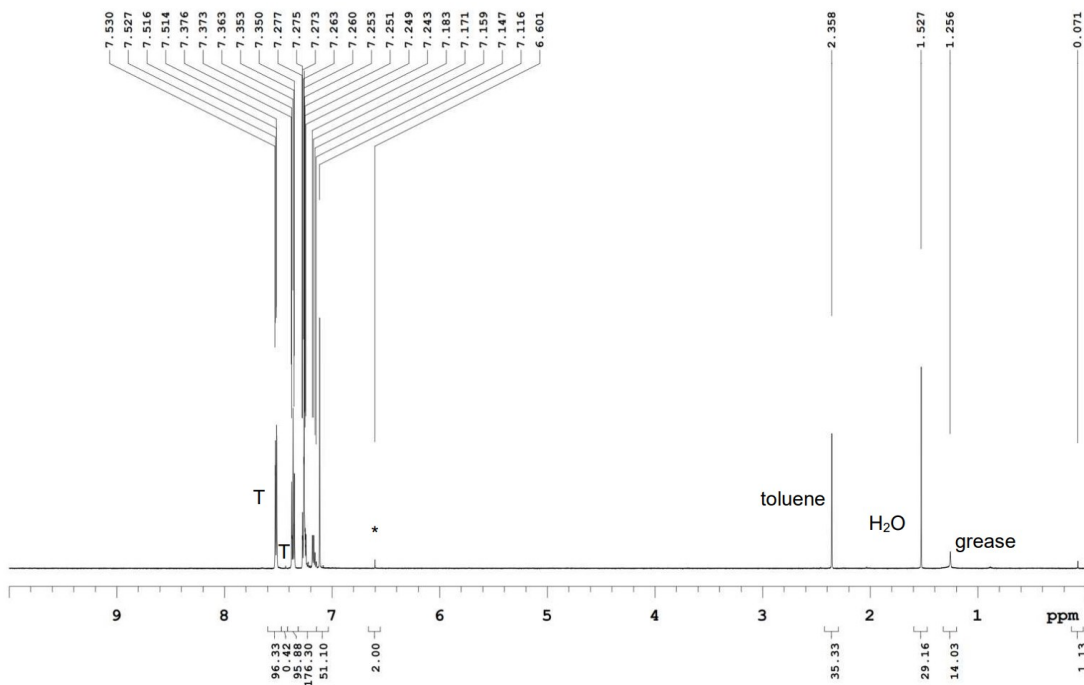


Figure S3.26. ¹H NMR of stilbene isomerization by the second run of 5-1-ITO-NP for 16 h; the δ region from 10 to 0 ppm

599.926 MHz ¹H 1D in cdcl3 (ref. to CDCl3 @ 7.26 ppm)
temp 26.2 C -> actual temp = 27.0 C, autoxid probe

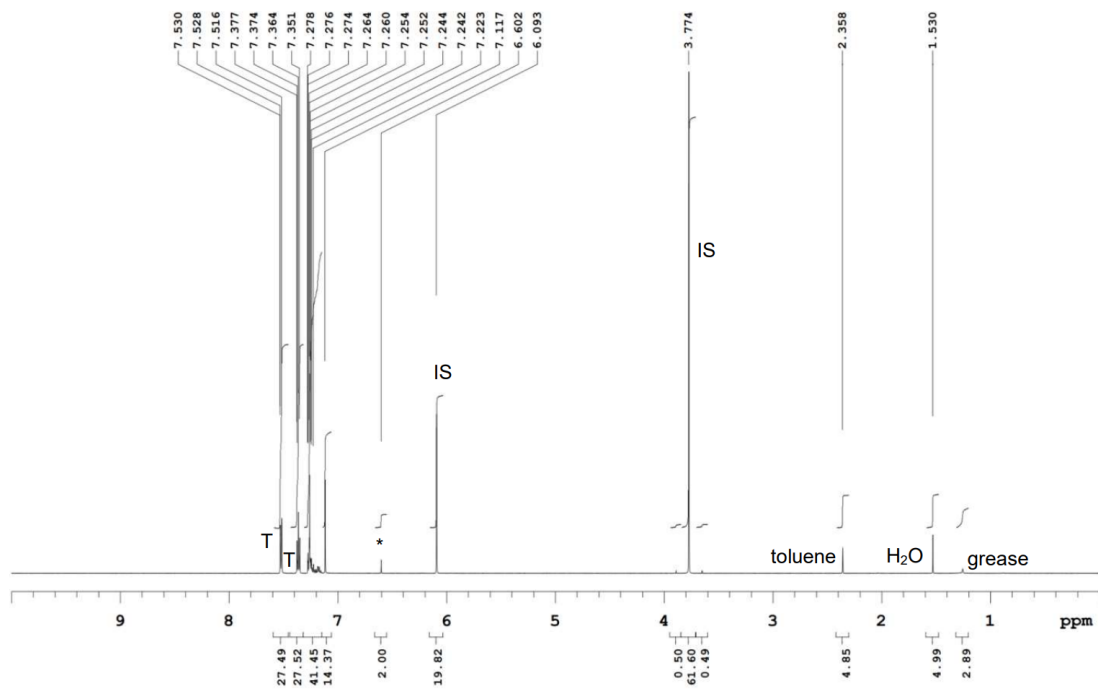


Figure S3.27. ¹H NMR of stilbene isomerization by the second run of 5-1-ITO-NP for 48 h; the δ region from 10 to 0 ppm

599.926 MHz ^1H 1D in cdCl_3 (ref. to CDCl_3 @ 7.26 ppm)
temp 26.2 C -> actual temp = 27.0 C, autoxid probe

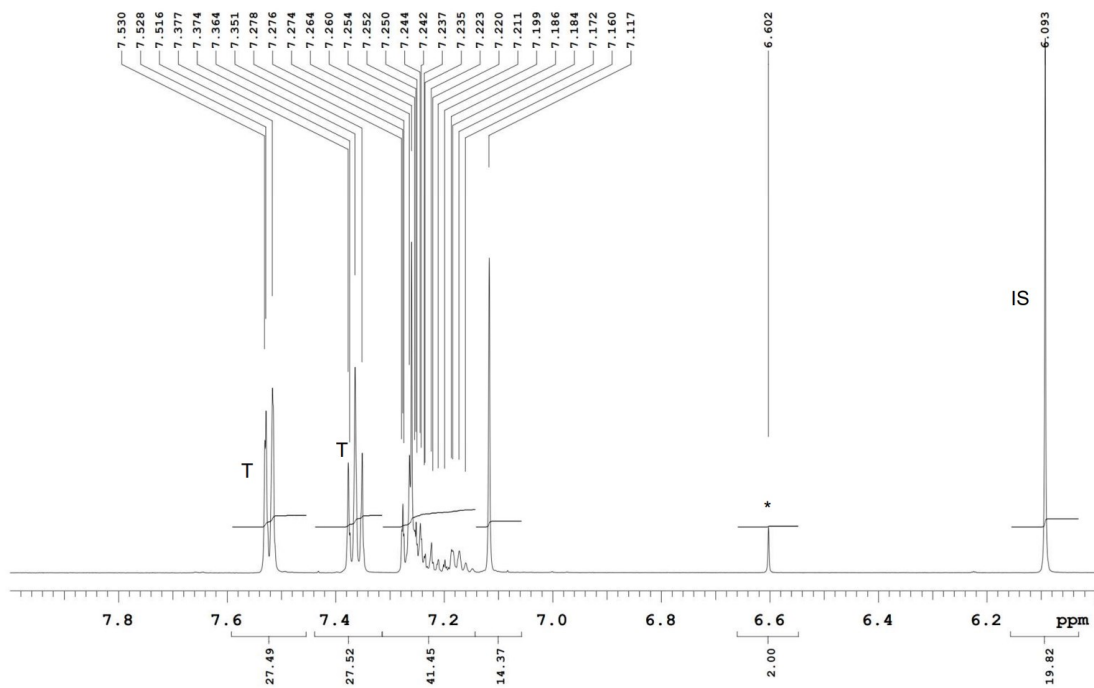


Figure S3.28. Zoom in ^1H NMR of stilbene isomerization by the second run of 5-1-ITO-NP for 48 h; the δ region from 6 to 8 ppm

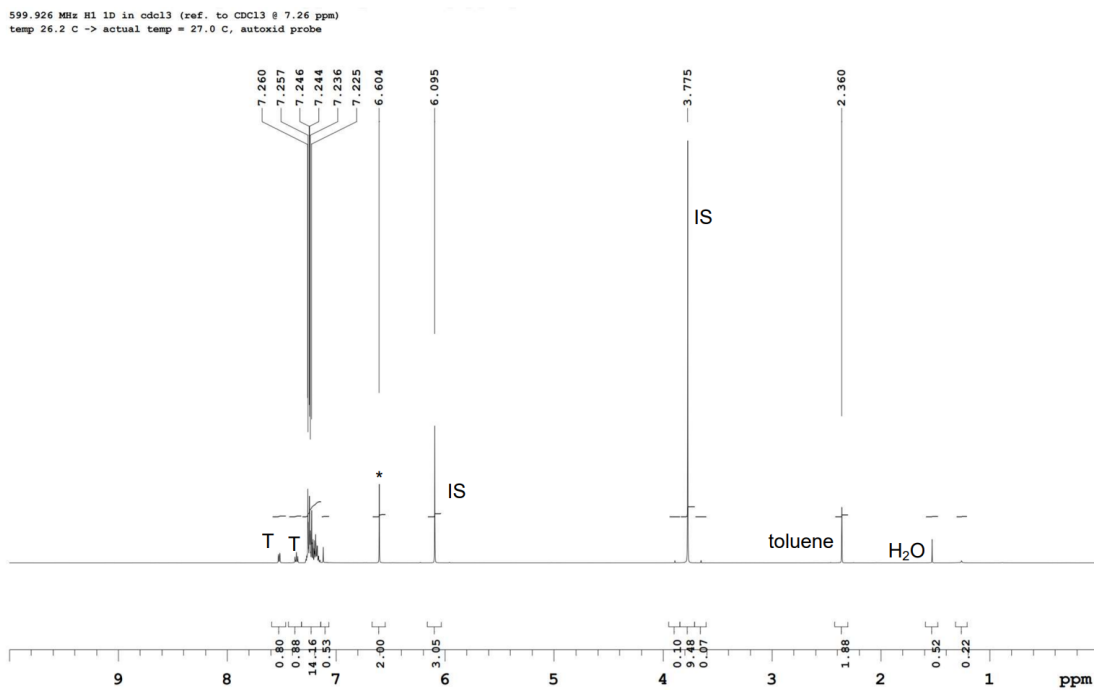


Figure S3.29. ¹H NMR of stilbene isomerization by new 5-1-ITO-NP for 88 h; the δ region from 10 to 0 ppm

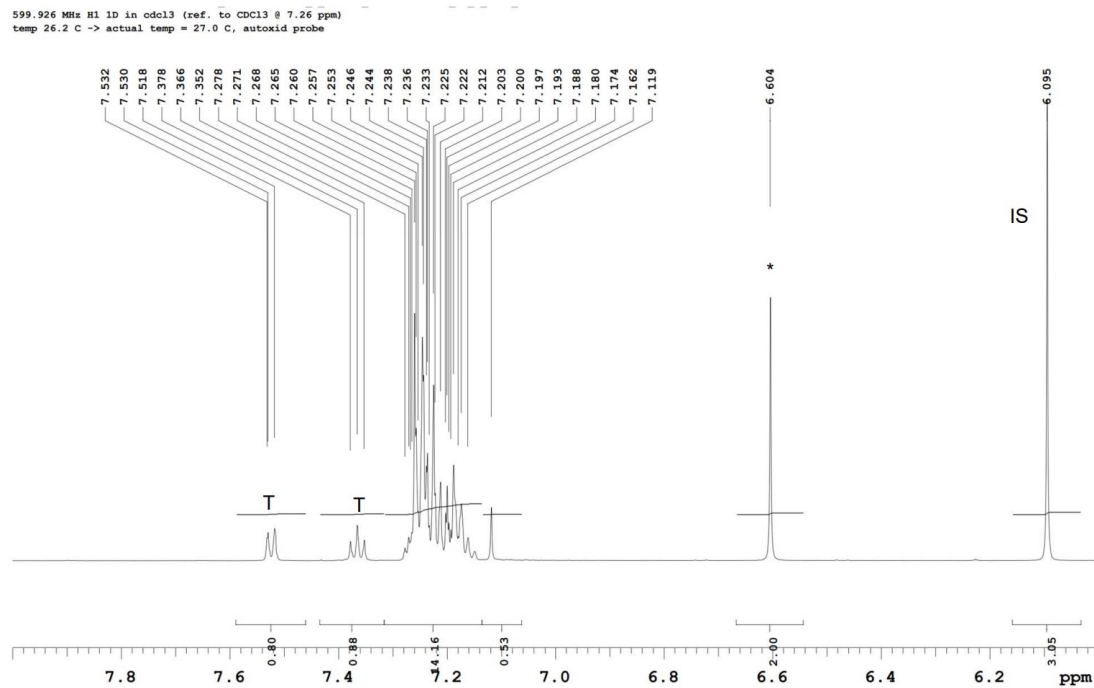


Figure S3.30. Zoom in ¹H NMR of stilbene isomerization by 5-1-ITO-NP for 88 h; the δ region from 6 to 8 ppm

Crystallographic Experimental Details for 3CzImIPN (1)

Crystals suitable for solid-state structure determination were prepared by liquid–liquid diffusion of Et₂O into a DCM solution of **1**.

Table S3.1. Crystallographic Experimental Details.

A. Crystal Data

formula	C ₄₇ H ₂₇ N ₇
formula weight	689.75
crystal colour and habit ^a	yellow plate
crystal dimensions (mm)	0.16 × 0.10 × 0.03
crystal system	orthorhombic
space group	<i>Pbcn</i> (No. 60)
unit cell parameters ^b	
<i>a</i> (Å)	42.8659(8)
<i>b</i> (Å)	11.9178(2)
<i>c</i> (Å)	14.3275(2)
<i>V</i> (Å ³)	7319.5(2)
<i>Z</i>	8
ρ _{calcd} (g cm ⁻³)	1.252
μ (mm ⁻¹)	0.596

B. Data Collection and Refinement Conditions

diffractometer	Bruker D8/APEX II CCD ^c
radiation (λ [Å])	Cu Kα (1.54178) (microfocus source)
temperature (°C)	–100
scan type	ω and φ scans (1.0°) (5-10-15 s
exposures) ^d	
data collection 2θ limit (deg)	147.59
total data collected	112845 (–52 ≤ <i>h</i> ≤ 53, –14 ≤ <i>k</i> ≤ 14, –17 ≤ <i>l</i> ≤ 17)
independent reflections	7372 (<i>R</i> _{int} = 0.0651)
number of observed reflections (<i>NO</i>)	5922 [<i>F</i> _o ² ≥ 2σ(<i>F</i> _o ²)]
structure solution method	intrinsic phasing (<i>SHELXT-2014</i> ^e)
refinement method	full-matrix least-squares on <i>F</i> ²
(<i>SHELXL-2018</i> ^f)	
absorption correction method	Gaussian integration (face-indexed)
range of transmission factors	1.0000–0.9079
data/restraints/parameters	7372 / 0 / 487
goodness-of-fit (<i>S</i>) ^g [all data]	1.031
final <i>R</i> indices ^h	
<i>R</i> ₁ [<i>F</i> _o ² ≥ 2σ(<i>F</i> _o ²)]	0.0427
<i>wR</i> ₂ [all data]	0.1074

largest difference peak and hole

0.152 and $-0.210 \text{ e } \text{\AA}^{-3}$

^aObtained by recrystallization from a dichloromethane / diethylether solution.

^bObtained from least-squares refinement of 9903 reflections with $7.70^\circ < 2\theta < 144.70^\circ$.

^cPrograms for diffractometer operation, data collection, data reduction and absorption correction were those supplied by Bruker.

^dData were collected with the detector set at three different positions. Low-angle (detector $2\theta = -33^\circ$) data frames were collected using a scan time of 5 s, medium-angle (detector $2\theta = 75^\circ$) frames using a scan time of 10 s, and high-angle (detector $2\theta = 117^\circ$) frames using a scan time of 15 s.

^eSheldrick, G. M. *Acta Crystallogr.* **2015**, *A71*, 3–8. (*SHELXT-2014*)

^fSheldrick, G. M. *Acta Crystallogr.* **2015**, *C71*, 3–8. (*SHELXL-2018/3*)

^g $S = [\sum w(F_o^2 - F_c^2)^2 / (n - p)]^{1/2}$ (n = number of data; p = number of parameters varied; $w = [\sigma^2(F_o^2) + (0.0469P)^2 + 2.3571P]^{-1}$ where $P = [\text{Max}(F_o^2, 0) + 2F_c^2]/3$).

^h $R_1 = \sum ||F_o| - |F_c|| / \sum |F_o|$; $wR_2 = [\sum w(F_o^2 - F_c^2)^2 / \sum w(F_o^4)]^{1/2}$.

Supplementary References

- (1) M. A. Robb, J. R. Cheeseman, G. Scalmani, V. Barone, G. A. Petersson, H. Nakatsuji, X. Li, M. Caricato, A. V. Marenich, J. Bloino, B. G. Janesko, R. Gomperts, B. Mennucci, H. P. Hratchian, J. V. Ortiz, A. F. Izmaylov, J. L. Sonnenberg, D. Williams-Young, F. Ding, F. Lipparini, F. Egidi, J. Goings, B. Peng, A. Petrone, T. Henderson, D. Ranasinghe, V. G. Zakrzewski, J. Gao, N. Rega, G. Zheng, W. Liang, M. Hada, M. Ehara, K. Toyota, R. Fukuda, J. Hasegawa, M. Ishida, T. Nakajima, Y. Honda, O. Kitao, H. Nakai, T. Vreven, K. Throssell, J. A. Montgomery, Jr., J. E. Peralta, F. Ogliaro, M. J. Bearpark, J. J. Heyd, E. N. Brothers, K. N. Kudin, V. N. Staroverov, T. A. Keith, R. Kobayashi, J. Normand, K. Raghavachari, A. P. Rendell, J. C. Burant, S. S. Iyengar, J. Tomasi, M. Cossi, J. M. Millam, M. Klene, C. Adamo, R. Cammi, J. W. Ochterski, R. L. Martin, K. Morokuma, O. Farkas, J. B. Foresman, and D. J. Fox, Gaussian, Inc., Wallingford CT, 2016.
- (2) Devlin, F. J.; Finley, J. W.; Stephens, P. J.; Frisch, M. J. Ab Initio Calculation of Vibrational Absorption and Circular Dichroism Spectra Using Density Functional Force Fields: A Comparison of Local, Nonlocal, and Hybrid Density Functionals. *J. Phys. Chem.* **1995**, *99* (46), 16883–16902. <https://doi.org/10.1021/j100046a014>.
- (3) McLean, A. D.; Chandler, G. S. Contracted Gaussian Basis Sets for Molecular Calculations. I. Second Row Atoms, $Z = 11-18$. *J. Chem. Phys.* **1980**, *72* (10), 5639–5648. <https://doi.org/10.1063/1.438980>.
- (4) Rasu, L.; Amiri, M.; Bergens, S. H. Carbazole–Cyanobenzene Dyes Electrografted to Carbon or Indium-Doped Tin Oxide Supports for Visible Light-Driven Photoanodes and Olefin Isomerizations. *ACS Appl. Mater. Interfaces* **2021**, *13* (15), 17745–17752. <https://doi.org/10.1021/acsami.1c05064>.